VOLUME 79 MAY 8, 1975 NUMBER 10

JPCHAx

THE JOURNAL OF PHYSICAL CHEMISTRY

PUBLISHED BIWEEKLY BY THE AMERICAN CHEMICAL SOCIETY

THE JOURNAL OF

PHYSICAL CHEMISTRY

AMERICAN CHEMICAL SOCIETY, *1155 Sixteenth St., N.W., Washington, D.C. 20036*

Books and Journals Division

JOHN K CRUM *Director*
VIRGINIA E. STEWART *Assistant to the Director*

CHARLES R. BERTSCH *Head, Editorial Processing Department*
D. H. MICHAEL BOWEN *Head, Journals Department*
BACIL GUILEY *Head, Graphics and Production Department*
SELDON W. TERRANT *Head, Research and Development Department*

 Published biweekly by the American Chemical Society at 20th and Northampton Sts., Easton, Pa. 18042. Second-class postage paid at Washington, D.C., and at additional mailing offices.

All manuscripts should be sent to *The Journal of Physical Chemistry,* Department of Chemistry, University of Minnesota, Minneapolis, Minn. 55455.

Additions and Corrections are published once yearly in the final issue. See Volume 78, Number 26 for the proper form.

Extensive or unusual alterations in an article after it has been set in type are made at the author's expense, and it is understood that by requesting such alterations the author agrees to defray the cost thereof.

The American Chemical Society and the Editor of *The Journal of Physical Chemistry* assume no responsibility for the statements and opinions advanced by contributors.

Correspondence regarding accepted copy, proofs, and reprints should be directed to Editorial Processing Department, American Chemical Society, 20th and Northampton Sts., Easton, Pa. 18042. Department Head: CHARLES R. BERTSCH. Associate Department Head: MARIANNE C. BROGAN. Assistant Editor: CELIA B. MCFARLAND. Editorial Assistant: JOSEPH E. YURVATI.

Advertising Office: Centcom, Ltd., 50 W. State St., Westport, Conn. 06880.

Business and Subscription Information

Send all new and renewal subscriptions *with payment* to: Office of the Controller, 1155 16th Street, N.W., Washington, D.C. 20036. Subscriptions should be renewed promptly to avoid a break in your series. All correspondence and telephone calls regarding changes of address, claims for missing issues, subscription service, the status of records, and accounts should be directed to Manager, Membership and Subscription Services, American Chemical Society, P.O. Box 3337, Columbus, Ohio 43210. Telephone (614) 421-7230. For microfiche service, contact ACS Journals Department, 1155 16th St. N.W., Washington, D.C. 20036. Telephone (202) 872-4444.

On changes of address, include both old and new addresses with ZIP code numbers, accompanied by mailing label from a recent issue. Allow four weeks for change to become effective.

Claims for missing numbers will not be allowed (1) if loss was due to failure of notice of change in address to be received before the date specified, (2) if received more than sixty days from date of issue plus time normally required for postal delivery of journal and claim, or (3) if the reason for the claim is "issue missing from files."

Subscription rates (hard copy or microfiche) in 1975: $20.00 for 1 year to ACS members; $80.00 to nonmembers. Extra postage $4.50 in Canada and PUAS, $5.00 other foreign. Supplementary material (on microfiche only) available on subscription basis, 1975 rates: $15.00 in U.S., $19.00 in Canada and PUAS, $20.00 elsewhere. All microfiche airmailed to non-U.S. addresses; air freight rates for hard-copy subscriptions available on request.

Single copies for current year: $4.00. Rates for back issues from Volume 56 to date are available from the Special Issues Sales Department, 1155 Sixteenth St., N.W., Washington, D.C. 20036.

Subscriptions to this and the other ACS periodical publications are available on microfilm. For information on microfilm write Special Issues Sales Department at the address above.

Notice to Authors last printed in the issue of January 16, 1975

THE JOURNAL OF

PHYSICAL CHEMISTRY

Volume 79, Number 10 May 8, 1975

JPCHAx 79(10) 951-1044 (1975)

ISSN 0022-3654

COMMUNICATIONS TO THE EDITOR

■ Miniprint material for this paper is available separately, in photocopy or microfiche form. Ordering information is given in the paper.

* In papers with more than one author, the asterisk indicates the name of the author to whom inquiries about the paper should be addressed.

AUTHOR INDEX

THE JOURNAL OF
PHYSICAL CHEMISTRY

VOLUME 79, NUMBER 10 MAY 8, 1975

Kinetics of Reduction of the Catalase–Hydrogen Peroxide Complex by Ethanol

Mordechai L. Kremer

Department of Physical Chemistry, The Hebrew University, Jerusalem, Israel *(Received September 12, 1974)*

Publication costs assisted by the Central Research Fund of the Hebrew University

The effect of donors (alcohol) on the kinetics of the enzyme–substrate complex (ES) of catalase and H_2O_2 has been investigated theoretically. It has been shown that low concentrations of the donor affect only the terminal stage of the kinetics by causing the otherwise stable complex to disappear. By increasing the concentration of the donor, at constant initial enzyme and substrate concentrations, the maximal concentration of the complex is also affected (decreased). The bimolecular rate constant of the reaction of ES with alcohol has been calculated by constructing simulated decay curves with the help of a computer and by comparing them with the experiment: $k_5 = (1.00 \pm 0.05) \times 10^3\ M^{-1}\ \text{sec}^{-1}$. The "spontaneous" decomposition of ES is discussed and it is shown that it may be due either to the reduction of ES by a residual donor in the system (exogenous or endogenous) or to an irreversible transformation of ES into ES′ (inactive). Some evidence favoring the latter possibility is discussed.

The reactions of the enzyme substrate complex (ES) of catalase and H_2O_2(S) with various hydrogen donors (H_2A), such as, alcohol, formate, etc., have been studied extensively by Chance,[1,2] and also by others.[3,4] It was observed that, when catalase was mixed with H_2O_2 in the presence of a hydrogen donor, the concentration of the enzyme substrate complex rose rapidly to a maximum, then declined, at a rate depending on the total concentration of the hydrogen donor (a_0), to zero. In a limited range of donor concentrations the decay of ES was pseudo-first order, the pseudo-first-order rate constant being proportional to a_0. The rate constant of the reaction of the donor with ES (k_5) was evaluated by using the equation

$$k_5 = 0.693/(a_0\tau_{off}) \qquad (1)$$

τ_{off} is the time necessary for the concentration of ES to decrease from its maximal value (p_m) to $0.5p_m$. Deviations from eq 1 were observed, however, when, at a constant initial enzyme and peroxide concentration, a_0 was increased or decreased beyond certain limits. No quantitative interpretation of the rate data has been given in this extended region of donor concentrations.[2,5]

Recently, a new kinetic analysis of the peroxidatic mechanism of catalase action has been performed. It has been found that, in a system containing catalase and H_2O_2 only, the enzyme substrate complex ES is stable.[6] In the presence of a reducing donor, this complex becomes labile and its concentration decreases eventually, toward the end of the reaction, to zero. It is the purpose of the present work (1) to investigate in a systematic fashion the effect of a reducing donor on the kinetics of the enzyme substrate intermediate and (2) to define conditions in which the decay of ES is of first order.

The Peroxidatic Mechanism

Our discussion is based on the peroxidatic mechanism of catalase action. It is given by the following set of reactions:[5,7]

$$\begin{array}{lll} & \mathrm{E} + \mathrm{S} \xrightarrow{1} \mathrm{ES} & \\ & e - p \quad x & \\ \mathrm{ES} + \mathrm{S} \xrightarrow{4} & \mathrm{E} + \mathrm{O_2} + 2\mathrm{H_2O} & \\ p \quad x & & \\ \mathrm{ES} + \mathrm{H_2A} \xrightarrow{5} & \mathrm{E} + \mathrm{A} + 2\mathrm{H_2O} & \\ p \quad a & & \end{array} \qquad (A)$$

E denotes a haematin group of catalase. Small type letters denote concentrations. e is the total concentration of catalase haematin.[8] If a is zero, the concentration of ES increases, in a given reaction, toward an upper limit as time tends to infinity.[6,9] This final concentration is a function of the initial concentrations of catalase and of peroxide and is itself bound by an upper limit given by $k_1e/(k_1 + k_4)$.[10]

The addition of a donor changes basically the kinetics of the intermediate. The concentration of the intermediate no

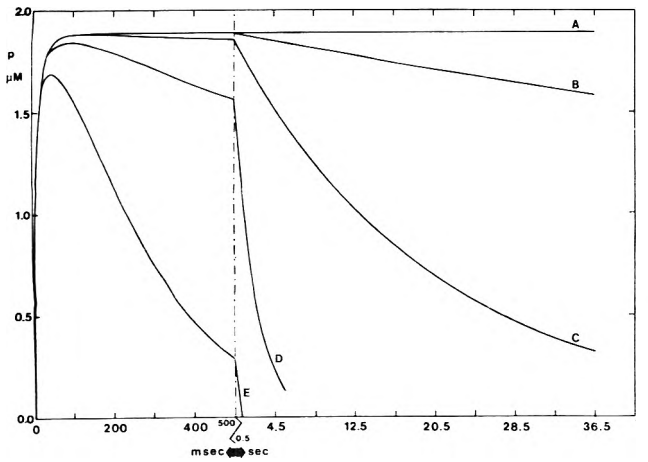

Figure 1. Formation and decomposition curves of the catalase–H_2O_2 intermediate in the presence of various concentrations of alcohol: $k_1 = 3.01 \times 10^6\ M^{-1}\ sec^{-1}$, $k_4 = 5.59 \times 10^6\ M^{-1}\ sec^{-1}$, $k_5 = 1.00 \times 10^3\ M^{-1}\ sec^{-1}$, $e = 5.44\ \mu M$, $x_0 = 12\ \mu M$, $a_0(A) = 0\ \mu M$, $a_0(B) = 5\ \mu M$, $a_0(C) = 50\ \mu M$, $a_0(D) = 500\ \mu M$, $a_0(E) = 5000\ \mu M$.

longer tends to a final upper limit, but passes instead through a maximum (Figure 1).

The time course of p is, in general, complicated. It depends both on the initial concentrations of the reactants and on the relative magnitudes of the various rate constants. The kinetics of the declining phase of p, however, is greatly simplified in the real case of catalase, in which k_5, for all known donors, is by at least three orders of magnitude smaller than either k_1 or k_4. Because of the condition $k_5 \ll k_4$, the consumption ratio of donor and peroxide is usually much smaller than one. As a consequence, the ratio a/x can reach very high values toward the end of the reaction, even in cases in which this ratio is very small initially. Thus, low concentrations of the donor may have a considerable effect on the kinetics of the final phase, although such concentrations are too small to have an effect on the maximal concentration of the complex. These qualitative considerations are illustrated by digital computer calculations, the results of which are summarized in Table I and are shown in Figure 1. The calculations were performed on the CDC 6400 computer of the Hebrew University, using a Fortran program. The time differentials dp/dt, $d[O_2]/dt$ etc., obtained from the rate equations, were used to calculate the approximate values of the respective concentration variables at a time $t + \Delta t$, assuming that the concentration at time t is known. By starting the process at $t = 0$ and by repeating it for subsequent time intervals, the approximate time curves for all concentration variables were obtained (some by using material balance equations). As the error in calculating concentrations in this way is cumulative, the approximation was regarded as adequate, when a decrease of the time interval Δt by a factor of 2 did not affect the final part of the concentration–time curves by more than 0.05%. Δt, used in the calculations, was in the range of 5 μsec–1 msec, depending on the speed of the reaction.[6]

Figure 1 shows the effect of donor on the kinetics of the intermediate complex. In the absence of donor, the intermediate is stable indefinitely (curve A). Small concentrations of donor affect the kinetics of the final stage, while the effect on p_m is negligible (curves B and C). Higher concentrations of the donor cause both a substantial increase of the rate of decomposition of ES and a decrease of p_m (curves D and E).

TABLE I: Effect of Donor on the Maximal Concentration of the Intermediate Complex[a]

a_0, μM	p_m, μM	a_m, μM	x_m, μM	t_m, msec
0	1.89	0	0	∞
5.00	1.89	5.00	0.0368	275
50.0	1.88	50.0	0.473	150
500	1.85	500	1.88	90
5000	1.69	5000	4.42	50

[a] $k_1 = 3.01 \times 10^6\ M^{-1}\ sec^{-1}$; $k_4 = 5.59 \times 10^6\ M^{-1}\ sec^{-1}$; $k_5 = 1.00 \times 10^3\ M^{-1}\ sec^{-1}$; $e = 5.44\ \mu M$; $x_0 = 12\ \mu M$.

Some results of the calculations, relevant to Figure 1, are shown in Table I. The rate constants refer to the respective steps of mechanism A. The subscript 0 denotes initial concentrations. The subscript m refers to quantities at the maximum of p. The following is seen from the data of Table I. (1) p_m approaches p_∞ (its upper limit for $a_0 = 0$) within 2%, up to 500 μM ethanol. (2) a_m is always practically identical with a_0; there is no consumption of ethanol up to $t = t_m$. At low a_0, this fact is due to the inability of ethanol to compete with S for ES. At high a_0, where competition already occurs, the fraction of ethanol reacting is very small, because of its large excess. (3) As a_0 is increased, t_m is decreased, while x_m is increased. The last effect is due to the repression of reaction 4 by reaction 5; increasing concentrations of ethanol cause an accumulation of unreacted peroxide at $t = t_m$.

The pair of values of a_m and x_m is an important indicator of the course of the reaction. A very low value of x_m together with $a_m = a_0$ implies that the reaction is biphasic: (a) in the first phase, x decreases to a low value, due to the reactions of S with E and ES. H_2A does not react at this stage of the reaction. (b) In the second phase, ES reacts with H_2A, in the practical absence of S.

It is noted that this separation of the kinetics into two phases is a prerequisite for the observation of a first-order decay of ES. At very low a_0, a second-order reaction ensues during phase b between ES and H_2A. With increasing a_0, the second-order reaction changes into a pseudo-first-order reaction, the rate constant being proportional to a_0. It is under these conditions that eq 1 holds. By further increasing a_0, x_m will increase and the separation of the two phases will become less distinct. The formation of ES will go on in the second phase, while alcohol will start to react with ES in the first phase. As a consequence, deviations from first-order decay kinetics of ES will occur. By further increasing a_0, the two phases of the reaction will coalesce into a single continuous process: the reactions of peroxide and alcohol will occur side by side. To show this effect quantitatively, the decaying parts of the curves of Figure 1 were replotted in a first-order presentation. These are shown in Figure 2.

t_m was taken as zero time, p_0 was set equal to p_m. Curve B ($a_0 = 5\ \mu M$) is concave downward. It shows that the true order of the reaction is higher than one (two). Curves C and D are reasonably straight, indicating the range of applicability of eq 1. Curve E is concave upward near origin. It shows that the formation of ES continues also during the initial part of phase b; it indicates the beginning of the coalescence of the two phases of the reaction into a single phase. Figure 3 shows the same behavior in a different presentation. Here log $(0.693/\tau_{off})$ is plotted as a function of log a_0. To construct the graph, computer calculations by

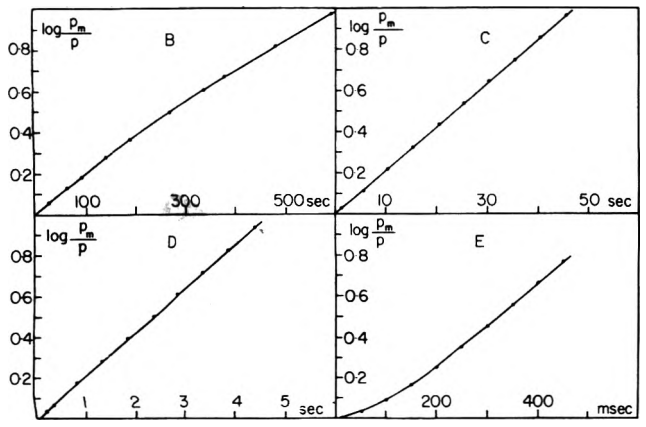

Figure 2. First-order presentations of the decaying parts of the curves of Figure 1.

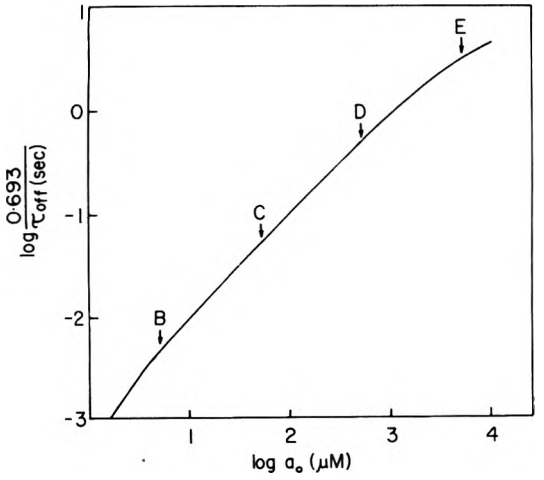

Figure 3. Logarithmic presentation of the "first-order rate constant" as a function of the alcohol concentration. The points corresponding to the curves of Figure 2 are indicated by arrows: $k_1 = 3.01 \times 10^6$ M^{-1} sec^{-1}, $k_4 = 5.59 \times 10^6$ M^{-1} sec^{-1}, $k_5 = 1.00 \times 10^3$ M^{-1} sec^{-1}, $e = 5.44$ μM, $x_0 = 12$ μM.

varying a_0 were performed. The points corresponding to the curves of Figures 1 and 2 are indicated by arrows. In the region, where first-order kinetics holds, a straight line with a slope of unity is obtained. At both high and low a_0 deviations from the straight line occur.

Comparison with Experiment

The accepted method for the determination of the rate constant of reaction of various donors with the intermediate complex of catalase and H_2O_2 consists of the measurement of the half time of decay (τ_{off}), in the presence of a known concentration of the donor (a_0). k_5 is then calculated from eq 1. In all cases studied, it was observed, that the pseudo-first-order rate constant $k_{fo} = 0.693/\tau_{off} = k_5 a_0$ did not become zero even in the absence of (deliberately added) donors. It tended, instead, to a more or less well-defined lower limit (k_{fo}(res)). This behavior was attributed to the presence of reducing donor(s) in the catalase preparations. The experimentally determined rate constants were corrected for this effect. This correction implies that in graphical presentation, essentially log Δk_{fo} was plotted against log Δa_0, where $\Delta k_{fo} = k_{fo} - k_{fo}$(res) and Δa_0 is the concentration of *added* donor. The residual rate constant has been determined experimentally as 0.02 sec^{-1}. The results obtained with ethanol as donor are given in Figure 4 (they are taken from Figure 2 of ref 2).

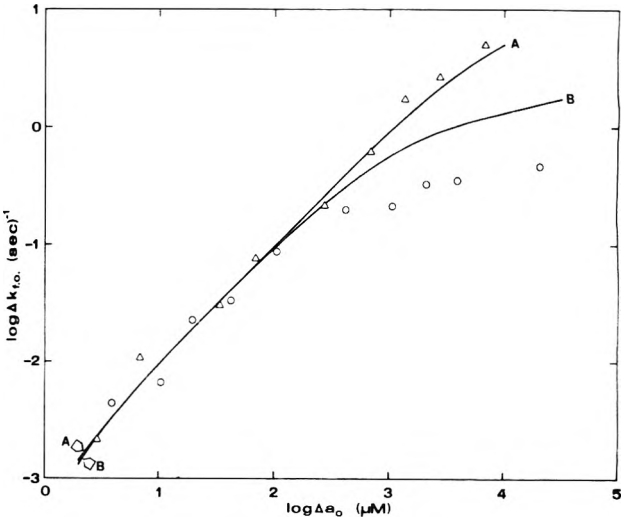

Figure 4. log Δk_{fo} as a function of log Δa_0 (experimental data of Chance[2]). Parameters for the theoretical curves are: $k_1 = 4.40 \times 10^6$ M^{-1} sec^{-1}, $k_4 = 8.17 \times 10^6$ M^{-1} sec^{-1}, $k_5 = 1.00 \times 10^3$ M^{-1} sec^{-1}, k_{fo}(res) $= 2.3 \times 10^{-2}$ sec^{-1}, a_0(res) = 23 μM, e(A) = 5.44 μM, x_0(A) = 15 μM, e(B) = 2.16 μM, x_0(B) = 200 μM; horse blood catalase.

To account for the these experimental results, theoretical plots of log $[(0.693/\tau_{off}) - 0.02]$ against log $[a_0 - a_0(\text{res})]$ were constructed. The varying parameter in these calculations was k_5. The values of k_1 and k_4 have been determined previously[6] (see also note added in proof). a_0(res) was estimated with sufficient accuracy, from the relation

$$a_0(\text{res}) = 0.02/k_5 \qquad (2)$$

It was thus a function of the parameter k_5. The best fitting curves, obtained by using $k_5 = 1.0 \times 10^3$ M^{-1} sec^{-1}, are shown in Figure 4. Curve A ($e = 5.44$ μM and $x_0 = 15$ μM) fits the experimental data well, both in the linear and in the nonlinear section. Curve B, on the other hand ($e = 2.16$ μM, $x_0 = 200$ μM), fits the data only at low a_0. It accounts for their trend at high a_0, however, the data fall in this range consistently below the calculated curve. It is not clear whether this discrepancy is due to a complication in the mechanism or to some systematic experimental error. (It may be noted that a very accurately fitting curve can be constructed by assuming an active hematein concentration of 0.65 μM and a spontaneous decay constant of 9×10^{-3} sec^{-1} in series B.) By applying the method of least squares to the data of series A and to the lower group of points of series B, the value $k_5 = (1.0 \pm 0.05) \times 10^3$ M^{-1} sec^{-1} was obtained. The residual alcohol concentration was calculated as a_0(res) = 23 μM.

Equation 1 holds in a limited section of curve A. log Δk_{fo} varies linearly in this region with log Δa_0. The slope of the line is unity and its intercept with the y axis is log k_5. Using this section of the curve Chance determined k_5 (1.0×10^3 M^{-1} sec^{-1}) in agreement with our results. There appears no linear region in curve B. The scatter of the data, however, at low a_0 is such that their deviation from linearity is not apparent.

The limitation of the use of eq 1 for the determination of k_5 have been discussed by Chance and coworkers.[2,9] The change of the decay kinetics was treated formally as a decrease of k_5, but no quantitative explanation for this effect

was found. It was assumed that the apparent decrease of k_5 was connected with H_2O_2 remaining in the system. To prove this point, the time t, necessary to reduce $[H_2O_2]$ from its initial value $[H_2O_2]_0$ to a certain lower limit, was calculated and compared with τ_{off}, the half-time of disappearance of ES.[2] It was argued, that at high c_0, t is not very much shorter than τ_{off} and, as a consequence, H_2O_2 does not disappear completely, before the decay of ES begins. As ES is formed continuously from H_2O_2, the decay of ES is retarded. While this conclusion is correct, its proof on the basis of the above reasoning is not exact. First, the equation used to calculate t

$$t = \frac{2.3}{ek_1'} \log \frac{[H_2O_2]_0}{[H_2O_2]} \qquad (3)$$

applies to the disappearance of H_2O_2 only in the absence of donors and only in the steady state. (k_1' is the second-order rate constant of decomposition of H_2O_2.) Neither of these conditions is fulfilled in the experiments. (1) When the alcohol concentration is high, the rate constant of disappearance of H_2O_2 is decreased.[7] (2) The steady-state approximation cannot be expected to hold down to very low $[H_2O_2]$, such as that existing toward the end of the time interval t.

More significantly, this approach cannot lead to the solution of the problem of overlap of the catalatic and peroxidatic reactions, which is the essential cause of the deviation of the kinetics from first order.

There is a discrepancy between the present value of k_5 and between that determined from overall kinetics: $1.8 \times 10^2\ M^{-1}\ sec^{-1}$.[7] There is no obvious explanation for this difference. It should be pointed out, however, that the latter experiments were performed using about 5000 times more dilute solutions of catalase. It has been found that k_1 and k_4 also vary between these extreme conditions.[6]

"Spontaneous" Decomposition

In the foregoing discussion it has been assumed that the spontaneous decomposition of ES is due to some residual alcohol content of the catalase preparations. While this explanation is a possible one, certain facts speak against it. (1) Repeatedly dialyzed and dried catalase preparations (to remove alcohol) showed the usual rate of disappearance of ES. (2) The spectrophotometric trace did not return in the end to the original base line (corresponding to free catalase), but overshot it perceptibly (Figures 3, 8, and 11 in ref 1). This excess optical absorption seems to have decreased with increasing concentration of alcohol.

These facts indicate that the process responsible for the disappearance of S is probably not its reaction with alcohol, in which catalase is freed, but a monomolecular transformation of ES

$$ES \xrightarrow{6} ES' \text{ (inactive)}$$

ES′ is an inactive complex of catalase and H_2O_2. It is not identical with the well-known red secondary complex, because in that case reaction 6 would not have been accompanied by a disappearance of the optical absorption decrement at 405 nm (the extinction coefficients of ES and of the red complex are very similar at this wavelength). Reaction 6 provides a possible pathway for the inactivation of catalase. It also explains why inactivation is retarded in the presence of alcohol (when step 5 competes with step 6), and why the excess optical absorption at the end of the reaction disappears at high alcohol concentrations.

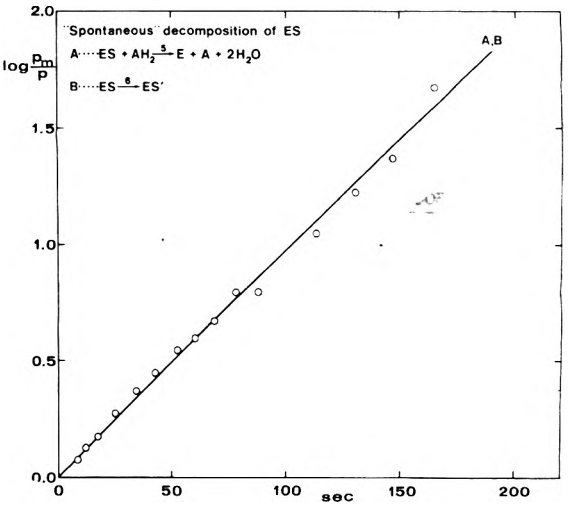

Figure 5. "Spontaneous" decomposition of the catalase–H_2O_2 intermediate (experimental data of Chance (ref 1, Figure 12, curve A)). Parameters for the theoretical curves: $k_1 = 4.40 \times 10^6\ M^{-1}\ sec^{-1}$, $k_4 = 8.17 \times 10^6\ M^{-1}\ sec^{-1}$, $e = 5.44\ \mu M$, $x_0 = 12\ \mu M$; (A) $k_5 = 1.00 \times 10^3\ M^{-1}\ sec^{-1}$, $a_0(res) = 23.7\ \mu M$; (B) $k_6 = 2.23 \times 10^{-2}\ sec^{-1}$; horse blood catalase.

Regarding the kinetics of the spontaneous decay of ES, Figure 5 shows two different curves. They are calculated (A) on the basis of peroxidation of residual alcohol (23.7 μM) in the final phase of the reaction and (B) on the basis of reaction 6 in the final phase ($k_6 = 2.23 \times 10^{-2}\ sec^{-1}$).

The two curves are practically indistinguishable one from the other. A closer examination of the curves (when plotted separately) reveals that, while curve B is a straight line, curve A is slightly bent; at this low concentration of alcohol, the decay of ES by path A is not strictly first order. It is seen that both curves account equally well for the experimental results (ref 1, Figure 12, curve A).

The determination of k_5 gives practically the same result, whether process A or B is assumed to be responsible for the spontaneous disappearance of ES. In case B, the fit of the data to the calculated optimal curve is slightly better.

The suggested reversal of step 1

$$ES \xrightarrow{2} E + S$$

as a possible route for the disappearance of ES has been ruled out already by Greenstein, who has shown that reaction 2 leads to a second-order disappearance of ES in the terminal phase of the reaction, contrary to the experiment.[11]

Separation of the Formation and Decomposition Phases of the Catalase–H_2O_2 Intermediate

In a recent discussion of the kinetics of catalase action it has been assumed that the formation and the spontaneous decomposition of the catalase–H_2O_2 intermediate can be treated separately.[6] This assumption implied that the observed maximal concentration of the intermediate was in fact the terminal concentration, on the time scale of the formation phase. The argument has been advanced that since the decay of ES is a first-order process, any formation of ES at this stage must have ceased, otherwise it would have interfered with the observed first-order kinetics. It follows from the same argument that, on the other hand, decay processes must have been negligible during the build-up of ES.

TABLE II: Maximal Concentration of Intermediate in the Presence of Decay Processes[a]

x_0, μM	p_∞, μM	p_m(A), μM	p_m(B), μM
2	1.566	1.558	1.558
4	2.556	2.546	2.544
8	3.666	3.651	3.650
10	3.980	3.965	3.964
20	4.610	4.598	4.596
40	4.754	4.749	4.747

[a] $k_1 = 4.40 \times 10^6\ M^{-1}\ sec^{-1}$; $k_3 = 1.00 \times 10^3\ M^{-1}\ sec^{-1}$; $k_4 = 8.17 \times 10^6\ M^{-1} sec^{-1}$; $e = 13.6\ \mu M$.

The present work allows a quantitative check of the separability of the two phases of the reaction. For this purpose, the maximal concentration of the intermediate in the presence of decay processes was calculated and compared with the limiting (terminal) value of p in the absence of such reactions. Both peroxidatic (A) and deactivation (B) modes of decay have been considered and the results are shown in Table II. The observed first-order rate constant of decay was taken as $5 \times 10^{-2}\ sec^{-1}$ (ref 1, Figure 9). In terms of mechanism A, it corresponds to a residual alcohol concentration of 50 μM. Assuming mechanism B, k_6 has been set equal to $5 \times 10^{-2}\ sec^{-1}$.

It is seen that the difference between p_∞ and p_m in every case is negligibly small, although the rate constant of the "spontaneous decay" in these experiments is relatively high. These results show that the formation and decomposition of the intermediate are well-separated processes, provided that only purified solutions of catalase are used and that no donors are added to the system deliberately.

Conclusions

Digital computer simulations extend considerably the range in which the kinetics of the enzyme–substrate complex of catalase and H_2O_2, in the presence of donors, can be investigated theoretically. With the aid of simulated curves the rate constant of reaction of ethanol with the catalase peroxide complex has been evaluated. The result agrees with the value obtained previously for this quantity in a limited range of alcohol concentrations. The investigation shows that it is not permissible, in general, to assume first-order kinetics for the decay of the intermediate and that the ratio $0.693/\tau_{off}$ does not have, in general, the meaning of a rate constant. Nevertheless, it is still a useful experimental parameter. The kinetics of disappearance of the intermediate at high a_0 is complex and no correction formula can extend the validity of first-order rate equations to this region.[9]

No unequivocal decision regarding the nature of the slow disappearance of the catalase–H_2O_2 intermediate can be made at present. It may be due to the reduction of the intermediate to free enzyme by residual alcohol of by some unknown reducing donor (endogeneous donor, reacting in a 1:1 stoichiometric ratio with ES).[12] Several lines of evidence indicate, however, that the actual process is a monomolecular deactivation of ES by its transformation into ES′ (inactive).

The slow spontaneous decay of ES does not interfere with the kinetics of its formation; the separation of the kinetics into a rapid and a slow phase, corresponding to the formation and decomposition of the enzyme substrate complex, is thus justified.

NOTE ADDED IN PROOF. After the completion of this work a revision of the values of k_1 and k_4 became necessary, due to the detection of a wrong parameter in the orginal calculations.[13] Thus, the revised values of k_1 and k_4 are 4.40×10^6 and $8.17 \times 10^6\ M^{-1}\ sec^{-1}$, respectively. All curves used for comparison with experimental data were, accordingly, recalculated (from Figure 4 onwards). The results were not altered significantly by this revision. Thus, the optimal value of k_5 became $1.00 \times 10^3\ M^{-1}\ sec^{-1}$, instead of $1.10 \times 10^3\ M^{-1}\ sec^{-1}$. Furthermore, the agreement between the respective values of p_∞ and p_m in Table II was improved to some extent.

Acknowledgment. I am indebted to Professor Britton Chance for helpful comments.

References and Notes

(1) B. Chance, *Acta Chem. Scand.*, **1**, 236 (1947).
(2) B. Chance, *J. Bicl. Chem.*, **182**, 643, 649 (1950).
(3) D. Keilin and P. Nicholls, *Biochim. Biophys. Acta*, **29**, 302 (1958).
(4) P. Nicholls and G. R. Schonbaum in "The Enzymes", Vol. **8**, P. D. Boyer, H. Lardy, and K. Myrback, Ed., 1963, p 147.
(5) B. Chance, D. S. Greenstein, and F. J. W. Roughton, *Arch. Biochem. Biophys.*, **37**, 30 (1952).
(6) E. Zidoni and M. L. Kremer, *Arch. Biochem. Biophys.*, **161**, 658 (1974).
(7) M. L. Kremer, *Biochim. Biophys. Acta*, **198**, 199 (1970).
(8) The numbering of the reactions follows the order adopted by Chance with the exception that Chance's reaction 4′ is denoted here as 4 and to Chance's reaction 4 is given the number 5.
(9) B. Chance, D. S. Greenstein, J. Higgins, and C. C. Yang, *Arch. Biochem. Biophys.*, **37**, 322 (1952).
(10) M. L. Kremer and S. Baer, *J. Phys. Chem.*, **78**, 1919 (1974).
(11) D. S. Greenstein, *Arch. Biochem. Biophys.*, **62**, 284 (1956).
(12) Calculations show that the concentration of the assumed donor is not appreciably decreased during a catalytic cycle. It could thus cause repeated reductions of ES.
(13) E. Zidoni and M. L. Kremer, *Arch. Biochem. Biophys.* (*Erratum*), in press.

Behavior of Hydrated Electrons in Micellar Solution. Studies with Cetyltrimethylammonium Bromide–Cetylpyridinium Chloride Mixed Micelles[1a]

Larry K. Patterson*[1b]

Radiation Research Laboratories and Department of Chemistry, Mellon Institute of Science, Carnegie-Mellon University, Pittsburgh, Pennsylvania 15213

and M. Grätzel

Radiation Laboratory, University of Notre Dame, Notre Dame, Indiana 46556 *(Received October 2, 1974)*

Publication costs assisted by Carnegie-Mellon University and the U.S. Atomic Energy Commission

Rates of electron disappearance have been measured in solutions of cetyltrimethylammonium bromide micelles (CTAB) labeled with varying quantities of highly reactive cetylpyridinium chloride (CPyCl). Investigations of systems containing more than one probe per micelle (P/M > 1) allow discrimination between interaction of e_{aq}^- with the micelle and with the reactive probe; in systems where (P/M < 1) the migration of electrons from micelle to micelle may be examined. The results of these studies are consistent with a model in which three separate processes influence electron behavior: (1) trapping of e_{aq}^- by the CTAB micelle surface ($k_T \sim 6 \times 10^{11}\ M^{-1}\ sec^{-1}$); (2) movement on the surface to a single reactive probe molecule ($\tau < 3$ nsec); (3) migration of the electron from micelle to micelle (dependent on surfactant concentration). These processes are interpreted in terms of e_{aq}^- interaction with the micellar surface potential field.

Introduction

Because surfactant micelles exhibit some characteristics comparable to those of more complex biological systems, their interaction with ionizing radiation has been the subject of several pulse radiolysis studies. Though these structural aggregates react readily with H· and ·OH, simple surfactants such as sodium lauryl sulfate (NaLS) and cetyltrimethylammonium bromide (CTAB) are quite unreactive toward hydrated electrons ($k_{e_{aq}^- + surf} < 10^6\ M^{-1}\ sec^{-1}$).[2] It has been shown, however, that the presence of these aggregates in aqueous solution may alter the reactivity toward e_{aq}^- of organic compounds which partition between the aqueous phase and micellar pseudo-phase. This behavior has been observed for such diverse substrates as benzene, biphenyl, naphthalene, CH_2I_2, duroquinone, and benzophenone.[2a,3-6] In all such cases, *anionic* micelles (NaLS) reduced the rate constant for reaction of e_{aq}^- with substrate ($k_{e_{aq}^- + sub}$) while *cationic* micelles enhanced it. The inhibiting effect observed with NaLS may be correlated with the high repulsive influence of the negatively charged surface layer which repels e_{aq}^- thus protecting solubilized substrate from electron attachment.[5] Conversely it would be expected that, even though e_{aq}^- is not annihilated by it, a positively charged micelle would accelerate e_{aq}^- toward its surface to enhance interaction with substrate. In fact, recent measurements using cetylpyridinium chloride (CPyCl)—whose headgroup imparts a high reactivity to the monomeric surfactant ($k_{e_{aq}^- + CPyCl} \sim 1 \times 10^{10}\ M^{-1}\ sec^{-1}$)—have shown that $k_{e_{aq}^- + micelle}$ alone may be as high as $5 \times 10^{12}\ M^{-1}\ sec^{-1}$.[7] This result was interpreted in terms of very rapid electron trapping in the positive potential field of the micelle. The interpretation was supported by ionic strength experiments. In the absence of a reactive headgroup this localization of e_{aq}^- in the region of the micelle would—with an accessible substrate—lead to an increased e_{aq}^-–substrate interaction.

In the present work an investigation has been undertaken to determine the behavior of the electron once trapped in the electrostatic field of the CTAB micelle. By labeling CTAB aggregates with reactive CPyCl monomers it has been possible to examine e_{aq}^- disappearance as a function of the number of CPyCl probes per micelle (P/M). Alternatively conditions may be employed where one probe is present for a number of micelles and the possibility of electron movement among micelles may be examined. Complimentary ionic strength studies and measurements of micelle effects on rates of e_{aq}^- reaction with positive ions in solution have also been carried out. It is shown in these studies that the behavior of e_{aq}^- in a CTAB micelle system containing a reactive probe may be expressed in terms of three basic processes outlined in Figure 1: (a) *trapping* of e_{aq}^- from the bulk phase by the potential field of the micelle; (b) *intramicellar electron scavenging* by a reactive probe residing on the micelle surface; (c) *electron migration* from one micelle to a second micelle in solution.

Experimental Section

Both cetyltrimethylammonium bromide (CTAB) and cetylpyridinium chloride (CPyCl) were obtained from Eastman Kodak and purified by repeated recrystallization from ethanol. The 3-(dimethyldodecylammonio)-propane-1-sulfonate (DDAPS) was supplied to us by Dr. J. H. Fendler. Nanosecond and computer controlled pulse radiolysis units used in this study have been previously described.[8]

Results and Discussion

Nature of the Surface Potential Field. Behavior of negative ions, such as the hydrated electron, in the presence of cationic micelles will be governed largely by the nature of the potential field surrounding the positively charged aggregate. This is true not only for rates of e_{aq}^- movement, namely, the trapping of e_{aq}^- in the electrostatic field of the micelle, but may also apply to the movement of e_{aq}^- on the micelle surface, and e_{aq}^- migration from micelle to micelle. In Figure 2 is illustrated the potential distance profile for a

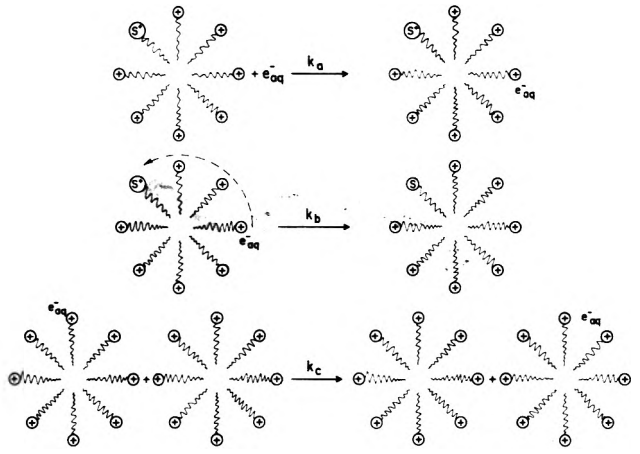

Figure 1. Schematic diagram for the behavior of the hydrated electron in a system of positively charged micelles. The e_{aq}^- trapping step is illustrated by k_a, intramicellar electron scavenging by k_b, and electron migration by k_c. The S^+ notation indicates a reactive probe.

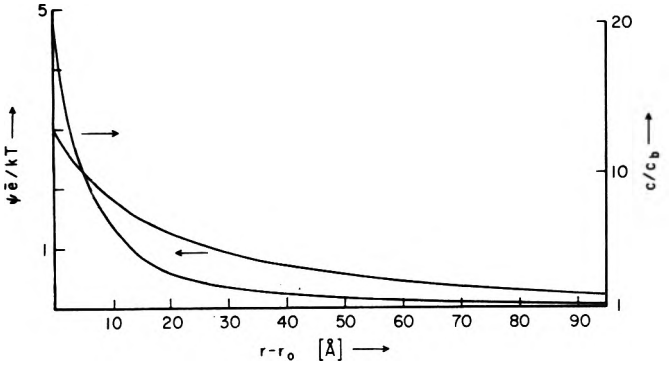

Figure 2. Reduced surface potential ($\bar{e}\psi_r/kT$) as a function of distance from the surface of a spherical micelle having a surface potential of 75 mV and a radius (R_0) of 10 Å. Ionic strength is assumed equal to the cmc of CTAB (8×10^{-4} *M*). The probability of finding e_{aq}^-, relative to that probability in the bulk phase (C/C_b), at a distance ($R - R_0$) from the surface is also given.

CTAB micelle with a surface potential of 75 mV and a diameter of 20 Å.[9a] This function was calculated from a numerical solution of the non-linear Poisson–Boltzmann equation for a system whose ionic strength is equal to a critical micelle concentration (cmc) of 8×10^{-4} *M*.[9b] The relative probability of finding a hydrated electron at a given distance ($R - R_0$) from the aggregate surface, compared to that in the bulk phase, under equilibrium conditions is calculated by introduction of the potential value (ψ_r) into the Boltzmann factor ($e^{-\bar{e}\psi_r/kT}$) where $\bar{e}$ is the elementary charge and k is the Boltzmann constant. This function, which is also presented in Figure 2, shows the strong attraction of the micellar surface for the negative entity, e_{aq}^-. However, it must also be noted that a significant probability exists for finding e_{aq}^- beyond the Onsager distance ($\bar{e}\psi_r/kT = 1$). In this model system the Onsager distance, where the electrostatic attraction is offset by thermal energy, corresponds to a separation from the surface of 28 Å.

The extension of the potential field into the surrounding aqueous phase will depend both on ionic strength and counterion binding. The first effect has been clearly demonstrated in the recent studies of e_{aq}^- reactions with CPyCl micelles.[7] In this study, ionic strength was varied by additions of NaCl whose negative ion component is the

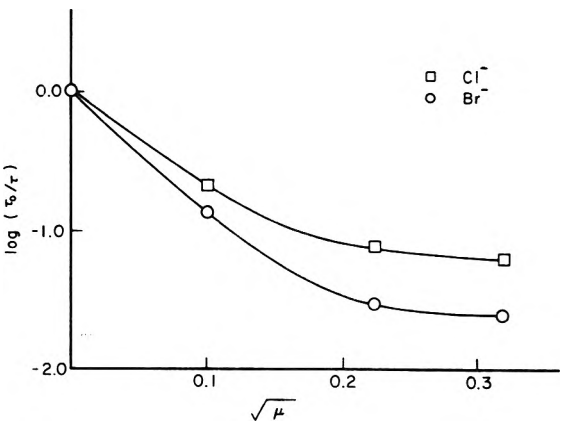

Figure 3. Relative effects of NaCl and NaBr on $(1/\tau)_{e_{aq}^- + CPy^+}$ as a function of ionic strength, μ. [CPyCl] = 2×10^{-3} *M*. τ_0 is e_{aq}^- lifetime in the absence of added electrolyte.

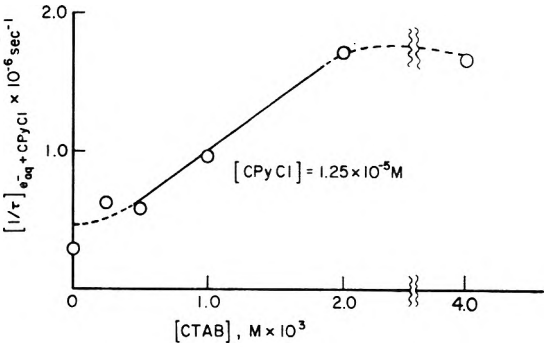

Figure 4. Dependence of $(1/\tau)_{e_{aq}^- + CPy^+}$ on CTAB concentration in the region of the CMC for CTAB. [CPyCl] = 1.25×10^{-5} *M*.

same as the surfactant counterion. A marked decrease in $k_{e_{aq}^- + CPyCl}$ was observed and is shown in Figure 3. It is reasonable to suppose that anions which bind to the CPyCl micelle surface more strongly than Cl^- would cause an even more pronounced decrease in $k_{e_{aq}^- + CPyCl}$. It has been observed that Br^- interacts more strongly with the cationic surface layer than does Cl^-.[10] Data are given in Figure 3 for the effect on $(1/\tau)_{e_{aq}^- + CPyCl}$ of addition of NaBr to CPyCl solutions. It is readily apparent that Br^- suppresses the rate much more effectively than Cl^-. Even at concentrations of electrolyte as low as 10^{-2} *M*, the decrease in rate $(1/\tau)$ observed with NaBr is a factor of 2 greater than that with NaCl. This underlines the efficiency with which Br^- replaces Cl^- at the surface and emphasizes the importance of the surface potential to interaction of e_{aq}^- with the micelle surface. Apparently the number of anions bound in the Stern layer is greater for NaBr solutions, leading to a diminished surface potential and, hence, smaller trapping rate. Having established the critical role of the surface potential and variations in it to electron behavior in micellar systems, one may now proceed to examine a more detailed mechanism of the micelle–electron interaction.

Comicellization of CPyCl and CTAB. A comparison of CTAB and CPyCl monomer structure suggests strongly that comicellization between these two compounds should occur. Both have similarly charged headgroups and aliphatic chains 16 carbons in length. As micelle structure with its associated potential field becomes defined above the critical micelle concentration (cmc), e_{aq}^- in bulk solution will be accelerated toward the surface. Changes in

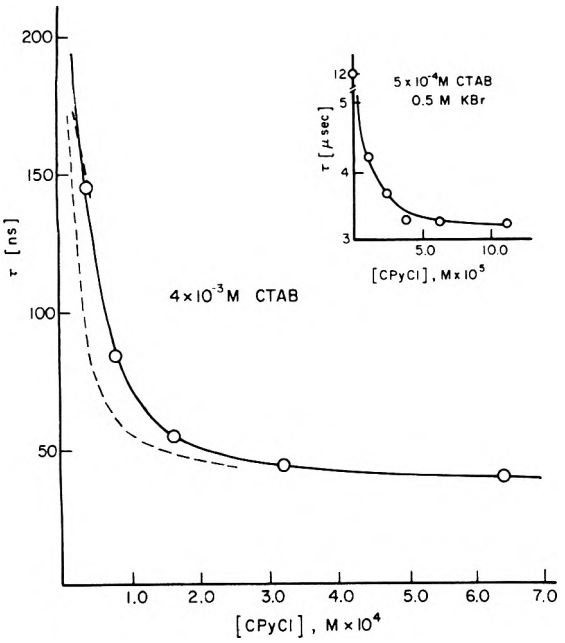

Figure 5. Effect of adding CPyCl to a 4 × 10^{-3} *M* CTAB solution. (. . . .) Calculated curve based on the binomial distribution formula[12] assuming τ for a system of singly occupied micelles to be 43 nsec (see text) and that the proportion of CPyCl in micellar form will equal that for CTAB, i.e., ([CTAB] − cmc)/[CTAB]. Insert shows similar experiment in 5 × 10^{-4} *M* CTAB and 0.5 *M* KBr. Here the cmc is expected to be ~10^{-5} *M*.[13]

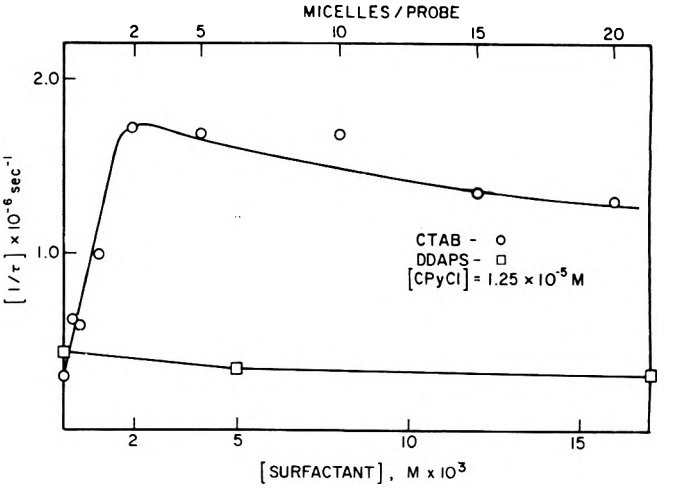

Figure 6. Dependence of $(1/\tau)_{e_{aq}^- + CPy^+}$ on CTAB and DDAPS concentrations where CPyCl is held constant at 1.25 × 10^{-5} *M*.

rates of electron attachment in very small concentrations of CPyCl with increasing CTAB concentration may then be used as a test of comicellization. Rates of e_{aq}^- disappearance, $1/\tau$, have been measured for 1.25 × 10^{-5} *M* CPyCl with concentrations of CTAB varying through the cmc. Results are given in Figure 4 and indicate an increase in the region of aggregate formation which continues until CPyCl uptake is complete. It is assumed that CPyCl will be incorporated in the same proportion as CTAB, i.e., under most conditions of this study only a negligible concentration of CPyCl will remain in bulk solution.

In the above discussion it has been pointed out that Br^- binds more strongly to the micelle surface than Cl^-. Hence small concentrations of Cl^- accompanying the cetylpyridinium cation will not disturb the micelle counterion atmosphere.

Multiple CPyCl Monomers per Micelle. Reaction of e_{aq}^- with the CPyCl probe on the micellar surface may be visualized as proceeding through two steps: (a) trapping of e_{aq}^- in the potential field; (b) translation within the field to the probe site. Should rate a ≫ b, $1/\tau$ will depend largely on the number of probes in the surface layer, where the rate-determining step occurs. However if step a is rate determining only the concentration of labeled micelles will govern $(1/\tau)$. Relative velocities of the two processes have been investigated by measuring electron disappearance in systems of fixed CTAB concentration and increasing CPyCl. Measurements were taken both in solutions with an ionic strength, μ, of 0.5 and in systems with no added salt. The results are plotted in Figure 5 and may be discussed in terms of average concentration of probes per micelle (P/M). The latter parameter was obtained by dividing the concentration of CPyCl monomers by the concentration of CTAB micelles. Concentrations of micelles can be calculated from the total surfactant concentration via [micelles] = ([CTAB] − cmc)/*n*, where *n* = aggregation number = 80 for CTAB solutions.[11] A principal feature of this data is that as (P/M) reaches ~2, the value of $1/\tau$ begins to approach a plateau and increases very little with additional probe. This effect is most pronounced under conditions of high ionic strength where rate a is inhibited by a decreased surface potential. From distribution calculations it may be shown that at about (P/M) = 2, about 90% of the micelles will be occupied by at least one probe.[12] Hence it is apparent that rate b > rate a at 4 × 10^{-3} *M* CTAB and that the inequality is more pronounced at lower micelle concentrations and high ionic strength. From these observations, it is apparent that at relatively low micelle concentrations trapping of the electron is the rate-determining step. The plateau value of τ in the absence of electrolyte is about 40 nsec. It may be implied that the specific rate for the intramicellar reaction of e_{aq}^- with probe is faster than the trapping rate by a factor of 10 or more. The rate for the trapping reaction of e_{aq}^- by CTAB micelles then governs the magnitude of τ and the extrapolated value of 40 nsec reflects a half-lifetime for this process of 30 nsec. With a concentration of 4 × 10^{-5} *M* micelles this may be expressed in terms of a pseudo-first-order electron trapping rate constant, k_T, of 6 × 10^{11} M^{-1} sec^{-1}. One may then also set an upper limit for the disappearance of e_{aq}^- by intramicellar scavenging of ~3 nsec or less.

The curve obtained at high ionic strength displays features similar to the data for low ionic strength. A plateau is again approached at (P/M) ~2, however, k_T obtained under these conditions is predictably much lower. The pronounced dependence of k_T on ionic strength again emphasizes the control exercised over the trapping mechanism by the potential field.

Multiple Micelles per Probe. By inverting the conditions under which data in Figure 5 have been gathered, e_{aq}^- behavior may be examined in systems containing only a small fraction of labeled micelles. Beginning with a CPyCl concentration of 1.25 × 10^{-5} *M*, $1/\tau$ has been determined in solutions of increasing CTAB. Changes in $1/\tau$ as a function of CTAB are illustrated in Figure 6 which extends the range of Figure 4 into regions well above the cmc. The rate increases sharply due to comicellization previously described but then falls very slowly at higher CTAB concentration, remaining well above the value of $1/\tau$ measured for CPyCl

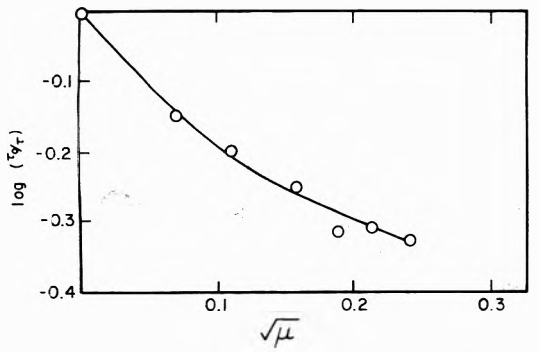

Figure 7. Ionic strength effects on the reaction of e_{aq}^- with 2.5×10^{-5} *M*. CPyCl in 0.025 *M* CTAB (P/M $\ll$ 1). Added electrolyte was NaCl.

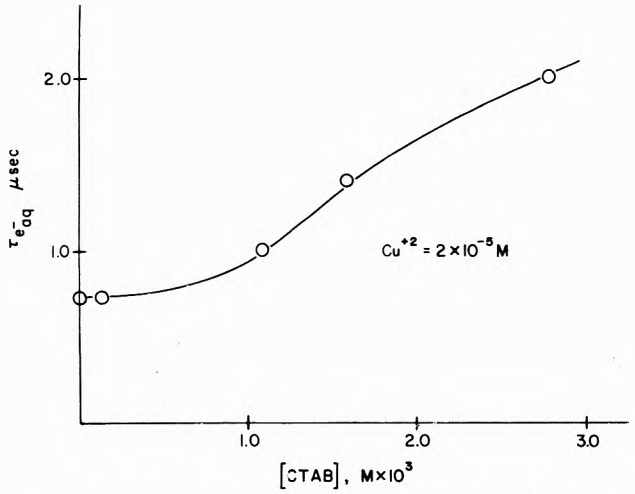

Figure 8. Effect on $(1/\tau)_{e_{aq}^- + Cu^{2+}}$ of adding CTAB to 2×10^{-5} *M* Cu^{2+} in the region of the cmc for CTAB.

monomer even at P/M ~ 1:100. Such behavior may only be understood in terms of e_{aq}^- migration from micelle to micelle as outlined in Figure 1c. This process continues until the electron: (1) reacts with CTAB; (2) encounters a reactive impurity or another electron; (3) is attached to a CPyCl probe by intramicellar scavenging. The values given in Figure 6 are corrected for (1) and (2) by measurements in CTAB solutions without probe. Assuming from the discussion above that intramicellar scavenging is very rapid compared to other processes and that random movement of e_{aq}^- among the aggregates occurs, a micelle to micelle migration time may be calculated for e_{aq}^- from the expression $[\tau(P/M)]$. Measurements were taken in more detail at CTAB concentrations of 0.01, 0.05, and 0.1 *M* varying (P/M) from (1:18–1:5), (1:100–1:10), and (1:50–1:10), respectively. Migration half times were determined to be 40 ± 5 nsec at 0.01 *M* CTAB, 23 ± 4 nsec at 0.05 *M*, and 12 ± 2 nsec at 0.1 *M*. In all cases the yield of e_{aq}^- reduction of CPy^+, measured by transient absorption, was found to approach unity assuring that e_{aq}^- annihilation is due to reaction with CPyCl. A similar set of experiments was carried out with 3-(dimethyldodecylammonio)-propane-1-sulfonate, DDAPS, as the micellar surfactant. This molecule is zwitterionic, forming an aggregate with no net charge and hence no surface potential field. It may be seen from Figure 6 that the presence of this surfactant produced very little effect on the reaction of e_{aq}^- with CPyCl though these two surfactants should also form comicelles. There are two possible mechanisms for the migration of e_{aq}^- from one positively charged micelle to another. The first alternative involves a two-step process: escape of e_{aq}^- from the host micelle followed by the retrapping by a second micelle. Since the dissociation requires sufficient energy to overcome the attractive potential of the host micelle it is reasonable to assume that this step is slow relative to the retrapping step in the region of CTAB concentration under study. This would explain why the migration half-life is not directly proportional to aggregate concentration at the lower concentrations. It is further reasonable to assume that the retrapping of e_{aq}^- does not differ from process a in Figure 1. One must also consider a second alternative involving direct intermicellar transfer of e_{aq}^- as a consequence of the close approach of two micelles during random diffusion. This would arise from overlap of potential fields sufficient to provide a thermodynamically favored path for migration. The latter mechanism may only be of consequence at high CTAB concentrations where the diffusion-controlled micelle–micelle collisions are relatively frequent.

Additional experiments were carried out to illustrate ionic strength effects on migration times. Figure 7 is a Debye-type plot of rate data as a function of ionic strength taken from solution of 2.5×10^{-5} *M* CPyCl and 0.025 *M* CTAB. Very marked increases in migration with increasing ionic strength are indicated by changes in τ and show that decreases in surface potential caused by additional electrolyte will be reflected in longer migration times. This finding is consistent with either of the two mechanisms proposed above. It may be noted that the ionic strength effect here is much less pronounced than for electron reaction with CPyCl micelles (Figure 3). In the migration mechanism a decreased surface potential will either enhance e_{aq}^- escape from the aggregate surface or enhance the approach of two micelles for overlap. Either of these effects will tend to increase migration and offset somewhat the decrease in trapping rate experienced in a diminished potential field.

Effect of CTAB on e_{aq}^- Reactions with Positive Ions. It was previously reported that unlike reactions involving hydrophobic substrates, the specific rate of reduction of Cu^{2+} by e_{aq}^- is decreased by a factor of 2 in the presence of 0.1 *M* CTAB.[3] The inhibition observed has been studied here in somewhat more detail. The half-lifetime of e_{aq}^- in 2×10^{-5} *M* Cu^{2+} is governed by a value for $k_{e_{aq}^- + Cu^{2+}}$ of 4.5×10^{10} M^{-1} sec^{-1}. With addition of CTAB above the cmc, the half-lifetime increases as a function of surfactant concentration (see Figure 8). This increase will be limited at higher CTAB concentrations by the decay of e_{aq}^- in CTAB.

A simple competition between ions, Cu^{2+}, and micelle would dictate that the e_{aq}^- decay curve would consist of two parts: a fast initial portion due to e_{aq}^- reduction of the ion followed by the slow decay of trapped electrons. However, in all cases e_{aq}^- decay obeys the first-order rate law. This is consistent with a mechanism of e_{aq}^- migration through the system until Cu^{2+} is encountered. The inhibition is then due to the cumulative time of e_{aq}^- residence in the CTAB field.

Conclusions

It has been shown that the fate of the hydrated electron in systems of positively charged aggregates such as cationic micelles is largely determined by interactions with the electrostatic field in the micelle–water interface. A probe such as CPyCl which efficiently comicellizes with CTAB is high-

ly suited for an investigation of these interactions. Kinetic behavior of e_{aq}^- in the presence of labeled and unlabeled CTAB micelles indicates that the reaction of e_{aq}^- with a molecule on a charged interface may be an extremely rapid process. This would indicate very fast diffusion on the micelle surface. Insights gained for the reactions of e_{aq}^- or other negatively charged species in micellar model systems may be found applicable to systems of more complex bioaggregates.

References and Notes

(1) (a) The Radiation Laboratory of the University of Notre Dame is operated under contract with the U.S. Atomic Energy Commission. This is AEC Document No. C00-38-972. Also supported in part by the U.S. Atomic Energy Commission under Contract No. AT(11-1)-3238 with Carnegie-Mellon University. (b) Address correspondence to this author at the Department of Medical Physics, Michael Reese Medical Center, Chicago, Ill. 60616.

(2) (a) K. M. Bansal, L. K. Patterson, E. J. Fendler, and J. H. Fendler, *Int. J. Radiat. Phys. Chem.*, **3**, 321 (1971); (b) C. L. Greenstock and I. Dunlop, *ibid.*, **5**, 237 (1973).

(3) S. C. Wallace and J. K. Thomas, *Radiat. Res.*, **54**, 49 (1973).

(4) J. H. Fendler, N. V. Klassen, and H. A. Gillis, *J. Chem. Soc., Faraday Trans. 1*, **70**, 149 (1974).

(5) P. P. Infelta, M. Grätzel, and J. K. Thomas, *J. Phys. Chem.*, **78**, 190 (1974).

(6) G. A. Infante, J. H. Fendler, and L. K. Patterson, unpublished results.

(7) M. Grätzel, J. K. Thomas, and L. K. Patterson, *Chem. Phys. Lett.*, **29**, 393 (1974).

(8) (a) T. Kajiwara and J. K. Thomas, *J. Phys. Chem.*, **74**, 2290 (1970); (b) L. K. Patterson and J. Lilie, *Int. J. Radiat. Phys. Chem.*, **6**, 129 (1974).

(9) (a) M. N. Jones and D. A. Reed, *Kolloid-Z.*, **235**, 1196 (1970); (b) A. L. Loeb, J. Th. Overbeek, and P. H. Wiersema, "The Electrical Double Layer Around a Spherical Colloid Particle", MIT Press, Cambridge, Mass., 1961.

(10) L. K. Patterson and E. Vieil, *J. Phys. Chem.*, **77**, 1192 (1973); R. R. Hautala, N. E. Schore, and N. J. Turro, *J. Am. Chem. Soc.*, **95**, 5508 (1973); M. Grätzel and J. K. Thomas, *ibid.*, **95**, 6885 (1973).

(11) P. Debye and E. W. Anacker, *J. Phys. Chem.*, **55**, 644 (1951).

(12) L. C. Parratt, "Probability and Experimental Errors in Science", Wiley, New York, N.Y., 1961.

(13) P. Mukerjee and K. J. Mysels, *Natl. Stand. Ref. Data Ser., Natl. Bur. Stand.*, **No. 36** (1971).

Pulse Radiolysis of Mercuric Oxide in Neutral Aqueous Solutions

Shin-ichi Fujita,* Hideo Horii, Toshiaki Mori, and Setsuo Taniguchi

Radiation Center of Osaka Prefecture Shinke-cho, Sakai, Osaka, Japan

(*Received August 22, 1974*)

The reduction of HgO in deaerated aqueous solutions was studied by the pulse radiolysis technique and spectrophotometric analysis after electron pulse irradiation. HgO reacts with e_{aq}^- with a rate constant of $(2.3 \pm 0.2) \times 10^{10}\ M^{-1}\ sec^{-1}$ to yield a transient species of HgOH having an absorption maximum at 233 nm and a shoulder at 260–270 nm (ϵ^{260} $(5.3 \pm 0.2) \times 10^3\ M^{-1}\ cm^{-1}$). The p$K$ of the equilibrium, $Hg^+ \leftrightarrow$ HgOH, was estimated as 5.1. HgOH dimerizes with a rate constant of $2k = (4.4 \pm 0.5) \times 10^9\ M^{-1}\ sec^{-1}$ at the lower concentration of HgO ($\lesssim 100\ \mu M$). The dimer, assigned to Hg_2O or $Hg_2(OH)_2$, has an absorption maximum at 215 nm with a shoulder at 230 nm and further decays according to a first-order rate law. At higher concentrations of HgO, however, the formation of polynuclear mercury oxide having a longer lifetime was taken into consideration from some evidence.

Introduction

It has been reported by many workers that the radiolytic reduction of the mercuric ion leads to the formation of Hg^+ as the initial reduced species in acidic aqueous solution[1,2] or acidic ice matrix.[3,4] From pulse radiolytic study of the solution neighboring pH 4,[2] the stable mercurous ion, Hg_2^{2+}, was formed via an additional step after the disproportionation reaction of the initial species:

$$Hg^+ + Hg^+ \longrightarrow Hg^0 + Hg(II)$$

$$Hg^0 + Hg(II) \longrightarrow Hg_2^{2+}$$

while Nazhat and Asmus[5] have demonstrated that the transient, HgCl, formed in the reduction of $HgCl_2$ reacts directly to give Hg_2Cl_2 in aqueous solution.

It is expected that the Hg^+ ion may be hydrolyzed to HgOH and also Hg_2^{2+} to Hg_2OH^+ (pK_1 = 5)[6] or $Hg_2(OH)_2$ in solutions of higher pH. However, X-ray diffraction studies[7] and some other results[8] have shown that the solid mercurous oxide does not exist as Hg_2O but as a mixture of Hg and HgO. These arguments as well as the concern of environmental pollution arouse interest in the behavior of mercury ions in neutral solutions.

In the present study, the pulse radiolysis technique has been applied to neutral solutions of HgO. The reaction mechanisms are discussed and compared with the results in acidic solutions.

Experimental Section

Experimental details of pulse radiolysis measurements have been described previously.[2] Most observations of the long-lived species were carried out in square quartz cells (1.0 × 1.0 × 4.0 cm) with Thermal quartz windows on a spectrophotometer (Shimadzu RS-27). Oscillographic studies longer than 1 msec were performed on the dc connection with the comparison voltage setup of the apparatus (National VP-541A).

HgO (Merck, GR grade, yellow), which has rather high solubility in water,[9] was dissolved in hot triply distilled water through a sintered glass filter. The excessively dissolved HgO (0.5~1 mM) thus obtained was found not to precipitate at room temperature for 1 month. However,

each solution containing the required HgO was prepared by diluting the freshly made stock solution and used within 1 day.

The concentration of mercuric oxide was determined spectrophotometrically as its EDTA complex in the acidic solution at 247 nm, similar to previous work.[2] The solutions were deaerated by bubbling with argon for periods longer than 2 hr. All materials were used without further purification from the commercial sources.

Results

Pulse radiolysis of deaerated aqueous solutions of mercuric oxide yielded initially a transient species of Hg(I) having an absorption maximum at 233 nm and a shoulder at 260–270 nm. Figure 1 shows the optical absorption spectra immediately, 2.5, and 250 msec after the pulse in a deaerated neutral solution of 200 μM HgO. After the decay of the initial species, the absorption increasing toward shorter wavelength remained. Figure 2 shows the oscillographic traces of the absorption obtained in the same solution. The absorption disappears by a second-order rate law at 260 nm, but reaches a constant value within about 2.5 msec at 220 nm. Later, the absorption at 220 nm is found to increase slightly within 250 msec. Essentially similar results were obtained in the solution containing 10 mM *tert*-butyl alcohol, although the spectrum of its radical slightly overlapped at an earlier stage. However, little absorption appeared in the solution saturated with N_2O.

The specific rate constant of the hydrated electron with mercuric oxide was determined from the pseudo-first-order decay rate of e_{aq}^- at 500 nm in deaerated neutral solutions of 0–30 μM mercuric oxide and 10 mM *tert*-butyl alcohol. $k(e_{aq}^- + HgO) = (2.3 \pm 0.2) \times 10^{10}\ M^{-1}\ sec^{-1}$ was thus obtained.

Figure 3 shows the second-order decay plots of the transient at different doses at 260 nm in a deaerated 200 μM HgO solution containing 10 mM *tert*-butyl alcohol. The slopes of the lines equal $2k/\epsilon l$ where k is the second-order rate constant, ϵ is the molar extinction coefficient, and l is the light path in the irradiation cell. The absorption quantity at 260 nm was linear against doses within 1500 rads per pulse in the solution of 200 μM HgO containing 10 mM *tert*-butyl alcohol. Taking the G value of the reducing species including a H radical as 3.2, the molar extinction coefficient of the species at 260 nm is calculated as $(5.3 \pm 0.2) \times 10^3\ M^{-1}\ cm^{-1}$. Hence k can be calculated. All values of $2k/\epsilon$ determined in solutions of 100–400 μM HgO by several doses yielded $(8.3 \pm 0.3) \times 10^5$ cm sec^{-1}. The result was not affected by any ionic strength in the solution containing $NaClO_4$ up to 0.1 M. Then, the rate constant $2k$ is calculated as $(4.4 \pm 0.4) \times 10^9\ M^{-1}\ sec^{-1}$.

As to the remaining absorption at 220 nm, it became nearly constant during oscillographic observation in a 100 μM HgO solution. In solutions of higher HgO concentrations, however, the absorption further increased during a longer time, as shown in Figure 2c. Figure 4 shows the changes of the absorption quantities vs. HgO concentrations at 2.5 and 250 msec after the pulse in solution with and without *tert*-butyl alcohol. The absorption at 2.5 msec becomes nearly constant at concentrations above 200 μM. However, the absorption at 250 msec further increases with increasing HgO concentration up to 1 mM.

Figure 5 shows the spectrum of the species remaining at 2.5 min after irradiation in a 100 μM HgO solution, where the solution was pulse irradiated repeatedly ten times giving approximately the same dose as that used for the oscillographic observations. The characteristics of the spectra under various conditions are listed in Table I. D^{254}/D^{215} varies with the concentrations of HgO or *t*-BuOH, while D^{230}/D^{215} is unchanged within experimental error. Data obtained in solutions of 200 μM HgO were hardly influenced by the number of repetitions of the pulse in the range of 10–40. These results suggest that the spectra origi-

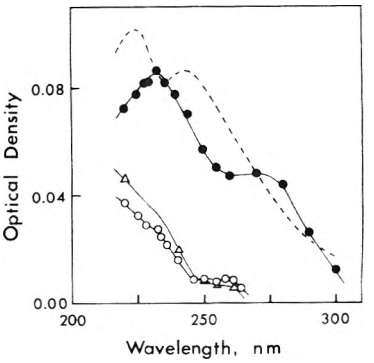

Figure 1. Absorption spectra obtained in a deaerated aqueous solution of 200 μM HgO: average dose, about 2000 rads immediately (●), 2.5 (○), and 250 msec (△) after the pulse; the dotted curve shows the spectrum of Hg^+ normalized at 236 nm.[2]

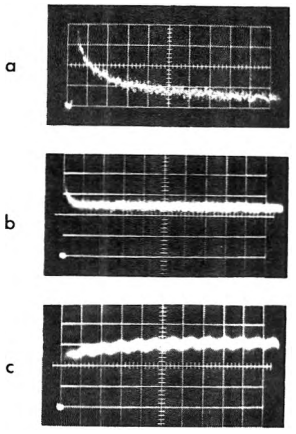

Figure 2. Oscillographic traces obtained in a deaerated aqueous solution of 200 μM HgO: average dose, about 2800 rads; ordinates, 4.5%/cm; abscissa (a) 20 μsec/cm, at 260 nm, (b) 0.5 msec/cm, at 220 nm, (c) 20 msec/cm, at 220 nm.

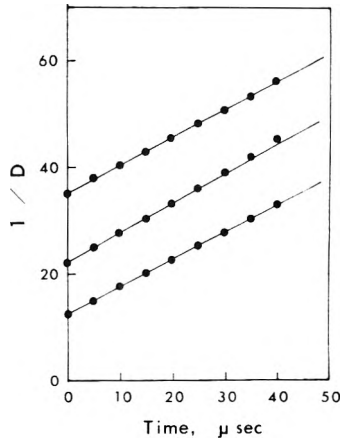

Figure 3. The second-order decay of absorption at 260 nm due to HgOH at several doses: upper, 1050; middle, 1800; bottom, 2900 rads.

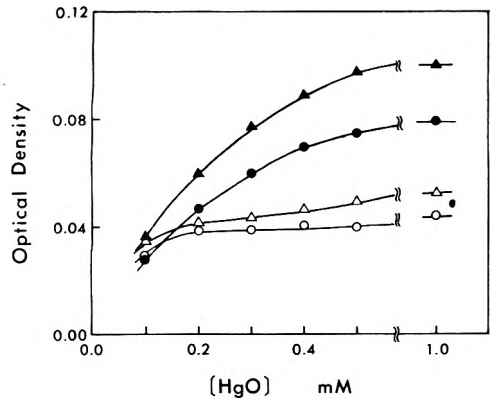

Figure 4. Dependence of the absorption quantity at 220 nm upon [HgO]: in the presence of 10 m*M* *t*-BuOH at 2.5 msec (△) and 250 msec (▲) after the pulse, and in the absence of the alcohol at 2.5 (○) and 250 msec (●) after the pulse; average dose, 2000 rads.

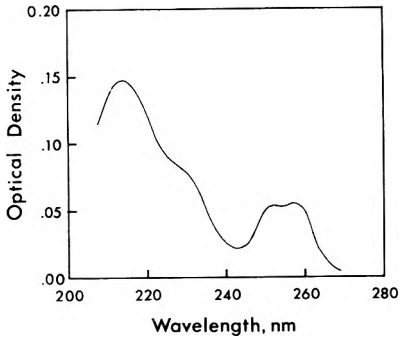

Figure 5. Absorption spectra on a spectrophotometer at 2.5 min after irradiation in a solution of 100 μM HgO: total dose, about 2.0×10^4 rads by ten repeated pulses.

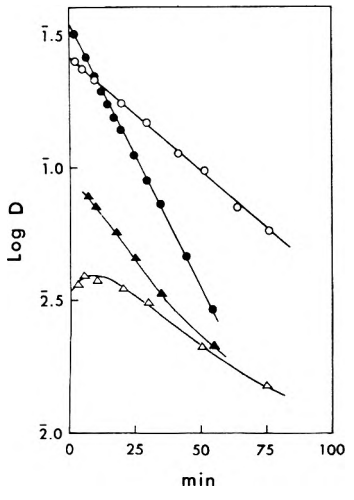

Figure 6. The first-order decay plots of the long-lived absorption in the 200 μM HgO solutions with 10 m*M* *t*-BuOH at 215 (●) and 254 nm (▲), and without the alcohol at 215 (○) and 254 nm (△).

nate from two species: one has a peak at 215 nm with a shoulder about 230 nm, the other two peaks split around 254 nm.

It was found that these absorptions further decayed slowly. Figure 6 shows the first-order decay plots of the long-lived absorptions at 215 and 254 nm in the solutions of 200 μM HgO with and without *t*-BuOH. The linearities are good at 215 nm, but not so good at 254 nm in both solutions. The absorption at 254 nm is found to increase in an earlier period of time in the absence of the alcohol. Table I also lists the first-order rate constants for the decay of the absorption calculated from the slopes under several conditions at 215 nm. The rate decreases with increasing HgO concentration, but increases in the presence of *t*-BuOH. These rates were little affected by aeration or the addition of H_2O_2 (~2 m*M*) after irradiation. The addition of perchloric acid to the irradiated solution changed the spectra to that of the Hg_2^{2+} ion. When the acid was added after most of the long-lived species had decayed, the quantity of Hg_2^{2+} ion observed was much reduced in comparison with the value which should be obtained on the addition of the acid immediately after irradiation. However, the quantity was found to increase slowly ($t_{1/2} \sim 1$ hr) to the expected value.

TABLE I: Characteristics of the Spectra due to the Long-Lived Absorption and Its First-Order Decay Rate in Various Conditions

HgO, μM	*t*-BuOH, m*M*	D^{230}/D^{215a}	D^{254}/D^{215a}	k, 10^{-2} min^{-1}
100	0	0.66	0.36	2
200	0	0.60	0.16	2
	10	0.64	0.21	5
	100	0.60	0.24	10
300	0	0.62	0.11	0.8
500	0	0.59	0.08	0.4

[a] Determined at 2.5 min after the pulse.

Discussion

A probable mechanism for the formation of Hg(I) in neutral solutions could be described by the following processes:

$$H_2O \longrightarrow e_{aq}^-,\ H,\ OH,\ \text{and other stable products} \quad (1)$$

$$e_{aq}^- + HgO \longrightarrow Hg(I) \quad (2)$$

$$H + HgO \longrightarrow Hg(I) \quad (3)$$

Here, the H radical would also contribute to the formation of the transient in analogy with the results in the acidic solutions of the mercuric ion.[1,2,10] The mechanism was supported by the results of scavenger effects. The retardation of the initial absorption by N_2O may be caused by the fast reaction 4 ($k_4 = 5.6 \times 10^9\ M^{-1}$ sec[1]).[11] OH radicals disappeared by their recombination without further oxidizing HgO. In solutions of HgO alone, however, the radical would consume some of the e_{aq}^- or Hg(I) formed in reactions 2 and 3 to lower the yield of the reduced species. When the absolute yield of Hg(I) was in question, therefore, *t*-BuOH was added to scavenge OH radicals:

$$e_{aq}^- + N_2O \longrightarrow N_2 + OH + OH^- \quad (4)$$

$$OH + t\text{-BuOH} \longrightarrow t\text{-BuOH radical} + H_2O \quad (5)$$

where $k_5 = 2.5 \times 10^8\ M^{-1}$ sec^{-1}.[12] The reaction of the H radical with *t*-BuOH can be neglected.[13] Although the *t*-BuOH radical has an absorption spectrum with a peak at 225 nm (ϵ^{225} 900 M^{-1} cm^{-1}),[14] the contribution may be neglected at wavelengths higher than about 250 nm. Because of these considerations, the determination of the absorption coefficient or the decay rate of the transient species was carried out at 260 nm in the presence of *t*-BuOH. In addition the contribution of the radical becomes negligible

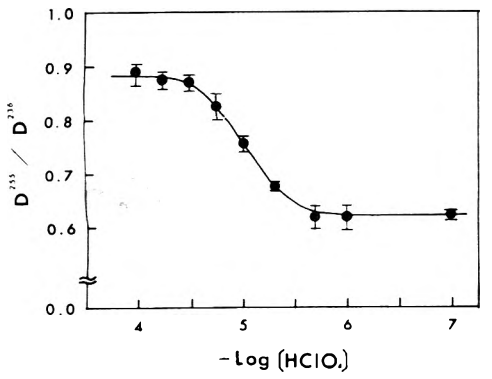

Figure 7. Dependence of D^{255}/D^{236} upon −log [$HClO_4$], [HgO] = 200 μM. The data without the acid are plotted at −log [$HClO_4$] = 7.

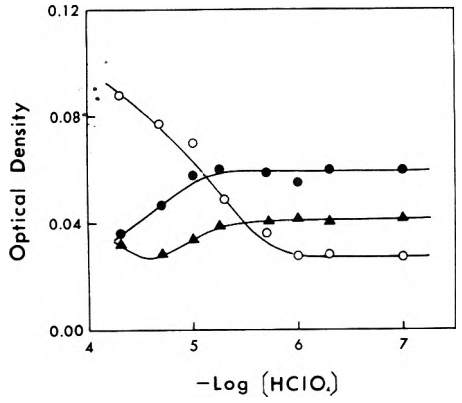

Figure 8. Dependences of the absorption quantities upon −log [$HClO_4$] in the deaerated aqueous solutions of 200 μM HgO and 10 mM t-BuOH: average dose, 2000 rads; 2.5 msec after the pulse at 236 (O) and 220 nm (▲); 250 msec after the pulse at 220 nm (●). The data without the acid are plotted at −log [$HClO_4$] = 7.

even at 225 nm about 500 μsec after the pulse irradiation due to its recombination reaction.

Reaction 2 is considered to be a diffusion-controlled process from the rate constant determined by the decay of e_{aq}^-. The rate constant of reaction 3 could not be determined in the present study.

The Short-Lived Species. The spectrum of the transient at the end of the pulse is different from that obtained in acidic solutions, particularly as to the shoulder around 260 nm. The spectrum of Hg^+ [2] normalized at 236 nm is shown by the dotted curve in Figure 1 for comparison.

As mercuric oxide dissolves as HgO the first step in its reaction with e_{aq}^- might form HgO^-. In neutral solutions, however, the second-order decay rate of the absorption is not affected by ionic strength. The result suggests that the transient may not carry any charge on it. Then, the absorption may originate most likely from the species, HgOH, which corresponds to a hydrolyzed form of Hg^+ ion. Noting

$$e_{aq}^- + HgO \longrightarrow HgOH + OH^- \quad (6)$$

$$HgOH + H^+ \longleftrightarrow Hg(H_2O)^+ \quad (7)$$

the difference between the two spectra in acidic and neutral solutions, the ratio, D^{255}/D^{236}, was taken as a measure for the compositions of Hg^+ and HgOH in equilibrium 7. Figure 7 shows the dependence of D^{255}/D^{236} upon −log [$HClO_4$]. Approximately regarding −log [$HClO_4$] as the pH value of the solution, the pK value is estimated as about 5.1 from the S-type curve in the figure.

The Long-Lived Species. Since the absorption quantity at 2.5 msec after the pulse at 220 nm is hardly affected by increasing the HgO concentrations higher than about 200 μM (Figure 4), it may be considered that the absorption formed at this time may originate from the recombination product of HgOH. This is supported by the pH dependence of the absorption quantity illustrated in Figure 8. The inclinations are inverse between the results at 220 and 236 nm where Hg_2^{2+} has an absorption maximum. Both inflection points are in agreement with the pK value (5.0) of the equilibrium, $Hg_2^{2+} \leftrightarrow Hg_2OH^+$.[6] In Figure 8, there is no evidence for the equilibrium, $Hg_2OH^+ \leftrightarrow Hg_2(OH)_2$. However, the recombination product of HgOH in the neutral solution was ascribed to Hg_2O or $Hg_2(OH)_2$, because Hg_2^{2+} hydrolyzes to precipitate in such a solution.

$$2HgOH \longrightarrow Hg_2O + H_2O \text{ or } Hg_2(OH)_2 \quad (8)$$

Considering the stoichiometry of the reaction, the absorption coefficient of Hg_2O was calculated as $(8.7 \pm 0.7) \times 10^3$ M^{-1} cm^{-1} at 220 nm from the saturated value obtained in the solution containing 10 mM t-BuOH (Figure 4). Slight increase of the absorption above 500 μM of HgO is appreciated as the influence from further increasing absorption within 250 msec. The shorter part of the spectra in Figure 5 is also assigned to Hg_2O (or $Hg_2(OH)_2$), since the absorption at shorter wavelength obtained in the solution of 100 μM HgO remains constant during oscillographic observation after the decay of the initial transient.

It has been reported[2] that in acidic solution Hg^+ ions disproportionate to form Hg^0 and Hg(II) and later Hg_2^{2+} is formed by the successive reaction of Hg^0 with Hg(II). On the contrary, dimerization in neutral solutions occurs instantaneously with the second-order decay of HgOH as seen in Figure 2b. The fast recombination of HgOH might be attributable to the fact that HgOH has no charge on it. This is similar with the result[5] that HgCl recombines in pulse radiolysis of aqueous $HgCl_2$ solution.

X-Ray diffraction study[7] and some other results[8] have revealed that solid Hg_2O does not exist and that the black powder precipitated from solutions of Hg_2^{2+} ion and alkali consists of fine particles of mercury and mercuric oxide. The unstability of the long-lived species is compatible with this fact. Since the possibility that O_2 as the impurity or H_2O_2 as the minor product from radiolyzed H_2O may contribute to the decay process was excluded experimentally as cited in the Result section, then, the first-order decay of the long-lived species may be explained by its decomposition to Hg and HgO.

$$Hg_2O \text{ or } Hg_2(OH)_2 \longrightarrow Hg + HgO \text{ (or } Hg(OH)_2) \quad (9)$$

The spectrum around 254 nm in Figure 5 is similar to that of atomic mercury in water.[15] However, the absorption to be found should be by far lower, considering the low solubility of mercury[16,17] and the shorter optical path length of the analytical light. Nevertheless, it was concluded that the absorption around 254 nm in Figure 5 originates from mercury dissolved temporarily in excess, which was produced by reaction 9. This may be well explained by the fact that the absorption at 254 nm is relatively high in solutions at a concentration of HgO (200 μM) containing t-BuOH, where Hg_2O decays faster than in the solution without t-BuOH (Table I). Mercury dissolved in excess may be regarded as an intermediate in successive reactions.

$$Hg_2O \text{ (or } Hg_2(OH)_2) \xrightarrow{k_a} Hg^0(aq) \xrightarrow{k_b} Hg^0(liq) \quad (10)$$

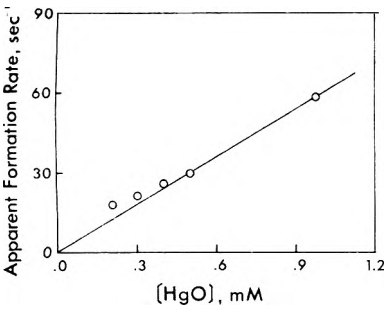

Figure 9. Dependence of the increasing rates of the absorption at 220 nm upon [HgO], [*t*-EuOH] = 10 m*M*.

The concentration of the intermediate is expressed by the equation

$$[Hg^0(aq)] = c_0 k_a'(k_a - k_b)(\exp(-k_b t) - \exp(-k_a t))$$

where c_0 is the initial concentration of Hg_2O (or $Hg_2(OH)_2$). This equation tells us that the concentration of $Hg^0(aq)$ has a maximum value depending upon k_a and k_b. If k_b is constant, the larger value of k_a leads to the higher maximum concentration of $Hg^0(aq)$. The experimental results are in agreement with this expectation as seen in Figure 6. However, the absorption around 254 nm already appears slightly at 2.5 msec after the pulse and is even found to decay slightly, as seen in Figure 1. This might be explained by the fact that a part of HgOH disproportionates to Hg + $Hg(OH)_2$.

Reaction 9 is also ascertained by the experiment where perchloric acid is added after irradiation. According to this mechanism, Hg_2^{2+} would be formed with the proton in the irradiated solution and its quantity should be unchanged on addition of the acid before or after the decay of Hg_2O. When the acid was added after most of Hg_2O had decayed, it took long time to reach the value obtained on the addition just after irradiation. However, the final value was in agreement with the expectation. The recovering process seems to be quite slow.

Figures 2c and 4 suggest that another species is formed within 250 msec in solutions of higher HgO concentrations, although any meaningful change of the spectrum is not observed except for the increase of absorption at shorter wavelengths. *t*-BuOH does not participate in the formation of the species, since the similar trend of the absorption with the HgO concentration is found in the presence or absence of the alcohol. The difference in the yields may be due to the scavenging effect of OH radical by the alcohol. The slow increase of the absorption apparently obeyed a first-order rate law, since plots of $-\ln(D_\infty - D)$ vs. t showed good linearities. Figure 9 shows the dependence of the increasing rate of the absorption at 220 nm calculated from the slopes upon HgO concentrations. Taking into consideration that the data at the lower concentrations of HgO would have rather the large uncertainty due to the smaller increases, the rate is proportional to the HgO concentrations. Then, the slow increasing process would occur by the pseudo-first-order reaction against HgO. The first-order decay rate of the absorption becomes lower at higher concentrations of HgO as shown in Table I. These facts may be explained by the formation of a polynuclear species of mercury which has a longer lifetime.

$$Hg_2O + nHgO \longrightarrow Hg_2O \cdot nHgO \qquad (11)$$

Some complexes having polynuclear structures have been proposed in solutions of stable mercuric ions. Hayek et al.[18] suggested the formation of polynuclear ions, $Hg(HgO)_2^{2+}$, in solutions of concentrated mercury perchlorate. According to Ahlberg,[19] Hg^{2+} ion is hydrolyzed to form successively the polynuclear ions, $HgOH^+$, ..., $Hg_2(OH)_2^{2+}$, $Hg_4(OH)_2^{5+}$, etc. Johansson has proposed[20] that these species contain the bridged structure where mercury atoms are combined with each other through H_2O, OH^-, or O_2^{2-}. If our assumption here is true, it seems reasonable that the recombination product from HgOH is also of the type HgOHg or

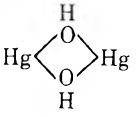

in place of the molecule directly binding between two mercury nuclei as Hg_2Cl_2. Then, trinuclear mercury oxide, for example, would have a structure such as HgOHgOHg or

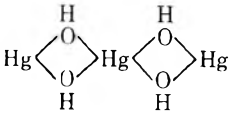

Such bridged complexes have generally been considered in many other metal compounds,[21] as well as in crystals of mercuric oxide.[22]

The HgOH radical might well react with *t*-BuOH radicals forming an Hg–organic compound. However, no essential differences were found between the product spectra in the presence and absence of *t*-BuOH. The faster decay of Hg_2O in aqueous alcoholic solutions could not be explained yet. It might be concerned with the ability of alcohols hydrolyzing mercury ions.

References and Notes

(1) M. Farragi and A. Amozig, *Int. J. Radiat. Phys. Chem.*, **4**, 353 (1972).
(2) S. Fujita, H. Horii, and S. Taniguchi, *J. Phys. Chem.*, **77**, 2868 (1973).
(3) D. N. Moorthy and J. J. Weiss, *Adv. Chem. Ser.*, **No. 50**, 209 (1965).
(4) R. S. Eachus, M. C. R. Symons, and J. K. Yandell, *Chem. Commun.*, 979 (1969).
(5) N. B. Nazhat and K.-D. Asmus, *J. Phys. Chem.*, **77**, 614 (1973).
(6) W. Forsling, S. Hietanen, and L. G. Sillén, *Acta Chem. Scand.*, **6**, 901 (1952).
(7) R. Fricke and P. Ackermenn, *Z. Anorg. Allg. Chem.*, **211**, 233 (1933).
(8) B. J. Aylett, "Comprehensive Inorganic Chemistry", Vol. 3, J. Bailer, H. J. Emeléus, R. Nyholm, and A. F. Trotmann-Dickenson, Ed., Pergamonn Press, Oxford, 1973, p 292.
(9) J. W. Mellor, "A Comprehensive Treatize on Inorganic and Theoretical Chemistry", Vol. 4, Longmann, London, 1960, p 776.
(10) M. Farragi and J. Désalos, *Int. J. Radiat. Phys. Chem.*, **1**, 335 (1969).
(11) J. H. Baxendale et al., *Nature (London)*, **201**, 468 (1964).
(12) M. Anbar and P. Neta, *Int. J. Appl. Radiat. Isotopes*, **18**, 493 (1967).
(13) (a) A. Appleby, G. Scholes, and M. Simic, *J. Am. Chem Soc.*, **85**, 3891 (1963); (b) J. Rabani, *J. Phys. Chem.*, **66**, 361 (1962); (c) A. Appleby, *J. Am. Chem. Soc.*, **67**, 1610 (1963).
(14) M. Simic, P. Neta, and E. Hayon, *J. Phys. Chem.*, **73**, 3794 (1969).
(15) H. Reichardt and K. F. Bonhoeffer, *Z. Elektrochem.*, **36**, 753 (1930); *Z. Phys.*, **67**, 780 (1931).
(16) S. S. Choi and D. G. Tuck, *J. Chem. Soc.*, 4080 (1962).
(17) A. Stock, *Z. Anorg. Allg. Chem.*, **217**, 241 (1934).
(18) (a) E. Hayek, *Z. Anorg. Allg. Chem.*, **223**, 382 (1935); (b) E. Hayek and E. Schnell, *Monatsh Chem.*, **85**, 472 (1954).
(19) I. Ahlberg, *Acta Chem. Scand.*, **16**, 887 (1962).
(20) G. Johansson, *Acta Chem. Scand.*, **25**, 2787, 2799 (1971).
(21) C. K. Jorgensen, "Inorganic Complexes", Academic Press, London, 1963, chapter 2; R. B. Hesiop and P. L. Robinson, "Inorganic Chemistry", Elsevier, Amsterdam, 1967, Chapter 30, etc.
(22) D. Grdenić, *Quart. Rev., Chem. Soc.*, **19**, 303 (1965).

A Simple Cell Model Treatment of Surface Tension Expansion

Y. Tamai

Chemical Research Institute of Non-aqueous Solutions, Tohoku University, Sendai, Japan
(Received March 7, 1974; Revised Manuscript Received December 12, 1974)

Publication costs assisted by Tohoku University

A theoretical basis is discussed on the surface tension expansion into its components due to intermolecular forces. The expansion, originally proposed by Fowkes and justified empirically, is verified approximately by applying the Lennard-Jones cell model for molecular analysis of surface tension.

Introduction

Fowkes has proposed that surface tension, γ, can be divided into several parts due to separable intermolecular forces acting in the bulk phase, that is, the part due to dispersion force, γ^d, the part due to electrostatic force, γ^e, and so forth (eq 1).[1] This expansion has proved very useful in

$$\gamma = \gamma^d + \gamma^e + \dots \quad (1)$$

many cases, but there are some critics. In fact, the origin of surface tension lies in molecular interactions. However, the surface tension is the surface excess free energy and consists of both an energy term and an entropy term. The energy term can well be divided into the parts due to molecular forces. On the other hand, the entropy term might not. Therefore one critic pointed out that the relation 1 is derived by ignoring surface entropy and holds only if the surface entropy is zero or proportional to surface energy.[2] Although it is commonly observed that the entropy change of a process is directly proportional to the energy change of that process, any further refinement is required to consider entropy explicitly.[3] The present treatment is concerned with this problem and intended to show how the entropy term is related to intermolecular forces.

Derivation of Additive Expansion

Applying the simple model of Lennard-Jones for a liquid, surface tension can be expressed as

$$\gamma = \frac{1}{\sigma}\left[\frac{1}{2}(W_s - W_b) + kT \ln\left(\frac{\nu_b}{\nu_s}\right)\right] \quad (2)$$

where σ is the surface area occupied by one molecule, W_s or W_b is the molecular energy, including both potential and thermal, in the surface or in the bulk, respectively, k the Boltzmann constant, T the absolute temperature, ν_b the frequency of molecular vibration in the bulk, and ν_s the frequency of vibration perpendicular to the surface.[4] Now, so far as the energy term is concerned, it can be divided into the parts due to molecular forces.

$$W_s - W_b = \Delta W = \Delta W^d + \Delta W^e + \dots \quad (3)$$

As for the entropy term, ν can be related to the force constant, K, controlling vibration, because of assumed harmonic oscillation.

$$\nu = \frac{1}{2\pi}\left(\frac{K}{m}\right)^{1/2} \quad (4)$$

where m is the mass of molecule. Then

$$\ln\left(\frac{\nu_b}{\nu_s}\right) = \frac{1}{2}\ln\left(\frac{K_b}{K_s}\right) \quad (5)$$

K_s, the force constant for vibration normal to the surface, is less than K_b, that for isotropic vibration in the bulk, a material constant. Therefore

$$K_s = K_b - \Delta K \qquad \Delta K > 0 \quad (6)$$

Introducing this expression into eq 5, and noting $\Delta K < K_b$

$$\ln\left(\frac{\nu_b}{\nu_s}\right) = -\frac{1}{2}\ln\left(\frac{K_s}{K_b}\right) = -\frac{1}{2}\ln\left(1 - \frac{\Delta K}{K_b}\right) \simeq \frac{1}{2}\frac{\Delta K}{K_b} \quad (7)$$

Then the entropy term is written as

$$kT \ln\left(\frac{\nu_b}{\nu_s}\right) = \frac{kT}{2}\frac{\Delta K}{K_b} \quad (8)$$

It may be reasonable to consider that the force constant can be divided, at least approximately, into the parts due to intermolecular forces.

$$\Delta K = \Delta K^d + \Delta K^e + \dots \quad (9)$$

After all, γ can be expressed as

$$\gamma = \frac{1}{\sigma}\left[\frac{1}{2}(\Delta W^d + \Delta W^e + \dots.) + \frac{kT}{2K_b}(\Delta K^d + \Delta K^e + \dots.)\right] = \frac{1}{2\sigma}\left(\Delta W^d + \frac{kT}{K_b}\Delta K^d\right) + \frac{1}{2\sigma}\left(\Delta W^e + \frac{kT}{K_b}\Delta K^e\right) + \dots \quad (10)$$

Now eq 1 is obtained in an explicit form, that is, for example

$$\gamma^d = \frac{1}{2\sigma}\left(\Delta W^d + \frac{kT}{K_b}\Delta K^d\right) \quad (11)$$

using the difference of energy and force constant between the bulk and the surface.

Conclusion

It may be noteworthy that this relation holds if the molecule or the surface segment of the molecule can be regarded to vibrate as an unit harmonically. So far as the harmonic vibration can be assumed, the change of entropy is approximately proportional to the change of energy.

References and Notes

(1) F. M. Fowkes, *Ind. Eng. Chem.*, **56**, No. 12, 40 (1964).
(2) R. E. Johnson and R. H. Dettre, "Surface and Colloid Science", Vol. 2, Wiley-Interscience, New York, N.Y., 1969, p 130.
(3) D. Hoernschemeyer, *J. Phys. Chem.*, **70**, 2629 (1966); R. J. Good and E. Elbing, *Ind. Eng. Chem.*, **62**, No. 3, 61 (1970).
(4) R. Defay, I. Prigogine, A. Bellemans, and D. E. Everett, "Surface Tension and Adsorption", Longmans, London, 1966, p 145.

On the Chemistry of Silica Supported Chromium Ions. I. Characterization of the Samples

A. Zecchina,* E. Garrone, G. Ghiotti, C. Morterra, and E. Borello

Istituto di Chimica Fisica dell'Università di Torino, Corso M. D'Azeglio, 48-10125 Torino, Italy *(Received September 11, 1974)*

Publication costs assisted by Italian CNR

A definite compound is formed between CrO_3 and SiO_2, the predominant surface structures being dichromates. By reduction in CO of the surface phase, Cr^{II} is mainly obtained. The activity of the reduced samples toward CO and ethylene polymerization is affected by chromium concentration and thermal treatments, both high Cr contents and high reduction temperatures decreasing the specific activity. The most active catalysts are characterized by Cr loading $\leq 0.5\%$ and reduction temperature equal to 350°. Reflectance spectra on reduced diluted samples show the presence of a small Cr^{III} percentage and of two Cr^{II} species differing in coordination.

Introduction

Because of the industrial importance of supported chromium oxides in the polymerization of ethylene, many authors have studied their properties. Although these studies have produced a great deal of information, neither a detailed picture of the polymerization mechanism has been achieved nor a comprehensive description of the chemistry of supported chromium ions is yet available.

Reasons for the discrepancies among published results are probably as follows. As the support does not merely disperse the Cr oxide, but instead a definite surface phase is formed upon Cr loading, both the nature of the support (SiO_2, Al_2O_3, Al_2O_3–SiO_2, etc.) and the Cr content as well as the pretreatment conditions deeply affect the structure and properties of the catalyst.

Consequently the study of differently treated catalysts has lead to conflicting experimental evidence and interpretations. The literature up to 1969 has been excellently reviewed by Clark[1] and this reference will be quoted hereafter for papers prior to that year.

Contributions from literature may be grouped into the following subjects: (a) the oxidation state of catalytically active chromium; (b) the structure of the supported phase; and (c) the polymerization mechanism.

Concerning point a, every oxidation number between II and V has been proposed. While the suggestion of III[2] and IV[3] as oxidation numbers has not been successful, for a long time Cr^V in tetrahedral or square pyramidal coordination was favored as the catalytic center or its precursor.

Reasons for this widespread success are as follows: the ease of its detection by EPR and some correlations found between the EPR signal and catalytic activity;[1,2] the suggestion from Ziegler–Natta polymerization that high valence ions are catalytically efficient; and finally the requirement of Cossee's model that only ions with less than four d electrons would be active in polymerization.[4] Among recently published contributions, Eley and coworkers[5] still consider the active species to be Cr^V on the basis of activity measurements as a function of the reduction time by ethylene.

On the other hand, Krauss[6–7] has shown by means of accurate analytical work that the oxidation number of Cr in thoroughly CO reduced samples is near two and that a straight correlation exists between Cr^{II} concentration and catalyst activity.[8]

As far as the structure of the surface phase is concerned (point b) the most relevant contribution has been brought by Hogan,[9] who has shown that after high-temperature activation in O_2, chromium is bound to the surface in the form of chromates or possibly dichromates formed through water elimination between chromic acid and surface silanols.

On the contrary, little is known about the structure of the reduced phase and, in particular, about the arrangement of the low-valence ions on the surface and the possible formation of ions clusters at high Cr content.

It is most important to note that these features are deeply affected by the nature of the reducing agent. In fact hydrogen containing compounds (as ethylene or H_2 itself) produce water during the reduction stage, which is known to prevent complete reduction to Cr^{II} and to favor clustering processes.[1,9] The use of CO as a reducing agent is therefore highly preferable.

The polymerization mechanism (point c) generally accepted is that proposed by Cossee[4] for the Ziegler–Natta process. Kinetic measurements[1,5,10] roughly agree with this model and give reaction orders between zero and one and, accordingly, different activation energies.

Moreover, Krauss[8] has recently shown the presence of both ethylene π bonded to the catalytic site and of a strong Cr–C σ bond, in agreement with the reaction scheme. However, the processes leading to chain initiation and termination[1,9] are still not well understood.

The chemistry of surface chromium is a topic which our laboratory has studied for many years. Characterization and ir studies on systems, such as α-Cr_2O_3[11,12] and 6.5% Cr_2O_3–SiO_2,[13,14] have shown that an accurate control of catalyst pretreatment is needed and that the chemical properties of the surface phase may only be understood by exploring the catalyst with a variety of probe molecules.

In agreement with such ideas, a series of papers about CrO_3–SiO_2 is presented here, the first of which deals with the characterization of the samples, and the following ones describe the complexes formed by coordination of a number of molecules, in order to discriminate the various types of surface ions and describe their reactivity.

Silica was chosen as a support for the following reasons: the CrO_3–SiO_2 is known to have the highest polymerization activity; no solid solution is formed, as in the case of Cr_2O_3–Al_2O_3;[15] the surface chemistry of SiO_2 is now well understood.[16-18]

Experimental Section

(1) *Sample Preparation.* The catalyst described in our previous series of papers[13-14] was prepared by impregnation with a Cr^{III} solution. Further work has shown that the use of high valence ions is more convenient and agrees with other published procedures[6] and with the patented industrial process.[1]

Therefore the present set of catalysts was prepared as follows: weighted samples of Degussa Aerosil (BET surface area 330 $m^2\ g^{-1}$) were impregnated with a titrated solution of aqueous chromic acid. The resulting slurry was dried in a rotary evaporator. Care was taken during this latter stage, since too rapid an evaporation can lead to chromatography of the chromic acid on the support with subsequent heterogeneity of the samples. After drying, the samples were ground and stored, all pretreatments being performed in situ. By this method samples containing 0.025, 0.1, 0.25, 0.5, 1.05, 2.1, 4.2, 6.3, and 8.4 wt % chromium were prepared.

(2) *Experimental Techniques.* The amounts of the adsorbed gases were either obtained using a Sartorius microbalance or a small dead space volumetric adsorption system.

Infrared measurements were made on a Beckman IR 7 double-beam spectrophotometer. The powder sample was compacted into a disk by pressing at $\sim 10^3$ kg cm^{-2} and the disk was placed in a cell, the design of which is described elsewhere.[19]

The cell allows for thermal treatments in situ and was attached to a conventional vacuum system which was positioned so that the cell was in the sample beam of the spectrometer. An arbitrary but reproducible 100% background was obtained by attenuating the reference beam with a micrometer controlled grid. The resolution was at least 3–6 cm^{-1} in the 1250–2800-cm^{-1} range and 5–10 cm^{-1} in the 2800–4000-cm^{-1} range.

A certain number of reflectance measurements in the uv–visible–near infrared were made by one of us (A.Z.) at Bath University (England). The instrument used for this work was a Pye-Unicam SP 700 C; details of the cell and other experimental features will be described elsewhere.[20]

Finally, some low-temperature infrared measurements were made using a cell which allows for both high temperature treatments and efficient cooling of the sample down to ~77°K.

A similar cell has been previously used for the study of CO physisorption on the same type of silica which in the present work is used as support.[21]

Results and Discussion

The discussion of the results can be conveniently divided into the following parts: (A) evidence for the formation of a surface phase in the activated catalyst; (B) the activity of CO-reduced samples and related parameters; and (C) the valence and coordination state of Cr ions in reduced diluted samples.

(A) *Formation of a Surface Phase in the Activated Catalyst.* The freshly prepared sample is heated at 600–750° for 0.5 hr under vacuum, then contacted at the same temperature and for the same time with 40 Torr of O_2. This procedure will be hereafter referred to as the activation. The color of the samples is unaffected by thermal treatments.

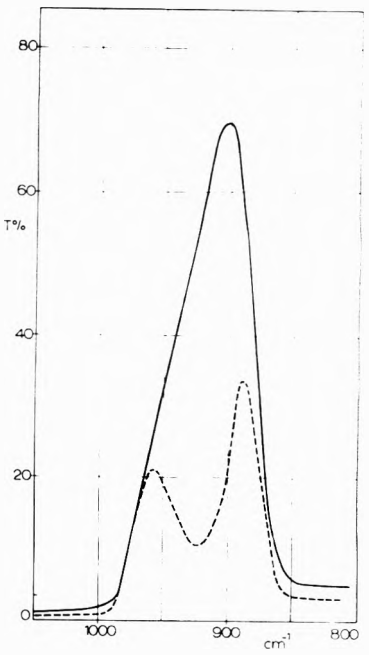

Figure 1. Ir absorption due to surface CrO_3 (transmittance vs. wavelength in cm^{-1}): dashed line, 6% sample activated at 600°; solid line, same quantity of pure silica outgassed at 600°.

As already pointed out by Hogan,[9] this fact clearly demonstrates that CrO_3 is bound to the surface as a definite compound, because at this temperature bulky CrO_3 is no longer stable.

The presence of CrO_3 bound to the surface causes two major changes in the ir spectrum of silica. The first is in the region between 800 and 1000 cm^{-1} (the so called silica "window") and is shown in Figure 1. The broken line corresponds to a 6% sample activated at 600° and the solid line corresponds to the same quantity of pure silica treated in the same way. A broad and complex absorption centered at 925 cm^{-1} is observed. The comparison with literature data strongly suggests that dichromates are likely present on the surface as they alone absorb in the 900–950-cm^{-1} range.[22,23]

The second important change occurs in the silanol stretching region. At the outgassing temperatures adopted here, the hydroxyl groups on the silica surface may be regarded as "free" so that the absorption due to the stretching mode is a narrow peak at 3748 cm^{-1}.

Upon CrO_3 loading no relevant changes may be observed as far as the position and the half-width of the OH band are concerned. On the contrary the intensity of the peak is an inverse function of the Cr loading.

Figure 2 shows the relationship between (OH) concentration and Cr content of a series of samples activated at 600°. Under identical instrumental conditions, the concentration of hydroxyl groups is proportional to the quantity:

$$F(\mathrm{OH}) = (\mathrm{OD})_{3748} S/W$$

where S is the geometrical area of the disk and W is the silica weight. Each point of this curve represents an average of three to four independent measurements. From this curve it can be seen that a linear decrease of surface hy-

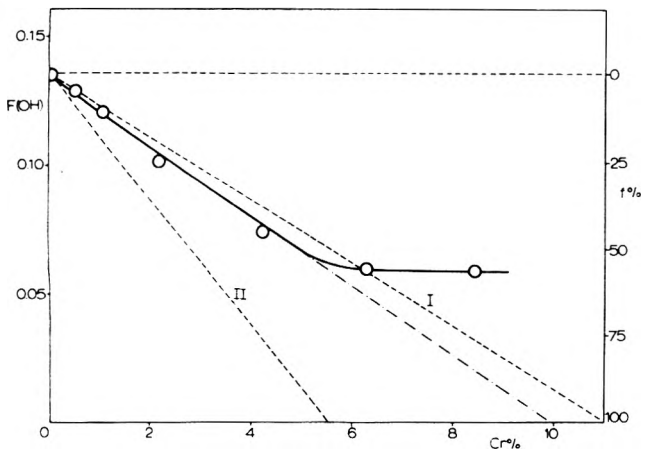

Figure 2. Surface occupation by CrO_3 as measured by the decrease of hydroxyls concentration: left-hand side, surface silanols concentration measured by $F(OH)$ (units are $cm^2\ g^{-1}$); right-hand side, percentage of the surface occupied by CrO_3. Lines corresponding to chromate-only (II) and dichromate-only (I) structures are reported, together with the extrapolation of the linear portion of the experimental curve (– • – • –).

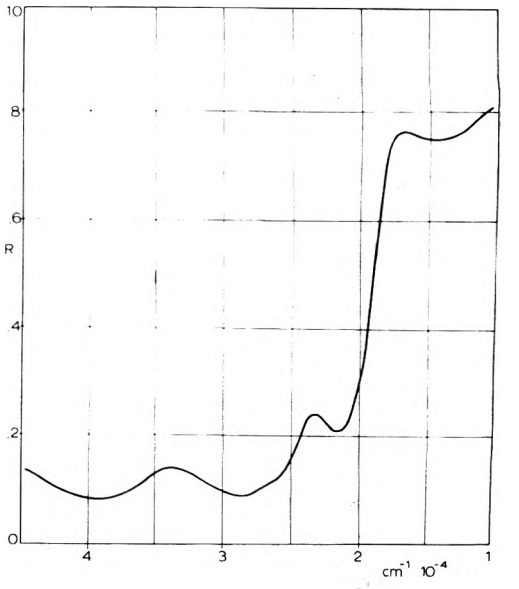

Figure 3. Uv-visible reflectance spectra of a 0.5% sample activated at 600° (reflectance vs. wavelength in cm^{-1}).

droxyls is caused by an increase in Cr loading up to about 5% Cr, at which point the OH concentration becomes independent of the Cr content. BET measurements show that the chromium loading does not cause an appreciable loss of the silica surface area, so that the hydroxyl concentration decrease is only due to the formation of a surface phase which partially occupies the surface.

As both position and half-width of the Si–OH stretching band are unaffected by CrO_3 loading, we assume that its intensity measures the fraction $(1 - f)$ of the silica surface that is not covered by the new phase; the corresponding scale is reported on the right-hand side of Figure 2. The interpretation of the figure is that, for Cr loadings below 5%, the new phase expands on the surface proportionally to the Cr content.

By extrapolating to zero optical density, it is found that the total coverage of the surface would be reached by a ~10% Cr loading, i.e., by a Cr surface density of ~4.5 atoms/100 Å^2. This figure is very near to the value normally accepted for the surface density of Si atoms in SiO_2.[17]

In conclusion, the surface phase is characterized by a ratio between surface chromium and silicon atoms near one. This value is accounted for by a structure of the surface phase made up of dichromate units (I) while a structure consisting of chromate units (II) would lead to a ratio 0.5.

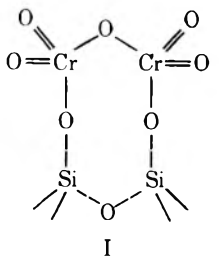

I

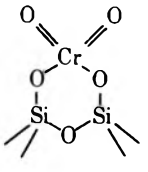

II

For the sake of clarity other curves in Figure 2 are reported: dotted line I represents the building up of a dichromate-only surface phase, while dotted line II represents a chromate-only surface phase. In conclusion, it may be stated that CrO_3 binds to the silica surface mainly as a dichromate in the whole 0–5% range, while chromates represent a minor component. For higher chromium loadings, the binding process stops, although 40% of the silica surface is still available. Unbinded CrO_3 likely undergoes the usual decomposition process,[9] when the temperature is raised, giving origin to crystallites of α-Cr_2O_3.

Further evidence for a high population of dichromates on the surface comes from the uv-visible reflectance spectra of activated samples. Figure 3 refers to a 0.5% sample activated at 600°. Strong signals appear from 18,000 to 45,000 cm^{-1} with maxima at 21,700, 28,500, and 39,000 cm^{-1} and a shoulder at 26,000 cm^{-1}. Below 18,000 cm^{-1} a small band is visible at 14,000 cm^{-1}.

Signals above 18,000 cm^{-1} can be assigned by reference to the absorption spectra of chromates and dichromates in solution, although some differences are to be expected: while the 39,000- and 28,500-cm^{-1} bands and the 26,000-cm^{-1} shoulder can be assigned to both chromates and dichromates, the band at 21,700 cm^{-1} is typical of dichromates. The relative intensity of this band qualitatively agrees with a dichromate-only surface phase.

Since chromates and dichromates do not absorb below 18,000 cm^{-1}, the band at 14,000 cm^{-1} must be due to chromium with an oxidation number lower than six. The idea that this band could be due to Cr^{III} in α-chromia-like crystallites must be ruled out since, at such light loading (0.5% Cr), segregation is unlikely to occur. The possibility of surface Cr^{III} species can also be discarded, since the sample was activated in oxygen before recording the spectrum and Cr^{III} would probably have undergone oxidation. In our opinion this band is due to a small quantity of Cr^{V}.

Evidence that Cr^{V} exists on the surface of activated catalysts derives from EPR measurements[1] and also from Kazansky's work[24] which shows that a band at 13,000 cm^{-1} is due to Cr^{V} in tetrahedral coordination.

The above picture of the surface phase agrees very well with literature data. Krauss has recently reported that dichromates are the most abundant surface species as suggested by his own visible relectance data[7] and by recent measurement of the esterification stoichiometry of surface hydroxyls by CrO_3.[8] On the contrary, Hogan[9] favored chromates as the supported species.

Moreover, the data of Figure 2 agree with the analytical

findings by Krauss et al.,[5] who showed that there is an upper limit of about 5% for the amount of Cr which can bind to the surface; further CrO_3 is converted by thermal treatments into Cr^{III} insoluble in dilute H_2SO_4 (which likely corresponds to chromium in α-chromia-like segregated phase).

The occurrence of dichromates as favored surface species requires some comments. First of all, it may be deduced from Figures 2 and 3 that the Cr content plays no role in stabilizing dichromate or chromate on the surface, as one could expect; in fact dichromates are found to predominate even at very high dispersion degrees (Figure 3); the curve of Figure 2 has a constant slope in the whole range 0–5%. So, the formation of dichromates has to be accounted for by structural reasons. In fact, inspection of structures II and I suggests that the former (chromate) likely involves some strain, while in the latter (dichromate) a good geometrical fit occurs between the dichromate and the silica moieties.[17-25]

(B) *Activity of CO-Reduced Samples and Related Parameters.* After activation at 750° (in order to eliminate most of the surface hydroxyls) the sample is reduced in situ with 40 Torr of CO at a chosen temperature, usually for 0.5 hr. As the gas was not passed over the sample, it is renewed several times. A liquid N_2 trap is placed as close as possible to the cell, in order to condense the CO_2 formed.

As already stated, the reduction procedure may affect the structure and the activity of the resulting catalyst so that a careful analysis of the experimental conditions is required. As a measure of catalytic activity, various properties may be chosen. The most obvious of these is the polymerization activity toward ethylene. Krauss[7] has shown that the activity is proportional to the Cr^{II} content of the sample, so that the measurement of the mean oxidation number may be used as a test of the activity as well. In our spectroscopic studies we require a quick and reversible test of the sample, so neither the polymerization activity nor the determination of the mean oxidation number can be used as a matter of routine.

We have observed that a suitable test of the overall activity is given by the quantity of CO adsorbed at a given pressure, as measured by the integrated intensity of ir bands in the 2150–2250-cm^{-1} region. A detailed description and assignement of the bands due to adsorbed CO is given in the following paper. The activity of a number of samples toward CO adsorption has been compared with the activity of the same samples toward C_2H_4 polymerization. As a strict proportionality was always found, the CO test proves to be reliable. The polymerizing activity was spectroscopically evaluated as described by Eley and coworkers[5] by following the change in OD of the CH_2 stretching modes at 2850 or 2919 cm^{-1}, when a low pressure of ethylene (diluted by He to dissipate heat) was added to the catalyst.

Both the reduction time and the pressure of gas play a minor role in the reduction process, so their influence has not been systematically studied. The most relevant parameters affecting the sample activity are the reduction temperature and the Cr content.

In order to study the effect of reduction temperature, a 0.5% sample activated at 750° was reduced following the above procedure, at increasing temperatures, and the activity was checked each time by means of the integrated intensity of the CO spectrum. The results are reported in Figure 4; the units in the ordinate scale are consequently cm^{-1}.

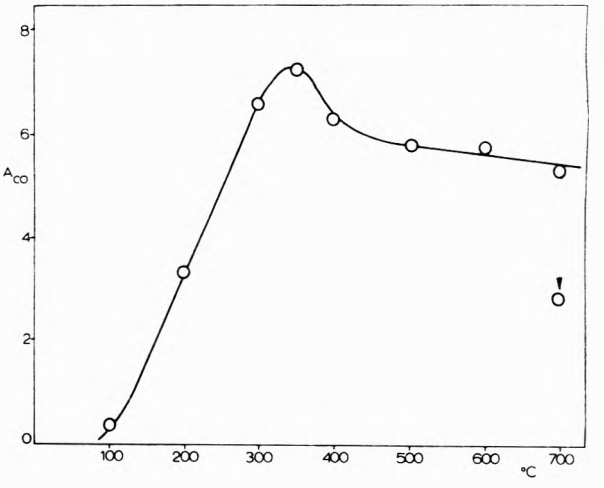

Figure 4. Activity toward CO (A_{CO}) of a 0.5% sample as a function of the reduction temperature. A_{CO} is in cm^{-1}. The arrow shows further decrease in activity due to prolonged heating.

It can be seen that the activity increases up to 350°, than a slow decrease is observed. While the left part of the curve is quite regular, the decrease of the activity for reduction temperatures higher than 350° requires some comment. A separate experiment carried out on a sample reduced at 350° shows that an identical decrease in activity is obtained when the sample is heated in the same way in vacuo. This means that in the right part of the curve, no changes in the oxidation number occur but instead a different phenomenon takes place related only with the high temperatures. An overall interpretation is as follows. As the reduction process has likely generated on the surface low-valence Cr ions coordinatively unsaturated, i.e., with a low crystal field stabilizing energy (cfse), an activated rearrangement to higher coordination states likely takes place, leading to a decrease of activity. In parts II and III this phenomenon is studied by means of the ir spectra of adsorbed CO and NO and the same conclusions are reached.

If higher temperatures are used, or heating is prolonged, the decrease of the sample activity is much more remarkable, as shown, for instance, by the arrow in Figure 4.

From the above results it clearly appears that 350° is the most efficient reduction temperature. So, the reduction processes are intended hereafter to be done at this temperature.

Also it must be noted that the activated rearrangement of Cr ions on the surface may be reversed by performing some "oxidation–reduction cycles", i.e., oxidation at high temperature (usually 550°) followed by a standard reduction at 350°. The performance of some oxidation–reduction cycles also proves to be useful in order to maximize the catalyst activity and stabilize its properties.

The changes in activity due to different Cr loadings have been measured over the whole series of catalysts prepared. All these, after a 750° activation, underwent reduction at 350° and some oxidation–reduction cycles until the maximum activity toward CO adsorption was developed. As a general trend, samples with higher Cr content are more resistant to complete reduction and require a higher number of oxidation–reduction cycles. In parts II and III, the effects of such oxidation–reduction cycles on the ir spectra of adsorbed CO and NO are reported.

Finally the activity toward C_2H_4 polymerization was determined in each case. Figure 5 reports the observed activi-

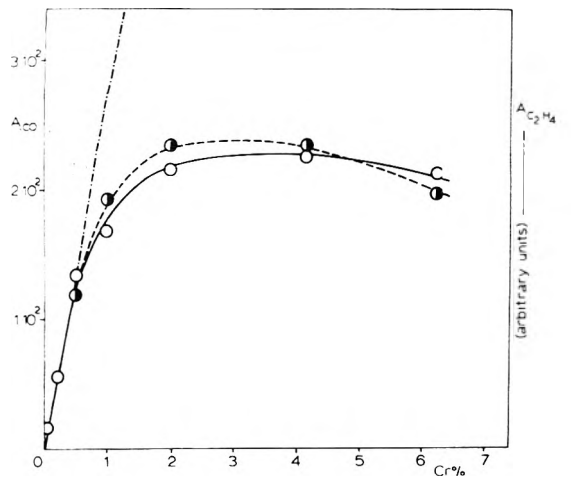

Figure 5. Activity toward CO (solid line) and ethylene (broken line) as a function of the Cr content: left-hand side, A_{CO} per unit weight of catalyst (the units are cm^{-1} g^{-1}; right-hand side, $A_{C_2H_4}$ per unit weight of catalyst in arbitrary units. The - · - · - line represents the extrapolation of the linear portion.

ty of the samples toward CO adsorption (solid line) and toward C_2H_4 polymerization (broken line).

Both activity measurements are reported per unit weight of the catalyst; while the unit scale for polymerization activity (right-hand side of the figure) is arbitrary, the unit scale for CO adsorption (left-hand side) is cm^{-1} g^{-1}. As previously stated, the two sets of data match fairly well. The curve of the polymerization activity is also very similar to previously published data.[1,9]

The curves of Figure 5 may be divided into two parts. In the range 0–0.5% the activity of the sample is nearly proportional to the Cr content, so that the specific activity (i.e., the activity per unit weight of Cr) is constant. By comparing the extrapolation of the linear portion with the actual behavior of the activity curve, it is observed that for Cr loadings higher than 0.5% a remarkable decrease in the catalyst specific activity occurs, as the overall activity is nearly constant.

The behavior of the activity curve is likely related to the structure of the reduced surface phase. In the 0–0.5% region, a very high dispersion degree is obtained, which favors the formation on the surface of elementary noninteracting structures, characterized by Cr ions of low valence, responsible for the light blue color of the sample. A constant specific activity is accordingly obtained. At increasing Cr content, a two-dimensional phase appears, in which an increasing part of the ions is coordinatively saturated and no longer active. At the same time the valence state III becomes favored[7] and the samples accordingly turn to green.

From the above considerations, it is inferred that it is preferable to begin the study of the chemical properties of silica-supported Cr ions with highly diluted catalysts, as in this case both maximum specific activity and simplest surface structures occur.

Finally, knowledge about highly diluted samples may give a reference frame for the study of catalysts at higher Cr content.

(C) *Valence and Coordination State of Cr Ions in Reduced Diluted Samples.* As it is well known,[1,8] after CO reduction surface Cr ions may undergo a great deal of reactions affecting the coordination and/or the oxidation state, and a number of these are discussed in the following papers.

We summarize here some information about the catalyst before any reaction.

The mean oxidation number was obtained by exposing fully reduced samples to O_2 at 550° and measuring the uptake. Catalysts with a loading up to 0.5% invariably show an oxidation number between 2.05 and 2.15. First of all, this fact confirms the abundance of Cr^{II} ions on the surface, in agreement with the literature.[7-8] The departure from the ideal value of 2.00 may be ascribed to the presence of Cr^{III} ranging from 5 to 15%. Higher valence states seem unlikely.

The presence of Cr^{II} and Cr^{III} on the surface may be accounted for by the reduction of dichromates (and chromates) by means of CO which is a two electron reducing agent. While the reduction of chromates only gives origin to isolated Cr^{II} ions, the reduction of dichromates may account for the presence of both Cr^{II} and Cr^{III} in pairs, as an even number of electrons is involved in both processes. At such low Cr loadings, the abundance of Cr^{III} seems to depend on the efficiency of CO_2 removal; in fact in a flow reducing system a mean oxidation number of 2.00 has been claimed.[8]

As already stated, little is known about the coordination state of Cr ions in the reduced samples. The structures obtained by the mere removal of the proper number of oxygen atoms from structures I or II as done by Hogan[9] and Krauss[8] have no meaning from a structural point of view. Surface Cr ions pairs surely rearrange in order to maximize the cfse, the extent of the rearrangement depending on their charge and the availability of surface oxygen atoms in suitable position.

A further possibility is that pairs of Cr^{II} could interact with each other forming metal–metal bonds such as those of chromous acetate.

Determination of coordinative states can be made, in principle, from uv–visible measurements. Figure 6 reports the reflectance spectra of a 0.5% sample both before (curve a) and after reduction (curve b).

Curve c refers to the adsorption of 20 Torr of NH_3 on the reduced sample, and is discussed later. Curve a actually coincides with that of Figure 3 and it is reported here to substantiate, by comparison with curve b, the large changes induced by the reduction process on the uv–visible spectra.

On the ground of the classical ligand field theory, curve b may be divided into two parts: the d–d region below 21,000 cm^{-1}, in which a complex absorption occurs with maxima at 12,000 and 7500 cm^{-1} and shoulders at ~15,000 and ~10,000 cm^{-1}; the electron-transfer (ET) region in which very intense absorptions occur at 31,000 and 38,500 cm^{-1}. By varying the reduction procedures, some changes in the spectra may be induced, from which a correlation is drawn between the 7500- and 31,000-cm^{-1} absorptions.

Let us discuss the two spectral regions separately.

In order to assign the d–d absorption of curve b, reference may be made to Cr^{III} and Cr^{II} in the various known coordinative states,[26-33] taking into account that the latter valence state largely predominates on the surface. No immediate results can be achieved, as nearly all coordinative situations lower than octahedral lead to a couple of absorptions in the 12,000–5000-cm^{-1} range. Moreover it must be taken into account that unusual coordinative states may occur on the surface.

Nevertheless, the comparison with literature data

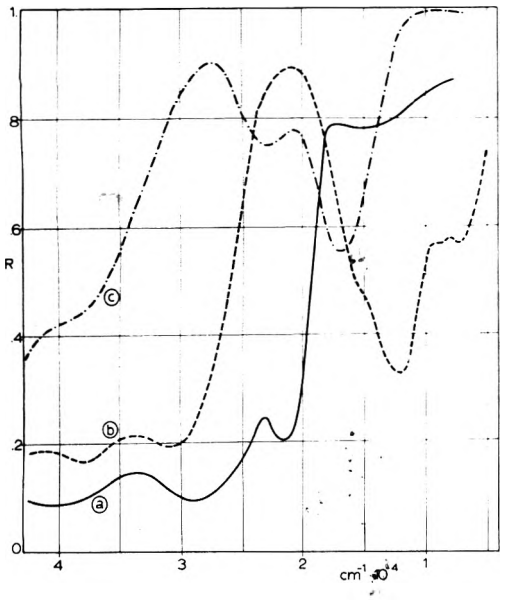

Figure 6. Uv-visible reflectance spectra of a 0.5% sample after various treatments (reflectance vs. wavelength in cm^{-1}): (a) after activation at 600°; (b) after reduction at 350°; (c) after adsorption of NH_3 (at a pressure of 20 Torr).

suggests that the complexity of curve b in the d–d region is due to the presence of more than one coordinative situation of Cr^{II}.

On the contrary, the interpretation of the spectrum after NH_3 interaction is easily done with reference to octahedral complexes of Cr^{II} and Cr^{III}.[34]

Curve c is very simple, as only two peaks occur at 23,000 and 17,000 cm^{-1}. The former is easily assigned to the $^4T_{1g} \leftarrow {}^4A_{2g}$ transition of an octahedral Cr^{III} ions. This transition is associated with another one $^4T_{2g} \leftarrow {}^4A_{2g}$ of lower intensity at about 17,000 cm^{-1}. As the 17,000-cm^{-1} absorption is on the contrary much more intense, this absorption can best be assigned to a superposition of the low intensity partner of the 23,000-cm^{-1} band with a higher intensity band due to the $^5T_{2g} \leftarrow {}^5E_{2g}$ transition of an octahedral Cr^{II} complex. The intensity ratio between the 23,000- and 17,000-cm^{-1} bands is consistent with a ~10% Cr^{III} content, as estimated from the mean oxidation number, if we take into account that the Cr^{III} (oct) $^4T_{2g} \leftarrow {}^4A_{2g}$ transition usually exhibits a larger molar extinction coefficient than the Cr^{II} (oct) $^5T_{2g} \leftarrow {}^5E_{2g}$ transition.

By comparing curves b and c in the d–d region, we may observe that after NH_3 adsorption the overall integrated intensity is lower and the corresponding frequencies higher.

All this means that, before adsorption, the ions are present in low coordinative states with accordingly small 10 *Dq* values and some d–p mixing. Kazansky[24] has claimed that a single type of tetrahedral coordination occurs, on silica, for a number of ions including Cr^{II}. This simple picture of the reduced phase is not confirmed by our spectra because of their complexity.

Also, caution must be exercised in assuming the same coordination for both Cr^{II} and Si^{IV} owing to the different ionic size. The adsorption of such a strong ligand, such as NH_3, places all the ions into the highest coordinative state (i.e., oct); the initial heterogeneity is consequently smoothed out and the only discriminating parameter is the ionic charge. For these reasons the absorptions due to Cr^{III} and Cr^{II}, strongly overlapped in curve b, are well separated in the final curve c.

Let us discuss the ET region of Figure 6 (curves b and c). The bands at 31,000 and 38,500 cm^{-1} of curve b are independent, as their intensity ratio can change by varying the experimental conditions. Thus these absorptions may be envisaged as electron transfers from oxygen ligands to Cr ions in different surface structures. Moreover, owing to the small Cr^{III} percentage, we assume that both these structures involve Cr^{II}.

As far as we know, the ET spectra of surface ions have never been discussed. The general theory of ET[34,35] is not well developed to be easily applied in surface studies.

The ET transitions are generally discussed in terms of "reducing" and "oxidizing" power of ligands and central metal ions, respectively, so that we will utilize these concepts in the present case.

As already done for the d–d region, some information can be gained from the comparison between the spectra run before and after reaction with a suitable ligand.

Figure 6 shows that NH_3 interaction destroys the 31,000-cm^{-1} band and strongly decreases the band at 38,500 cm^{-1}. Even loosely interacting ligands, such CO_2 (see paper II), may selectively affect the ET bands.

In all cases the bands are shifted to much higher frequencies (>40,000 cm^{-1}), i.e., into the normal ET range of complexes without π-acceptor ligands.

As the reducing power of the oxygen ligands is likely unchanged upon adsorption, it is inferred tht the shift is due to decreased oxidizing power of the metal ion. This decrease is obviously related to the increased stability of Cr^{II} ions in higher coordination states.

On this grounds the occurrence of a couple of ET bands at very low frequency (31,000 and 38,500 cm^{-1}) on the reduced sample can be explained by the presence of two different types of coordinatively unsaturated Cr^{II} ions.

Also it may be deduced that the 31,000-cm^{-1} band should correspond to less coordinated Cr^{II} species. Two main observations support this assignement: the 31,000-cm^{-1} species is more reactive than the one at 38,500 cm^{-1}; the 31,000-cm^{-1} band is associated, as previously stated, with the lowest component of the d–d spectrum, i.e., with the lowest ligand field value.

Conclusions

Further evidence has been gained in this paper concerning the formation of a definite compound between CrO_3 and SiO_2. In particular it has been shown that dichromate groups are mainly formed on the surface in the whole 0–5% Cr range. For higher Cr loadings, the surface phase stops growing and CrO_3 is transformed, upon activation, into chromia-like crystallites.

A number of parameters can affect the structure and reactivity of CO-reduced catalyst, among which the most relevant are Cr loading and the temperature of reduction. The maximum activity per Cr ion is reached in the 0–0.5% range, when a 350° reduction temperature is used. Both higher Cr content and higher reduction temperatures lead to a decrease of specific activity of the Cr ions. In the former case clusters are formed in which some of the ions are fully coordinated and consequently inactive. In the latter case high temperature treatments allow the ions to rearrange on the surface and to reach high coordination states with subsequent decrease in activity.

Samples showing highest activity possess on the surface

pairs of Cr ions coming from the reduction of dichromates. A little fraction of them (less than 15%) is in the trivalent state, while the predominant part is in the divalent state. Optical measurements on reduced diluted samples show that Cr^{II} ions are in two different low-coordination states, so that at least three different Cr surface species can be envisaged.

As a consequence of coordinative unsaturation, surface ions can coordinate a great deal of ligands. Some of these reactions are described in the following papers, in which, for the sake of clarity, surface compounds formed by gas interaction are grouped into three classes according to their stoichiometry.

Acknowledgment. We thank Professor F. S. Stone, who allowed one of us to carry out some reflectance spectra, and Dr. M. Lofthouse for reading the manuscript.

Support for the research has been partially provided by the Consiglio Nazionale delle Ricerche.

References and Notes

(1) A. Clark, *Catal. Rev.*, **3**, 145 (1969).
(2) K. G. Miesserov, *J. Catal.*, **22**, 340 (1971).
(3) C. Eden, M. Feichenfelder, and Y. Haas, *J. Catal.*, **9**, 367 (1967).
(4) P. Cossee, *J. Catal.*, **3**, 80 (1964).
(5) D. D. Eley, C. H. Rochester, and M. S. Scurrell, *Proc. R Soc., London, Ser. A*, **329**, 361 (1972); **329**, 375 (1972); *J. Catal.*, **29**, 20 (1973); *J. Chem. Soc., Faraday Trans. 1*, **69**, 660 (1973).
(6) H. L. Krauss, F. Weber, and N. Mövik, *Z. Anorg. Chem.*, **338**, 121 (1965).
(7) H. L. Krauss and H. Stach, *Inorg. Nucl. Chem. Lett.*, **4**, 393 (1968); *Z. Anorg. Chem.*, **366**, 34, 280 (1969).
(8) H. L. Krauss, *Proc. Int. Congr. Catal. 5th, 1972*, **1**, 207 (1973).
(9) J. P. Hogan, *J. Polym. Sci.*, **8**, 2637 (1970).
(10) Y. I. Ermakov, V. A. Zacharov, and E. G. Kushnareva, *J. Polym. Sci.*, **9**, 771 (1971).
(11) A. Zecchina, et al., *J. Phys. Chem.*, **75**, 2774, 2783, 2790 (1971); **76**, 571 (1972); *J. Catal.*, **25**, 65 (1972).
(12) E. Borello, et al., *Inorg. Chim. Acta*, **6**, 45 (1972); *Ind. Chim. Belg.*, **38**, 508 (1973).
(13) E. Borello, A. Zecchina, C. Morterra, and G. Ghiotti, *J. Phys. Chem.*, **73**, 1286 (1969).
(14) A. Zecchina, et al., *J. Phys. Chem.*, **73**, 1292, 1295 (1969); *J. Chem. Soc. A*, 2196 (1969).
(15) C. P. Poole and D. S. McIver, *Adv. Catal.*, **17**, 223 (1966).
(16) E. Borello, A. Zecchina, and C. Morterra, *J. Phys. Chem.*, **71**, 2938 (1967).
(17) J. B. Peri and A. L. Hensley, *J. Phys. Chem.*, **72**, 2926 (1968).
(18) C. Morterra and M. J. D. Low, *Ann. N.Y. Acad. Sci.*, **220**, 135 (1973), and references therein.
(19) E. Borello, A. Zecchina, and M. Castelli, *Ann. Chim. (Rome)*, **53**, 690 (1963).
(20) A. Zecchina, M. G. Lofthouse, and F. S. Stone, *J. Chem. Soc., Faraday Trans. 1*, in press.
(21) A. Zecchina, G. Ghiotti, L. Cerruti, and C. Morterra, *J. Chim. Phys.*, **68**, 1479 (1971).
(22) C. G. Barraclough, J. Lewis, and R. S. Nyholm, *J. Chem. Soc.*, 3552 (1959).
(23) H. Stammreich, D. Sala, and K. Kawai, *Spectrochim. Acta*, **17**, 226 (1961).
(24) V. B. Kazansky, *Kinet. Katal.*, **11**, 455 (1970).
(25) A. Cotton and G. Wilkinson, "Advanced Inorganic Chemistry", Interscience, New York, N.Y., 1962.
(26) F. Mani and L. Sacconi, *Inorg. Chim. Acta*, **4**, 365 (1970).
(27) J. P. Fackler, Jr., and D. G. Holah, *Inorg. Chem.*, **4**, 954, 1112 (1965); **4**, 1722 (1965); **5**, 479 (1966).
(28) D. E. Scaife, *Aust. J. Chem.*, **20**, 845 (1967).
(29) E. C. Alyea, et al., *J. Chem. Soc., Dalton Trans.*, 185 (1973).
(30) D. H. Gerlach and R. H. Holm, *Inorg. Chem.*, **8**, 2293 (1969).
(31) C. S. Kelley and F. Williams, *Phys. Rev. B*, **2**, 3 (1970).
(32) G. Groube and H. J. Schulz, *Phys. Status Solidi B*, **54**, K69 (1969).
(33) R. Pappalardo and R. E. Dietz, *Phys. Rev.*, **123**, 1188 (1961).
(34) B. N. Figgis, "Introduction to Ligand Fields", Interscience, New York, N.Y., 1967.
(35) C. K. Jorgensen, *Prog. Inorg. Chem.*, **12**, 101 (1970).

On the Chemistry of Silica Supported Chromium Ions. II. One-Ligand Complexes. Adsorption of Carbon Monoxide, Carbon Dioxide, and Pyridine

A. Zecchina,* E. Garrone, G. Ghiotti, and S. Coluccia

Istituto di Chimica Fisica dell'Università di Torino, Corso M. D'Azeglio, 48-10125 Torino, Italy *(Received September 11, 1974)*

Publication costs assisted by Italian CNR

Py, CO_2, and CO interaction with reduced diluted silica supported Cr catalysts is presented. Py shows the presence of Lewis acidity on the surface. CO_2 only interacts in a linear form with surface Cr ions. CO is the most interesting ligand, as three different kinds of surface ions are observed (Cr^{III} and two Cr^{II} species). At high pressures or low temperatures CO also adsorbs in a bridged form thus revealing chromium ions pairs.

Introduction

In part I, the characterization of a chromia–silica catalyst has been described, in which a high specific activity is achieved by both a low Cr loading and careful pretreatment.

In this and the following papers we discuss the reactivity of such samples toward simple molecules, while the chemistry of nondiluted samples is used mainly as a reference.

In particular the adsorption of CO, CO_2, and Py is described here, as these molecules mainly produce, at room temperature, 1:1 surface complexes, while other molecules, that will be discussed next, show a more involved behavior. These three molecules are widely adopted as "test molecules", so that no justification is needed for their use. For the sake of clarity, the discussion of experimental results is divided into three independent parts, each dealing with

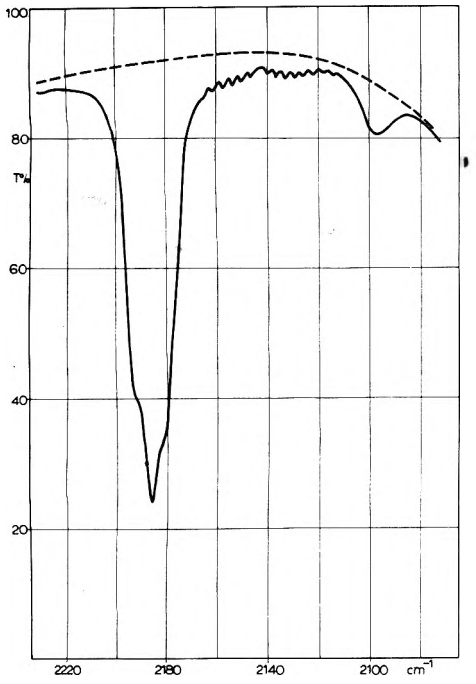

Figure 1. Room temperature spectrum of adsorbed CO on a 0.5% standard reduced sample (transmittance vs. wavelength). Gas pressure = 40 Torr.

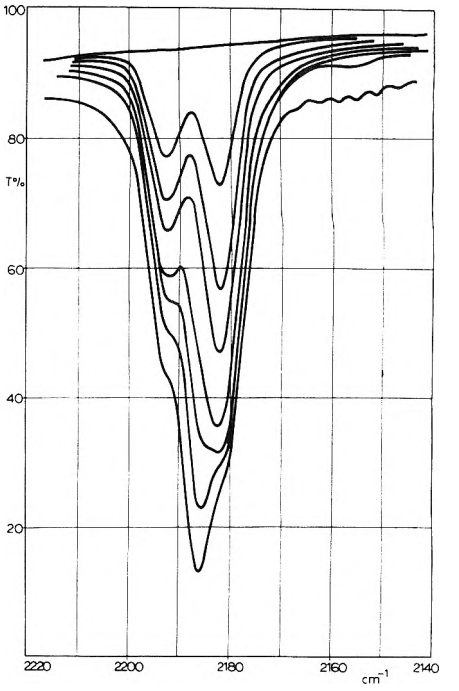

Figure 2. Ir spectrum as in Figure 1 recorded on an expanded scale. CO pressures in Torr are: 40, 4, 4×10^{-1}, 3×10^{-2}. Other spectra obtained by pumping for 30 sec, 1 min, and 3 min.

one simple gas, while the comparison among different reactivities is made in the last paragraph, devoted to the conclusions.

Experimental Section

The samples, infrared equipment, reflectance spectrometer, microbalance, and volumetric adsorption system were described in part I.

Results and Discussion

(1) *CO Adsorption.* At room temperature carbon monoxide readily interacts with standard reduced diluted samples, which assume a light violet color.[1,2] The related uv–visible reflectance spectrum, showing a single unassigned peak at ~19,000 cm^{-1}, has been published by Krauss.[2] Our own spectra are much more complex, and are not reported here, as a full assignment requires further work to be carried out.

The corresponding ir spectrum is, on the contrary, rather simple. Figure 1 shows the ir spectrum in the 2050–2220-cm^{-1} range of a 0.5% sample contacted with 40 Torr of gas, while in Figure 2 the same spectrum is shown in a narrower range (2140–2220 cm^{-1}) and with an expanded abscissa scale. In Figure 2 spectra recorded at decreasing CO coverages are also reported.

Besides a small contribution from the gas, only visible at high pressures, four bands can be evidenced from Figures 1 and 2: a very weak one at 2095 cm^{-1} (Figure 1) and three heavily overlapping bands at 2181, 2186, and 2191 cm^{-1} (Figures 1 and 2). CO adsorption is reversible at room temperature and the background spectrum is completely recovered by prolonged pumping at room temperature.

Accordingly, the bands intensity largely depends on CO pressure; in particular the 2095-cm^{-1} band is only present at pressures above 10 Torr. The heavy overlap between the triplet components does not allow exact intensity evaluation of the single peaks to be performed. Nevertheless it is evident from Figure 2 that the 2186-cm^{-1} band is strongly pressure dependent, while both the higher and the lower frequency components are more resistent to evacuation.

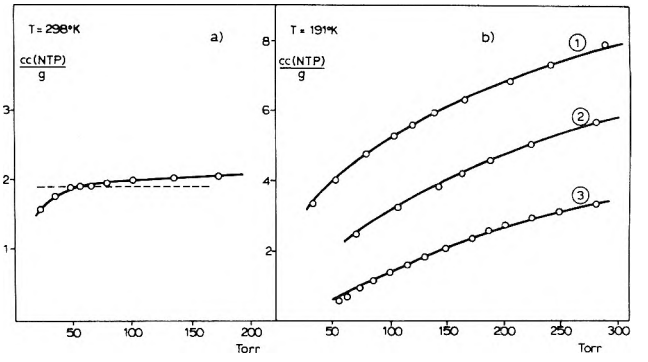

Figure 3. CO adsorption isotherms (adsorbed volumes per unit weight of catalyst vs. CO pressure). (a) Room temperature measurements on a 0.5% sample: full line, experimental curve; broken horizontal line, reference amount corresponding to Cr:CO = 1:1, (b) low temperature measurements (T = 191°K) on the same sample: (curve 1) primary isotherm; (curve 2) secondary isotherm; (curve 3) physisorption on identically pretreated pure silica.

The isotherm of CO adsorption at room temperature is shown in Figure 3a. The horizontal broken line corresponds to an average composition of one CO molecule per Cr ion. It can be seen that such a situation is roughly achieved under a pressure of 40 Torr, to which Figure 1 refers. At higher pressures, the CO/Cr ratio slightly increases. A 1:1 average composition strongly suggests that each surface Cr ion adsorbs one CO molecule, to form Cr–CO linear complexes.

In order to verify the above hypothesis, some low temperature ir measurements have been performed, one of which is reported in Figure 4.

Curve a refers to the room temperature interaction of 40 Torr of CO and coincides with the spectrum of Figure 1.

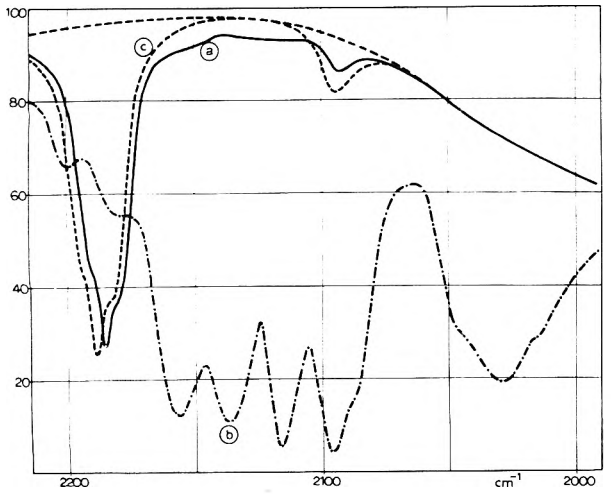

Figure 4. Low temperature ir spectra of CO adsorbed on a 0.5% standard treated sample (transmittance vs. wavelength): (curve a) CO adsorption (40 Torr) at room temperature; (curve b) after cooling to liquid N_2; (curve c) after prolonged outgassing of the cooled sample.

Cooling with liquid nitrogen[3] leads to the striking spectrum b in which maxima are visible at 2200, 2184, 2157, 2137, 2115, 2095, and 2035 cm^{-1}. Curve c is obtained by prolonged outgassing at the same temperature.

Low-temperature quantitative measurements have also been carried out. As at liquid N_2 temperature physical adsorption on the support overcomes the interaction with Cr ions, the temperature of −80° has been chosen, and the data so obtained are reported in Figure 3b. At this temperature the physisorption isotherm on the pure support (curve 3) and the isotherm on the reduced catalyst (primary isotherm, curve 1) are sufficiently separated to allow the mean stoichiometry of the surface complexes to be measured. A CO:Cr ratio close to two is found.

Curve 2 represents what we term the secondary isotherm, i.e., the CO adsorption isotherm on the catalyst saturated with CO at −80° and then outgassed at the same temperature.

By comparing primary and secondary isotherms, it is inferred that the outgassing at −80° leaves on the surface an amount of CO corresponding to a Cr:CO = 1:1 ratio. This means that those surface CO complexes which are pressure dependent at room temperature, become stable at −80°.

On this grounds, it is possible to assign the observed ir bands.

In a previous paper,[4] we showed that CO physisorbs on silica at low temperature yielding two bands at 2137 and 2157 cm^{-1} that are also present in the spectrum b of Figure 4.

The triplet of bands around 2185 cm^{-1} is assigned to the CO stretching mode of 1:1 Cr–CO linear complexes both at room and low temperatures. In fact, these bands reach their maximum intensity when the average composition is Cr:CO = 1:1 (compare curves a and c in Figure 4) and disappear when the CO/Cr ratio increases (curve b in Figure 4). The small frequency change that the triplet exhibits in curve c is a second-order effect due to the low temperature; such an effect is a common feature of low-temperature ir spectra and will be discussed in detail elsewhere.

As nearly all of surface Cr ions are present in pairs (see part I), a schematic picture of these complexes is given in structure a. No coupling is expected between the two CO

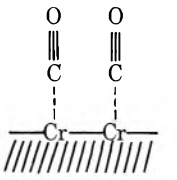

a

vibrators and the two Cr sites may be regarded as independent.

The assignment of the remaining bands (2200, 2184, 2115, 2095, 2035 cm^{-1}) and shoulders is rather troublesome, and goes beyond the scope of this paper, as complexes with more than one CO per Cr ion are surely involved.

Nevertheless something must be said about the 2095-cm^{-1} band, as it already appears in the room temperature spectrum. The simplest structure that can be expected to form when more CO is adsorbed is represented in b but it

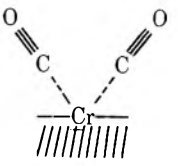

b

has to be discarded, as it cannot account for CO stretching frequencies some 100 cm^{-1} below the original triplet. In fact, the coordination of extra ligands by a CO-supporting Cr ion affects the CO stretching frequency by some wave numbers as observed, for example, on α-chromia[5] or with the $Cr^{II}(NO)_2CO$ complex described in part IV of this series. Also the study of mixed $Cr^{II}(CO)$–olefin complexes, that will be described elsewhere, confirms this observation. Thus, more sophisticated structures have to be considered, in which nonlinear CO ligands are involved.

Taking into account structure a, structure c is envisaged,

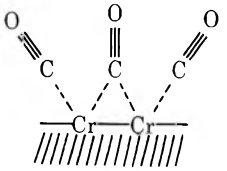

c

in which a CO molecule is shared by two neighboring ions which already chemisorbed CO. Structure c can account for a CO stretching frequency as low as 2095 cm^{-1}, as the central CO ligand must have a C atom with some sp^2 character and, accordingly, a lower bond order. Of course, the central CO molecule must not be regarded as a real bridged carbonyl, as it is known to absorb at definitely lower frequencies, but rather as a CO molecule in which a partial sp^2 hybridization occurs.

In our opinion, the whole curve b of Figure 4 has to be interpreted on the grounds of structure c and/or structure d

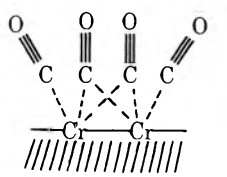

d

which can be formed from structure c if at least part of the Cr ions possess three coordination vacancies. A variety of structures such as c and d may occur on the surface differing by the Cr–Cr distance, valence, and the coordination state of the ions, so explaining the great complexity of spectrum b of Figure 4. Structure d has a CO/Cr ratio of two, in agreement with experimental findings.

In both structures c and d the insertion of bridging CO ligands likely affects the frequency (and the extinction coefficient) of the linear CO oscillators, so accounting for the disappearance of the initial triplet with increasing CO coverage. We intend to stress here that the detection of Cr pairs by CO adsorption at low temperature is rather peculiar, as all other molecules considered in this paper only coordinate to a single Cr center; therefore a systematic study of this aspect will be reported elsewhere.

Let us discuss now in more detail the band triplet at 2191, 2186, and 2181 cm^{-1}. As it is due to one-ligand complexes, two main conclusions can be immediately drawn. First, in the standard experimental conditions (0.5% sample, 40 Torr of CO), CO reveals nearly all of the surface Cr ions, as the average composition is close to 1:1 and the Cr ions carrying two CO (2095-cm^{-1} band) are very few. Secondly, the band structure shows how at least three different species of Cr ions are on the surface. This result entirely agrees with the conclusions of the preceeding paper, in which the presence of Cr^{III} and of two kinds of Cr^{II} was suggested.

It is known that the CO coordination may be explained in terms of a synergic σ donation/π back donation,[6] according to which the lower the π contribution, the higher the stretching frequency. The π contribution from ions is normally small[6] so that in the present case high frequencies are justified. In particular, Cr^{III}–CO complexes should be associated with the highest frequency band (2191 cm^{-1}), as the smallest back donation would occur.

Experimental evidences that the high-frequency band (2191 cm^{-1}) is related to Cr^{III} are as follows.

(a) In part I it was shown that a high-temperature treatment causes some surface rearrangements, leading to an overall decrease of the activity toward CO. Surface Cr^{III} pairs are expected to be more stable than the corresponding Cr^{II} structures, as additional oxygen ligands likely increase the cfse of the involved Cr ions. This hypothesis, if correct, should be confirmed by the CO spectrum. In Figure 5 the CO spectra (40 Torr) are compared of a standard sample (curve a) and of the same sample successively heated in vacuo for 2 hr at increasing temperatures (curves b, c, and d). It is easily seen that, in agreement with the above picture, the decrease in activity is entirely due to the 2181–2186-cm^{-1} bands (Cr^{II}) while the 2191-cm^{-1} band is unaffected (Cr^{III}). We recall here that the coordinative reorganization to which Cr^{II} ions have been submitted may be reversed by some oxidation–reduction cycles, and the original CO spectrum a may be recovered.

(b) It is observed that the 2191-cm^{-1} band is favored by those pretreatments which likely favor a high Cr^{III} content: preparation from Cr^{III} salts,[7] reduction with hydrogen-containing reductants, presence of water during reduction,[8] high Cr content, etc.

We think that the last point, i.e., the effect of high Cr contents on the ir spectrum of adsorbed CO deserves a more detailed discussion. Figure 6 refers to the adsorption of 40 Torr of CO on a 4% sample at the end of successive oxidation–reduction cycles. While a 0.5% sample only requires one reduction process to be fully reduced, the same treatment on a 4% sample only leads to a partial reduction, as revealed by the high intensity of the 2191-cm^{-1} component (curve a). Successive treatments (oxidation–reduction cycles) improve the overall activity of the sample, as already pointed out in part I, and also affect the relative intensity of the triplet components (curves b and c). This phenomenon can be understood on the grounds of an increasing reduction of the surface at least in part due to the transformation of Cr^{III} into Cr^{II} structures.

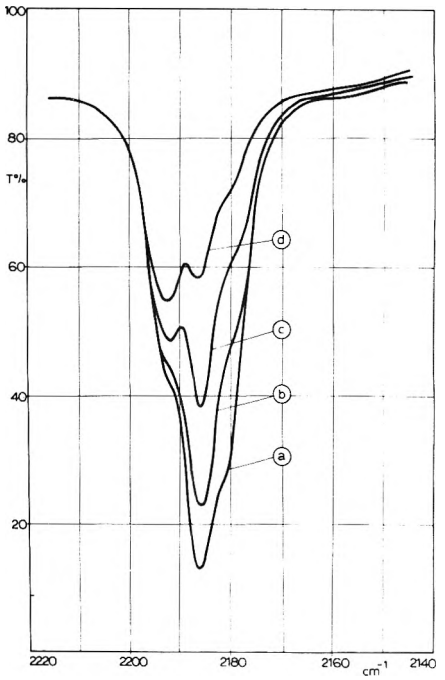

Figure 5. Activity loss of the catalyst due to thermal treatments (transmittance vs. wavelength). All curves refer to the adsorption of 40 Torr of CO: (curve a) regular spectrum as in Figure 1; (curve b) after 2 hr at 600° in vacuo; (curve c) the same at 700°; (curve d) the same at 850°.

It must be recalled here that in this concentration range, a large fraction of Cr ions is no longer accessible to CO, owing to the formation of a two-dimensional phase (see part I). Thus the CO molecule only reveals, at room temperature, highly coordinatively unsaturated ions.

The comparison of our results with those of other authors is difficult, due to different preparation and pretreatment conditions. Some papers deal with catalysts of high Cr loading[7,9,10] that on CO adsorption form carbonates[9] and carboxylates, both of which species are totally absent on our low Cr loaded samples. In our previous work[7] two main band envelopes were found at about 2200–2187 and 2145–2136 cm^{-1}. At present we have no assignment for the latter group of bands. Both Clark et al.[9] and Eley et al.[10] report bands in the 2200–2180-cm^{-1} region. In particular Eley et al.[10] observe peaks at 2207, 2187, and 2185 cm^{-1}, the former only being present on ethylene-reduced samples. As their catalysts were of high Cr loading and used in heavy pellets, they were probably unable to resolve the band envelope at ~2190 cm^{-1}.

On the other hand, our ir data well agree with those obtained by Krauss,[11] while the interpretation is different, as he assigns all the absorptions to 1:1 Cr^{II} complexes.

(2) *CO_2 Adsorption.* Carbon dioxide is widely used to reveal basic surface groups, i.e., basic hydroxyls, basic oxygen

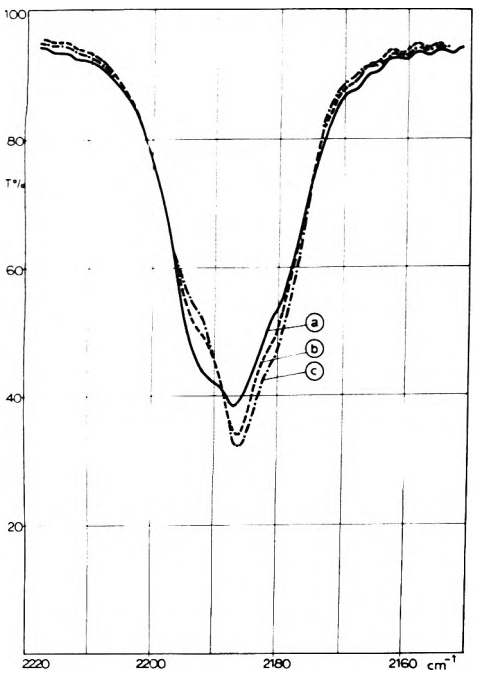

Figure 6. Changes in the CO spectrum of a 4% sample (40 Torr of gas) induced by successive oxidation–reduction cycles.

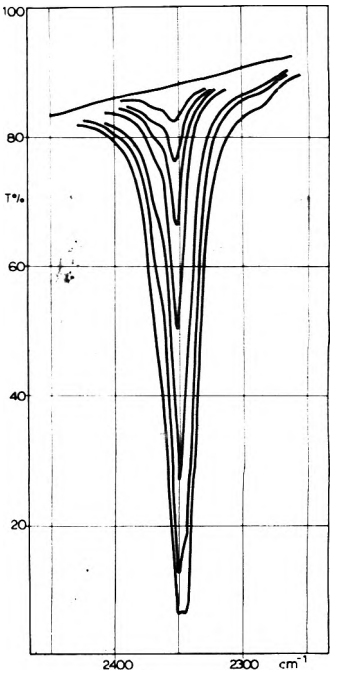

Figure 7. Ir spectra of CO_2 adsorbed on a standard reduced sample. Pressures in Torr are 10, 3, 5×10^{-1}, 6×10^{-2}, 3×10^{-2}. Other spectra obtained by pumping for 5, 15, and 45 sec.

ions, and dual sites consisting of cation–basic oxygen pairs, as the formation of spectroscopically well-known species takes place (bicarbonates and carbonates of various nature). See, for example, the results we have obtained in the study of crystalline α-chromia.[12]

The interaction of CO_2 with a standard pretreated 0.5% sample does not cause any signal in the range from 1300 (limit imposed by the silica cut-off) to 1950 cm^{-1} (upper limit of the organic carbonates-like species), except for a very weak band at 1380 cm^{-1}, which shall be discussed later. This clearly rules out the presence of basic oxygens in both single and dual sites, and of basic OH groups.

Figure 7 shows the strong absorption formed at 2350 cm^{-1} on CO_2 adsorption, whose complex nature is revealed by the presence of three components which heavily overlap and exhibit different pressure dependence. This absorption is surely due to the asymmetric stretching mode of linear CO_2 molecules loosely bound to the surface, as the frequency is very close to that of the gas. Accordingly, the weak band at 1380 cm^{-1} is assigned to the Raman active symmetric stretching mode of linear CO_2, which is activated here by the asymmetry caused by the surface.

Figure 8 shows the quantitative data concerning the interaction of CO_2 with the sample at room temperature (curve b). Carbon dioxide also weakly interacts with the silica support, as already observed by Peri.[13] Curve a of Figure 8 refers to the adsorption of CO_2 on a pure silica sample pretreated in the same way as the catalyst.

The difference between the two curves is ascribed to CO_2 linearly adsorbed onto Cr ions: at high pressure the average composition tends to 1:1. This fact likely means that each surface Cr may interact with CO_2 forming a 1:1 linear complex. More sophisticated structures (as in the case of CO) are ruled out, as the adsorption merely involve a polarization of the electronic charge, in agreement with the extreme bond weakness.

The whole complex absorption of Figure 7 must be ascribed to Cr–CO_2 complexes. In fact, under the adopted ex-

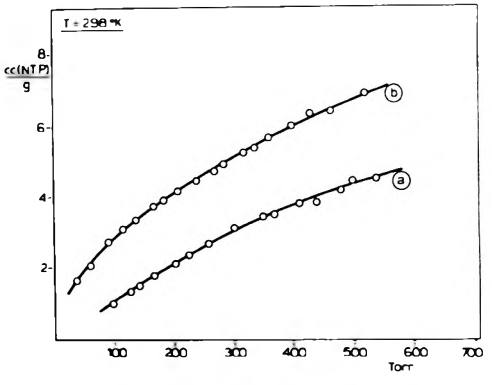

Figure 8. CO_2 isotherms at room temperature (adsorbed volumes per unit weight of catalyst vs. pressure): (curve a) physisorption on the support; (curve b) interaction with a 0.5% sample.

perimental conditions, the physisorption is negligible as can be seen from the isotherms and from the absence of any perturbation of the silanol stretching band.[13] As a consequence, it is inferred that the CO_2 molecule reveals the presence on the surface of three unsaturated Cr species, in agreement with previous results.

Strong changes in the uv–visible reflectance spectrum are produced by CO_2 adsorption. Figure 9 shows the spectra due to a standard reduced sample before (curve a) and after contact with 200 Torr of CO_2. From the isotherm of Figure 8 it may be inferred that, at this pressure, the coverage is very near to one, so that curve b would refer to surface Cr···O=C=O complexes. As far as curve a is concerned, reference must be made to part I. In the ET region we observe that the 31,000- and 38,500-cm^{-1} bands are destroyed upon CO_2 adsorption and that a new broad band at the upper end of the spectrum is formed.

The adsorption of small doses of CO_2 (the relevant spectra are not reported here for the sake of simplicity) shows that the 31,000-cm^{-1} band is destroyed first, in agreement

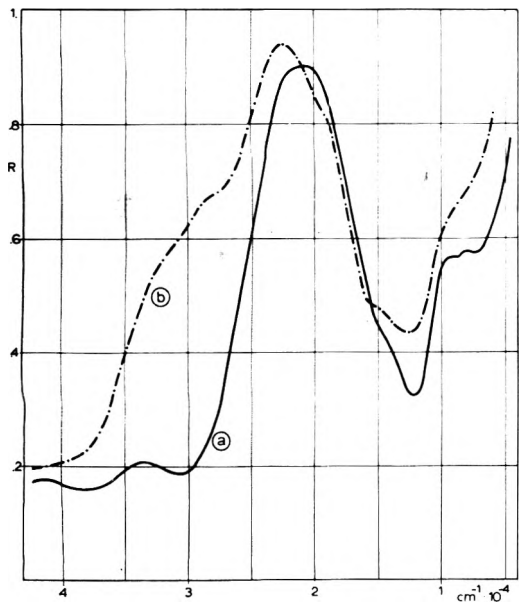

Figure 9. Reflectance spectrum of a 0.5% sample (reflectance vs. wavelength): (curve a) reduced sample; (curve b) after CO_2 adsorption (equilibrium pressure 200 Torr).

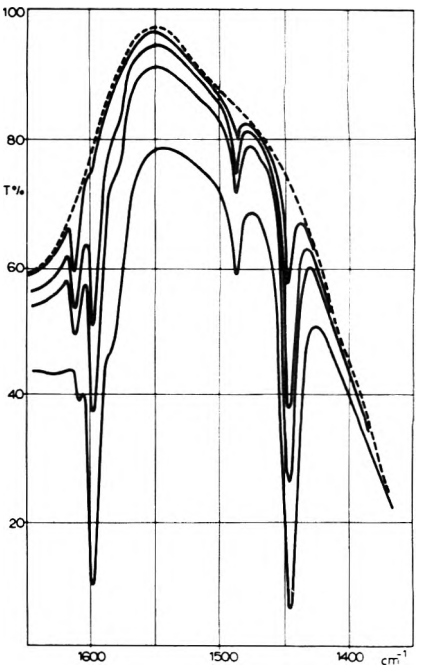

Figure 10. Ir spectra of Py adsorbed on a standard reduced sample. Pressures in Torr are 15, 3, 1, 10^{-3}.

with the discussion in part I. In the d–d region, a small decrease in the intensity as well as an overall small shift toward higher frequencies of the absorption is observed. Both these features fairly agree with an increase of the coordination number of one unit. The building up of sixfold coordinated complexes leads to a different spectrum, as was shown in the case of NH_3 (see part I).

Linear surface complexes of carbon dioxide have already been found on γ-Al_2O_3,[14] α-Cr_2O_3[12] and supported Cr_2O_3;[7] in all cases some correlation exists between the frequency increase and the interaction strength. On the contrary, only very recently homogeneous phase complexes involving linear CO_2 have been isolated.[15]

(3) *Pyridine (Py) Adsorption.* It is well known that Py adsorption provides an insight into the various kinds of surface acidity. Brønsted acidity is normally revealed by an absorption at 1540 cm^{-1}, characteristic of the pyridinium ion.

Cationic acidity can be monitored by the frequency of mode 1, which is very sensitive to coordination. The notation adopted here is that used by Pichat and coworkers.[16] In the present case, the samples are not transparent in the ν_1 spectral region and so the ν_{8a} and ν_{8b} modes have been chosen, which fall at 1583 and 1587 cm^{-1} in the free molecule. The 8a mode is fairly sensitive to coordination, being a nuclear mode of class A_1.[16] The 8b mode, on the contrary, is rather insensitive.

Figure 10 shows the ir spectrum in the 1350–1650-cm^{-1} range of increasing amounts of Py adsorbed on a standard reduced sample. In the high-frequency region three absorptions occur around 1600 cm^{-1} consisting of two definite bands at 1612 and 1598 cm^{-1} and a shoulder at 1580 cm^{-1}. The latter band can be assigned to the unresolved 8a and 8b modes of "liquid-like" Py physically adsorbed on the covalent part of the support. The 1598-cm^{-1} band is strongly dependent on Py pressure and reference to Pichat's paper allows it to be assigned to the 8a mode of Py hydrogen bonded to silica hydroxyls. This leaves the 1612-cm^{-1} band which is assigned to the 8a mode of a Py molecule irreversibly adsorbed on surface Cr ions. Such a frequency increase is a common feature of Py complexes. Quantitative measurements of Py interaction have not been performed, so that any information about the number of Py molecules involved in this kind of complexes only comes from ir evidence. As it was pointed out in the first part of this paper, the use of high-temperature thermal treatments induces some surface rearrangements leading to a better shielding of the ions. While this process largely affects the CO spectrum, no change may be observed in the intensity of the 1612-cm^{-1} band. We infer that both highly unsaturated and nearly saturated Cr ions irreversibly adsorb the same number of Py molecules, so that in all cases Cr:Py = 1:1 complexes are envisaged.

The adsorption of NO (which is described in the following paper) definitely confirms that shielded Cr ions still present one residual coordination vacancy. It is noteworthy that the adsorption of such a "hard" ligand as Py does not reveal any surface heterogeneity as was found with CO. This lack of sensitivity of Py to features of the ion it coordinates to is well known in inorganic chemistry.

At high Py relative pressures, complexes with a higher number of Py ligands may occur, as suggested by a small decrease of the 1612-cm^{-1} band. The 8a modes of the Py ligands in these complexes are expected to fall at lower frequencies and to overlap with the 1598-cm^{-1} band.

These complexes with more than one Py molecule are likely to be very labile, as a short outgassing at room temperature fully restores the 1612-cm^{-1} band. This lability fairly agrees with the instability of inorganic complexes with a large number of Py ligands.[17]

Conclusions

The use of these three molecules allows different information to be acquired.

Py adsorption merely shows the presence of Lewis acidity on the surface, while no details are obtained about heterogeneity both in coordination and in valence states.

Carbon dioxide very loosely interacts in a linear form

with each Cr ion. Accordingly, the asymmetric stretching frequency is not strongly shifted with respect to the gas. Nevertheless, the related absorption is complex and reveals three different types of surface Cr ions. Despite the small interaction energy, the uv–visible reflectance spectra show spectacular changes upon adsorption, in agreement with the one unit increase of the coordination number of the adsorbing Cr centers.

Carbon monoxide is by far the most interesting ligand. On one hand it is not as "hard" as Py, and on the other hand it possesses (while CO_2 does not) a σ–π bonding system very sensitive to both valence and coordination of the central ion. Also, different coordination modes are possible, i.e., linear and bridged.

Consequently the CO interaction with the reduced sample allows a detailed picture of the surface to be drawn that agrees well with the results in part I. On the surface both Cr^{III} and Cr^{II} are present, the latter in two forms differing by the coordinative situation. CO interacts with each form of the Cr ion and three bands are formed at 2191, 2186, and 2181 cm^{-1}.

On high-temperature treated samples and on samples with higher Cr contents other Cr species are present, which do not react with CO at room temperature.

As chromium ions predominantly occur in pairs, resulting from the reduction of surface dichromates, structures with bridged CO that predominate at low temperature also form under high CO pressures at room temperature (2095-cm^{-1} band).

Acknowledgment. Support for the research has been partially provided by the Consiglio Nazionale delle Ricerche.

References and Notes

(1) J. P. Hogan, *J. Polym. Sci.*, **8**, 2637 (1970).
(2) H. L. Krauss and H. Stack, *Z. Anorg. Chem.*, **366**, 34 (1969).
(3) The temperature of the sample in the low-temperature cell is not precisely known as the light beam causes some heating of the sample. We think that the actual temperature of the sample is higher than 77°K by some 20°.
(4) A. Zecchina, G. Ghiotti, L. Cerruti, and C. Morterra, *J. Chim. Phys.*, **68**, 1479 (1971).
(5) A. Zecchina, S. Coluccia, E. Guglielminotti, and G. Ghiotti, *J. Phys. Chem.*, **75**, 2774 (1971).
(6) E. Borello, *Discuss. Faraday Soc.*, **52**, 170 (1971).
(7) E. Borello, A. Zecchina, C. Morterra, and G. Ghiotti, *J. Phys. Chem.*, **73**, 1286 (1969).
(8) L. L. van Reijen, W. M. H. Sachtler, P. Cossee, and D. M. Brouwer, *Proc. Int. Congr. Catal., 3rd*, 829 (1964).
(9) A. Clark, J. N. Finch, and B. H. Ashe, *Proc. Int. Congr. Catal., 3rd*, 1010 (1964).
(10) D. D. Eley, C. H. Rochester, and M. S. Scurrell, *J. Catal.*, 29, 20 (1973).
(11) H. H. Krauss, *Proc. Int. Congr. Catal., 5th*, **1**, 207 (1973).
(12) A. Zecchina, S. Coluccia, E. Guglielminotti, and G. Ghiotti, *J. Phys. Chem.*, **75**, 2790 (1971).
(13) J. B. Peri, *J. Phys. Chem.*, **70**, 3168 (1966).
(14) N. D. Parkyns, *J. Phys. Chem.*, **75**, 526 (1971).
(15) J. Vlckova and J. Barton, *J. Chem. Soc., Chem. Commun.*, 306 (1973).
(16) P. Pichat, M. V. Mathieu, and B. Imelik, *Bull. Soc. Chim. Fr.*, 2611 (1969).
(17) D. G. Holah and J. P. Fackler, Jr., *Inorg. Chem.*, **4**, 1112 (1965).

On the Chemistry of Silica Supported Chromium Ions. III Two-Ligand Complexes. Nitric Oxide Adsorption

A. Zecchina,* E. Garrone, C. Morterra, and S. Coluccia

Istituto di Chimica Fisica dell'Universita di Torino, Corso M. D'Azeglio, 48-10125 Torino, Italy *(Received September 11, 1974)*

Publication costs assisted by Italian CNR

Three kinds of surface complexes are formed upon NO contact: $Cr^{II}(NO)_2$, absorbing at 1747 and 1865 cm^{-1}; $Cr^{III}(NO)_2$ absorbing at about 1755 and 1880 cm^{-1}; Cr(NO), with a single band at about 1810 cm^{-1}. The concentration of these surface species varies with the Cr content and with the nature of thermal pretreatments. This behavior is discussed and compared with the results obtained on CO adsorption, that we reported in the preceding paper. It is inferred that the Cr ions yielding the 1810-cm^{-1} band are not revealed by CO, which, on the contrary, discriminates between two kinds of Cr^{II} ions, that the strong NO interaction cannot differentiate. The peculiar behavior of NO to bind by pairs is discussed on the ground of cooperative effects between the two unpaired electrons.

Introduction

Nitric oxide is long since known as an interesting ligand molecule and a number of transition metal nitrosyls have been therefore prepared and studied. Some reviews on the subject have been published.[1-4] Many attempts have been made to classify nitrosyl complexes assigning a charge to the NO group and correlating the involved physical properties with such a charge.

NO is a stable free radical which can undergo both oxidation and reduction. NO^+ (nitrosonium ion) is a known entity and some nitrosonium salts are known. As the electron affinity of NO is very small,[5] the reduction process does not produce NO^-, that only very recently has been evidenced by matrix isolation,[6] but rather the dimeric species $N_2O_2^{2-}$ is formed. Despite NO^- instability as a free molecule in respect to NO^+, both can be usefully postulated as ligands.

NO charge evaluation in complexes of transition metal ions was done in the past on the basis of the involved NO stretching frequencies. Nowadays reference is made to the Me–N–O bond angle, which is observed to range between 120 and 180°.

Nearly linear complexes are supposed to contain the group NO^+, isoelectronic with CO, while bent complexes are considered to contain NO^-, as the nitrogen atoms are sp- or sp^2-hybridized, respectively. Little deviations from these figures may also be explained.[7]

However, it must be recalled here that these are merely formal charges that only represent, on the basis of the generally adopted scheme, the first coordinative step. The actual charge localized on the NO ligand is generally unknown and can vary appreciably following the extent of the back donation.[1-4]

On the contrary NO has been paid less attention as a probe molecule for adsorption studies than this molecule actually deserves. It has been mainly studied as an air pollutant, due to its presence in engine exhaust gases. Accordingly, interest has been mainly focused on reactions leading to either nitrogen or nitrous oxide.

The literature up to 1970 has been reviewed by Shelef and Kummer.[8] The ir results by Terenin et al.[9-11] are summarized in ref 8 with the related classification into seven kinds of bonding, which nowadays has to be regarded as questionable. A number of papers[12-19] has been recently devoted to the ESR study of NO adsorption, owing to its radical-like nature. Among them, the paper by Nacchache and Ben Taarit[20] also includes some ir measurements of Cr exchanged zeolites which may be usefully compared with the results described in the present paper.

Eley and coworkers recently studied the interaction of NO with catalysts similar to those employed in the present study. Their results are described in a paper[21] which is the fourth of a series they devoted to the reactivity of supported CrO_3.

Very recently Peri[22] published an infrared study of NO adsorption on chromia–alumina characterized by high Cr^{II} content. All these results may be usefully compared with ours, although the overall interpretation of the involved phenomena is often quite different.

We studied the interaction of NO with a number of samples differing by the preliminary treatments and/or the Cr content. For the sake of clarity, the description of experimental results and the discussion of them are divided into paragraphs. In the last paragraph some observations on the structure of nitrosyl complexes are discussed.

Experimental Section

The materials, infrared equipment, reflectance spectrometer, microbalance, and volumetric adsorption system were described in part I.

Results and Discussion

Two-ligand Cr^{II} Complexes. The 1747–1865-cm^{-1} Pair. Figure 1 shows the ir spectrum in the 1950–1650-cm^{-1} range, due to the adsorption of small doses of NO on a 0.5% sample pretreated following the standard procedure described in part I. As it was shown in part I, in this way a very high Cr^{II} content is achieved, together with the maximum specific activity toward CO. We noted that this procedure also assures the maximum specific activity toward NO. No signals related to adsorbed NO appear in any other frequency range.

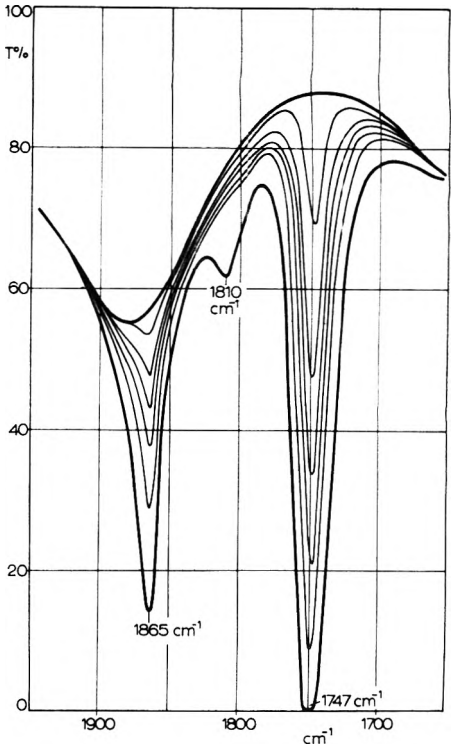

Figure 1. Ir spectra of the adsorption of small doses of NO on a standard reduced 0.5% sample (transmittance vs. wavelength in cm^{-1}). The final pressure is 0.07 Torr, i.e., the vapor pressure at 77°K.

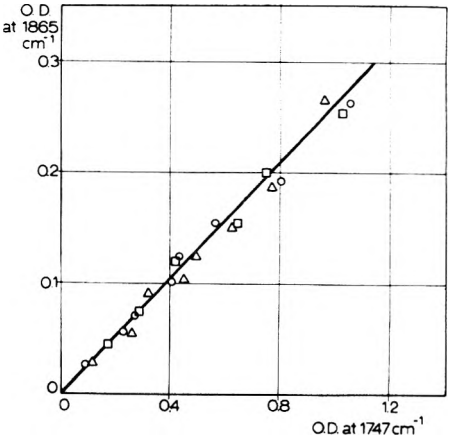

Figure 2. Correlation diagram between the OD at 1865 and 1747 cm^{-1}. Different symbols refer to different experiments all carried out on diluted samples. A least-squares straight line is given.

The most relevant feature of Figure 1 is the appearance of two peaks at 1747 and 1865 cm^{-1}, which are not affected by room temperature pumping. Minor features are both a very weak band at 1810 cm^{-1}, whose frequency and intensity are partially pressure dependent (the most intense spectrum corresponds to 7×10^{-2} Torr of NO) and a shoulder at about 1880 cm^{-1}. This shoulder only appears in Figure 1 as an asymmetry of the intense 1865-cm^{-1} band, but the existence of a peak at 1880 cm^{-1} will be clearly evidenced on differently activated or more concentrated samples.

The correlation diagram between the OD at the two quoted frequencies, shown in Figure 2, clearly indicates that the intensities of the two bands are strictly proportional. This fact strongly suggests that these two bands are

due to two normal modes of the same surface structure. Quantitative data show that, under the adopted experimental conditions, the ratio between adsorbed NO molecules and Cr ions is near to two. Thus, it sounds reasonable to explain the 1747–1865-cm^{-1} pair in terms of structures such as $Cr^{II}(NO)_2$. Cr^{II} ions are assumed to be involved because they largely predominate on the surface of diluted reduced samples, as already pointed out.

Some simple considerations justify the presence of two bands. Assuming that the NO ligands are equivalent, so that the local symmetry group is at least C_{2v}, two normal modes can be foreseen, belonging to the A_1 and B_1 class, respectively, corresponding to the in phase and out of phase stretching motions. The two modes are expected to be well resolved if a strong coupling between the single NO vibrators occurs, i.e., if the metal–ligand bond is sufficiently strong.

The formation of a strong bond between NO and adsorbing centers is consistent with the irreversible nature of the NO species at room temperature, as a heating at 300° in vacuo is required to remove the 1747–1865-cm^{-1} bands. Such thermal treatment brings about the decomposition of the $Cr^{II}(NO)_2$ complexes with subsequent oxidation of the catalyst. The effect of outgassing at lower temperatures is considered later.

The proposed assignment is supported by the comparison with homogeneous NO complexes. Pairs of nitrosyls in cis position always show a couple of bands in the 1650–1950-cm^{-1} region, that are several tens of wave numbers apart and in which the class B_1 mode exhibits lower frequencies and higher intensities, in agreement with the results of Figures 1 and 2.[2,23] Comparison with coordination chemistry data suggests that nearly linear Cr–N–O structures are built on the surface, as the so-called NO^- complexes absorb at definitely lower frequencies.

On the contrary, no straightfoward information can be drawn from inorganic chemistry data about the coordination state of the Cr ions after NO adsorption, as both tetrahedral and octahedral complexes carrying a couple of nitrosyls in cis absorb in the same region.

In order to achieve some information on the coordinative situation of Cr ions after NO adsorption, the interaction of surface nistrosyl complexes with other ligands has been checked. The results are reported in detail in the following paper; evidence is given there that at least a part of Cr ions may coordinate a further ligand, thus showing that the coordination state after NO adsorption is not the highest one.

Let us note that the total absence of any signal related to NO adsorption in the 1250–1350-cm^{-1} frequency range (although in this region measurements are rather difficult due to silica poor transparency) seems to rule out the presence of any anionic species, such as NO_2^-, which, for instance, form on α-chromia.[24]

For the same reason, we also exclude the presence of a hyponitrite species $N_2O_2^{2-}$ both in the mononuclear form (a)[25] and in the binuclear form (b), which could in fact form because of the presence of Cr ions pairs.

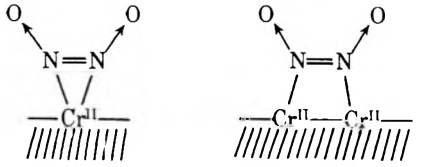

a b

Some other possible structures involving Cr pairs may be also disregarded. For example, an average composition $Cr(NO)_2$ is also exhibited by structure c which could, in

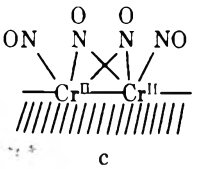

c

principle, form on the surface. In this case, besides other considerations, it is sufficient to recall that bridged nitrosyls absorb at definitely lower frequencies.[26] It is inferred that, although Cr ions mainly exhibit a pairwise distribution (see part I), each Cr site may be regarded as independent as far as the interaction with NO is concerned. In conclusion the 1747–1865-cm^{-1} bands are assigned to class A_1 and B_1 NO stretching modes of mononuclear surface complexes, as represented by structure d, where the Cr ion is in

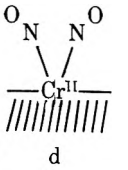

d

the divalent state and in a coordinating situation less than octahedral.

In Figure 3 the spectra of NO adsorbed on a 0.5% reduced sample (full line) and of NO on the same sample pretreated in O_2 at room temperature (dashed line) are compared. It can be seen that oxygen preadsorption completely prevents the formation of two-nitrosyls complexes. This fact well agrees with the proposed assignment, as at least twofold coordinated unsaturated ions are likely to dissociate an oxygen molecule even at room temperature to form surface chromates and dichromates.

One-Ligand Cr Complexes. The 1810-cm^{-1} Band. Let us discuss next the central band of Figure 1, which we refer to as the 1810-cm^{-1} band, although some shifts depending on the coverage are observed. From Figure 1 it can be seen that this absorption has a quite weak intensity when diluted and carefully pretreated samples are considered.

Figure 3 shows that this band is not hindered by O_2 preadsorption at room temperature, meaning that the involved Cr ions do not react with molecular oxygen at room temperature. From Figure 3 it is also inferred that this band must be assigned to surface one-nitrosyl complexes, as it is not associated with any other absorption. This fact likely indicates the presence of a single coordination vacancy in the coordination sphere of the involved Cr ions, in total agreement with their poor reactivity toward room temperature oxidation.

A final further support to this picture comes from the effect of high temperature thermal treatments on the spectrum of adsorbed NO.

In Figure 4 the spectra are compared due to the adsorption of NO (7×10^{-2} Torr) on a standard reduced sample (solid line) and on the same sample which had first undergone a standard reduction followed by a 1 hr heating at 750° in vacuo (dashed line). The thermal treatment causes a striking increase of the 1810-cm^{-1} band, accompanied by a small shift toward higher frequencies. Also a large decrease of the 1747–1865-cm^{-1} pair is observed.

It was shown in the preceding papers that such high tem-

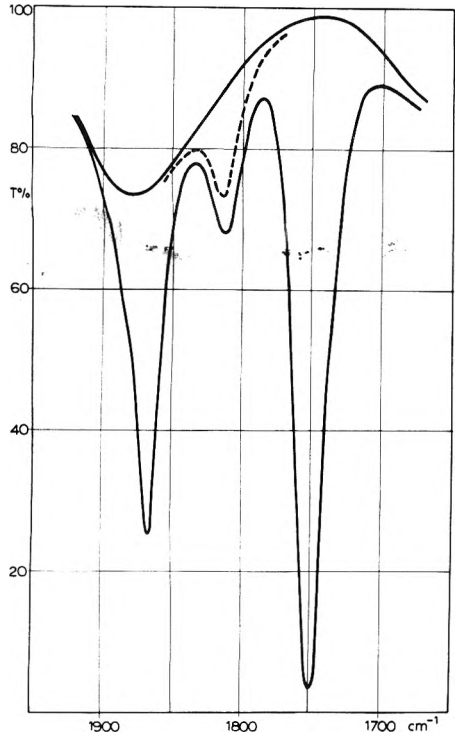

Figure 3. The effect of oxygen preadsorption at room temperature on the ir spectrum of adsorbed NO (transmittance vs. wavelength in cm^{-1}): solid line, adsorption of NO (pressure 0.07 Torr) on a 0.5% reduced sample; broken line, adsorption of NO (pressure as above) on a sample contacted at room temperature with 40 Torr of O_2.

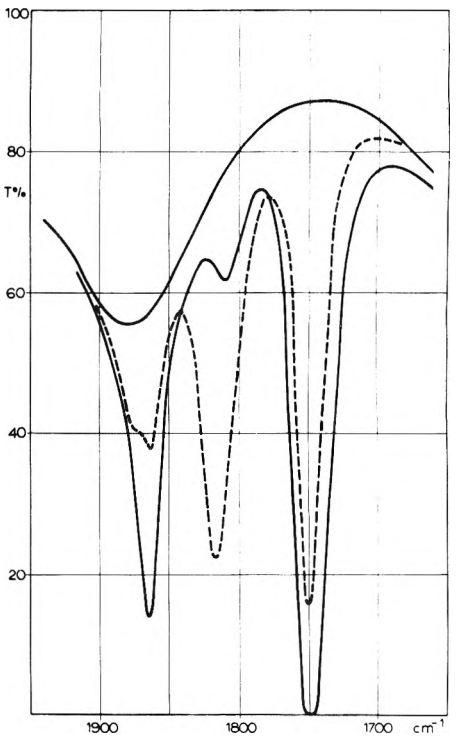

Figure 4. The effect of a pretreatment at high temperature on the spectrum of adsorbed NO (transmittance vs. wavelength in cm^{-1}): solid line, adsorption of NO (0.07 Torr) on a 0.5% standard reduced sample; broken line, the same, after 1 hr heating at 750° in vacuo.

perature treatments convert some coordinatively unsaturated surface ions into better "shielded" species which, for example, cannot interact with CO at room temperature.

The NO interaction gives better insight into the rearrangement process, as it clearly indicates that "shielded" ions still conserve a coordinative vacancy which is not revealed by CO at room temperature. This conclusion is in agreement with the results of part II, according to which no relevant changes are induced by the high temperature treatments on the amount of irreversibly chemisorbed pyridine.

Let us now discuss the oxidation state of these "shielded" ions. As thermal treatment does not affect the average oxidation number of the sample, we conclude that one-nitrosyl complexes mainly involve divalent Cr ions. Some contribution from Cr^{III} is not excluded, since the intensity of the 1810-cm^{-1} band is also enhanced by an increase in Cr loading (see, for example, Figure 6) which is known to favor the Cr^{III} content.

Two-Ligand Cr^{III} Complexes. The 1755–1880-cm^{-1} Pairs. In the preceding papers, it was pointed out that small amounts of Cr^{III} occur on the surface of diluted and carefully pretreated samples. Also, it was shown, by means of the spectra of adsorbed CO, that the involved surface structures are rather stable, as they are not affected by high temperature treatments. In this way, the NO complexes due to Cr^{III} may be singled out in the spectrum of Figure 4. The 1880-cm^{-1} shoulder is not weakened by thermal treatments, being on the contrary exposed by the decreased intensity of the 1865-cm^{-1} band. Meanwhile, the 1747 cm^{-1} band is shifted upward by some wave numbers thus revealing itself as complex in nature. From these facts, we infer that two pairs of bands are present in the spectrum of Figure 1, the former a couple at 1747–1865 cm^{-1} (Cr^{II}) already discussed and the latter at about 1755–1880 cm^{-1}, which we ascribe to Cr^{III}. In both cases, the bands are due to the in-phase and out-of-phase vibrations of surface complexes involving two NO molecules. The qualitative comparison of the intensities is consistent with the Cr^{II} and Cr^{III} populations on well-reduced diluted samples. Also, let us note that the higher stretching frequencies of the $Cr^{III}(NO)_2$ complex agree with the higher formal charge of the central ion, as in this case the back bonding contribution to NO bonds is obviously lowered. Additional evidence results from the spectra of NO adsorbed on samples at higher Cr loadings.

Figure 5 describes the adsorption of NO (0.07 Torr) on a 2% sample after a first reduction run (curve a) and after successive oxidation–reduction cycles (curves b and c). This experiment is very similar to that described in the preceding paper (Figure 6), showing the effects of successive oxidation–reduction cycles on the CO spectrum of a heavily loaded sample. Similar conclusions can be drawn here.

Evidence in favor of the proposed assignment results from the relevant intensity of the 1755–1880-cm^{-1} pair in this case, as well as from the decrease of the 1755–1880-cm^{-1} pair in favor of the 1747–1865-cm^{-1} pair. We recall that a similar behavior of the spectrum of adsorbed CO was discussed in part II. From these considerations, it is inferred that the 1775–1880-cm^{-1} pair involves the same Cr^{III} ions that originate the 2191-cm^{-1} CO band. On the contrary, two different $Cr^{II}(CO)$ species (band at 2181, 2186 cm^{-1}) correspond to the same $Cr^{II}(NO)_2$ complex, i.e., to the 1747–1865-cm^{-1} pair.

Some differences in the ir properties of the Cr^{II} and Cr^{III} complexes can be briefly pointed out. The frequency shift,

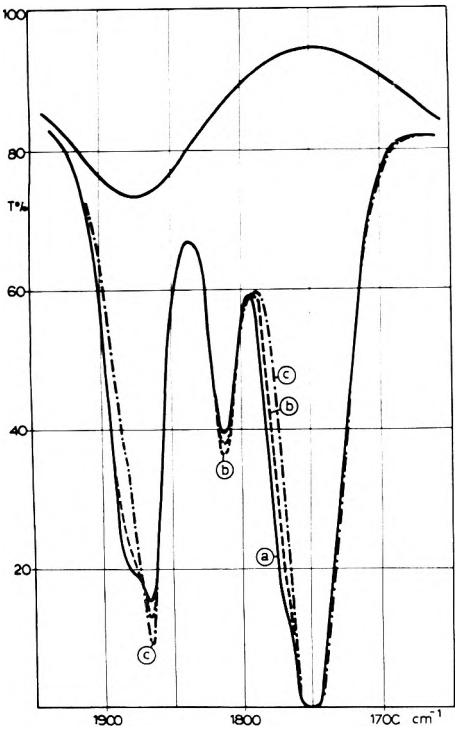

Figure 5. The effect of successive reduction–oxidation cycles on the ir spectrum of adsorbed NO on a 2% sample (transmittance vs. wavelength in cm^{-1}): curve a, NO adsorption (0.07 Torr) after the first reduction run; curves b and c, the same after successive reduction–oxidation cycles.

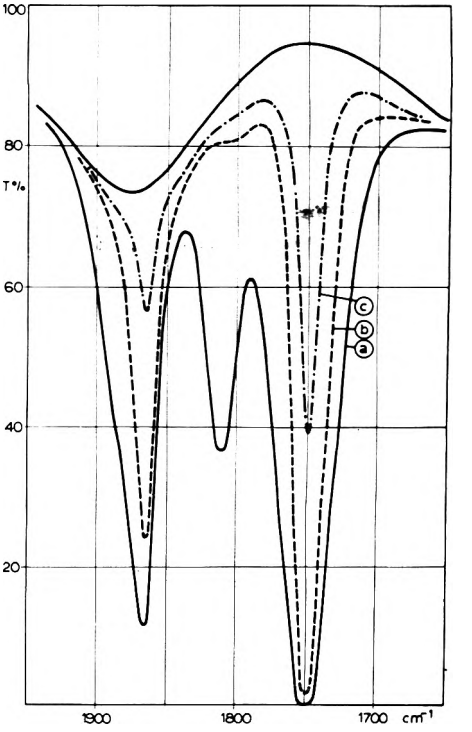

Figure 6. The effect of outgassing on the ir spectrum of NO adsorbed on a 2% sample (transmittance vs. wavelength in cm^{-1}): curve a, the same as curve c of Figure 5; curve b, after 10 min outgassing at 100°; curve c, after 10 min outgassing at 200°.

passing from Cr^{II} to Cr^{III}, is not very large, although in the expected direction. More relevant changes are observed in both the I_A/I_S intensity ratio (a) and the resistance to outgassing (b).

(a) The two pairs of bands heavily overlap, thus preventing exact considerations of the intensities. Nevertheless, on the basis of the NO spectra on highly loaded samples not reported here, it can be stated that the $Cr^{III}(NO)_2$ has ν_A and ν_S modes of similar intensity, while the $Cr^{II}(NO)_2$ was shown (Figure 2) to have a ν_S mode much stronger than ν_A. This fact is discussed in detail in the following paper.

(b) Figure 6 shows the effect of the outgassing at increasing temperatures on the spectrum of NO adsorbed on a 2% sample. The band at 1810 cm^{-1} disappears first, in agreement with its partial reversibility even at room temperature. The high-frequency pair is observed to be markedly more labile than the low frequency. This is a noteworthy result, as during the adsorption process the two pairs of bands grow together. This fact can only be explained by assuming the desorption path to be different from the adsorption one. Evidence of a desorption mechanism involving the decomposition of surface NO complexes, with partial sample oxidation, has been obtained by studying the subsequent CO adsorption, however, it is not reported here for brevity.

Some Considerations about the Structure of the Complexes. An interesting feature is evidenced by the whole of the experimental results: NO molecules markedly prefer to adsorb by couples.

The coordination of a single molecule (1810 cm^{-1}) appears to be only possible when a single coordination vacancy is present and leads to a labile, pressure-dependent complex.

As the NO stretching frequency is just below that of the gas, it is inferred that nearly linear NO^+ complexes are formed. The metal–nitrosyl link can be considered in terms of a donation from the lone pair of the NO^+ ligands together with a synergic back donation from occupied metal d orbitals to the unoccupied π^* orbitals of NO^+.

When two coordinating unsaturations are available, contemporary coordination of two molecules occurs; in no case was it possible to observe one-ligand intermediates, either in adsorption or in desorption runs.

We think that the striking stability of the two-nitrosyls complexes is due to the cooperative effect between the two unpaired electrons.

Let us compare the stability of these structures with the instability of structures such as e which differs from struc-

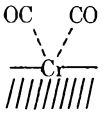

e

ture d by two electrons and is not formed upon CO adsorption, at least at room temperature (see part II of this series). The cooperation between the two unpaired electrons is likely given by the formation of a molecular orbital delocalized over the whole complex, so that its actual structure would be better described by f. Evidence for such a struc-

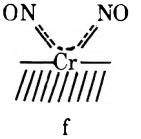

f

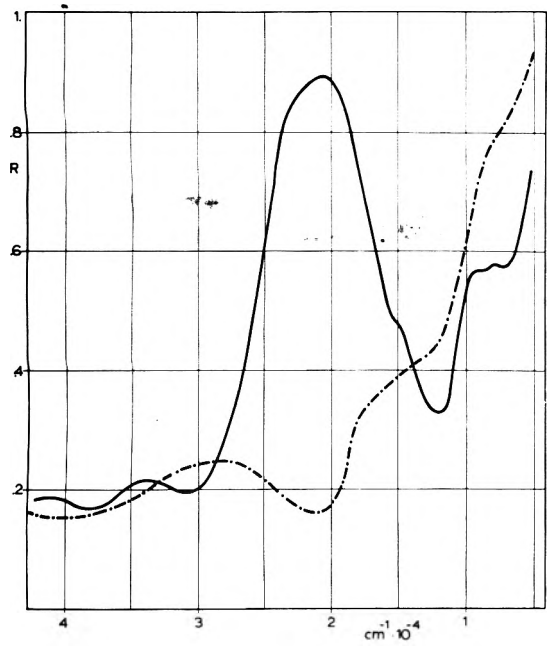

Figure 7. Uv-visible reflectance spectrum of a 0.5% sample (reflectance vs. wavelength in cm^{-1}): solid line, reduced sample before adsorption; broken line, after adsorption of NO (0.07 Torr).

ture comes from the reflectance spectrum of the NO treated samples.

Figure 7 shows the reflectance spectra of a 0.5% standard reduced sample before (curve a) and after (curve b) interaction with NO. Curve a has been already described and discussed in part I. The main features of curve b are the two bands at 40,000 and 21,000 cm^{-1} and the two shoulders at about 13,000 and 7000 cm^{-1}.

The first band may be assigned with confidence to an electron-transfer band because of its position. Both the 13,000 and 7000-cm^{-1} shoulders are assigned to ligand field transitions both because of their position and intensities. The most interesting feature of Figure 7 is the band at 21,000 cm^{-1} that is responsible for the yellow color of the sample after NO adsorption. Its position recalls a d–d transition but the intensity is typical of an electron transfer. Such bands are usually accounted for in the literature by an electronic transition in which an appreciable mixing of metal and ligand orbitals occurs as in transition metal complexes where strong π-acceptor ligands are involved.[27]

This result matches very well with the description in terms of $Cr(NO)_2$ complexes, as obtained from the infrared and gravimetric data.

Conclusions

NO interacts with a CrO_3–SiO_2 reduced system giving interesting information concerning both the surface heterogeneity and the reactivity of silica supported Cr ions. A useful comparison may be done between the information resulting from the adsorption of NO and that of CO, previously discussed.

The results can be summarized as follows. (a) A fraction of Cr ions that are partially shielded saturates its own coordinative sphere by adsorption of one NO molecule, giving rise to the band at 1810 cm^{-1}. The population of this kind of ion is very small on standard reduced samples and is favored by high temperature pretreatments and by high Cr concentrations. These ions are mainly in the divalent state and are not revealed by CO adsorption at room temperature. (b) Most of the Cr^{II} ions coordinate a couple of NO molecules, to form very stable $Cr(NO)_2$ surface complexes, with bands at 1747 and 1865 cm^{-1}. These ions are unstable at high temperatures because of their low coordination state and transform themselves into the partially shielded species mentioned above. With CO they originate two different 1:1 complexes, absorbing at 2181 and 2186 cm^{-1}, respectively. CO adsorption is able to discriminate between two types of exposed Cr^{II} ions, which the strong NO interaction cannot bring into evidence. (c) The small fraction of Cr^{III} ions coordinates two NO molecules to yield $Cr^{III}(NO)_2$ complexes absorbing at 1755–1880 cm^{-1}. These ions are very stable toward thermal treatments and are favored by high Cr loadings. With CO they produce a 1:1 complex absorbing at 2191 cm^{-1}. (d) If a sufficient number of coordinating unsaturations is present on the Cr ions, NO is adsorbed by couples, because a large cooperative action between the two unpaired electrons leads to a strong stabilization of the complex. (e) The Cr–NO structures are probably nearly linear, i.e., what is normally termed NO^+ complexes are formed.

Acknowledgment. Support for the research has been partially provided by the Consiglio Nazionale delle Ricerche.

References and Notes

(1) B. F. G. Johnson and J. A. Mc Cleverty, *Prog. Inorg. Chem.*, **7**, 277 (1966).
(2) N. G. Connelly, *Inorg. Chim. Acta Rev.*, **6**, 47 (1972).
(3) J. A. Mc Ginnety, *MTP Int. Rev. Sci.*, **5**, 229 (1972).
(4) J. Masek, *Inorg. Chim. Acta Rev.*, **3**, 99 (1969).
(5) D. Spence and G. J. Schultz, *Phys. Rev. A*, **3**, 1968 (1971).
(6) D. E. Milligan and M. E. Jacox, *J. Chem. Phys.*, **55**, 3404 (1971).
(7) J. H. Enemark, *Inorg. Chem.*, **10**, 1952 (1971).
(8) M. Shelef and J. T. Kummer, *Chem. Eng. R. Symp. Ser.*, **67**, 74 (1971).
(9) A. N. Terenin and L. N. Roev, *Actes Congr. Int. Catal., 2nd, 1960*, **2**, 2188 (1961), and references therein.
(10) L. N. Roev and A. N. Terenin, *Opt. Spektrosk.*, **7**, 756 (1959).
(11) L. N. Roev and A. V. Alekseev in "Elementary Photoprocess in Molecules", B. S. Neporent, Ed., English translation, Consultant Bureau, New York, N.Y., 1968, p 260.
(12) J. H. Lunsford, *J. Phys. Chem.*, **72**, 4163 (1968).
(13) B. M. Hoffman and N. J. Nelson, *J. Chem. Phys.*, **50**, 2518 (1969).
(14) C. L. Gardner and M. A. Weinberger, *Can. J. Chem.*, **48**, 1318 (1970).
(15) P. H. Kasai and R. J. Bishop, Jr., *J. Am. Chem. Soc.*, **94**, 5560 (1972).
(16) C. Naccache, M. Che, and Y. Ben Taarit, *Chem. Phys. Lett.*, **13**, 109 (1972).
(17) C. C. Chao and J. H. Lunsford, *J. Phys. Chem.*, **76**, 1546 (1972).
(18) P. Gallezot, Y. Ben Taarit, and B. Imelik, *J. Catal.*, **26**, 481 (1972).
(19) Y. Ben Taarit, C. Naccache, and B. Imelik, *J. Chim. Phys.*, **70**, 728 (1973).
(20) C. Naccache and Y. Ben Taarit, *J. Chem. Soc., Faraday Trans. 1*, **69**, 1475 (1973).
(21) D. D. Eley, C. H. Rochester, and M. S. Scurrell, *J. Chem. Soc., Faraday Trans. 1.*, **69**, 660 (1973).
(22) J. B. Peri, *J. Phys. Chem.*, **78**, 588 (1974).
(23) G. R. Van Hecke and W. De W. Horrocks, Jr., *Inorg. Chem.*, **5**, 1960 (1966).
(24) L. Cerruti and E. Guglielminotti, *Discuss. Faraday Soc.*, **52**, 285 (1971).
(25) S. Cenini, R. Ugo, G. La Monica, and S. D. Robinson, *Inorg. Chim. Acta*, **6**, 132 (1972).
(26) M. Poliakoff and J. J. Turner, *Chem. Commun.*, 1008 (1970).
(27) B. N. Figgis, "Introduction to Ligand Field", Interscience, New York, N.Y., 1966.

On the Chemistry of Silica Supported Chromium Ions. IV. Three-Ligand Complexes. Interaction of Pyridine, Ammonia, Carbon Monoxide and Water with Preadsorbed Nitric Oxide

E. Garrone, G. Ghiotti, S. Coluccia, and A. Zecchina*

Istituto di Chimica Fisica dell'Università di Torino, Corso M. D'Azeglio, 48-10125 Torino, Italy (Received September 11, 1974)

Publication costs assisted by Italian CNR

The interaction of the NO-treated samples with other molecules allows some information to be achieved about the coordination state of Cr ions after NO adsorption. While $Cr^{II}(NO)$ and $Cr^{III}(NO)_2$ only undergo ligand displacement reactions, the $Cr^{II}(NO)_2$ species coordinate a further ligand, forming $Cr^{II}(NO)_2L$ complexes. Relevant ir features are summarized and discussed. The results can be interpreted in terms of the chemistry of inorganic complexes. In the conclusion, the properties of each Cr ion are summarized.

Introduction

In the preceeding paper, the interaction of NO with the reduced surface of CrO_3–SiO_2 samples was described. Two ligand complexes were shown to be mainly formed and some of their features have been distinguished. As already stated, no straightforward information about the coordination state of the central ion in these complexes is yet available. In order to single out any residual coordinative unsaturation of the central ions, the interaction with some other ligands has been tested. In this paper only standard reduced dilute samples are considered, i.e., the reactivity of $Cr^{II}(NO)_2$ complexes is mostly investigated. The extension of this study to heavily loaded samples requires further work, as more involved processes take place.

Experimental Section

The materials and ir equipment are as described in part I.

Results

The properties of the NO treated surfaces have been studied by following the changes in the ir spectra caused by contact with a number of molecules. Some molecules do not affect the ir spectrum at all, at least at room temperature. Among them are C_2H_4, CO_2, N_2, and N_2O. On the contrary, the 1747–1865-cm^{-1} pair is deeply affected on contacting the sample with strong bases such as Py, NH_3, and H_2O.

In Figure 1 the NO–Py interaction is described. The solid bold line refers to the adsorption of NO (0.07 Torr) on a 0.5% sample and coincides with the standard ir spectrum discussed in the previous paper. The broken bold line refers to the saturation of the NO treated sample with Py (about 0.5 Torr). A spectrum recorded at intermediate Py coverage is also reported. NO partial pressure was kept constant at 0.07 Torr.

The major features of Figure 1 are: the gradual decrease of the 1747–1865-cm^{-1} pair; the corresponding increase of a new couple of bands at 1702 and 1850 cm^{-1}; the presence of a growing band at 1612 cm^{-1} due to the adsorbed Py.

Minor features which may be considered are the following: the disappearance of the 1810-cm^{-1} band; the appearance of a shoulder at about 1725 cm^{-1}; the presence of a small fraction of the 1747–1865-cm^{-1} pair which is not destroyed by Py. This fraction ranges in an unpredictable way between zero and few percent on going from one sample to another.

In order to assign the new absorptions at 1702–1850 cm^{-1} it is important to note that the increased absorbance of the new pair is well related with the decreased absorbance of the 1747–1865-cm^{-1} pair. Figure 2 (left-hand side) shows that a linear proportionality exists between the OD at 1702 cm^{-1} and the OD decreases at 1742 cm^{-1}.

The absorbances at 1702 and 1850 cm^{-1} are correlated as well (Figure 2, right-hand side). It results that

$$(OD)_{1702\ cm^{-1}}/\Delta(OD)_{1747\ cm^{-1}} = -0.58$$

$$(OD)_{1702\ cm^{-1}}/(OD)_{1850\ cm^{-1}} = 1.83$$

The NO–NH_3 interaction is shown in Figure 3. The solid line refers to the usual NO spectrum on a 0.25% sample, while the broken curve is the spectrum recorded after surface saturation with NH_3. The formation of a new pair of bands at 1706 and 1856 cm^{-1} is observed, accompanied by the disappearance of the original 1747–1865-cm^{-1} pair.

Let us point out, still as minor features, the disappearance of the 1810-cm^{-1} band and the formation of a shoulder at about 1725 cm^{-1}. The small band at 1627 cm^{-1} is due to the ν_4 mode of adsorbed NH_3. Intermediate curves are not shown here for the sake of clarity.

The correlation diagram between the absorbances at 1706 and 1856 cm^{-1} and the one between the increase of the new pair and the decrease of the old one show that

$$(OD)_{1706\ cm^{-1}}/\Delta(OD)_{1747\ cm^{-1}} = -0.96$$

$$(OD)_{1706\ cm^{-1}}/(OD)_{1856\ cm^{-1}} = 1.92$$

The H_2O–NO interaction gives similar results; in the spectrum of adsorbed NO, which is not reported here, two new bands are formed at 1737 and 1878 cm^{-1} at the expense of the original pair.

The proportionality constants are

$$(OD)_{1737\ cm^{-1}}/\Delta(OD)_{1747\ cm^{-1}} = -0.74$$

$$(OD)_{1737\ cm^{-1}}/(OD)_{1878\ cm^{-1}} = 2.8$$

The spectrum of adsorbed NO is found to be perturbed also by CO. As the interaction is very weak, 100 Torr of CO

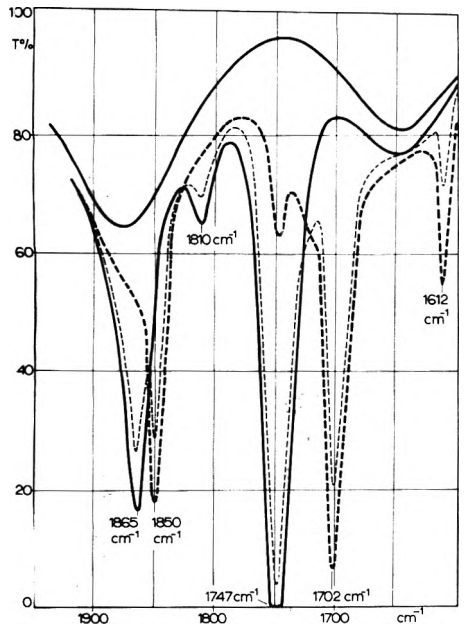

Figure 1. Ir spectra of a 0.5% NO-treated sample before and after Py adsorption (transmission vs. wavelength in cm^{-1}): upper solid curve, background; solid curve, adsorption of 7×10^{-2} Torr of NO; broken bold curve, surface saturation with Py; thin broken curve, intermediate Py coverage.

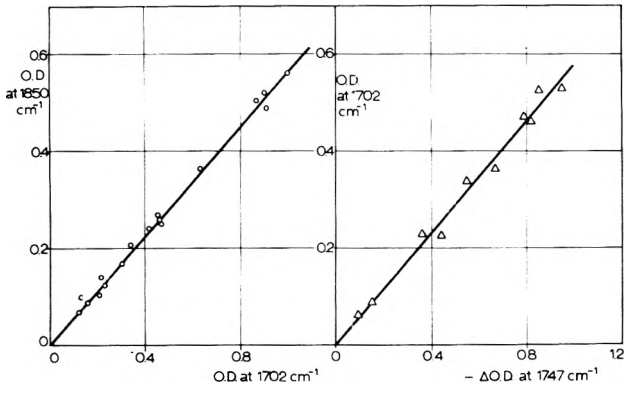

Figure 2. Left-hand side: correlation diagram between the OD of the newly formed bands in Figure 1. Right-hand side: correlation diagram between the OD of a new band and the decrease in OD of an old one.

is required to obtain relevant changes. In Figure 4, the solid line is the usual NO spectrum of a 0.5% sample while the other curves refer to increasing CO pressures.

Two new absorptions occur at 1760 and 1886 cm^{-1}, while the original pair decreases. As in the previous cases, a linear proportionality is found between the absorbance increases at 1886 and 1760 cm^{-1}, as well as between the increase of the new bands and the decrease of the old ones. The results are

$$(OD)_{1760\ cm^{-1}}/\Delta(OD)_{1747\ cm^{-1}} = -0.47$$

$$(OD)_{1760\ cm^{-1}}/(OD)_{1886\ cm^{-1}} = 0.83$$

It must be pointed out that the original pair's bands are not destroyed even at a CO pressure of 400 Torr.

The spectra corresponding to the end of the experiments reported in Figures 1 and 3 can be also obtained in a reversed order, i.e., first saturating the catalyst with either Py and NH_3 and then allowing NO to adsorb onto it. In the

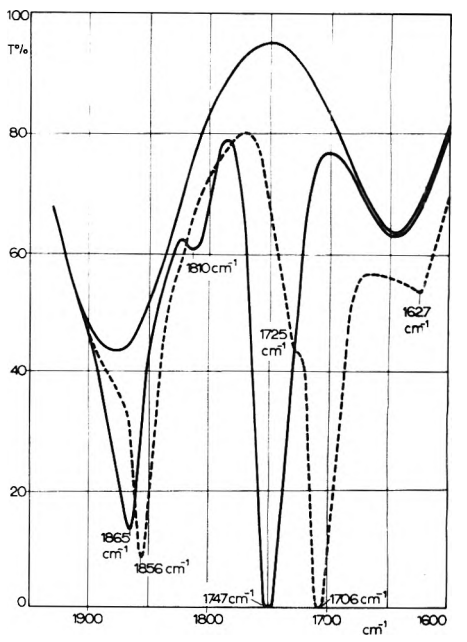

Figure 3. Ir spectra of a 0.25% NO-treated sample before (lower solid curve) and after (broken curve) NH_3 saturation (transmittance vs. wavelength in cm^{-1}).

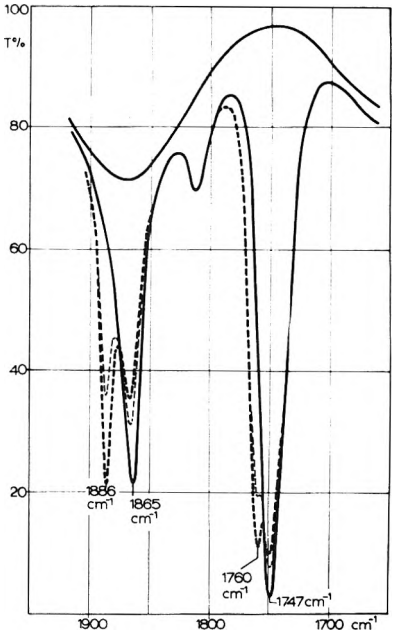

Figure 4. Ir spectra of a 0.5% NO-treated sample before and after contact with CO (transmission vs. wavelength): upper solid curve, background; solid curve, adsorption of 7×10^{-2} Torr of NO; thin broken curve, 40 Torr of CO; bold broken curve, 400 Torr of CO.

case of CO a similar experiment is shown in Figure 5, where the spectra are reported due to the adsorption of small doses of NO in the presence of a CO atmosphere. In fact 7×10^{-2} Torr of NO was allowed to diffuse into the cell containing 365 Torr of CO and the spectra were recorded at increasing NO coverages. It is observed that the bands of both pairs are present and grow proportionally, the ratio between them at a given CO pressure being independent on the NO coverage. In this way the different intensity ratio between the two components of the two pairs is observed.

The interaction of CO with a NO treated sample may

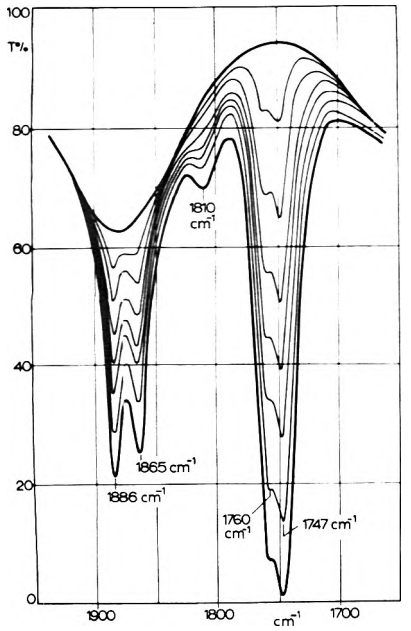

Figure 5. Ir spectra of small doses of NO adsorbed on a 0.5% sample under 365 Torr of CO (transmission vs. wavelength in cm^{-1}).

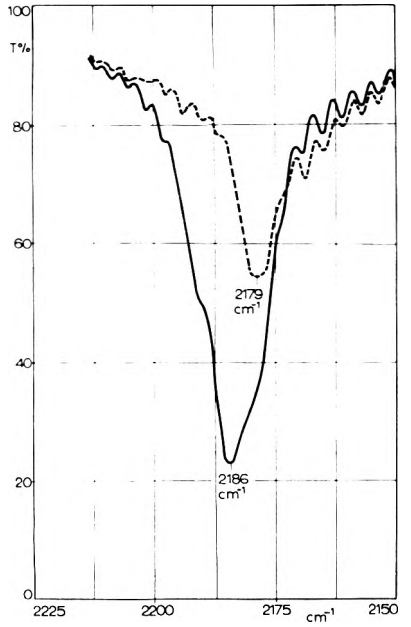

Figure 6. Ir spectra of CO adsorbed on a 0.5% clean (solid curve) and NO-covered (broken curve) sample (transmission vs. wavelength in cm^{-1}): CO pressure, 365 Torr.

also be followed in the CO stretching region. Figure 6 compares the spectrum due to the contact of 365 Torr of CO with a NO treated sample (broken curve) and with the spectrum due to the same pressure of CO over the unreacted catalyst. In the former case a band at 2179 cm^{-1} is observed. Any possible confusion with the triplet components is to be ruled out, both because of the definite frequency difference and of a stronger pressure dependence.

Discussion

In all cases here studied, similar features have been found. Namely, the interaction with an extra ligand brings

TABLE I:

N-O stretching frequency of $Cr^{II}(NO)_2L$ complexes	ν_a cm^{-1}	ν_s cm^{-1}	$\Delta\nu$ cm^{-1}	$\bar{\nu}$ cm^{-1}	I_a/I_s
L = c.v.*	1747	1865	118	1806	3.79
L = Py	1702	1850	148	1776	1.83
$L = NH_3$	1706	1856	150	1781	1.92
L = CO	1760	1886	126	1823	0.83
$L = H_2O$	1737	1878	141	1807	2.8
Cr = Cr	1755	1880	122	1819	~1

1900 1800 1700 cm^{-1}

* c.v. = coordination vacancy

about the decrease of the 1747–1865-cm^{-1} pair, which we assigned to the NO stretching modes of $Cr^{II}(NO)_2$ complexes, while a new pair of bands is formed. A linear proportionality is always found between the absorbances of the two new bands, as well as between the decrease of the old pair and the increase of the new one. From the former observation and in the same manner as it was done in the preceding paper for the 1747–1865-cm^{-1} pair, it is inferred that the new couple of bands has to be assigned to in-phase and out-of-phase stretching modes of $Cr^{II}(NO)_2$ structures. Owing to the latter correlation it is concluded that the new nitrosyl complexes arise from the old ones following the coordination of an extra ligand molecule, according to the reaction scheme a where L is the extra ligand.

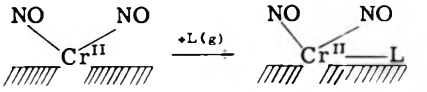

(a)

The spectroscopic features of the three-ligand complexes so formed are summarized in Table I, whose left part is a correlation chart of the NO stretching modes. The bands are represented as thin rectangles of equal width, as the half-band widths are fairly constant. The heights represent, in an arbitrary scale, the related intensities, as computed from the correlation diagrams (see Figure 2).

The data concerning the two-ligand complexes $Cr^{II}(NO)_2$ and $Cr^{III}(NO)_2$ that have been discussed in the preceeding paper are also reported for comparison (see part III of this series). In the latter case, the intensities of the NO modes are not well known, although their ratio has been estimated to be about one.

On the right-hand side of Table I, the frequencies are reported, together with the intensity ratio I_a/I_s between the asymmetric and the symmetric mode. In order to better characterize the frequency changes we have also reported the mean frequency $\bar{\nu} = \frac{1}{2}(\nu_a + \nu_s)$ together with the band splitting $\Delta\nu = \nu_s - \nu_a$.

It is evident that Py and NH_3 have similar effects, as in both cases the extra ligand coordination causes the donation of electron charge to the transition metal ion. The back bonding contribution to NO π^* orbitals is thus increased and the NO bond order decreased with a consequent shift of the NO stretching frequencies to lower values. On the contrary, no relevant changes are induced by this electron rearrangement in the ir spectrum of the ligand. For example, the 8a mode of Py in the $Cr^{II}(NO)_2Py$ complex falls at 1612 cm^{-1} as in the Cr^{II}–Py complex (see

part II). It is noteworthy that the electron rearrangement mentioned above weakens the NO–Cr bond, so that a room temperature outgassing of the sample brings about the desorption of NO. The involved processes are quite complex, so that further work is required on this subject.

The interaction with CO is quite different; in fact both ν_a and ν_s are increased, suggesting that CO behaves in this case as an electron acceptor.

The decrease of the stretching mode of the CO ligand, as reported in Figure 6, confirms that an electron transfer to CO π^* orbitals is taking place, although very limited. No relevant energy gain is likely involved in the CO-complex formation as rather high CO pressures are needed to form it and the original $Cr^{II}(NO)_2$ complexes are completely recovered upon short outgassing at room temperature. The results of Figure 5 lend further support to this assumption, as the parallel growth of both $Cr^{II}(NO)_2$ and $Cr^{II}(NO)_2CO$ can only be explained in terms of noninteracting structures of close energy.

The mechanism thus far adopted to explain the three-ligand complexes' formation is probably oversimplified as far as the electron back donation from the central ion can also occur toward the σ^* orbitals of NO. In this case[1] the Cr–N–O bond angle would decrease and the frequencies would shift in an unpredictable way. This is, perhaps, the case of H_2O containing complexes, in which ν_s and ν_a modes are observed to move in opposite directions.

From the data of Table I, it is observed that relevant variations in the intensities of the NO stretching modes occur upon coordination. A detailed explanation of these effects is impossible, as full knowledge of the complexes' structure would be required. We only note that, upon coordination, the I_a/I_s intensity ratio decreases, as one would expect, since the adsorption of an extra ligand brings about an increase of coordination. For example, we recall that Beck et al.[2] have pointed out that I_a/I_s usually decreases on passing from tetrahedral to octahedral complexes.

While no regular trend is observed for $\bar{\nu}$, Table I clearly shows that $\Delta\nu = \nu_s - \nu_a$ is always increased upon coordination.

On the basis of this increase, the adopted ligands can be classified as follows: $NH_3 \sim Py > H_2O \gg CO$. It is most interesting to note that the order of the ligands is the same as in the "spectrochemical series".[3]

At this point, some comments about the coordinative state of Cr^{II} ions should be made. We assume that the coordination configuration of the three-ligand complexes is the highest one, i.e., octahedral. As the ligand adsorption is usually thought of as the filling of a coordinative unsaturation, the NO–L (L = Py, NH_3, H_2O, CO) interaction seems to show three coordination holes in the Cr coordination sphere, i.e., to suggest that Cr^{II} ions have, before adsorption, only three oxygen ligands. Consequently the involved coordination state of Cr^{II} would be nearly trigonal. The presence of so many coordinative vacancies seems to somehow contradict the results of the preceeding two papers, in which the observed formation of 1:1 and 2:1 complexes seemed to suggest a higher coordinative state of Cr ions before adsorption. This contradiction is probably overcome if the dynamic character of surface complex formation is taken into account. We do not expect Cr ions before adsorption to be merely placed on the top of three surface oxygens, but rather to be partially "sunk" in order to maximize the cfse. Ligand adsorption would therefore "extract" to some extent the ions from the initial position.

As a first step, the coordination of one molecule would be favored as in the case of CO, Py, and CO_2, bringing the ion into a tetrahedral coordination.

NO behaves differently, due to its peculiar cooperative mechanism of bonding. Under even more drastic conditions, a larger "extraction" of the central ion could be achieved, so allowing an octahedral configuration to be attained. Examples are the NO–L complexes studied here; the low-temperature CO complexes hypothesized in part II; and the NH_3 complexes at high pressure, revealed by reflectance spectroscopy in part I.

The reactivity of the Cr(NO) and $Cr^{III}(NO)_2$ complexes will be now briefly outlined.

The former structures have been shown to be related to Cr ions that before NO contact have only one coordination vacancy, so that the adsorption of one NO completes the coordination sphere of the ion. The reactions envisaged for such complexes may only consist of the displacement of the NO ligand as in reaction b. In fact the 1810-cm^{-1} band was

$$Cr\text{–}NO + L(g) \longrightarrow Cr\text{–}L + NO(g) \qquad (b)$$

shown to be destroyed upon NH_3, Py, and H_2O adsorption, while no new bands due to bound NO are formed. CO does not affect the 1810-cm^{-1} band (Figure 4) in agreement with the previous observation that no Cr(CO) complexes are formed by this kind of ion.

As far as the $Cr^{III}(NO)_2$ complexes are concerned, the fact that the I_a/I_s intensity ratio is nearly one, as it is for $Cr^{II}(NO)_2L$ complexes, seems to suggest that Cr^{III} ions have no residual coordinative vacancies. Also in this case only ligand displacement reactions are expected such as in reaction c. The NO stretching mode of the resulting one-

$$Cr^{III}(NO)_2 + L(g) \longrightarrow Cr^{III}NO\,L + NO(g) \qquad (c)$$

nitrosyl complexes may be singled out in the ir spectrum. In both Figures 1 and 3 a shoulder is present at ~1725 cm^{-1} that we ascribe to $Cr^{III}(NO)L$ structures. This assignment is supported by the fact that the intensity of this absorption is unaffected by those preliminary high-temperature treatments which have been shown to affect only the Cr^{II} species.

From the above results it is inferred that Cr^{III} ions possess, before adsorption, only two coordinative unsaturations. The presence of four oxygen ligands in the coordination sphere of Cr^{III} agrees well with the charge of the ion and justifies the thermal stability of the involved structures.

Conclusions

By means of the NO–L interaction, further information about the Cr ions dispersed on the silica surfaces has been achieved, so that a final picture can be drawn. Four kinds of ions have been shown to be present on the surface of diluted samples, their population being a function of the pretreatment conditions.

(1) Cr^{III}, whose percentage is less than 15% on carefully treated diluted samples, resulted from the incomplete reduction of surface dichromates. The oxygen atom not removed on reduction is possibly bridged between the two Cr^{III} ions thus explaining the stability of such structures on the surface, as well as the presence of only two unsaturations. Because of the higher charge of the central ion, the adsorption of both CO and NO leads to surface complexes with stretching frequencies higher than those due to Cr^{II}.

(2) Cr^{II} is the major component of the samples, resulting

from the total reduction of dichromates. Pairs of Cr^{II} are thus expected on the surface. The cooperative effects of the two ions in the pair are revealed by CO adsorption at low temperature through the formation of bridged carbonyl-like structures. In all other interactions, the two ions behave independently. Three coordination vacancies per ion are brought into view in a number of cases. As the ultimate coordination is assumed to be octahedral, the coordinating state of Cr^{II} before adsorption is suggested to be trigonal. This picture is likely oversimplified, because two kinds of Cr^{II} have been revealed by CO adsorption and by reflectance measurements. The different reactivity of these two kinds of ions that we pointed out in parts I and II has perhaps to be related to different degrees of "sinking" into the trigonal base of oxygen ligands. Such low-coordination arrangements of Cr^{II} ions likely explain their instability to thermal treatments.

(3) "Shielded Cr" (mainly Cr^{II}) is nearly absent in carefully treated samples. These ions only show one coordinating unsaturation, accessible to Py and NO but not to CO, at least at room temperature. This kind of ions is favored by high Cr loadings, which likely cause the formation of a two-dimensional reduced phase. More striking increases of concentration are obtained by high temperature treatments in vacuo as coordinatively unsaturated Cr^{II} are converted into shielded ions.

Acknowledgment. Support for the research has been partially provided by the Consiglio Nazionale delle Ricerche.

References and Notes

(1) J. A. McGinnety, *MTP Int. Rev. Sci.*, **5**, 229 (1972).
(2) W. Beck, A. Melnikoff, and R. Stahl, *Chem. Ber.*, **99**, 3721 (1966).
(3) W. Beck and K. Lottes, *Chem. Ber.*, **98**, 2657 (1965).

Raman Spectra of Gases. XVI.[1] Torsional Transitions in Ethanol and Ethanethiol

J. R. Durig,*[2] W. E. Bucy,[3] C. J. Wurrey,

Department of Chemistry, University of South Carolina, Columbia, South Carolina 29208

and L. A. Carreira

Department of Chemistry, University of Georgia, Athens, Georgia 30601 *(Received December 2, 1974)*

Publication costs assisted by the University of South Carolina

The Raman spectra of gaseous ethanol and ethanethiol have been investigated. Thiol torsional fundamentals for the gauche conformer of EtSH and EtSD have been observed and the asymmetric potential function for this vibration has been calculated. Methyl torsional transitions and overtones have also been observed for both of these molecules. Barriers to internal rotation for the methyl top are calculated to be 3.77 and 3.84 kcal/mol for the EtSH and EtSD compounds, respectively. Hydroxyl torsional fundamentals were observed at 207 and 170 cm^{-1} in the EtOH and EtOD spectra, respectively. Overtones of the methyl torsion in both molecules yield a barrier to internal rotation of 3.62 kcal/mol for the gauche conformer.

Introduction

Gas-phase Raman spectroscopy has recently been applied to the study of torsional transitions. We have shown that double jumps in the Raman effect can lead to very accurately determined barriers to internal rotation for molecules with symmetric tops attached to symmetric or asymmetric frames.[4,5] A logical extension was to look at molecules with symmetric and asymmetric tops; ethanol and ethanethiol proved to be very interesting molecules to study in the Raman effect.

The existence of two different conformers, gauche and trans, has been established for both ethanethiol and ethanol.[6-16] The magnitude of the barrier separating these two conformers is intimately associated with a detailed knowledge of the SH or OH torsional motion.

Extensive microwave work has been done and is continuing on ethanol.[10-14,17,18] Quantum mechanical tunneling between the two gauche forms leads to ground state splitting

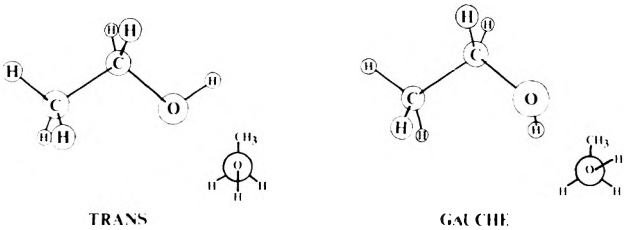

on the order of 3 cm^{-1}.[14] The extreme complexity of the spectrum due to this splitting plus a μ_b dipole approximately equal to zero for the gauche isomer has led to misassignments and some controversy in the determination of the barrier to internal rotation.[12] Tunneling of the OH top is quenched[13] in the CH_3CDHOH molecule. From the splitting due to tunneling of the methyl top a barrier to internal rotation around the C–C bond was calculated to be 3.37 kcal/mol.[18] More recently Culot has completed a structural and internal rotation study on 13 isotopes of ethanol.[17]

From his study of the trans conformer, a barrier of 3.32 kcal/mol was established for the methyl top of ethanol. Recently,[14] an estimated value for the barrier to internal rotation between the gauche minima was obtained from the tunneling frequency. Using a simplified threefold barrier, assuming no intramolecular mixing, and neglecting the rotational–vibrational interaction, a 1.20 kcal/mol (420.8 cm^{-1}) barrier was calculated for the OH torsion. Earlier thermodynamic work,[19] gave barriers of 3.3 and 0.8 kcal/mol to the methyl and hydroxyl tops, respectively.

The direct observation of torsional transitions, however, has been limited. Intermolecular association of ethanol gives rise to low vapor pressure at room temperature and also causes overlapping of infrared bands in every phase.[15] The far-infrared spectrum of solid ethanol showed bands at 282 and 251 cm^{-1} shifting to 198 and 184 cm^{-1} in the $-d_6$ compound.[20] Using the average frequency of the two bands a barrier of 4.05 kcal/mol was calculated for the methyl top in the solid phase. The infrared matrix isolation work[15] showed a band at 264 cm^{-1} in the light compound, which is in good agreement with the previous solid work. The far-infrared spectrum of the gas[15] shows a band at 243 cm^{-1} which is assigned as the methyl torsion. This agrees with the barrier to internal rotation for the trans conformer as determined by microwave spectroscopy.[17] The OH torsion has been observed in the infrared spectrum of the gas at 199 cm^{-1},[21] in the infrared spectrum of the cyclohexane solution at 208 cm^{-1},[22] and in the infrared spectrum of the matrix at 211 cm^{-1}.[15] The OD torsion has been observed at 169 and 175.5 cm^{-1} in the gas phase and matrix, respectively.[15]

Ethanethiol, the sulfur analog of ethanol, has been the subject of a number of studies also. The change in internal energy (ΔE) between the gauche and trans forms of ethanethiol has been calculated from thermodynamic data[7] and a value of about 100 cm^{-1} was obtained. This is in good agreement with the two far-infrared studies which gave values of ΔE of 123 cm^{-1} [9] and 84 cm^{-1}.[8] In the gas phase the gauche form is the dominant conformer.[7,8] The potential barrier to internal rotation of the SH top, unlike the OH top which is thought to be nearly symmetric, is quite asymmetric.[8,9] For the methyl top of ethanethiol, however, there seems to be no change in the methyl torsional barrier between the two conformers.[9] Normal coordinate analyses[8,23] have shown that the methyl and SH torsions are virtually uncoupled.

The mid-infrared spectrum of the solid[7] has shown three bands in the region from 264 to 320 cm^{-1}. These were assigned as thiol torsions, profoundly affected by hydrogen bonding. However, the far-infrared spectrum of the gas has conclusively shown that the fundamental of the methyl torsion falls at 247.5 cm^{-1}.[9] This gives a methyl barrier of 3.88 kcal/mol in contrast to the earlier thermodynamic value of 3.3 kcal/mol.[24] The 3.3 kcal/mol barrier to internal rotation about the carbon–carbon bond was based on threefold barriers for both tops. The thermodynamic barrier was later modified to 3.75 kcal by considering the asymmetry of the SH barrier to internal rotation.[7] This thermodynamic calculation gave a value of ΔE = 100 cm^{-1} between the two conformers. The far-infrared spectrum of the gas also shows a sharp Q branch at 191 cm^{-1},[7-9,23] which is confidently assigned as the 0 → 1 SH torsion of the gauche conformer.

The direct observation of torsional transitions, whether single or double jumps, is a necessity for good barrier calculations. In order to determine asymmetric potential functions transitions in both wells are a requirement. With the advent of high-powered lasers we are able to see these transitions in the gas phase using the Raman effect. Symmetry species can be characterized from the Raman effect using polarization data. Thus, it was felt that ethanol and ethanethiol provided ideal chances to study both symmetric and asymmetric torsional transitions, since previous work could be of assistance in assigning our spectra. Also, it was felt that the gas-phase Raman data could be useful in clearing up the controversies mentioned above.

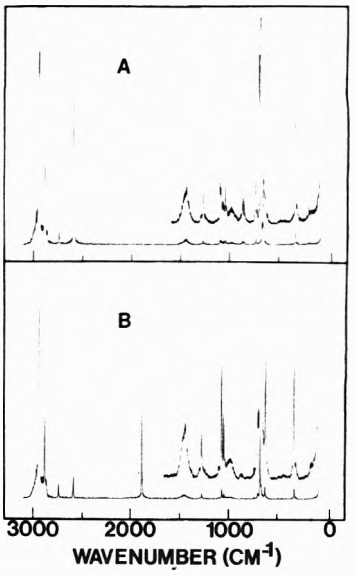

Figure 1. Raman spectra of gaseous thiols: (A) EtSH, (B) EtSD. Spectra were recorded at room temperature with 4-cm^{-1} spectral band width.

Experimental Section

The sample of EtSH was obtained from Columbia Organics Co., and its purity was checked by vapor-phase chromatography and found to be better than 99% pure. EtSD was prepared from EtSH by the method of Hobden et al.[25] with slight variations. Carbon dioxide was not used and the preparation was done under vacuum to contain the aroma of EtSH and to get better isotopic yield. About 90% isotopic purity was obtained. Absolute EtOH was also checked by vpc and found to contain less than 1% impurities. EtOH was converted to the OD compound using the same method as for the EtSD. However, vacuum techniques were not employed for the OD compound. Preparation under a nitrogen blanket gave about 80% isotopic purity. However, the isotopic purity varied greatly due to exchange with the glassware. All samples were dried over molecular sieves.

The Raman spectra were recorded with a Cary Model 82 Raman spectrophotometer[26] equipped with a CRL Model 53G argon ion laser which produced from 1.5 to 2.5 W of power in the 5145-Å line at the sample. The laser beam was multipassed through a standard Cary multipass cell which was adapted with a PTFE greaseless stopcock and a side-arm reservoir. The windows of the cell and the sample area were heated to 65–75° to increase the vapor pressure of the EtOH and EtOD. At high laser power, 3 W, the sample of EtSH "streamed" badly and deposited liquid on the windows. This occurred with supposedly no excess liquid in the cell. Heating the windows prevented the liquid from form-

Table I. Raman Frequencies of Gaseous EtSH and EtSD and their Tentative Assignments[a,b,c]

EtSH			EtSD		
cm^{-1}	Depolarization	Assignment	cm^{-1}	Depolarization	Assignment
2971 vw	dp	CH_3 antisymmetric stretch	2971 vw	p?	?
2946 vs	p	CH_3 antisymmetric stretch	2961 vw	p	?
2940 vs	p	CH_2 symmetric stretch	2951 vw	p	?
2886 m	p	CH_3 symmetric stretch	2945 vs	p	CH_3 antisymmetric stretch
2864 w	p	Deformation overtone	2940 vs	p	CH_2 symmetric stretch
2745 w	p	Deformation + wag	2882 m	p	CH_3 symmetric stretch
2598 w	p	?	2867 w	p	Overtone
2590 w	p	S-H stretch	2730 w	p	Overtone
1450 b w	dp	CH_3 deformations	2669 vw	p	?
1275 w	p	CH_2 wag	2597 vw	p	S-H impurity
1098 w	p	CH_3 rock	2591 w	p	S-H impurity
1093 sh	p	?	1886 sh m	p	?
1068 vw	p	CH_2 rock + C-C-S bend	1881 m	p	S-D stretch
1043 w	p	C-C stretch	1450 b w	dp	CH_3 deformations
985 b w	dp	CH_3 rock	1300 vw	p	C-S stretch + C-S-D bend
877 w sh	p	?	1271 w	p	CH_2 wag
870 w	p	C-S-H bend	1095 vw	p	S-H impurity
855 w	p	C-S stretch + S-H torsion	1069 w	p	CH_3 rock
736 w	p	CH_2 rock	1046 w	p	C-C stretch
725 vw	p	Deformation - CH_2 rock (?)	978 w	dp	CH_3 rock
675 w	p	?	870 w	p	S-H impurity
			855 w	p	S-H impurity
662 m	p	C-S stretch	735 w	p	S-H impurity
482 vvw		0→2 CH_3 torsion	696 w	p	CH_2 rock
468 vvw		C-S stretch - S-H torsion	676 m	p	C-S stretch; mixed with C-SD bend
454 vvw		1→3 CH_3 torsion	662 sh	p	S-H impurity
440 vw		S-H torsion + CH_3 torsion	625 w	p	C-S-D bend; mixed with C-S stretch
330 w	p	C-C-S bend	487 vw		0→2 CH_3 torsion
			441 vw		CH_3 rock (1069) - C-S-D bend
246 vvw		0→1 CH_3 torsion	325 w	p	C-C-S bend
232 vvw		1→2 CH_3 torsion	301 vvw		C-S-D bend - C-C-S bend
220 ?		2→3 CH_3 torsion (?)			
191 w	p	0→1 S-H torsion	250 vw		0→1 CH_3 torsion
169 vvw	p	1→2- S-H torsion	232 vw		0→2 S-D torsion (C_s)
157 vvw	p	1→2+ S-H torsion	150 vw		0→1 S-D torsion
			136 vw		1→2 S-D torsion

[a]Abbreviations used: v, very; s, strong; m, medium; w, weak; b, broad; sh, shoulder; p, polarized; dp, depolarized. [b]See Reference 7. [c]All frequencies from the gauche conformer unless marked otherwise.

Table V. Raman Frequencies of Gaseous EtOH and EtOD and Their Tentative Assignments[a,b,c]

EtOH			EtOD		
cm^{-1}	Depolarization	Assignment	cm^{-1}	Depolarization	Assignment
3675 m	p	O-H stretch[c]	3675 w	p	O-H impurity
3659 m	p	O-H stretch[c]	3659 w	p	O-H impurity
2985 s	p	CH_3 antisymmetric stretch	2987 m	p	CH_3 antisymmetric stretch
2939 s	p	CH_3 symmetric stretch	2944 sh	p	Deformation overtone
2914 vw	p	?	2940 s	p	CH_3 symmetric stretch
2887 s	p	CH_2 symmetric stretch	2887 s	p	CH_2 antisymmetric stretch
2810 vw	p	Overtone	2715 m		O-D stretch[c]
2770 vw	p	Overtone	2704 m		O-D stretch[c]
2730 vw	p	Overtone	1476 b w		CH_3 antisymmetric deformations
1460 b w	dp	CH_3 antisymmetric deformations	1413 vw sh		CH_2 scissors
1430 sh		CH_2 scissors	1394 vw		CH_3 symmetric deformation
1395 vw	p	CH_3 symmetric deformation	1370 vvw		?
1370 vw	p	?	1292 vw b		C-C-O bend + C-C stretch; CH_2 wag
1270 vvw		CH_2 wag	1246 vw b		O-H impurity
1245 vw	p(?)	O-H bend	1118 vw		CH_3 rock
1142 vvw	p	?	1093 vw		O-H impurity
1117 vw	p	CH_3 rock	1054 vw		C-O stretch (C-C-O)
1093 vw	p	O-H torsion + C-C stretch	1028 vw		O-H impurity
1055 vw	p	C-O stretch (C-C-O)	882 m		C-C stretch (C-C-O)
1026 w	p	CH_3 rock	856 m		O-D bend
883 w	p	C-C stretch (C-C-O)	670 vw		?
855 sh	p	?	487 vvw		0→2 CH_3 torsion
490 vvw	p	0→2 CH_3 torsion	450 vvw		1→3 CH_3 torsion (?)
453 vvw		1→3 CH_3 torsion (?)	416 w		C-C-O bend
422 w	p	C-C-O bend	170 vvw		O-D torsion
207 vvw		O-H torsion			

[a]Abbreviations used: see Table I. [b]See References 7 and 16. [c]See text.

ing and allowed us to run EtSH at full power. All frequencies are expected to be accurate to ±2 cm^{-1}.

Results and Discussion

A. Ethanethiol. The Raman spectra of EtSH and EtSD in the gas phase from 50 to 3100 cm^{-1} are shown in Figure 1. Tentative assignments are listed in Table I (see paragraph at end of text regarding miniprint material). In the survey spectra, we looked for evidence of the two conformers in an attempt to estimate ΔH. In the mid-infrared spectra of the solid and liquid, the CH_2 rock seems to be the only mode in which a detectable difference between the gauche and trans frequencies is observed.[7] The gauche CH_2 rock occurs at 737 cm^{-1} and the trans at 783 cm^{-1}. In the Raman effect, the trans CH_2 rock would be depolarized. We found no evidence of the trans CH_2 rock in the gas or the liquid. However, splittings of the C–S stretch, S–H stretch, and S–D stretch were observed. These splittings merited a temperature study to determine if they are actual differences in frequencies due to the two conformers or if

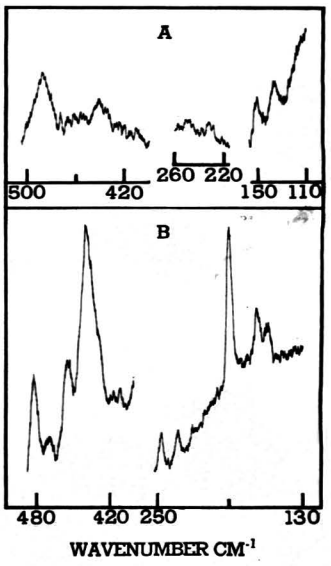

Figure 2. Torsional transitions in gaseous thiol. (A) EtSD. Spectra were recorded at room temperature with 10-cm^{-1} spectral band width for methyl transitions and 6-cm^{-1} spectral band width for thiol torsions. (B) EtSH. Spectra were recorded at room temperature with 4-cm^{-1} spectral band width for the thiol torsions and 7-cm^{-1} spectra band width for the methyl overtones.

they are overtones or combination bands. A temperature study from 25 to 90° of the gas phase of EtSH showed no significant difference in the peak areas (half-width times height) of the 675- and 662-cm^{-1} bands. With increasing temperature, the 2598-cm^{-1} shoulder coalesced in the 2590-cm^{-1} S–H stretch. Therefore, we could not obtain any thermodynamic information from our temperature study.

Figure 2 shows the torsional regions for the SH and SD compounds. In the SH compound, the 0 → 1 methyl torsion was observed at 246 cm^{-1}, the 1 → 2 at 233 cm^{-1}, and possibly the 2 → 3 at 221 cm^{-1}. In the region of methyl torsional overtones, four bands were observed. The bands at 482 and 454 cm^{-1} are assigned as the 0 → 2 and 1 → 3 of the CH_3 torsion, respectively. These frequencies agree very well with the far-infrared data of 247.5, 233.5, and 220.5 cm^{-1} for the 0 → 1, 1 → 2, and 2 → 3 methyl torsional transitions, respectively.[9] Table II shows the calculated and observed frequencies and the barrier to internal rotation. A 3.77 ± 0.03 kcal/mol barrier is very reasonable. The barriers were calculated using the program described previously.[4] No V_6 term was used because only two frequencies in the overtone region were observed. The bands in the spectrum at 468 and 440 cm^{-1} are combination and difference bands. The difference band between the C–S stretch at 662 cm^{-1} and the SH torsion at 191 cm^{-1} gives rise to the 468-cm^{-1} band. The 440-cm^{-1} band arises from a combination of the SH torsion at 191 cm^{-1} and the methyl torsion at 246 cm^{-1}. However, the difference of a band at 1099 cm^{-1} and the C–S stretch at 662 cm^{-1} may add intensity to the band at 440 cm^{-1}.

The bands at 191, 169, and 157 cm^{-1} are confidently assigned as the 0± → 1±, 1− → 2−, and 1+ → 2+ SH torsions of the gauche conformer. All three of these lines are definitely polarized, which means they arise from the gauche (C_1) form for which this vibration is totally symmetric.

In the SD compound we observed the fundamental of the methyl torsion at 250 cm^{-1}. A peak was also observed at 487 cm^{-1} and is assigned to the 0 → 2 methyl torsional

TABLE II: Raman Torsional Transitions and Barriers to Methyl Internal Rotation in Ethanethiol and Ethanol

Molecule	F	V_3, kcal/mol	Transition	Obsd	Calcd	Δ
CH_3CH_2SH	5.85	3.70	0 – 1	246	247.1	+1.1
			1 – 2	233	232.0	−1.0
			2 – 3	221[a]	215.7	−5.3
CH_3CH_2SH	5.85	3.77	0 – 2	482	484.1	−2.1
			1 – 3	454	452.1	1.9
			0 – 1		249.6	
CH_3CH_2SD	5.79	3.84	0 – 1	250	250.8	+0.8
			0 – 2	487	486.6	−0.4
CH_3CH_2OH (gauche)	6.32	3.62	0 – 2	490	490	0.0
			0 – 1		253.3	
CH_3CH_2OH (trans)	6.44	3.55	0 – 2	490	490	0.0
			0 – 1		253.4	
CH_3CH_2OD (gauche)	6.23	3.62	0 – 2	487	487	0.0
			0 – 1		251.7	
CH_3CH_2OD (trans)	6.44	3.52	0 – 2	487	487	0.0
			0 – 1		252.0	

[a] Not used in calculation.

overtone. The barrier is calculated to be 3.84 kcal/mol for the methyl internal rotation. This barrier is calculated using the gauche structure F number since the gauche conformer is the dominant molecule in the gas phase. The methyl torsional fundamentals of both the SD and SH compounds are polarized which means they arise from the gauche form. Therefore, in both EtSH and EtSD, differences between the gauche and trans methyl barriers are not observable. This is in agreement with the far-infrared observations.[9] The difference in the methyl barriers between the light and heavy compounds may be attributed to the inherent error in the experimental measurement and the lack of knowledge of the structure.

The SD torsional fundamental region shows bands at 150 and 136 cm^{-1}. These transitions were confidently assigned as the 0 → 1 and 1 → 2 of the gauche torsion. Splitting of the 1 → 2 transition was not resolvable. A band at 232 cm^{-1} is assigned as the 0 → 2 of the trans SD torsion. An assignment of this band as the 1 → 2 of the methyl torsion seems to be incorrect. The predicted 1 → 2 using the 487- and 250-cm^{-1} bands gives a frequency of 236 cm^{-1}.

A computer program was written to vary the torsional angle and calculate the resulting F number. The calculated F numbers were then fit to equations of the form

$$F(\alpha) = F_0 + F_1 \cos \alpha + F_2 \cos 2\alpha + F_3 \cos 3\alpha + \ldots$$

with one to seven terms. Only a two or three term series is necessary because of the lack of knowledge of the molecular structure and the fast convergence of the series. The program described previously[4] was modified to calculate coordinate-dependent F numbers.[27] The resulting potential functions have the form

$$V(\alpha) = \frac{V_1}{2}(1 - \cos \alpha) + \frac{V_2}{2}(1 - \cos 2\alpha) + \frac{V_3}{2}(1 - \cos 3\alpha) + \frac{V_6}{2}(1 - \cos 6\alpha)$$

It is believed that some top-top coupling exists in EtSH.[9] However, in the heavy molecule, coupling is reduced because the energy levels are further apart. The higher barrier for the EtSD molecule supports this belief. We therefore calculated the potential constants for the heavy molecule first and then used those potential constants to fit the observed frequencies in the light molecule.

Within experimental accuracy our frequencies are the same as those from the far-infrared spectra.[8,9] Because the resolution and accuracy of the interferometer is superior to the Raman effect in this instance, we chose to use the frequencies of the far-infrared[9] supplemented by our additional frequencies. With the total data present, we are able to fit the three potential constants, V_2, V_3, and V_6, with five frequencies. The V_1 term was found to be insignificant and was deleted from the calculation. Using these potential constants, we calculated the frequencies for EtSH. The agreement between the observed and calculated frequencies for EtSH averaged about 1.6 cm^{-1} or 0.9% error.

It was felt that a better set of potential constants could be obtained for EtSH. The five known frequencies of the EtSH molecule were used to fit V_1, V_2, V_3, and V_6. The potential constants generated fit the observed frequencies to better than 0.7 cm^{-1}. However, the dispersion of all the potential constants was too large. The dispersion of the V_1 term was 196 cm^{-1} while the V_1 term was only 8.0 cm^{-1}. Again, for this reason the V_1 term was set equal to zero and the five frequencies were fit to three potential constants (V_2, V_3, and V_6). With just three potential constants, the fit improved and the dispersion of the potential constants was reduced greatly. Our calculations are summarized in Table III.

From the energy levels calculated it is possible to calculate ΔE, the internal energy difference between the two conformers. For the SD molecule, ΔE = 115.0 cm^{-1} and for the SH molecule, ΔE = 111.3 cm^{-1} if the SD potential constants are used with the SH $F(\alpha)$. The minimum in the potential energy occurs at 115.2° from trans in the SD molecule. Using the potential constants from the SH data, ΔE is calculated to be 117.7 cm^{-1} and the dihedral angle is 115.2°. At 55.8° from trans in the light molecule, a gauche to trans barrier of 493.4 cm^{-1} (1.41 kcal) is calculated. The trans to gauche barrier is 359.7 cm^{-1} (1.03 kcal). The gauche to gauche barrier is 617.1 cm^{-1} (1.76 kcal/mol). The SD compound has a g → t barrier of 485.4 cm^{-1} (1.39 kcal), a t → g barrier of 359.3 cm^{-1} (1.03 kcal), and a g → g barrier of 602.7 cm^{-1} (1.72 kcal/mol).

Our calculations show a 5.3% difference in V_2 and a 1.4%

TABLE III: Far-Infrared[a] and Raman Torsional Transitions and Asymmetric Potential Function for Thiol Internal Rotation in Ethanethiol and Ethanethiol-d_1

Transition		Obsd	Calcd	Δ
		CH_3CH_2SD[b]		
g	0± → 1±	148.5 (150)[e]	148.5	0.0
g	1+ → 2−	135.1 (136)[e]	134.9	0.2
g	1− → 2+	134.0	134.3	−0.3
t	0 → 1	125.0	124.9	0.1
t	0 → 2	232[e]	231.9	0.1
		V_2	V_3	V_6
		−162.1 ± 1.3	476.6 ± 1.1	−14.4 ± 0.9
		CH_3CH_2SH[c,d]		
g	0+ → 1−	193.0 (191)[e]	193.0	0.0
g	0− → 1+	191.8	192.2	−0.4
g	1− → 2−	169[e]	166.7	+2.3
g	1+ → 2+	157[e]	153.5	+3.5
t	0 → 1	158	159.8	−1.8
		CH_3CH_2SH[c]		
g	0+ → 1−	193.0	192.8	0.2
g	0− → 1+	191.8	192.1	−0.3
g	1− → 2−	169[e]	169.1	−0.1
g	1+ → 2+	157[e]	157.0	0.0
t	0 → 1	158	157.9	0.1
		V_2	V_3	V_6
		−170.9 ± 1.5	483.5 ± 0.8	−21.1 ± 0.7

[a] Reference 9. [b] EtSD: F_0, 6.0810; F_1, −0.1604; F_2, 0.0425; F_3, −0.0034; F_4, 0.0004; α = 0 for trans. See ref 8. [c] EtSH: F_0, 10.9752; F_1, −0.1620; F_2, 0.0362; F_3, −0.0018; F_4, 0.0002; α = 0 for trans. See ref 8. [d] Using the potential constants of EtSD. [e] Raman data.

TABLE IV: Barriers to Methyl Rotation of Some First and Second Row Ethanes

Molecule (gas phase)	V_3, kcal/mol	Ref
$CH_3CH_2CH_3$	3.3 (V_3 = 0.17)[e]	*a*
$CH_3CH_2NH_2$	3.74	*a*
CH_3CH_2OH	3.62	*b*
CH_3CH_2F	3.33	*a*
$CH_3CH_2SiH_3$	2.65	*a*
$CH_3CH_2PH_2$	3.08	*c*
CH_3CH_2SH	3.80	*b*
CH_3CH_2Cl	3.72	*d*

[a] Reference 28. [b] This work. [c] Reference 29. [d] Reference 4. [e] Two tops.

difference in the V_3 term for the two isotopes. Lack of knowledge of the molecular structure could account for these differences. However, top–top coupling of the energy levels in the light molecule would change the potential function with respect to the heavy molecule. We believe this coupling to be very small in the light molecule and nonexistent in the heavy molecule. However, coupling would explain the slightly lower methyl barrier in EtSH relative to EtSD. The internal energy differences between the two conformers of the both molecules are in excellent agreement with the thermodynamic value.[7]

It is also interesting to note the trend in the methyl barriers in going across the periodic table from Si → Cl. A gradual increase in observed in the barrier from Si → S with a slight decrease in the chloride barrier. (See Table IV.)

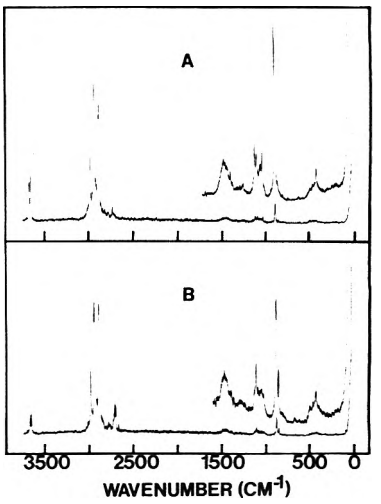

Figure 3. Raman spectra of gaseous alcohols. (A) EtOH. Spectrum was recorded at room temperature with 5-cm^{-1} spectral band width. Expansion below 1500 cm^{-1} was recorded at 10-cm^{-1} spectral band width. This spectrum was also recorded at 60° and 7.5-cm^{-1} spectral band width. No changes were observed. (B) EtOD. The survey spectrum was recorded at room temperature with 4-cm^{-1} spectral band width. Expansion below 1500 cm^{-1} was recorded at 8-cm^{-1} spectral band width.

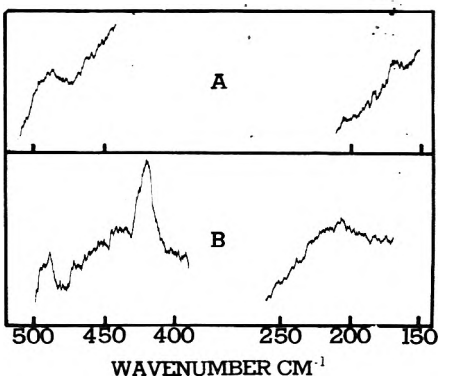

Figure 4. Torsional transitions in gaseous alcohols. (A) EtOD. Spectra were recorded at 55° with 12-cm^{-1} spectral band width. (B) EtOH. Spectra recorded at 55° with 9-cm^{-1} spectral band width.

B. Ethanol. The Raman spectrum EtOH and EtOD in the gas phase from 50 to 3750 cm^{-1} are shown in Figure 3. Tentative assignments are listed in Table V (see paragraph at end of text regarding miniprint material). The overall weakness of the spectrum is the most important feature. The OH and OD stretching regions show two peaks of almost identical intensity. These peaks are assigned as the OH and OD stretches of the trans and gauche conformers. In the infrared spectrum of the matrix, the gauche conformer was assigned to the higher frequency component.[15] From peak heights in the Raman spectrum of the gas, using the Boltzmann distribution, an energy difference of 179 cm^{-1} is calculated using the gauche form as the 3675-cm^{-1} line. If the gauche conformer is the 3659-cm^{-1} line, then an energy difference of 110 cm^{-1} is calculated. These calculations show the trans to be the most stable conformer.

Figure 4 shows the torsional regions of EtOH and EtOD. Bands at 490 cm^{-1} in EtOH and 487 cm^{-1} in EtOD are as-

signed as the methyl torsional overtones. If the gauche conformer is used to calculate the F number a consistent barrier of 3.62 kcal/mol is obtained. However, if the trans isomer is used, values of 3.55 and 3.52 kcal/mol are obtained for the OH and OD compounds, respectively. The average value of the trans barrier heights of both compounds, 3.54 kcal/mol, is about 0.2 kcal/mol higher than the microwave results.[17] The frequency of 490 cm^{-1} calculated the $0 \rightarrow 1$ to fall at 253 cm^{-1}, 10 cm^{-1} higher than the microwave and infrared[15] results. However, the results seem in good agreement with the solid work done in the infrared. A frequency shift of 11 cm^{-1} from solid to gas seems reasonable, with a corresponding shift of the barrier from 4.05 to 3.54 kcal/mol for the trans conformer.

The methyl barriers in the first row of the periodic table rise from $-CH_3$ to $-NH_2$ then steadily fall from OH to F (see Table IV).

The OH and OD torsional fundamentals are very weak and polarization data could not be obtained. Experience in gas-phase Raman spectroscopy has led us to believe it is very difficult to see torsional fundamentals which are not totally symmetric vibrations. We, therefore, conclude that the bands at 207 and 170 cm^{-1} in the OH and OD compounds, respectively, arise from the gauche conformer. These frequencies correspond well to the bands at 199 and 169 cm^{-1} previously reported.[15] Association bands have been reported around 214 cm^{-1} in both compounds.[15] It is possible, with large spectral band widths, an association band and a torsion might have distorted frequencies.

From the almost equal intensity of the trans and gauche OH stretches, it is concluded that the OH torsional potential barrier is asymmetric, with the trans being the stable conformer. However, a threefold barrier seemed a reasonable assumption since no hot bands were observed. Barriers of 357 cm^{-1}, 1.02 kcal, and 177 cm^{-1}, 0.51 kcal/mol were obtained for the OD and OH torsions, respectively. The OD barrier is in good agreement with the 1.20 kcal/mol (420 cm^{-1}) barrier calculated from the microwave data for the gauche conformer.[14] However, more data are needed to reach a conclusive hydroxyl barrier.

Summary

Barriers to methyl internal rotation in ethanethiol and ethanol have been calculated using gas-phase Raman spectroscopy. An asymmetric potential function has been calculated for the thiol torsion. An attempt was made to fit a symmetric potential function to the hydroxyl torsion. However, it was found that the trans conformer is more stable by at least 300 cal/mol.

Acknowledgment. The authors wish to thank A.W. Cox for his ingenuity in computer programming. The authors also wish to acknowledge support of this research by the National Aeronautics and Space Administration by Grant No. NGL-41-002-003.

Miniprint Material Available. Full-sized photocopies of the miniprinted material (Tables I and V) from this paper only or microfiche (105 × 148 mm, 24 × reduction, negatives) containing all of the miniprinted and supplementary material for the papers in this issue may be obtained from the Journals Department, American Chemical Society, 1155 16th St., N.W., Washington, D.C. 20036. Remit check of money order for $4.00 for photocopy of $2.50 for microfiche, referring to code number JPC-75-988.

References and Notes

(1) For part XV, see J. R. Durig, M. G. Griffin, and R. W. MacNamee, *J. Raman Spectrosc*, in press.
(2) Author to whom inquiries should be addressed.
(3) To be submitted in partial fulfillment of the Ph.D. requirements.
(4) J. R. Durig, W. E. Bucy, L. A. Carreira, and C. J. Wurrey, *J. Chem. Phys.*, **60**, 1754 (1974).
(5) J. R. Durig, W. E. Bucy, and C. J. Wurrey, *J. Chem. Phys.*, **60**, 3293 (1974).
(6) P. Tarte and R. Deponthiere, *J. Chem. Phys.*, **26**, 962 (1957).
(7) D. Smith, J. P. Devlin, and D. W. Scott, *J. Mol. Spectrosc.*, **25**, 174 (1968).
(8) F. Inagaki, I. Harada, and T. Shimanouchi, *J. Mol. Spectrosc.*, **46**, 381 (1973).
(9) A. S. Manocha, W. G. Fateley, and T. Shimanouchi, *J. Phys. Chem.*, **77**, 1977 (1973).
(10) J. Michielsen-Effinger, *J. Mol. Spectrosc.*, **29**, 489 (1968).
(11) L. M. Imanov, Ch. O. Kadzhar, and I. Dzh. Isaev, *Opt. Spectrosc., USSR*, **18**, 508 (1965).
(12) M. Takano, Y. Sasada, and T. Satoh, *J. Mol. Spectrosc.*, **26**, 157 (1968).
(13) Y. Sasada, *J. Mol. Spectrosc.*, **38**, 33 (1971).
(14) R. Kakar and P. J. Seibt, *J. Chem. Phys.*, **57**, 4060 (1972).
(15) A. J. Barnes and H. E. Hallam, *Trans. Faraday Soc.*, **66**, 1932 (1970).
(16) J. P. Perchard and M. L. Josien, *J. Chim. Phys.*, **65**, 1834 (1968); **65**, 1856 (1968).
(17) J. P. Culot, Fourth Austin Symposium on Gas Phase Molecular Structure, 1972, p 47.
(18) L. M. Imanov and C. O. Kadzhar, *Izv. Akad. Nauk Azerb. SSR*, **3–4**, 33–42 (1967).
(19) G. M. Barrow, *J. Chem. Phys.*, **20**, 1739 (1952).
(20) J. R. Durig and C. W. Hawley, *J. Phys. Chem.*, **75**, 3993 (1971).
(21) R. F. Lake and H. W. Thompson, *Proc. Roy. Soc. Ser. A*, **291**, 469 (1966).
(22) S. M. Craven and F. F. Bentley, *Appl. Spectrosc.*, **26**, 242 (1972).
(23) D. W. Scott and G. A. Crowder, *J. Mol. Spectrosc*, **26**, 477 (1968).
(24) J. P. McCullough, D. W. Scott, H. L. Finke, M. E. Gross, K. D. Williamson, R. E. Pennington, G. Waddington, and H. M. Huffman, *J. Am. Chem. Soc.*, **74**, 2801 (1952).
(25) F. Hobden, E. Johnston, L. Weldon, and C. Wilson, *J. Chem. Soc.*, 61 (1939).
(26) The Raman spectrophotometer was purchased with funds from a National Science Foundation Grant No. GP-28068.
(27) J. D. Lewis, T. B. Malloy, Jr., T. H. Chao, and J. Laane, *J. Mol. Struct.*, **12**, 427 (1972).
(28) J. R. Durig, S. M. Craven, and W. C. Harris in "Vibrational Spectra and Structure," Vol. I, J. R. Durig, Ed., Marcel Dekker, New York, N.Y., 1972.
(29) A. W. Cox, private communication.

Ionic Photodissociation of Excited Electron Donor–Acceptor Systems. I. An Empirical Equation on the Relationship between the Yield and the Solvent Dielectric Constant

Hiroshi Masuhara,* Tetsuro Hino, and Noboru Mataga

Department of Chemistry, Faculty of Engineering Science, Osaka University, Toyonaka, Osaka 560, Japan *(Received September 30, 1974)*

Ionic photodissociation yields of some 1,2,4,5-tetracyanobenzene complexes and of the pyrene–*N,N*-dimethylaniline exciplex system in various solvents were obtained by using the nanosecond laser photolysis method. On the basis of the results obtained, a new empirical equation representing the relationship between the yield and the solvent dielectric constant was proposed, which was discussed from the viewpoints of three different theories: (i) Horiuchi–Polanyi's relation for the activation energy; (ii) Onsager's ion recombination model; and (iii) phenomenological theory of reaction rates based on Fick's law. With i and ii the empirical rule was verified qualitatively but not with iii, which seems to mean that the ions produced begin to diffuse with excess energy from the excited state nonrelaxed with regard to solvent orientation. The correlation of the rate constant of dissociation with various solvent polarity parameters was also examined. The solvent effect on ionic photodissociation seems to be well explained in terms of dielectric constant.

Introduction

The excited singlet and triplet states of electron donor–acceptor (EDA) complexes, which are stable in the ground state, and exciplexes are all called in this paper the excited EDA systems. These systems are suitable to clarify the relationship between photophysical as well as photochemical primary processes and molecular interactions, and some detailed investigations have been performed by conventional flash photolysis, laser photolysis, and transient photocurrent measurements. Ionic photodissociation to donor cation and acceptor anion in polar solvents is one of the most important primary processes, which is directly related to radiationless transitions or to fluorescence quenching.[1–4] Moreover, results on this process have been referred to in many fields of chemistry. In fact, some investigations have been made which relate ionic photodissociation to photoinduced ionic polymerization,[5] mechanistic organic photochemistry,[6] electrochemistry,[7] and photosynthesis.[8]

Ionic photodissociation processes are sensitive to the nature of solvent, which is the subject of the present paper. At present, solvent effects on ionic photodissociation can be classified into two groups. The first is the solvent effect on the nature of the dissociative states. Excited singlet and triplet states are known as dissociative states of EDA complexes,[2,7–9] while the thermalized exciplex state as well as the excited state nonrelaxed with respect to solvent orientation may be important for exciplex systems.[1,4] Which state is dissociative is determined by the surrounding environment, namely, by the nature of the solvent and also by the temperature. The second is the solvent effect on quantum yields of ionic photodissociation. In general, the yield changes from solvent to solvent even when the dissociation is occurring from the same kind of state. It increases as the solvent polarity increases, which has been qualitatively explained from the viewpoint of the lowering of free energy of dissociated ionic states.[1]

In the present paper the second solvent effect will be studied and a new empirical equation on the relationship between the yield and solvent dielectric constant will be proposed. The mechanism of ionic dissociation and the proposed empirical equation will be discussed on the basis of three different theories. Moreover, the correlation of the rate constant of dissociation with various solvent polarity parameters will be examined. Although there have been many investigations on stable ions and ion pairs in various solvents, studies concerning the solvent effect upon the dynamical processes of ionic dissociation in the excited state is rather scarce.

Experimental Section

The laser photolysis method used was the same as reported previously.[1a,2b] Solid samples were the same as used before.[1,2] All the solvents were spectrograde (Nakarai or Wako) and used without further purification. Solutions were completely degassed by freeze–pump–thaw methods.

Results

1. Dissociative States of the TCNB Complexes and the Pyrene–DMA Exciplex System. Ionic dissociation processes have been considerably elucidated based on transient absorption and photocurrent measurements with the laser photolysis method. In the present paper some 1,2,4,5-tetracyanobenzene (TCNB) complexes and the pyrene–*N,N*-dimethylaniline (DMA) system are dealt with as typical examples of excited EDA systems. It is necessary to identify the dissociative state of the present systems, since several different dissociative patterns (dissociations from excited singlet or triplet states, and from the excited states relaxed or nonrelaxed with respect to solvent orientation) have been demonstrated.[1,2,8,9] In the case of TCNB complexes all photocurrent and absorption rise curves due to the ions produced are identical with a time-integrated function of an exciting pulse, namely, quite rapid formation of ions was observed. Hence, the dissociation of these complexes is deemed to occur from the excited CT singlet state in various solvents. The further problem of these

complexes is the nature of the excited CT singlet state, which depends upon the surrounding environment.[10] Namely, in the case of liquid donor solutions a 2:1 ($D_2^+A^-$) complex is formed, while a 1:1 (D^+A^-) complex is formed with low toluene concentration or in a rigid matrix. Which is the dissociative state should be now clarified, and for this purpose the measurement of fluorescence spectra in mixed solvents may be useful. When the volume ratio of toluene to dichloromethane was changed, the fluorescence spectra showed a peculiar change as shown in Figure 1. As the concentration of toluene is increased, the peak of broad band shifts to shorter wavelength, which may be due to the decrease of electrostatic interactions between the complex and the solvent. When the volume ratio of toluene exceeds 25% the shoulder at the longer wavelength region cannot be neglected, and dual emission was clearly observed in the case of a 1:1 volume ratio. This behavior cannot be explained in terms of the simple bulk solvent effect on fluorescence spectra and the red-shifted band is considered to be due to the ($D_2^+A^-$) complex.[10,11] On the other hand, the solvent effect on the fluorescent state of the TCNB–toluene complex was examined, fixing the volume ratio (~5%) of toluene to the solvent. The results, which were analyzed by the usual electrostatic theory of solvent effect, showed that the fluorescent state is a contact ion pair of the (D^+A^-) complex.[12] Therefore, in the present work the solvent effect on ionic dissociation should be examined under the condition of low toluene concentration (lower than 25% volume ratio), where the dissociation occurs from the 1:1 (D^+A^-) complex.

In the case of exciplex systems, the observed ionic species (ion pair or free ions) are produced in the course of the quenching of pyrene fluorescence due to electron transfer. Accordingly the problem of dissociative states is not on the spin state but on the excited states relaxed or nonrelaxed with respect to solvation. Both rapid and slow photocurrent rise curves were first observed in pyridine solutions by Taniguchi and Mataga.[1b] The same results on dichloromethane and 1,2-dichloroethane solution are given in the present work. Since the rapid formation of ions is completed before decay of the thermalized exciplex, the dissociation was concluded to occur from the excited state, nonrelaxed with respect to solvent reorientation, competing with exciplex formation. The rise of the slow component does not correspond to the decay of the exciplex emission and such slow formation cannot be recognized in transient absorption measurements. It may be due to the dissociation from the ion-pair state relaxed with respect to solvation. On the other hand, only the rapid dissociation process was observed in polar solvents. Although the real nature of the nonrelaxed dissociating state is not very clear at the present stage of investigation, it seems to be an encounter complex immediately after the electron transfer.

2. Solvent Dependence of the Quantum Yields of Ionic Photodissociation. The quantum yield of dissociation of the present excited EDA systems depends significantly on the nature of solvents. This fact was confirmed by measuring transient absorption spectra as well as the laser-induced photocurrent. The transient spectra of the TCNB–toluene complex are characterized by the TCNB anion band at 462 nm,[13,14] and the solvent effect was examined by changing the volume ratio of toluene to dichloromethane, as given in Figure 2. The optical density decreases as the volume percentage of toluene increases. The observed relationship between the absorbance of ions and the dielectric constant (ϵ) of solvents is given in Figure 3, calculating ϵ values of mixed solvents by using the equation, $\epsilon_{mix} = a\epsilon_{toluene} + b\epsilon_{solvent}$. Coefficients a and b represent the volume fraction of toluene and the solvent, respectively. Similar results for the TCNB–toluene complex in various solvents are also shown in Figure 3, where the volume ratio of toluene was fixed at 5%. Curves A and B are similar in shape, except that they have different slopes.

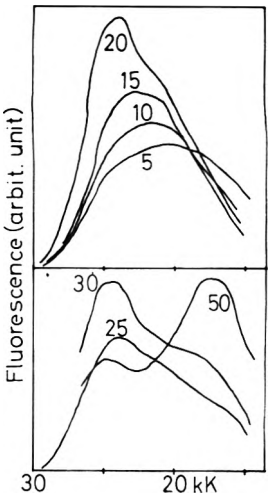

Figure 1. Corrected fluorescence spectra of the TCNB–toluene–dichloromethane system. The concentration of TCNB was adjusted to give an almost constant absorbance (~1.0) of the CT band at 350 nm, which is an excitation wavelength. Numbers in the figure represent the volume percent of toluene.

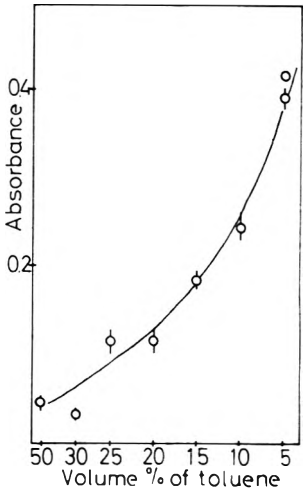

Figure 2. Dependence of ionic photodissociation of the TCNB–toluene–dichloromethane system on the solvent composition. The vertical scale represents the absorbance of ion radical bands at 100 nsec after excitation: (O) at 462 nm of TCNB anion. The sample solutions were the same as used in Figure 1.

Ionic dissociation of the pyrene system quenched by DMA was investigated by transient photocurrent measurements.[15] Since the photocurrent shows a rapid rise in the nanosecond time region and a slow decay in the microsecond time region,[1] the peak value is deemed to be proportional to the concentration of the initially produced ions. The relationship between the concentration of the ions produced and ϵ is given in Figure 4. Since in moderately polar solvents the ion radicals are produced via two states, the maximum peak photocurrent value attained after the slow rise process and the value obtained immediately after

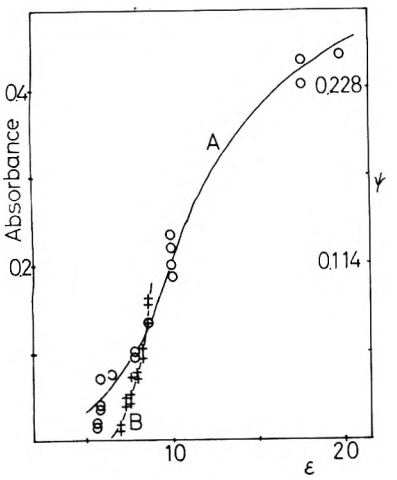

Figure 3. Solvent dependence of quantum yields of ionic photodissociation of the TCNB–toluene complex. The vertical line represents the absorbance of the TCNB anion band as well as the quantum yields (see text). The volume percent of toluene was fixed at 5 (A). The solvent composition was varied in the case of TCNB–toluene–dichloromethane systems (B). The concentration of TCNB was adjusted to give an almost constant absorbance of the CT band.

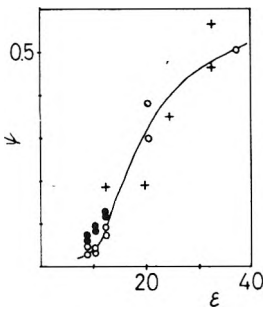

Figure 4. Solvent dependence of quantum yields of ionic photodissociation of the pyrene–DMA system. The concentrations of pyrene and of DMA are 5×10^{-4} and 8×10^{-2} *M*, respectively. Since oscillograms in dichloromethane, 1,2-dichloroethane, and pyridine show both rapid and slow formations of ion radicals, maximum yield (O) and the yield obtained immediately after excitation (●) are given in the figure. The values in alcohols were also shown (+).

laser excitation are both plotted in Figure 4. The obtained S-shaped curve is similar to those in Figure 3.

3. Linear Relations between log $[(1/\psi) - 1]$ *and* $1/\epsilon$ *or between log* $1/\psi$ *and* $1/\epsilon$. In the first place, the absolute quantum yield of ionic photodissociation was determined for the TCNB–toluene–acetone system (5% volume ratio of toluene) by the same method as used before.[2b] The value of the molar extinction coefficient of the TCNB anion band at 460 nm was assumed to be 1×10^4. The number of photons per exciting pulse was 1×10^{17} which was the same value as measured before.[2b] The quantum yield in acetone was 0.26, from which all ionic photodissociation yields of TCNB complexes have been evaluated by comparing the absorbance of the ion band. For the pyrene–DMA system, we have used the absolute yield in acetonitrile solution determined by Taniguchi et al. as a standard.[16] The significant figures of calculated quantum yields are one or two, which are ascribed to the fluctuations of the output of the exciting pulse and to a low S/N ratio in the fast kinetic spectroscopy. All results are listed in Tables I–III. Using these values,

TABLE I: Quantum Yields of Ionic Photodissociation and Free Energies of the TCNB–Toluene Complex in Various Solvents

Solvents	ϵ	ϵ_{mix}	ψ	ΔF ($A_s^- + D_s^+$), eV	ΔF ($A_s^- \cdots D_s^+$), eV
Ethyl acetate	6.02	5.84	0.03	3.38	3.02
Methyl acetate	6.68	6.47	0.04	3.30	3.00
Tetrachloroethane	8.20	7.91	0.05	3.19	2.93
Dichloromethane	8.93	8.60	0.07	3.15	2.91
1,2-Dichloroethane	10.36	9.96	0.11	3.08	2.88
Methyl ethyl ketone	18.5	17.69	0.23	2.90	2.79
Acetone	20.7	19.78	0.26	2.88	2.77

TABLE II: Quantum Yields of Ionic Photodissociation and Free Energies of the TCNB–Toluene–Dichloromethane System

Toluene, vol %	ϵ_{mix}	ψ	$\Delta F(A_s^- + D_s^+)$, eV	$\Delta F(A_s^- \cdots D_s^+)$, eV
5	8.601	0.07	3.15	2.91
10	8.274	0.04	3.17	2.92
15	7.946	0.03	3.19	2.93
20	7.619	0.02	3.21	2.94
25	7.291	0.02	3.23	2.95
30[a]	6.964	0.01	3.26	2.96
50[a]	5.654	0.01	3.39	3.03

[a] In this case dual fluoresence spectra were observed and the situation is different from the case of low percentage of toluene. See text.

TABLE III: Quantum Yields of Ionic Photodissociation and Free Energies of the Pyrene–*N,N*-Dimethylaniline Exciplex System in Various Solvents

Solvent	ϵ	ψ	ΔF ($A_s^- + D_s^+$), eV	ΔF ($A_s^- \cdots D_s^+$), eV
Acetonitrile	37.5	0.5	2.86	2.80
Acetone	20.7	0.34	2.95	2.86
Pyridine	12.3	0.08	3.08	2.92
1,2-Dichloroethane	10.4	0.04	3.15	2.95
Dichloromethane	9.08	0.03	3.20	2.98

the following linear relations between log $[(1/\psi) - 1]$ and $1/\epsilon$ was found:

$$\log\left(\frac{1}{\psi} - 1\right) = \frac{p}{\epsilon} + q \qquad (1)$$

where p and q are constants independent of ϵ. The results on TCNB–toluene and pyrene–DMA systems are given in Figures 5 and 6, respectively. In the case of the pyrene–DMA system a straight line is obtained using the values obtained immediately after excitation. If the value of the maximum yield is used, there arises a deviation from the straight line. Moreover, we have reexamined our previous data on TCNB complexes (Table IV)[2b,c,15] and the same relation was obtained as indicated in Figure 7. A plot of log $1/\psi$ vs. $1/\epsilon$ was also examined and it was shown that the lin-

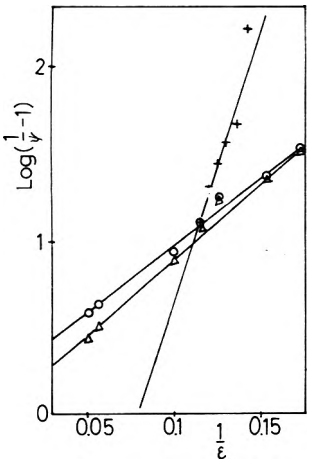

Figure 5. The relations between log $[(1/\psi) - 1]$ and $1/\epsilon$ (O) or between log $1/\psi$ and $1/\epsilon$ (Δ) for the TCNB–toluene complex in some solvents. In the case of the TCNB–toluene–dichloromethane system (+) the difference between the two plots cannot be recognized.

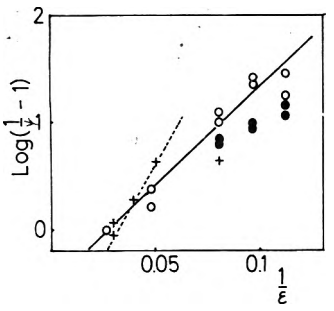

Figure 6. The relation between log $[(1/\psi) - 1]$ and $1/\epsilon$ for the pyrene–DMA system. The solid line is expected for values obtained immediately after excitation (O). The dashed line holds for the systems in alcohols (+). There is a systematic deviation from the straight line, if the value (●) of the maximum yield instead of the values immediately after the excitation are used for moderately polar solvents.

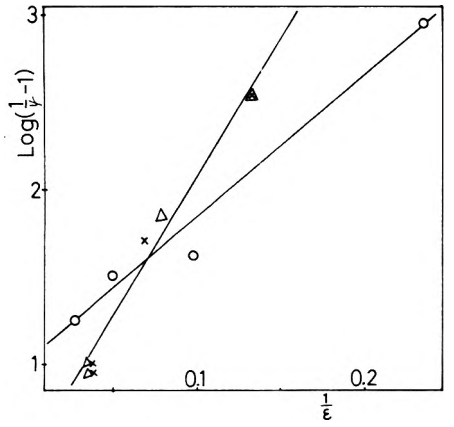

Figure 7. The relation between log $[(1/\psi) - 1]$ and $1/\epsilon$ for some TCNB complexes. Almost the same relation was obtained between log $1/\psi$ and $1/\epsilon$. The donors are naphthalene (O), toluene (X), and benzene (Δ). Data in ref 2 are reexamined.

ear relationship of eq 1′ holds almost equally as well for all of these systems.

$$\log \frac{1}{\psi} = \frac{p'}{\epsilon} + q' \qquad (1')$$

TABLE IV: Quantum Yields of Ionic Photodissociation of Some TCNB Complexes

Systems	Solvents	ϵ	ψ
TCNB–naphthalene	Ether	4.34	0.001
	1,2-Dichloroethane	10.36	0.024
	Butyronitrile	20.3	0.031
	Acetonitrile	37.5	0.053
TCNB–toluene[b]	1,2-Dichloroethane	7.7[a]	0.003
	Acetone	14.6[a]	0.019
	Acetonitrile	25.8[a]	0.1
TCNB–benzene[b]	1,2-Dichloroethane	7.7[a]	0.003
	1-Methylethyl alcohol	13.0[a]	0.014
	Acetonitrile	25.8[a]	0.1

[a] Calculated dielectric constant, using the same equation as given in the text. [b] The volume ratio of donor vs. solvent was 1:2.

Discussion

1. Free Energy Consideration. Ionic dissociation may be possible when the free energy of the final ionic states is lower than that of the initial dissociative state. The free energy of ion and ion-pair states in various solvents has been estimated for the present excited EDA systems according to the usual formula.[1,16,17] The values obtained are listed in Tables I–III and schematically shown in Figure 8, which can qualitatively explain the present ϵ dependence of the quantum yield shown in Figures 3 and 4. The yield increases as the free energy of ions as well as ion pairs becomes lower. The rather significant decrease of energy in the region of moderate polarity ($\epsilon = 5 \sim 10$) seems to correspond to the appreciable change of the yields in this range of solvent polarity. However, only slight change is observed in energy from 1,2-dichloroethane to acetone and acetonitrile, although the yield increases to some extent. This result will be explained in terms of the following theoretical considerations.

2. Theoretical Considerations. Empirically obtained eq 1 and 1′ are now discussed from the viewpoints of three different theories. The first is based on the usual molecular mechanism of primary processes of excited EDA systems. Since the yield of the transient ions produced is less than unity, other deactivation processes undoubtedly compete with ionic dissociation. It is reasonable to divide primary processes of the dissociative excited state into ionic dissociation (with rate constant of k_i) and other quenching mechanisms (with k_q). The latter includes internal conversion and intersystem crossing processes and is now assumed to be independent of ϵ. The yield of dissociation is given as follows:

$$\psi = k_i/(k_i + k_q) \qquad (2)$$

The unimolecular rate constant k_i, of course, depends upon solvent polarity and may be written as

$$k_i = Z \exp(-E/RT) \qquad (3)$$

Here Z, E, and R represent the frequency factor, activation energy, and gas constant, respectively. Although we have no information on E, its change may be correlated with that of the free energy of initial and final states. In the present case, the initial state of the dissociation process of TCNB complexes is the excited CT singlet state nonrelaxed with regard to solvation. The dissociative state of the

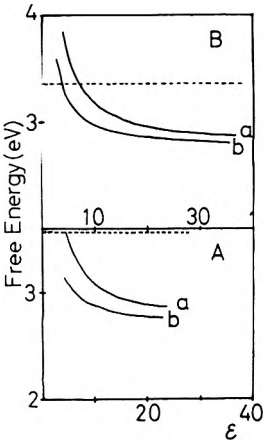

Figure 8. Calculated free energies of ion radical (a) and ion-pair (b) states: (A) TCNB–toluene (5% volume); (B) pyrene–DMA. Dashed lines represent the energy of the dissociative states.

pyrene–DMA exciplex system is the encounter complex, which is isoenergetic with the excited pyrene. It is easily recognized that the free energy of the initial state is almost constant in various solvents while the energy of the final ion radical state is strongly dependent upon ϵ. The energy of ion radicals as well as ion pairs can be written in the following form:[16,17]

$$F_{ion} = (A/\epsilon) + B \tag{4}$$

where A and B are constants irrelevant of the solvent polarity. The change of this energy with static dielectric constant (from ϵ^0 to ϵ) is given by

$$\Delta F_{ion} = A(1/\epsilon^0 - 1/\epsilon) \tag{5}$$

Using the following Horiuchi–Polanyi's relation for the activation energy:[18]

$$\Delta E = \alpha \Delta F_{ion} \qquad 0 < \alpha < 1 \tag{6}$$

the ratio of the rate constants of dissociation may be written as

$$k_i(\text{in } \epsilon)/k_{i0}(\text{in } \epsilon^0) = \exp(\alpha \Delta F_{ion}/RT) \tag{7}$$

Equations 5 and 7 lead to the following expression for k_i:

$$k_i = k_{i0} \exp(\alpha A/RT\epsilon^0) \exp(-(\alpha A/RT)(1/\epsilon)) \tag{8}$$

Using eq 2 and 8, theoretical relation 9 between ψ and ϵ can be derived easily.

$$\log((1/\psi) - 1) = \log k_q - \log k_{i0} - (\alpha A/2.303RT\epsilon^0) + (\alpha A/2.303RT)(1/\epsilon) \tag{9}$$

Only the last term depends upon ϵ and empirical rule of eq 1 is now theoretically verified.

The second theoretical consideration is based on Onsager's ion recombination model[19] and on its extensions by Mozumder.[20] This model has been applied to radiation-physical and -chemical problems and fruitful results have been obtained. However, applications of this theory to photochemical primary processes seem to be quite scarce.[21] According to Onsager's model, it is reasonable to assume that the ionic dissociation process of the present systems consists of two steps. The first is the production of geminate ion pairs of donor cation and acceptor anion with the distance r_0. The second are their recombination and separation, which compete with each other through the mutual coulomb force. The escape of ions from this field determines the quantum yield of ionization or ionic dissociation.

TABLE V: Calculated Distance of the Ion Pair According to Onsager's Ion Recombination Model

(1) TCNB–Toluene (5% Volume Ratio) Systems

Solvent	ϵ	ϵ_{mix}	r_c, Å	r_0,[a] Å	r_0',[b] Å
Ethyl acetate	6.02	5.8	92.3	23.9	29.1
Methyl acetate	6.68	6.46	83.0	26.2	33.5
Dichloromethane	8.20	8.60	67.8	26.5	36.4
1,2-Dichloroethane	10.36	9.96	53.6	25.1	37.1
Acetone	20.7	17.7	26.8	20.1	41.9

(2) TCNB–Toluene–Dichloromethane Systems

Toluene, vol %	ϵ_{mix}	r_c, Å	r_0,[a] Å	r_0',[b] Å
5	8.602	65	28.3	40.4
10	8.274	67	22.2	28.8
15	7.946	70	21.0	26.5
20	7.619	73	20.2	24.9
25	7.291	77	19.8	24.2

(3) Pyrene–DMA Systems

Solvents	ϵ	r_c, Å	r_0,[a] Å	r_0',[b] Å
Dichloromethane	8.20	67.8	24.7	33.3
1,2-Dichloroethane	10.36	53.6	23.1	32.9
Pyridine	12.3	45.5	21.4	31.8
Acetone	20.7	26.8	22.4	52.5
Acetonitrile	37.5	14.8	21.2	(~3000)

[a] r_0 was calculated with eq 10, using ψ and assuming $\alpha = 1$. [b] r_0' was calculated with eq 10, using ψ and assuming $\alpha = 0.5$.

Now, we examine the ionic photodissociation of EDA systems by means of Onsager's model.[22] Although the cage effect is omitted in this model, this effect on dissociation may not be neglected. Moreover, it seems probable that other processes such as relaxation to the ground as well as fluorescent states compete with the formation of the ion pair in question.[2,4] Therefore it is assumed that the fraction α of the dissociative state is converted into the geminate ion pair with distance r_0, which is followed by recombination and separation. α is of course smaller than unity and is assumed to be independent of the static dielectric constant. The quantum yield of ionic photodissociation, therefore, may be written as follows:

$$\psi = \alpha \exp(-r_c/r_0) \tag{10}$$

r_c is called the Onsager length and equal to $e^2/\epsilon KT$. The modified form of eq 10 is

$$\log(1/\psi) = -\log \alpha + (e^2/2.303r_0kT)(1/\epsilon) \tag{11}$$

Hence, the linear relation between $\log(1/\psi)$ and $1/\epsilon$ is expected from this model and the experimental results are consistent with the present consideration.

The validity of this theory was numerically examined, assuming that α is equal to unity or to one-half. Using r_c values and obtained quantum yields, r_0 values in various solvents were calculated. The results are listed in Table V. In general, the distance between the cation and the anion diffusing during an exciting pulse can be roughly estimated

from the simple diffusion theory, and is almost equal to $(D\tau)^{0.5}$. D is the diffusion coefficient and τ is the duration of an exciting pulse. As in the case of most organic solvents D is about 10^{-5} cm^2/sec, and τ is 10 nsec, the several tens of ångströms is calculated for $(D\tau)^{0.5}$. This value is in the same order as the values of r_0 estimated from the observed dissociation yields. In the case of TCNB–toluene (5%) and pyrene–DMA systems with $\alpha = 1$, the r_0 value is almost constant independent of solvent. However, r_0 increases with ϵ in other cases. Although these examinations are still rough, the present treatment of dynamics of ionic photodissociation seems promising.

The third one is based on the phenomenological theory of reaction rates.[23] The reaction rates are in general correlated with phenomenological laws of various macroscopic processes which have been established experimentally. The rate with which two ionic molecules can come together and dissociate is determined with Fick's law, including electrostatic interactions. The rate of dissociation is given as

$$k_i = (8\pi De^2/\epsilon kT\Delta V)(1 - \exp(-e^2/\epsilon kTx))^{-1} \quad (12)$$

where D, ΔV, and x represent the diffusion coefficient, the volume containing the dissociative EDA complex, and the sum of the radii of the donor cation and the acceptor anion, respectively. Other competing quenching processes with ionic dissociation were also assumed to be independent of ϵ. Then the quantum yield of ionic dissociation can be derived as follows:

$$\psi = k_i/(k_i + k_q) = G/(G + k_q\epsilon(1 - \exp(-B/\epsilon))) \quad (13)$$

Here G and B are constants irrelevant of ϵ. Empirical rules of eq 1 and 1′ cannot be derived from eq 13.

3. Dissociation from the Excited State Nonrelaxed with Respect to Solvent Orientation. As mentioned in the Results, the direct demonstrations on the dissociation from the nonrelaxed states were given in the case of the pyrene–DMA exciplex in moderately polar solvents. Although no such direct experimental proof was possible in the case of strongly polar solvents, the same dissociation mechanism may be suggested from the following reasons. (1) A linear relationship between log $[(1/\psi) - 1]$ and $1/\epsilon$ holds only when the yields obtained immediately after excitation were used. From the first theory this linear relation means that the same mechanism of ionic photodissociation is expected in all solvents. Namely, ionic photodissociation in polar solvents also occurs from the nonrelaxed state. (2) It should be noted that the present experimental results cannot be verified with the phenomenological law of reaction rates, but can be with Onsager's ion recombination model. The phenomenological laws are derived by assuming Fick's diffusion theory, which means that the reaction rate is determined by the diffusion in the thermalized system. On the other hand, Onsager's model may include the nonrelaxed (nonthermalized) state as initial dissociative and geminate ion-pair states, shown concretely by Mozumder.[19,20] Therefore, the present result might be ascribed to the fact that the produced ions begin to diffuse with excess energy, which is equal to the energy difference between the dissociative and final ion radical states.

4. Another Explanation for the Mixed Solvent System. In the case of the TCNB–toluene–dichloromethane system, the dissociation yield depends considerably upon solvent composition, even though the change in dielectric constant is small. Although the general relation of log $[(1/\psi) - 1]$ vs. $1/\epsilon$ holds in this case, another possible explanation for this result is to assume solvent sorting, which leads to a cybotactic region with a composition different from that of the bulk solvent. In connection with the latter problem, the results listed in Table II were reexamined. Assuming that the k_i value in eq 2 is irrelevant to the solvent composition and that the quenching is induced by excess toluene molecules, the dependence of the dissociation yield on the deactivation process may be given by

$$(1/\psi) - 1 = k_q/k_i = k_0[\text{toluene}]^n/k_i \quad (14)$$

The plot of log $((1/\psi) - 1)$ vs. log [toluene] is given in Figure 9, which gives the slope of 0.8. This result seems to indicate that the interaction of the excited complex with another toluene molecule leads to unknown degradation. Such a molecular analysis of mixed solvent systems will give a clue for the elucidation of the solvent sorting phenomena, whose entire picture is not clear at present.

5. Empirical Parameters of Solvent Polarity. Until now, the solvent effect on ionic photodissociation has been specified by the dielectric constant of the solvent in the present

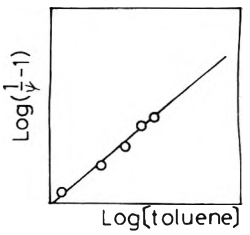

Figure 9. The relation between log $[(1/\psi) - 1]$ and log [toluene] for the TCNB–toluene–dichloromethane system.

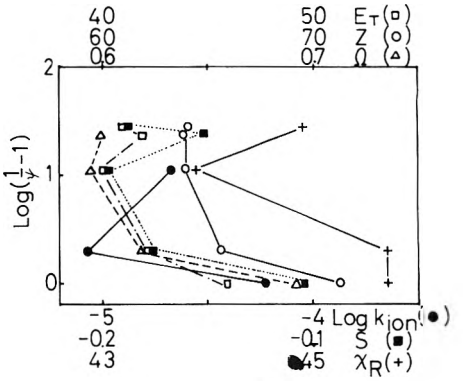

Figure 10. The relation between log $[(1/\psi) - 1]$ and some polarity parameters for the pyrene–DMA system in aprotic solvents.

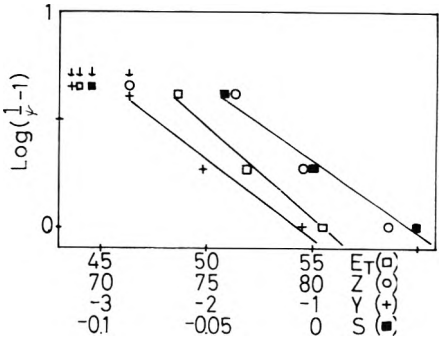

Figure 11. The relation between log $[(1/\psi) - 1]$ and some polarity parameters for the pyrene–DMA system in alcoholic solvents. The points with arrows represent the parameters of *tert*-butyl alcohol.

work. However, for a real understanding of the observed relationship between ψ and ϵ, which seems to represent an average over individual solute–solvent molecular interactions, studies from a more molecular viewpoint may be necessary. Comprehensive measure of the polarity of a solvent has been given by empirical parameters, which was obtained by examining the standard chemical process in various solvents and by regarding the latter process as probes for the solvent effect. E_T, Z, Y, S, log k_{ion}, Ω, and X_R values are usually used for this subject.[24] All of these parameters were derived from the reaction rate constants or absorption maxima of some specific molecules in various solvents, and good linear relations between these values were confirmed. All of these parameters except log k_{ion} are linear to the logarithm of the rate of the probe reaction process. In the present work, we have examined a plot of log $[(1/\psi) - 1]$ vs. polarity parameter for the pyrene–DMA system, since $[(1/\psi) - 1]$ is correlated with the rate constant of ionic photodissociation. The results in aprotic solvents and in alcoholic solvents are given in Figures 10 and 11, respectively. In aprotic solvents no linear relation was found, which shows that the role of the solvent in ionic dissociation is different from that in the above-mentioned standard chemical processes. On the other hand, a good linear relation was obtained for methanol, ethanol, and 2-propanol solvents.[25] As shown in Figure 6, linear relations between log $[(1/\psi) - 1]$ and $1/\epsilon$ were confirmed both in alcohols and in aprotic solvents. However, their slopes are different from each other. These results may show that ionic photodissociation in alcohols is influenced not only by the static dielectric constant but also by the comprehensive polarity of solvent.

In any case, there is a good linear relation between log $[(1/\psi) - 1]$ and $1/\epsilon$, in spite of the macroscopic (bulk) nature of the dielectric constant. Since the dissociative state of the present EDA systems is quite polar, the solvent effect may be due to pure solvation process to relaxed ion radical states, and this solvation effect seems to be well explained in terms of the dielectric constant ϵ.

References and Notes

(1) (a) Y. Taniguchi, Y. Nishina, and N. Mataga, *Bull. Chem. Soc. Jpn.*, **45**, 764 (1972); (b) Y. Taniguchi and N. Mataga, *Chem. Phys. Lett.*, **13**, 596 (1972).

(2) (a) H. Masuhara, M. Shimada, and N. Mataga, *Bull. Chem. Soc. Jpn.*, **43**, 3316 (1970); (b) H. Masuhara, M. Shimada, N. Tsujino, and N. Mataga, *ibid.*, **44**, 3310 (1970); (c) M. Shimada, H. Masuhara, and N. Mataga, *ibid.*, **46**, 1909 (1973); (d) M. Shimada, H. Masuhara, and N. Mataga, *Chem. Phys. Lett.*, **15**, 364 (1972).

(3) H. Leonhardt and A. Weller, *Ber. Bunsenges. Phys. Chem.*, **67**, 791 (1963); H. Knibbe, D. Rehm, and A. Weller, *ibid.*, **72**, 257 (1968); K. H. Grellmann, A. R. Watkins and A. Weller, *J. Lumin.*, **1, 2**, 678 (1970); K. H. Grellmann, A. R. Watkins, and A. Weller, *J. Phys. Chem.*, **76**, 469, 3132 (1972); H. Schomburg, H. Staerk, and A. Weller, *Chem. Phys. Lett.*, **21**, 433 (1973); T. Okada, H. Oohari, and N. Mataga, *Bull. Chem. Soc. Jpn.*, **43**, 2750 (1970); H. Yamashita, H. Kokubun, and M. Koizumi, *ibid.*, **41**, 2312 (1968); K. Kawai, N. Yamamoto, and H. Tsubomura, *ibid.*, **42**, 369 (1969); O. D. Dmitriefski and A. N. Terenin, *Dokl. Akad. Nauk SSSR*, **151**, 122 (1963).

(4) C. R. Goldschmidt, R. Potashnik, and M. Ottolenghi, *J. Phys. Chem.*, **76**, 1133 (1972); N. Orbach, J. Novros, and M. Ottolenghi, *ibid.*, **77**, 2831 (1973); M. Ottolenghi, *Acc. Chem. Res.*, **6**, 153 (1973).

(5) Y. Taniguchi, Y. Nishina, and N. Mataga, *Bull. Chem. Soc. Jpn.*, **46**, 1646 (1973); M. Irie, H. Masuhara, N. Mataga, and K. Hayashi, *J. Phys. Chem.*, **78**, 341 (1974); M. Irie, S. Tomimoto, and K. Hayashi, *ibid.*, **76**, 1419 (1972); Y. Shirota, K. Kawai, N. Yamamoto, K. Tada, T. Shida, H. Mikawa, and H. Tsubomura, *Bull. Chem. Soc. Jpn.*, **45**, 2683 (1972); M. Yamamoto, M. Ohoka, K. Kitagawa, S. Nishimoto, and Y. Nishijima, *Chem. Lett.*, 745 (1973).

(6) R. F. Bartholomew, R. S. Davidson, P. F. Lambeth, J. F. Mckellar, and P. H. Turner, *J. Chem. Soc., Perkin Trans. 2*, 577 (1972); S. Arimitsu and H. Masuhara, *Chem. Phys. Lett.*, **22**, 543 (1973); S. Arimitsu, H. Masuhara, N. Mataga, and H. Tsubomura, submitted to *J. Phys. Chem.*

(7) T. Imura, T. Furutsuka, H. Sasai, and K. Kawabe, to be submitted for publication.

(8) D. F. Ilten and M. Calvin, *J. Chem. Phys.*, **42**, 3760 (1965); R. M. Haines, A. Pryce, and L. Shields, *J. Chem. Soc. B*, 820 (1970).

(9) F. E. Stewart, M. Eisner, and W. R. Carper, *J. Chem. Phys.*, **44**, 2866 (1966); F. E. Stewart and M. Eisner, *Mol. Phys.*, **12**, 173 (1967); R. Potashink, C. R. Goldschmidt, and M. Ottolenghi, *J. Phys. Chem.*, **73**, 3170 (1969); Y. Achiba, S. Katsumata, and K. Kimura, *Chem. Phys. Lett.*, **13**, 213 (1972); Y. Achiba, S. Katsumata, and K. Kimura, *Bull. Chem. Soc. Jpn.*, **45**, 1272 (1972); Y. Achiba and K. Kimura, *Chem. Phys. Lett.*, **19**, 45 (1973); K. Kimura, Y. Achiba, and S. Katsumata, *J. Phys. Chem.*, **77**, 2520 (1973); Y. P. Pilette and K. Weiss, *ibid.*, **75**, 3805 (1971).

(10) We have studied the electronic structure of TCNB complexes in the fluorescent state in detail. The $S_n \leftarrow S_1$ spectra of a toluene solution of TCNB (corresponding to a very high concentration system) can be reproduced by the superposition of the bands of acceptor anion and donor dimer cation. We have concluded from this fact the formation of a 2:1 ($D_2^+A^-$) complex in the fluorescent state. On the other hand, the fluorescent state in a rigid toluene matrix or of low toluene concentration system was concluded to be 1:1 (D^+A^-) complex. See, N. Tsujino, H. Masuhara, and N. Mataga, *Chem. Phys. Lett.*, **21**, 301 (1973).

(11) The problem of electronic structure of the TCNB–toluene complex was summarized in H. Masuhara and N. Mataga, *Chem. Phys. Lett.*, **22**, 305 (1973).

(12) K. Egawa, N. Nakashima, N. Mataga, and C. Yamanaka, *Bull. Chem. Soc. Jpn.*, **44**, 3287 (1971).

(13) It is well known that for excited EDA complexes the $S_n \leftarrow S_1$ spectra can also be reproduced by the superposition of the spectra of the donor cation and acceptor anion. However, the behavior is different from that of the spectra due to dissociated ions.

(14) For $S_n \leftarrow S_1$ spectra, see H. Masuhara and N. Mataga, *Chem. Phys. Lett.*, **6**, 608 (1970); H. Masuhara and N. Mataga, *Z. Phys. Chem. (Frankfurt am Main)*, **80**, 113 (1972); H. Masuhara, N. Tsujino, and N. Mataga, *Bull. Chem. Soc. Jpn.*, **46**, 1088 (1973); R. Potashnik and M. Ottolenghi, *Chem. Phys. Lett.*, **6**, 525 (1970); R. Potashnik, C. R. Goldschmidt, M. Ottolenghi, and A. Weller, *J. Chem. Phys.*, **55**, 5344 (1971).

(15) In previous works,[1,2] an erroneous equation was used. In the present paper, we have reevaluated the concentrations of ions produced according to the equation $i(t) = en(t)(\mu_{anion} + \mu_{cation})E_{app}$. The error was kindly pointed out by Dr. D. Goodall, to whom the authors are indebted.

(16) Y. Taniguchi, Ph.D. Thesis, Osaka University, 1972.

(17) K. A. Zachariasse, Ph.D. Thesis, Free University, Amsterdam, 1972.

(18) S. Glasstone, K. J. Laidler, and H. Eyring, "The Theory of Rate Processes", McGraw-Hill, New York, N.Y., 1941, p 145.

(19) A. Mozumder in "Advances in Radiation Chemistry", Vol. 1, M. Burton and J. L. Magee, Ed., Wiley-Interscience, New York, N.Y., 1969, p 83.

(20) A. Mozumder, *J. Chem. Phys.*, **48**, 1659 (1968); **50**, 3153, 3162 (1969).

(21) The ultraviolet photoejection of electrons from ferrocyanide was analyzed by the Mozumder equation. See M. Shirom and M. Tomkiewicz, *J. Chem. Phys.*, **56**, 2731 (1972).

(22) Although the time-dependent dielectric constant is taken into consideration, an effective one is used for the actual formulation in Mozumder's theory. In the present work, it is assumed that the effective dielectric constant is equal to the static one, since the diffusion coefficients in the nonrelaxed state of the medium is not well known. Therefore the Mozumder's equation becomes identical with that of Onsager, with which the present experimental results are analyzed.

(23) I. Amdur and G. G. Hammes, "Chemical Kinetics Principles and Selected Topics", McGraw-Hill, New York, N.Y., 1966.

(24) M. Senoo and T. Arai, "Solvent Effects in Organic Chemical Reactions" (in Japanese), Sangyotosyo, Tokyo, 1970; E. M. Kosower, "An Introduction to Physical Organic Chemistry", Wiley, New York, N.Y., 1968; C. Reichardt, *Angew. Chem., Int. Edit., Engl.*, **4**, 29 (1965).

(25) In *tert*-butyl alcohol the yield is larger than the value expected from dielectric constant or from solvent polarity parameters. The reason for this deviation is not clear.

Contact Ion Pairing of the Perchlorate Ion. A Chlorine-35 Nuclear Magnetic Resonance Study. I. Solutions in Pure Solvents

Harvey Alan Berman and Thomas R. Stengle*

Department of Chemistry, University of Massachusetts, Amherst, Massachusetts 01002 *(Received September 5, 1974)*

The NMR relaxation time (T_2) of the ^{35}Cl nucleus has been used to study the ion pairing behavior of the perchlorate ion. Free ClO_4^- in solution has a long relaxation time compared with a perchlorate ion in a contact ion pair. This is caused by quadrupolar relaxation, and it is observed by its effect on the NMR line width. The tendency of ClO_4^- to form contact ion pairs has been studied as a function of cation and solvent. Factors favoring contact ion pairing are high charge to radius ratio of cation, low dielectric constant of solvent, and low basic strength (measured by Gutmann's donor number) of solvent.

Introduction

Electrolytes in solution often exist as complex mixtures of several species: solvated ions, solvent-separated ion pairs, contact ion pairs, and more complex ion aggregates. Since the rates of chemical reactions are often affected by the state of aggregation of ions, it is important to have an understanding of the equilibrium among the many ionic species. A host of experimental methods has been developed to study ion association.[1] Electrical conductivity is an obvious approach, and it has been used to study a wide variety of solutions. However, this technique fails to distinguish between contact and solvent-separated ion association. In fact, this is a difficult distinction to make, and many of the classical methods fail at this point. To solve this problem it is necessary to study a parameter which is sensitive to the short range interactions between ions in intimate contact. Spectroscopic methods have proven to be a fruitful approach here.

The infrared and Raman spectra of polyatomic ions have been used to detect ion pair formation.[2] Recently nuclear magnetic resonance techniques have been developed to deal with the problem. For example, the NMR signal of a diamagnetic ion is affected by the presence of a paramagnetic counterion. The interaction is short ranged, and its effect has been used to study a number of systems.[3] In purely diamagnetic solutions, chemical shift methods can be used. The ^{23}Na chemical shift is sensitive to contact ion pairing,[4] and this technique has been widely applied. Here we report an NMR method based on the relaxation time of the ^{35}Cl nucleus in the perchlorate ion. This parameter is easily measured, and it reveals the presence of contact ion pairs, while it is insensitive to solvent-separated ion aggregation.

In the ^{35}Cl nucleus the interaction of the nuclear electric quadrupole moment with an electric field gradient provides an efficient mechanism of relaxation.[5] In almost every situation this mechanism predominates, and other relaxation pathways can be ignored. In the liquid state the extreme narrowing conditions apply, and the relaxation rates are given by

$$\frac{1}{T_1} = \frac{1}{T_2} = \frac{2\pi^2}{5h^2}\left(1 + \frac{\eta^2}{3}\right)(e^2Qq)^2\tau_c \qquad (1)$$

for a nucleus of spin $I = 3/2$. Here η is the asymmetry parameter, Q is the nuclear quadrupole moment, q is the electric field gradient at the nucleus, and τ_c is the correlation time for molecular reorientation. If the environment of the chlorine nucleus has cylinderical symmetry, the asymmetry parameter is zero. Relaxation times are especially sensitive to the electric field gradient, q. This field arises from the distribution of charge around the nucleus, i.e., the surrounding electrons and nearby nuclei. If a counterion comes into contact with a ClO_4^-, a large field gradient will be generated at the chlorine nucleus, and the relaxation rate will be greatly enhanced.

In our observations the shape of the ^{35}Cl resonance has been lorentzian. This implies that the relaxation rate is related to the line width by

$$\Delta\nu = 1/\pi T_2 \qquad (2)$$

where $\Delta\nu$ is the full width of the NMR line at half height. This relation affords a convenient method of measuring relaxation times, and it is customary to report data as line widths in hertz rather than as the relaxation times themselves.

The field gradient at the chlorine nucleus in the free gaseous perchlorate ion is zero because of the tetrahedral symmetry. When the ion is in solution, its solvation shell will not possess such high symmetry, and a small fluctuating field gradient will be generated. The gradient will not be large, because solvent molecules are disposed about the ion in a way which is approximately symmetrical. In solution the free ClO_4^- gives a ^{35}Cl signal which is only a few hertz wide.[6] The close approach of a counterion destroys the approximate symmetry of the solvation shell and generates a large field gradient at the chlorine nucleus. The result is a large ^{35}Cl line width when the ClO_4^- is in contact with a counterion. It is not uncommon for the line width to increase by a factor of 100 upon formation of contact ion pairs. The magnitude of the field gradient due to the counterion is strongly dependent on interionic distance; therefore, solvent-separated ion pairs yield a line broadening that is negligible when compared with the effect of ions in contact. These conclusions are borne out by a calculation based on a simple electrostatic model (cf. Discussion).

In extremely dilute solutions of perchlorate salts it is safe to assume that all of the ClO_4^- is free; the line width will be a few hertz due to ion–solvent interactions. In a more concentrated solution, contact ion pairs may form which will produce large line widths. Contact ion pairing

can be detected by examining the line width as a function of concentration. Unfortunately the sensitivity of the NMR experiment is low, and it is often not possible to obtain spectra at concentrations where only free ions are present. In such cases the line widths of concentrated solutions must be compared with data from solvents in which it is certain that contact ion pairs do not exist.

In making comparisons from one solvent to another (or from one concentration to another in the same solvent) we are primarily concerned with changes in the field gradient, q. However, changes in the correlation time will also affect the line width; a change in τ_c will tend to obscure the effect of a change in q. It is desirable to express the line width data in terms of a parameter which reflects changes in q without being affected by changes of τ_c. It is not possible to accomplish this rigorously, but an approximate quantity can be derived from a simple model. If τ_c is governed by the same factors which influence a sphere turning in a viscous liquid, it will be proportional to the viscosity of the solution.[5] The effect of τ_c will be removed if the line width is divided by the viscosity. This approach seems to be valid for some simple systems,[7,8] but there are cases where the macroscopic viscosity does not accurately reflect changes in τ_c.[9,10] In concentrated solutions, or in solutions of macromolecules, there is no clear way to separate the effects of τ_c and q.

In moderately concentrated salt solutions there can exist a number of distinct species which are in facile equilibrium with each other. Since the lifetime of an ion aggregate is short compared with the NMR time scale, only a single signal is observed. The relaxation time is the average of the relaxation times of the individual species weighted by their concentrations

$$\frac{1}{T_2} = \sum_i \frac{x_i}{T_{2i}} \tag{3}$$

where T_2 is the observed relaxation time, x_i is the mole fraction of ClO_4^- present in species i, and T_{2i} is the relaxation time in that species.

Experimental Section

Materials. All salts and solvents were of the highest purity available. The perchlorate salts were obtained from G. Frederick Smith Chemical Co., and they were used without further purification except for drying. Acetonitrile was purified and dried by a standard procedure;[11] ethanol was dried by distillation from magnesium turnings and iodine under nitrogen. The solvents were stored over molecular sieves in dark bottles.

The salt solutions were prepared directly before use by diluting a freshly prepared stock solution. A violent explosion occurred during the preparation of a solution of $Mg(ClO_4)_2$ in dimethyl sulfoxide at room temperature, and our results in this solvent are incomplete due to the hazardous nature of the system. The other perchlorate salts are also unstable in this solvent.

NMR Measurements. The ^{35}Cl spectra were observed with a Varian DP instrument operating at 4.3 MHz. Signals which had a width of less than 300 Hz were recorded as absorption spectra, and the line width at half height was measured directly. Broader signals were recorded as the first derivative of the absorption mode. The line width was derived from the peak to peak distance, d_{pp}, by assuming a lorentzian shape function, i.e., $\Delta\nu = \sqrt{3}d_{pp}$. Each measurement is the average of at least five determinations. The precision of the measurements varied with the width of the line in question. It ranged from 5% for line widths less than 500 Hz to 20% for line widths greater than 3000 Hz.

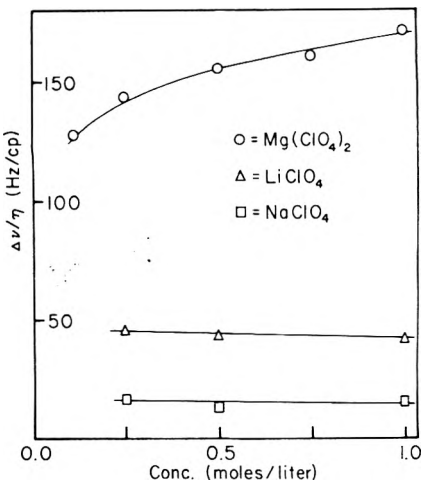

Figure 1. Line width of ^{35}Cl signal divided by viscosity for solutions of perchlorate salts in acetonitrile as a function of concentration.

The magnetic field inhomogeniety placed a lower limit of 5 Hz on the observed line width. In solutions containing only free perchlorate ion, the line width is expected to be quite small,[6] and the inhomogeniety limit was observed. In such cases the line width is reported as <5 Hz.

Conductance Measurements. Conductances were measured with a Beckman RC16B2 bridge operating at either 1000 or 60 Hz, depending on whether the sample had a high or a low conductance, respectively. The medicine dropper type cell (a = 2.21 cm^{-1}) was calibrated with 0.01 M KCl solution. The conductances of the pure solvents were negligible compared with the sample solutions.

Viscosity and Density Measurements. These measurements were made at 30°. Viscosity was determined in a Ubbelohde viscometer in which dilutions were allowed to be made. No kinetic energy corrections were made. Density measurements were made in 10- and 25-ml pycnometers.

Results

NMR Measurements. The essential NMR results are given in the tables. (A more complete listing of all the experimental data has been recorded elsewhere.[12]) Table I is a collection of line width data taken over a wide range of solvents. In all cases the concentration of the solute is constant at 0.5 M. Both the line width ($\Delta\nu$) in hertz and the "viscosity corrected" line width ($\Delta\nu/\eta$) in hertz per centipoise are recorded. The concentration dependence of the line width is presented for several systems in Table II. Here the lower limit was usually determined by the sensitivity of the spectrometer, while the upper limit was imposed by the solubility of the salt. Water is a notable exception. All three perchlorate salts are extremely soluble in water, but the line width is quite small for all the salts, and it is essentially independent of concentration, even to saturation.

Acetonitrile was selected as a typical solvent, and it was studied in some detail. The data are shown in Figure 1. Magnesium perchlorate exhibits the largest value of $\Delta\nu/\eta$ which reflects extensive contact ion association. Similar plots for other solvents are shown in Figure 2 where the data of Table II are illustrated. A remarkably wide range of values is observed. It is noteworthy that those solvents which give the highest $\Delta\nu/\eta$ values also show large negative

TABLE I: The ^{35}Cl Line Width for 0.5 *M* Solutions of Perchlorate Salts in Various Solvents

Solvent	ϵ_0	DN	$Mg(ClO_4)_2$		$LiClO_4$		$NaClO_4$	
			$\Delta\nu$, Hz	$\Delta\nu/\eta$, Hz/cP	$\Delta\nu$, Hz	$\Delta\nu/\eta$, Hz/cP	$\Delta\nu$, Hz	$\Delta\nu/\eta$, Hz/cP
Water	78.4	18.0	<5		<5	<5	<5	
Dimethyl sulfoxide	45.0	29.8	<5		<5		<5	
Dimethylacetamide	38.9	27.8	<5					
Dimethylformamide	36.1	26.6	<5		<5		<5	
Methanol	32.6	25.7	15	7	10	15	7	11
Acetonitrile	38.0	14.1	109	156	20	43	6	14
Acetone	20.7	17.0	138	200				
Ethanol	24.3	31.5	270	117	20	14	13	10
Propanol	20.1		1900	410	46	16	26	14
1-Butanol	17.7		3100	413	62	17	36	14
Ethyl acetate	6.0	17.1	1200	1500				

TABLE II: Concentration Dependence of the ^{35}Cl Line Width of $Mg(ClO_4)_2$ in Various Solvents

Concn, *M*	$\Delta\nu$, Hz	$\Delta\nu/\eta$, Hz/cP	Concn, *M*	$\Delta\nu$, Hz	$\Delta\nu/\eta$, Hz/cP
Acetone			Ethyl acetate		
1.00	210	124	1.35	3600	610
0.75	160	147	1.25	3000	698
0.50	138	200	0.96	2300	1100
0.25	128	291	0.75	2100	1615
0.125	128	346	0.48	1200	1520
Acetonitrile			0.24	850	1570
1.00	255	170	0.12	1000	2100
0.75	161	161	1-Butanol		
0.50	110	156	0.90	2000	100
0.25	72	144	0.67	3300	275
0.10	51	128	0.50	3100	413
Propionitrile			0.28	2900	660
1.00	800	420	0.14	3000	1000
0.50	326	375			
0.25	200	340			

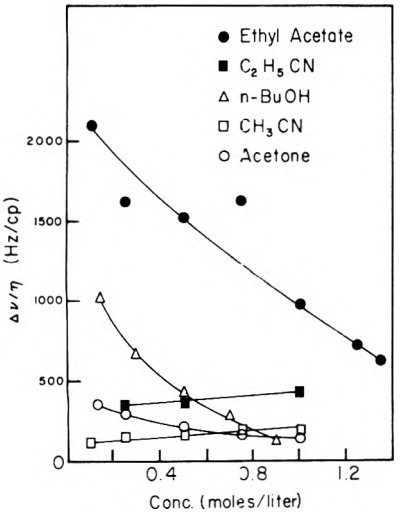

Figure 2. Line width of ^{35}Cl signal divided by viscosity for solutions of $Mg(ClO_4)_2$ in various solvents as a function of concentration.

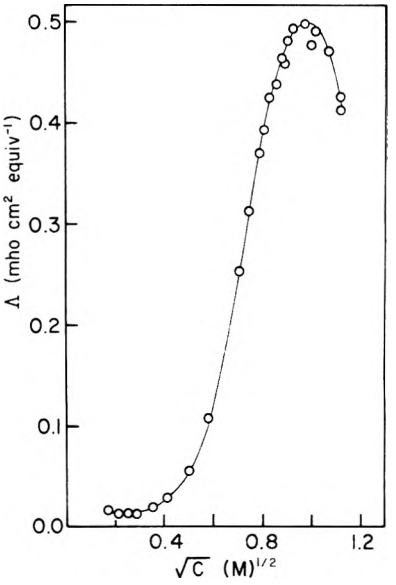

Figure 3. Equivalent conductance of $Mg(ClO_4)_2$ in ethyl acetate vs. (concentration)$^{1/2}$.

slopes, while the other solvents show smaller slopes which can be either positive or negative.

Conductance. Ethyl acetate is an especially interesting solvent since it has the lowest dielectric constant ($\epsilon_0 = 6$) of all materials studied. The line widths in this solvent are exceptionally large. To clarify the nature of $Mg(ClO_4)_2$ in this system, the equivalent conductance was measured as a function of concentration. The result is shown in Figure 3. The spectacular increase of the conductance at higher concentrations indicates the formation of ion aggregates more complex than the nonconducting species (ion triples).

Discussion

The NMR data indicate that there are three distinct classes of solvents. One group exhibits very small line widths which do not change appreciably with concentration. These solvents are water, dimethyl sulfoxide (DMSO), dimethylacetamide (DMA), and dimethylformamide (DMF). For the most part, line widths in these solvents are determined by the inhomogeniety limit. The solvents in this class are characterized by high dielectric constants and

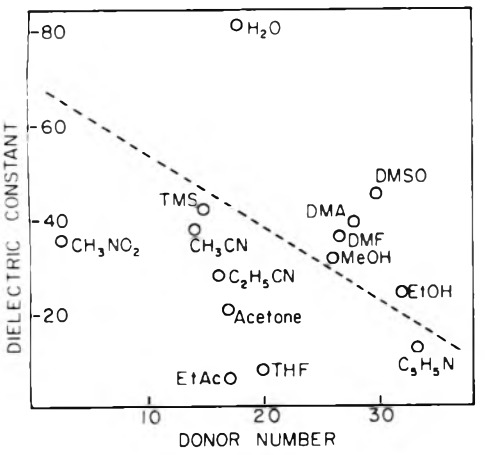

Figure 4. Dielectric constant vs. donor number diagram of various solvents. The dotted line divides solvents which promote contact ion association of $Mg(ClO_4)_2$ from those which inhibit it. (TMS = tetramethylenesulfone.)

high basic strengths as measured by Gutmann's donor number.[13] These factors prevent ion association. In the solvents studied here, the perchlorate ion is very weakly solvated compared with the cation. For contact ion association, a solvent molecule must be removed from the cation and replaced by a ClO_4^-. Solvents with high donor numbers are difficult to replace, and therefore, a high donor number (along with a high dielectric constant) inhibits ion association.

A second group of solvents is made up of propanol, butanol, and ethyl acetate. Here there is extensive contact ion association; the line widths are large, and they are concentration dependent. This behavior is apparent in Figure 2 which shows large negative slopes for this class. These solvents are characterized by very low dielectric constants, and they probably have moderate donor numbers. The donor numbers of the alcohols have not been reported.

The rest of the solvents (acetone, methanol, ethanol, acetonitrile, propionitrile) show intermediate line widths which are caused by an intermediate degree of ion association. These solvents are characterized by dielectric constants and donor numbers in the middle range. It is clear from these data that ion association is favored in solvents of low donor number and low dielectric constant. Similar conclusions have been recently reported by Popov and his coworkers[14] who made an extensive study of $LiClO_4$ ion pairing utilizing ^7Li and ^{35}Cl NMR.

The properties of all the solvents are summarized in Figure 4. Each point on the diagram corresponds to a particular solvent, and it is plotted according to its dielectric constant and donor number. The diagram is divided into two regions, one containing solvents which promote the ion association of $Mg(ClO_4)_2$, and one with solvents which inhibit it. Solvents lying close to the dividing line are intermediate cases, and $Mg(ClO_4)_2$ can exist as a mixture of several ionic forms in these media. The division of Figure 4 is valid only for the solute $Mg(ClO_4)_2$. Other salts will give rise to different dividing lines depending on the interplay of dielectric constant and basic strength.

As an example of an intermediate class solvent, acetonitrile was chosen for further study. The line width data for three perchlorate salts are displayed in Figure 1. The curve for $Mg(ClO_4)_2$ shows a slight concentration dependence with a positive slope. This can be interpreted in terms of enhanced contact ion association at higher concentrations in accordance with the law of mass action. The magnitude of $\Delta\nu/\eta$ would indicate that a significant fraction of the ClO_4^- ion is in contact with the Mg^{2+} at all concentrations.

In contrast with the $Mg(ClO_4)_2$ line width data, $NaClO_4$ has a quite small value of $\Delta\nu/\eta$, and it is independent of concentration. This indicates an absence of contact ion association, but it does not preclude the existence of solvent separated ion pairs. Evidence for this species is given by the conductance,[15] the infrared spectrum,[16] and the fact that the value of $\Delta\nu/\eta$ is larger in acetonitrile than in water. Apparently solvent-separated ion pairs do produce a slight electric field gradient at the chlorine nucleus.

The line width behavior of $LiClO_4$ is intermediate between the sodium and magnesium salts. Presumably $LiClO_4$ in acetonitrile exists as an equilibrium among free ions, solvent-separated ion pairs, and contact ion pairs. This view is supported by conductance data. The conductance of $LiClO_4$ in acetonitrile increases remarkably on the addition of a small quantity of water. This effect indicates the breakup of ion associated species. These results will be presented in a future publication.[17]

Ethyl acetate is an example of a solvent of low dielectric constant, and solutions of $Mg(ClO_4)_2$ in this medium present some unusual features. The slope of the ethyl acetate curve in Figure 2 is not in accord with the picture proposed for acetonitrile solutions based on the law of mass action. A likely explanation of the high $\Delta\nu/\eta$ values and the large negative slope proposes the existence of sizable ion aggregates containing more than three individual ions. Such aggregates would tumble slowly in solution; this would increase τ_c, and in turn lead to a larger value of $\Delta\nu/\eta$.

The conductance data presented in Figure 3 lend support to this hypothesis. The equivalent conductance of $Mg(ClO_4)_2$ is quite small in dilute solution, and it remains small up to a concentration of ca. 0.1 *M*. Beyond this point the conductance increases at a rapid rate to reach a maximum at ca. 1.0 *M*. This is reminiscent of the behavior of tetraisoamylammonium nitrate in tetrahydrofuran, a 1:1 electrolyte observed by Fuoss and Kraus.[18] In that system the increase in conductance was ascribed to the formation of ion triples. The parallel behavior of $Mg(ClO_4)_2$ in ethyl acetate is likely due to the formation of ion quadruples and higher aggregates. Similar higher aggregates of ions have been reported recently in solutions of nitrates in tetrahydrofuran by Wang and Hemmes.[19]

Ethyl acetate and butanol are the two solvents which exhibit anomalous behavior. Both the line widths and the viscosities are exceptionally high in these media. The negative slopes in Figure 2 indicate that τ_c is not proportional to the macroscopic viscosity in these systems. The correlation time is determined by the rates of translational and rotational diffusion of the ions. These rates can be described in terms of a microscopic viscosity which depends on short-range solute–solvent and solute–solute interactions. The macroscopic viscosity is affected by an additional factor: the obstruction to flow caused by large solute particles. This situation is frequently encountered in solutions of macromolecules where the correlation times are much shorter than would be predicted on the basis of macroscopic viscosity. The exceptionally high viscosities of the butanol and ethyl acetate solutions lend support to the conclusion that τ_c does not parallel viscosity in these cases.

It remains to demonstrate that the line width effects observed here are due to contact ion association and not sol-

vent-separated ions. This point could be easily resolved if it were possible to make a reliable calculation of the ^{35}Cl quadrupole coupling constant and the correlation time of a typical ion pair. Unfortunately this can not be done rigorously, but rough estimates can be obtained from a simple model. Assume that the Mg–Cl distance is 0.2 nm when the ClO_4^- is in contact with the Mg^{2+}. If the field gradient at the chlorine nucleus is due entirely to the point charge of the Mg^{2+}, the quadrupole coupling constant is $e^2qQ/h = 1.38 \times 10^6$ Hz. In a 1.0 *M* solution of $Mg(ClO_4)_2$ in acetonitrile, the chlorine line width is 25 Hz, and the viscosity is 0.0145 P. With this line width eq 1 gives a correlation time of 1.07×10^{-10} sec. This figure must be the lower limit for the lifetime of the associated species. If this species is taken as a sphere turning in a viscous liquid,[5] its radius is 0.42 nm. These figures are certainly plausible, but they must be taken with caution, because they depend on several adjustable parameters. Furthermore, the effect of the Mg^{2+} on the perchlorate ion has not been taken into account. The perchlorate ion is known to be distorted when in contact with a cation, and this effect will influence the field gradient.

If ion association takes place through a layer of solvent, the quadrupole coupling constant and the line width will be much different. In the point charge model, the line width is proportional to r^{-6}, where r is the Mg–Cl distance. If the value of r is doubled as a layer of solvent intervenes, the line width will be reduced by a factor of 64, which is below experimental error in most systems. Furthermore, it is likely that τ_c will be reduced, leading to additional reduction in the line width. Solvent-separated ion association has been identified in solutions of $Mg(ClO_4)_2$ in certain mixed solvent systems. The ^{35}Cl NMR line is found to be quite narrow, yet the conductance is low. Such results indicate that a wide NMR line must arise from ions in contact. These results will be presented in a later publication.[17]

Acknowledgments. This work was supported by a grant from the Directorate of Chemical Sciences of the Air Force Office of Scientific Research. We are grateful to Professor Cooper H. Langford for his encouragement and for many stimulating discussions.

References and Notes

(1) C. W. Davies, "Ion Association", Butterworths, Washington, D.C., 1962.
(2) R. E. Hester and R. A. Plane, *Inorg. Chem.*, **3**, 769 (1964).
(3) T. R. Stengle and C. H. Langford, *J. Phys. Chem.*, **69**, 3299 (1965).
(4) M. S. Greenberg, R. L. Bodner, and A. I. Popov, *J. Phys. Chem.*, **77**, 2449 (1973).
(5) J. A. Pople, W. G. Schneider, and H. J. Bernstein, "High Resolution Nuclear Magnetic Resonance", McGraw-Hill, New York, N.Y., 1959.
(6) A line width of about 1 Hz has been reported for 2.2 *M* $NaClO_4$ in aqueous solution. R. G. Bryant, private communication.
(7) M. Eisenstadt and H. L. Friedman, *J. Chem. Phys.*, **44**, 1407 (1966).
(8) C. Hall, R. E. Richards, G. N. Schulz, and R. R. Sharp, *Mol. Phys.*, **16**, 529 (1969).
(9) M. St. J. Arnold and K. J. Packer, *Mol. Phys.*, **14**, 241 (1968).
(10) T. E. Bruke and S. I. Chan, *J. Magn. Reson.*, **3**, 55 (1970).
(11) G. A. Forcier and J. W. Olver, *Anal. Chem.*, **37**, 1447 (1965).
(12) H. A. Berman, Ph.D. Thesis, University of Massachusetts, Amherst, Mass., 1974.
(13) The donor number is related to the enthalpy of reaction of the liquid solvent with $SbCl_5$. V. Gutmann, "Coordination Chemistry in Nonaqueous Solvents", Springer Verlag, Vienna, 1968, p 19.
(14) A. I. Popov, private communication.
(15) R. L. Kay, B. J. Hales, and G. P. Cunningham, *J. Phys. Chem.*, **71**, 3925 (1967).
(16) J. F. Coetzee and W. R. Sharpe, *J. Solution Chem.*, **1**, 77 (1972).
(17) H. A. Berman, H. J. C. Yeh, and T. R. Stengle, to be published.
(18) C. A. Kraus and R. M. Fuoss, *J. Am. Chem. Soc.*, **55**, 21 (1933).
(19) H. Wang and P. Hemmes, *J. Am. Chem. Soc.*, **95**, 5115, 5119 (1973).

Carbon-13 Nuclear Magnetic Resonance Relaxation in Hydrogen Bonded *tert*-Butyl Alcohol and Phenol

Edwin E. Tucker, Thomas R. Clem, Jeffrey I. Seeman, and Edwin D. Becker*

Laboratory of Chemical Physics, National Institutes of Health, Bethesda, Maryland 20014 *(Received August 12, 1974)*

Publication costs assisted by the National Institutes of Health

The spin–lattice relaxation time (T_1) of the carbinol carbon of *tert*-butyl alcohol is found to increase by a large factor on dilution in *n*-hexadecane-d_{34} or in CCl_4. The data in $C_{16}D_{34}$ are analyzed in detail on the basis of a previously proposed hydrogen bonding association model, together with the assumption that a single rotational correlation time for each hydrogen bonded species is proportional to the molecular weight of that species. The variation of T_1 for the carbons of phenol as it is diluted in cyclohexane is also reported, but these data are not analyzed quantitatively. ^{13}C relaxation times appear to have great promise in testing association models and in providing useful insight into hydrogen bonding.

Spin–lattice relaxation of ^{13}C nuclei is often dominated by intramolecular dipolar interactions with nearby protons.[1] The relaxation rate, R_1 ($\equiv 1/T_1$), is then directly proportional to the rotational correlation time, τ_c, provided the molecule tumbles rapidly and isotropically. Intermolecular association, such as hydrogen bonding, should increase τ_c, hence increase R_1. Alger, Grant, and Lyerla[2] demonstrated such an effect in the hydrogen bonded acetic and formic acids, relative to their methyl esters. Levy et al.[3] found a pronounced lengthening of T_1 for the carbons in phenol as it is diluted in CCl_4 to break up the hydrogen bonded aggregates, but they were able to carry the dilution

only to about 0.4 M, where phenol is still highly associated. We have repeated some of Levy's measurements and carried the study to lower concentration, and we report those results briefly.

In order to assess more quantitatively the effect of hydrogen bonding on T_1 (^{13}C) we have synthesized *tert*-butyl alcohol enriched at the carbinol carbon and measured its T_1 at concentrations as low as 0.06 M. While the CH_3 carbons in *t*-BuOH may be strongly relaxed by spin–rotation interactions, the carbinol carbon is relaxed primarily by dipolar interactions, as we shall show. The dependence of its T_1 value on concentration provides a means to monitor the degree of hydrogen-bonded association.

Experimental Section

Carbon-13 spectra of *tert*-butyl alcohol were obtained at 55.3 MHz with a pulse spectrometer built by NIH and the superconducting magnet of our Varian HR-220 spectrometer. Data analysis by Fourier transformation was carried out in the Varian 620 l computer attached to the HR-220 system. The arrangement of the ^{13}C spectrometer in close proximity to the HR-220 proved quite convenient, for the HR-220 served as the source of 220-MHz power for proton decoupling and could also be used in continuous wave mode to optimize magnetic field homogeneity with each sample prior to the initiation of a ^{13}C experiment. In addition, this system facilitated the measurement of sample temperature. An ethylene glycol sample was placed in the probe and subjected to the same level of decoupling power and the same flow of cooling air for a long enough period to achieve a steady-state temperature. The decoupling power was turned off, the proton spectrum scanned immediately, the peak separation measured, and the temperature determined from a standard calibration curve.[4] The temperature measured in this way was 28.5°, with an estimated reliability of ±1°.

The nuclear Overhauser enhancement of the carbinol carbon of *t*-BuOH was measured by a gated decoupling experiment; the decoupling power was turned off during a period of $5T_1$, then was applied during the observation pulse and data acquisition. The peak height obtained after Fourier transformation was compared with that in a conventional noise decoupling experiment.

The ^{13}C enriched *t*-BuOH was synthesized by the reaction of acetone-2-^{13}C (Merck, 60% enriched) and CH_3Li in diethyl ether. After hydrolysis, volatiles from the reactant mixture were removed and fractionated on a vacuum line. The *t*-BuOH fraction was dried by condensation onto CaH_2. The final product was a crystalline material at room temperature. Samples for NMR measurements were prepared by condensing small amounts of *t*-BuOH vapor at low pressure into 5-mm sample tubes containing approximately 1 cc of degassed CCl_4 or *n*-$C_{16}D_{34}$ and a trace of TMS. The OH proton spectra of the samples were consistent with those previously reported,[5] and the intensity of the ^{13}C satellites was consistent with that expected from 60% ^{13}C enrichment at the tertiary carbon. $^2J_{^{13}CH}$ was approximately 4.2 Hz.

Phenol (reagent grade) was diluted in reagent grade cyclohexane (including 10% perdeuteriocyclohexane as an internal lock). The phenol T_1's were obtained by the inversion-recovery (180°, τ, 90°) method[6] at 25 MHz with a Varian XL-100 spectrometer and associated Digilab pulse and data processing system.[7]

Some measurements of T_1 at the highest concentrations of *t*-BuOH studied were also made by the inversion-recovery method. However, for the lower concentrations, as T_1 increased to nearly 100 sec, this method became inefficient, since it requires a waiting time of about $5T_1$ between successive runs. We found the saturation-recovery (90°, τ, 90°) method[8] more satisfactory and employed this method for most of the experiments. For those samples where both methods were used, agreement was good, as shown in the tabulated data. Even with the saturation-recovery method excessive times were required for measurement of the equilibrium magnetization, S_∞ ($\tau \approx 5T_1$), so in some cases we did not measure this quantity but rather treated it as an adjustable parameter and used a computer program to fit the data to the best least-squares values of T_1 and S_∞. This treatment provided sufficiently accurate values of T_1 for our present purposes, but the method requires further tests to ascertain is reliability and utility in various circumstances.

TABLE I: ^{13}C Spin–Lattice Relaxation Time of $(CH_3)_3{}^{13}COH$ at 28°, 55.3 MHz

Solvent	Concn, M	Method[a]	T_1, sec
None	~10	Sat-rec	14.0 ± 1
CCl_4	1.006	Inv-rec	39.5 ± 1.5
		Sat-rec	37.0 ± 1.5
	0.516	Inv-rec	48 ± 2
		Sat-rec	44 ± 2
	0.192	Inv-rec	74 ± 3
		Sat-rec[b]	68 ± 4
	0.123	Sat-rec[b]	79 ± 4
	0.051	Sat-rec[b]	90 ± 10
$C_{16}D_{34}$	1.017	Sat-rec	24 ± 1
	0.403	Sat-rec	26 ± 2
		Sat-rec	24.6 ± 1
	0.209	Sat-rec	30 ± 2
	0.126	Sat-rec	48 ± 4
	0.060	Sat-rec[b]	50 ± 8

[a] Sat-rec, saturation-recovery (90°, τ, 90°) method; inv-rec, inversion-recovery (180°, τ, 90°) method. [b] S_∞ not measured (see text).

Results and Discussion

Values of T_1 for the carbinol carbon of *t*-BuOH at several concentrations in CCl_4 and in hexadecane-d_{34} are given in Table I. Clearly T_1 increases substantially as the alcohol is diluted in either solvent. The macroscopic viscosities of *t*-BuOH and *n*-hexadecane are very close (3.31 and 2.78, both at 30°), so in this solvent almost the entire effect must be ascribed to changes in the hydrogen bonded species present.[9] The lower viscosity of CCl_4 (0.84 at 30°) accounts qualitatively for much of the larger effect observed in this solvent, but in addition the alcohol is less associated at a given concentration in CCl_4 than it is at the same concentration in a hydrocarbon solvent.[10]

Tucker and Becker[5] have reported a careful study by several physical methods of hydrogen bonding of *t*-BuOH in hexadecane. There is a rough correlation between the T_1 values reported in the present work and the OH chemical shift, as measured previously.[5] The observed chemical shift is the weighted average of the chemical shifts of the various molecular species present, and the observed relaxation rate, $1/T_1$, represents a similar weighted average, provided all species are exchanging rapidly. For the *t*-BuOH system, data on vapor pressure, infrared spectra, and proton nmr

TABLE II: Analysis of Relaxation Data for $(CH_3)_3{}^{13}COH$ in $C_{16}D_{34}$ by the 1-3-6 Association Model

Concn, *M*	% contribution: 1-mer *C*	1-mer R_1	3-mer C^a	3-mer R_1	6-mer C^a	6-mer R_1	R_1(calcd), sec^{-1}	R_1(obsd), sec^{-1}
0.060	80	56	19	39	1	5	0.016	0.020
0.126	59	29	33	49	8	22	0.023	0.021
0.209	44	17	39	44	17	39	0.029	0.033
0.403	28	8	39	34	33	58	0.037	0.040
1.017	15	3	31	22	54	75	0.047	0.042
10.5[b]	2	<1	12	7	86	93	0.071	0.071

[a] Percentage of monomer units. [b] Neat liquid.

chemical shifts have all been quantitatively interpreted in terms of models involving monomer, trimer, and various higher polymers.[10] One satisfactory model (1–3–∞ model) accounts for the presence of all species higher than the trimer on a statistical basis. Another model found to represent the data almost as well is the 1–3–6 model, in which only these three species are considered as present in any significant amounts. Although this model seems inherently less reasonable physically, we shall use it in interpreting the relaxation data, since it permits a clear demonstration of the factors involved.

We found a value of 2.6 (±0.3) for the nuclear Overhauser enhancement of the carbinol carbon resonance in *t*-BuOH in $C_{16}D_{34}$ (1.0 *M*). The relaxation is thus primarily dipolar, and $R_1 \propto \tau_c$, the rotational correlation time. If internal motions are unimportant and rotation is isotropic, then τ_c will be proportional to the size of the molecule, and thus we might expect that for an *n*-mer

$$\tau_c^{(n)} = n\tau_c^{(1)}$$

where $\tau_c^{(1)}$ refers to the monomer. For the 1–3–6 system, then, at a monomer concentration *m*, the average τ_c is given by

$$\tau_c = (m\tau_c^{(1)} + 3K_3m^3\tau_c^{(3)} + 6K_6m^6\tau_c^{(6)})/(m + 3K_3m^3 + 6K_6m^6) = (m\tau_c^{(1)} + 9K_3m^3\tau_c^{(1)} + 36K_6m^6\tau_c^{(1)})/(m + 3K_3m^3 + 6K_6m^6)$$

From the published values[5] for K_3 and K_6, we obtain the contributions to τ_c, hence to R_1, given in Table II. Even at the lowest concentration studied, where monomer accounts for 80% of the alcohol, the monomer contributes only a little over half of the relaxation. At higher concentrations the monomer contribution to R_1 drops rapidly to become of little significance. The weighting of the higher polymer contributions in R_1 is quite different from that in the chemical shift. Thus the two types of data are complementary and provide independent tests for an association model.

The proportionality between the calculated τ_c and the observed R_1 is fairly good. The values of R_1(calcd) in Table II were obtained by choosing $R_1^{(1)}$ to give the best least-squares fit with the observed values of R_1. The monomer value, $R_1^{(1)}$, is found to be 0.0112 ($T_1^{(1)}$ = 89 sec).

The model we have used for molecular tumbling may well be oversimplified. It assumes isotropic rotation and no internal motions that contribute to relaxation. The nearly spherical shape of the *t*-BuOH monomer should encourage isotropic rotation, but the hydrogen bonded species might tumble anisotropically, depending on their exact structure.

TABLE III: ^{13}C Relaxation Times in Phenol[a]

Solvent	Concn: Mol fraction	Concn: *M*	T_1, sec: C-2	C-3	C-4
Cyclohexane	0.088	1.0	4.2	4.5	2.4
	0.028	0.3	6.6	6.0	3.2
	0.0009	0.1	15	15	8.7
CCl_4[b]	0.5		2.4	2.4	1.4
	0.33		2.9	2.9	2.1
	0.14		4.2	3.9	2.4
	0.077		5.5	5.3	3.1
	0.038		6.4	7.4	5.4

[a] 25 MHz, 38°. [b] Data in CCl_4 from ref 3b.

Burnett and Roeder[11] showed that neat liquid glycerol behaves as though it tumbles very anisotropically, presumably because of its hydrogen bonded configuration. Internal (segmental) motions are, of course, known tc be important in ^{13}C relaxation,[12] especially in long chain molecules. Open (chain) hydrogen bonded polymers of *t*-BuOH could also possess such segmental motions. It is gratifying that the simple tumbling model used here works so well, but further detailed studies are needed to define its limitations.

The 1–3–6 association model, too, represents only one of several possibilities. Our purpose in presenting this analysis is not to promote any particular model, but rather to indicate that relaxation rates are quite sensitive tc molecular size in hydrogen bonded systems and may well prove valuable in elucidating the details of multiple equilibria. Clearly for a system as complex as *t*-BuOH, values of T_1 at many additional concentrations are required and very accurate data are needed. It may be emphasized that good thermodynamic data on the equilibria (from vapor pressure, ir, etc.) are also needed in order to treat the relaxation results meaningfully.

We have also carried the work of Levy et al.[3] on phenol to somewhat lower concentrations, but lack of ^{13}C-enriched phenol limited our study to 0.1 *M*. Our data, in cyclohexane solvent, are given in Table III, together with some of those of Levy for comparison. At 0.1 *M* T_1 has lengthened considerably, but about 25% of the phenol is still associated at this concentration. We have not yet analyzed these data quantitatively. In phenol anisotropic tumbling is a factor that must almost certainly be taken into account.[3]

The use of ^{13}C relaxation data[13] appears to offer a valuable complement to the techniques usually used in

studying hydrogen bonding. Careful studies of simple systems are needed to check the validity of the assumptions inherent in the use of a single correlation time for a given species. Perhaps relaxation data will be able to provide information not only on size of individual hydrogen bonded species but also on their conformations.

References and Notes

(1) See, for example, K. F. Kuhlman, D. M. Grant, and R. K. Harris, *J. Chem. Phys.*, **52**, 3439 (1970); T. D. Alger and D. M. Grant, *J. Phys. Chem.*, **75**, 2538 (1971).
(2) T. D. Alger, D. M. Grant, and J. R. Lyerla, Jr., *J. Phys. Chem.*, **75**, 2539 (1971).
(3) (a) G. C. Levy, *J. Magn. Reson.* **8**, 122 (1972); (b) G. C. Levy, J. D. Cargioli, and F. A. L. Anet, *J. Am. Chem. Soc.*, **95**, 1527 (1973).
(4) Varian Associates calibration curve.
(5) E. E. Tucker and E. D. Becker, *J. Phys. Chem.*, **77**, 1783 (1973).
(6) See, for example, T. C. Farrar and E. D. Becker, "Pulse and Fourier Transform NMR", Academic Press, New York, N.Y., 1971.
(7) We thank R. J. Highet and E. A. Sokoloski for the use of this instrument.
(8) G. G. McDonald and J. S. Leigh, Jr., *J. Magn. Reson.*, **9**, 358 (1973).
(9) It is, of course, the microscopic, rather than macroscopic, viscosity that influences relaxation, and the macroscopic quantity can sometimes be misleading. Estimates of microscopic viscosities are difficult to obtain and may be unreliable because of limitations on models of molecular motion. In the present study, however, the principal emphasis is on solutions of 1 *M* or less, where the viscosity should be largely determined by the solvent and should be nearly independent of concentration.
(10) E. E. Tucker, unpublished work; for similar results with phenol association see, for example, T. Gramstad and E. D. Becker, *J. Mol. Struct.*, **5**, 253 (1970); K. B. Whetsel and J. H. Lady in "Spectrometry of Fuels", Plenum Press, New York, N.Y., 1970, p 259.
(11) L. J. Burnett and S. B. W. Roeder, *J. Chem. Phys.*, **60**, 2420 (1974).
(12) See, for example, D. Doddrell and A. Allerhand, *J. Am. Chem. Soc.*, **93**, 1558 (1971); G. C. Levy and G. L. Nelson, *ibid.*, **94**, 4897 (1972).
(13) Deuterium relaxation, which also depends on a rotational correlation time, should be a valuable technique, as well.

Micelle Formation by Ionic Surfactants. III. Model of Stern Layer, Ion Distribution, and Potential Fluctuations

Dirk Stigter

Western Regional Research Center, Agricultural Research Service, U.S. Department of Agriculture, Berkeley, California 94710

(Received September 9, 1974; Revised Manuscript Received February 21, 1975)

Publication costs assisted by the U.S. Department of Agriculture

A detailed model is presented of the Stern layer between the core surface and the hydrodynamic shear surface of ionic micelles, in particular of sodium alkyl sulfates. The Stern layer contains about half the countercharge of the micelle. The distribution of head groups and counterions in the Stern layer is discussed with the help of the lattice and cell theories of two-component liquids. Electrostatic interaction between nearest neighbor ions and changes of ionic self potentials are taken into account. The hexagonal lattice model serves to evaluate the statistical frequency of nearest neighbor ion pairs for three approximate distributions. The results for the Bethe–Guggenheim or quasichemical distribution are the most accurate and, in all cases, are found to be close to those for the regular or low temperature distribution. The completely random or high temperature distribution appears to be the least probable. Fluctuations are investigated on the basis of a cell model, with the nearest neighbor configurations taken from the low temperature distribution. It is found that, in spite of the lack of symmetry, the average position of a counterion is very close to the geometric center of its cell. Potential variations of an ion moving around in its cell are presented for a variety of micelles and are found to be rather large, up to $1kT$ for counterions, and up to $2.5kT$ for head groups. Nevertheless, the average potential of an ion is not very different from the potential of the ion at its average position. This difference is from $0.07kT$ to $0.26kT$ for counterions, and up to $0.21kT$ for head groups in the micelles under investigation. Contributions of potential fluctuations to thermodynamic micelle properties are relatively small, but difficult to evaluate correctly.

Introduction

In the first two papers of this series[1,2] the main free-energy changes were considered when micellization takes place in ionic surfactant solutions. For a number of systems such changes were evaluated[1] on the basis of the Gouy–Chapman model of the electrical double layer around the micelles. It is of interest to determine in how far the results may be distorted by deficiencies of the Gouy–Chapman theory. The present paper deals with the charge distribution in an improved double layer model that allows for the size and for the high concentration of the charge carriers at the micelle surface. Free-energy calculations for the improved model will be given in the following paper.

The classical Gouy–Chapman theory[3] assumes a uniform, continuous, interfacial surface charge which is neutralized by a diffuse, ionic layer of point charges in the aqueous solution, that is, a space charge whose distribution obeys the Poisson–Boltzmann equation. This means that in the diffuse layer all changes perpendicular to the interface are assumed to be smooth and continuous, while parallel to the interface all possible variations or inhomogeneities are ignored. As reviewed by Levine, Mingins, and Bell,[4] much work has been done on improvements in the diffuse layer,

in particular in the area close to the interface (Stern layer), where specific adsorption, as well as fluctuations in the lateral distribution of discrete counterions of finite size, have been introduced. Such discrete-ion models are designed mostly to refine interpretations of the double layer properties at the interface between mercury and aqueous salt solutions. For mercury the assumption of a continuous surface charge is reasonable. However, this is not so for ionic micelles in aqueous solutions. In this case the concept of discrete ionic charges of finite size applies not only to the counterions, but with at least equal force to the head group ions that form the native charge of the micelle surface.

The best currently available physical model of a micelle[5] is a liquid core formed by the associated alkyl chains, with the ionic head groups projecting out into the water. About one-half of the total number of counterions is accommodated in spaces between the head groups, in the Stern layer. The remaining counterions are further away from the core surface, in a diffuse, Gouy–Chapman type layer. A model with these general features has been used[6] to investigate the adsorption of counterions at the micelle surface. That treatment of the Stern layer introduced elements of the lattice and cell theories of binary mixtures.[7] The present paper deals with two outstanding questions of the model. (1) Which kind of ions occupy nearest neighbor lattice sites, and (2) what are the potential fluctuations of an ion when it moves around in its cell?

The present results justify the relevant assumptions in the earlier adsorption work,[6] and form a good basis for the free-energy calculations in the following paper. The discussion is for micelles of sodium alkyl sulfates. Modifications for dodecyl ammonium chloride are indicated as necessary. We shall assume that the dielectric constant of the micelle core is the same as that of bulk hydrocarbons, $\epsilon_c = 2$, and that a stepwise change to the value $\epsilon_w = 78.5$ of bulk water occurs at or near the core surface. This allows us to use the earlier results[6] for the charge–potential relation near a dielectric sphere. Before examining the ion distribution, we define a model for the physical structure of the micelle surface.

Geometry of the Stern Layer

In general the Stern layer indicates the inner part of an electrical double layer system.[3] For micelles we define the Stern layer as the layer between the core/water interface and the hydrodynamic shear surface of the micelle. The position of the core/water interface has been correlated with the specificity of surfactant head groups. An average location at 0.8 ± 0.4 Å above the α-carbon atoms of the associated alkyl chains has been found.[2] The Stern layer can be delineated further by the measurement of transport properties. In the solutions under study viscosity and micellar self-diffusion indicate that the shear surface of micelles coincides with the surface enveloping the hydrated head groups.[5] This means that the thickness s of the Stern layer is equal to the length of the hydrated head group. Electric conductance and micellar electrophoresis have shown that about half the countercharge is inside the shear surface.[5] So the Stern layer resembles a concentrated aqueous electrolyte solution. When n is the micelle number, the Stern layer contains the n fully ionized head groups and $(1 - \alpha)n$ counterions, with $\alpha \approx 0.5$. The remaining αn counterions neutralizing the micelle charge are distributed outside the shear surface in a Gouy–Chapman diffuse ionic atmosphere.

The electrostatic calculations are made for spherical micelles. So the Stern layer is outlined by the core radius b. This radius depends on the micelle number n and on the molar volume $V_k/2$ of the micellized alkyl groups. The volume $V_k/2$ is extrapolated from the molar volume V_k of normal alkanes C_kH_{2k+2} with the empirical relation

$$V_k = 35.33/k + 26.39 + 16.57k \text{ ml/mol} \quad (1)$$

Experimental data for the C_5 to C_{17} liquid alkanes[8] at 25° and 1 atm fit eq 1 with an average deviation of 0.07%. It is not certain that the pressure inside a micelle core is equal to 1 atm.[5,9] Even the existence of a well-defined, uniform pressure in the micelle core may be in doubt.[10,11] Nevertheless, the results of eq 1 for micellized methylene groups, 16.45 to 16.50 ml/mol for C_8 to C_{12} surfactants, are close to experimental results derived from the density of micellar solutions[12,13] which range from 16.8 to 17.4 ml/mol for methylene groups. On this basis we use eq 1 to calculate the density of micelle cores.

The detailed geometry of the Stern layer is discussed with reference to Figures 1 and 2 which show part of the main cross sections of a sodium alkyl sulfate micelle. We consider the sulfate groups and the sodium ions as hard spheres with radii r_h and r_c, respectively, and charge $-e$ or $+e$ at the center. The distribution of these ions is based on the lattice and cell theories of binary mixtures.[7] The Stern layer is divided into $(2 - \alpha)n$ cells. The centers of the cells form a regular hexagonal lattice at the surface of the micelle sphere. Inside each cell one ion moves in the potential field of its six nearest neighbor ions assumed fixed at their average positions. Electric interaction with more distant ions is nearly constant in the cell and will not be considered here.

The center of a head group is at a fixed distance $h = s - r_h$ from the core surface, that is, in a two-dimensional cell. The counterions may move also in radial direction, in three-dimensional cells with thickness $s - r_c$, the outer cell boundary for the ion center being the shear surface of the micelle. The cell dimensions are further defined by the average distance between nearest neighbors. At distance $t = b + h$ from the micelle center the distance between adjacent head groups is

$$a = 2t \sin(\theta/2) \quad (2)$$

where θ is the angle between the radial rays through the two adjacent lattice points, compare Figures 1 and 2. For a total of $M = (2 - \alpha)n$ lattice points it can be derived from spherical geometry that

$$\cos\theta = \cos A/(1 - \cos A) \quad (3)$$

where

$$A = \frac{\pi}{3}\left(1 + \frac{2}{M - 2}\right) \quad (4)$$

The position of a counterion is determined with the cartesian coordinate system (X, Y, Z) attached to the center of the bottom of the cell, as shown in Figures 1 and 2. The actual shape of the cell is simplified by assuming circular cross sections with radius

$$\rho_0(Z) = a - [(\sigma - 0.3)^2 - Z^2]^{1/2} \quad (5)$$

where the exclusion radius σ equals the sum of the ionic radii, $\sigma = r_h + r_c$ Å. It is further assumed that the bottom and the top surfaces of the cell are planar. So the cell volume becomes

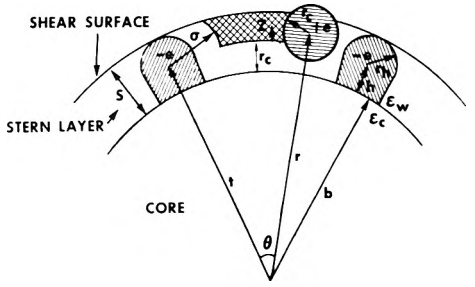

Figure 1. Partial cross section through micelle of sodium alkyl sulfate. Cross hatched area indicates cell of sodium ion in Stern layer.

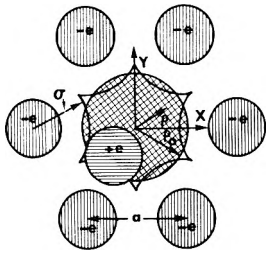

Figure 2. Partial cross section of the Stern layer of sodium alkyl sulfate micelle through centers of sulfate head groups. Cross hatched area indicates cell of sodium ion.

$$V = \int_0^{s-r_c} dZ \int_0^{\rho_0(Z)} 2\pi\rho \, d\rho \qquad (6)$$

with $\rho_0(Z)$ taken from eq 5.

The later evaluation of electric interactions will be carried out with the help of the relative spherical coordinates (t, r, θ) indicated in Figure 1. For a head group at $(X_i, Y_i, 0)$ and a counterion at (X, Y, Z) we shall use the good approximations

$$r = b + r_c + Z \qquad (7)$$

and

$$\cos\theta = 1 - [(X - X_i)^2 + (Y - Y_i)^2]/(2t^2) \qquad (8)$$

For the sodium alkyl sulfates we adopt $s = 4.6$ Å for the thickness of the Stern layer,[5] and $r_h = r_c = 2.3$ Å for the ionic radii.[14] For micelles of dodecyl ammonium chloride[5,14] we use $s = 2.6$ Å and $r_h = r_c = 1.9$ Å. This places the sulfate charges at $h = s - r_h = 2.3$ Å and the ammonium charges at $h = 0.7$ Å from the core, consistent with the location of the core/water interface derived in ref 2. Actually, the uncertainty in the foregoing values of s and the ionic radii is of the order of 0.5 Å, that in the position of the core surface may be more.[2]

It is well known that it is impossible to cover a spherical surface with a perfect hexagonal lattice. However, the potential calculations in this and in the following paper do not require a lattice with perfect long-range order. In fact, long-range order is unrealistic for micelles with a fluid structure and, hence, we treat only nearest neighbor ions as discrete charges. Moreover, we are interested only in average potentials, and possible contributions of lattice imperfections are expected to be of second-order magnitude. This surmise is supported by some data in the last section.

Nearest Neighbor Statistics in the Stern Layer

A rigorous treatment of the configurational statistics of the ions in the Stern layer is difficult. The present discussion is limited to the pairing of nearest neighbor ions. As a further simplification in this section, every ion is assumed to occupy its average position. This permits the use of lattice statistics. We include the configurations assumed during the imaginary charging process, employed in the following paper to evaluate the electrical free energy of the micelle. So we consider the general case of a micelle with n sulfate head groups, each with charge $-\lambda e$, where the charging parameter λ runs from 0 to 1. During the charging process the sodium counterions retain their full charge e per ion. Since we do not allow empty sites the lattice spacing, calculated with eq 2–4, decreases during the charging at constant micelle size, when n_c increases from 0 to $(1 - \alpha)n$. The total number of lattice sites M in eq 4 increases from $M = n$ for $\lambda = 0$ to $M = (2 - \alpha)n$ for $\lambda = 1$. In general there are $n_c = (1 - \alpha)\lambda n$ counterions in the Stern layer, where they occupy a fraction $\Theta = n_c/(n + n_c)$ of the lattice sites, the remaining fraction $1 - \Theta$ being occupied by head groups.

The configuration count is based on the numbers of distinguishable pairs of ions on adjacent sites: N_{hh} (hh) pairs, that is, nearest neighbor sites occupied by head groups; N_{cc} paired sites with counterions, (cc) pairs; and N_{hc} (hc) pairs. In any distribution of n head groups and n_c counterions on a hexagonal lattice we have[7]

$$N_{hh} = 3n - N_{hc}/2 \qquad (9)$$

and

$$N_{cc} = 3n_c - N_{hc}/2 \qquad (10)$$

An additional relation is derived with the quasichemical approximation[7] in which the exchange between pairs

$$2(hc) \rightleftharpoons (hh) + (cc) \qquad (11)$$

is treated as a chemical equilibrium:

$$N_{hh}N_{cc}/N_{hc}^2 = (e^{-\Delta W/kT})/4 \qquad (12)$$

where ΔW is the change in the pair interaction energy for the forward reaction 11.

The solution of eq 9, 10, and 12 in terms of N_{hc} yields

$$N_{hc} = 12(n + n_c)\Theta(1 - \Theta)/(\beta + 1) \qquad (13)$$

with

$$\beta = \{1 - 4\Theta(1 - \Theta)[1 - \exp(-\Delta W/kT)]\}^{1/2} \qquad (14)$$

The energy change ΔW depends on λ and on the interaction energies W_{hh}, W_{cc}, and W_{hc} between the fully charged pairs (hh), (cc), and (hc), respectively

$$\Delta W = \lambda^2 W_{hh} + W_{cc} - 2\lambda W_{hc} \qquad (15)$$

The evaluation of the pair energies is based on the earlier expression[6] for the potential field ψ of an electric charge e in water near a dielectric sphere with radius b. The mixed pair energy W_{hc} depends on the relative spherical coordinates t, r, and θ indicated in Figure 1

$$W_{hc} = -e\psi(t, r, \theta) \qquad (16)$$

$$\psi = \frac{e}{\epsilon_w(t^2 - 2tr\cos\theta + r^2)^{1/2}} + \frac{e(1 - \omega)}{\epsilon_w b(1 + \omega)}\left\{\frac{x}{(1 - 2x\cos\theta + x^2)^{1/2}} - x^{\omega/(1+\omega)}\int_0^{x^{1/(1+\omega)}} \frac{dy}{(1 - 2y^{1+\omega}\cos\theta + y^{2+2\omega})^{1/2}}\right\} \qquad (17)$$

where $x = b^2/tr$, and the ratio of the dielectric constants of the micelle core and of water is $\omega = \epsilon_c/\epsilon_w$. The energies of

TABLE I: Size Factors for a Variety of Micelles[a]

	n	b, Å	a, Å	$s - r_c$, Å	$\langle Z \rangle$, Å
$C_8H_{17}SO_4Na$	23.7	11.13	8.46	2.3	1.103
	47.8	14.31	7.41	2.3	1.085
$C_{12}H_{25}SO_4Na$	57.3	16.91	7.90	2.3	1.099
	123	22.54	6.91	2.3	1.079
$C_{12}H_{25}NH_3Cl$	100.7	20.40	6.49	0.7	0.350
	163	25.37	6.38	0.7	0.350

[a] Micelle number n; core radius b; distance a between adjacent head groups; thickness $s - r_c$ of counterion cell; average position $\langle Z \rangle$ of counterion from eq 26.

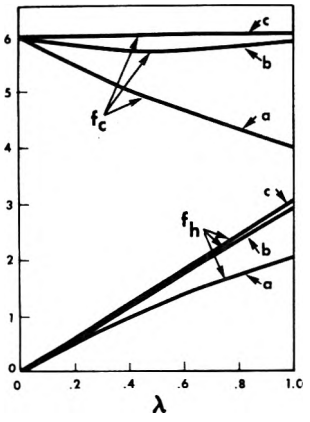

Figure 3. Factors f_c and f_h for average numbers of nearest neighbor pairs vs. charging parameter λ of head groups in the Stern layer of sodium octyl sulfate micelles with n = 23.7 and α = 0.5 for three different distributions: a = random or high temperature model, eq 19 and 20; b = quasichemical model; c = regular or low temperature model, eq 21 and 22.

(hh) and (cc) pairs are also obtained with eq 17

$$W_{hh} = e\psi(t, t, \theta) \qquad W_{cc} = e\psi(r, r, \theta) \qquad (18)$$

Equations 15–18 have been applied to the micelles described in Table I. It was found that ΔW ranges from $0.71kT$ to $1.18kT$ for $\lambda = 0$, and from $3.72kT$ to $6.18kT$ for $\lambda = 1$.

The number of mixed pairs N_{hc} in eq 13 is useful to characterize the immediate environment of the ions. On the average each head group has $f_h = N_{hc}/n$ counterions as nearest neighbors and, since we have a hexagonal lattice, $6 - f_h$ other head groups. Similarly, each counterion has $f_c = N_{hc}/n_c$ head groups and $6 - f_c$ other counterions as nearest neighbors. It is interesting to compare the quasichemical approximation with two extreme situations, The Bragg–Williams or high temperature limit is the random distribution, derived with $\beta = 1$ in eq 13

$$f_h = 6(1 - \Theta) \qquad \Delta W/kT = 0 \qquad (19)$$

$$f_c = 6\Theta \qquad \Delta W/kT = 0 \qquad (20)$$

The low temperature limit, with $\beta = 1 - 2\Theta$ in eq 13, is given by

$$f_h = 6n_c/n \qquad \Delta W/kT = \infty \qquad (21)$$

$$f_c = 6 \qquad \Delta W/kT = \infty \qquad (22)$$

In Figure 3 f_h and f_c are plotted vs. λ for the three models in the case of sodium octyl sulfate in water with α = 0.5. We note that the results of the quasichemical approximation are close to those of the low temperature distribution.

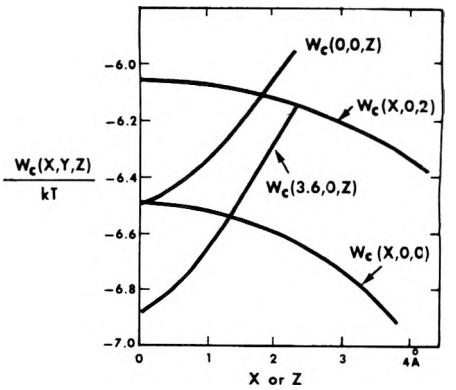

Figure 4. Potential W_c of sodium ion at various positions (X, Y, Z) in the Stern layer cell. Micelles of sodium dodecyl sulfate with n = 57.3 and α = 0.5.

In fact, the case presented in Figure 3 is the most unfavorable one, with the smallest micelles, n = 23.7. In all other cases the micelles are larger and, hence, ΔW is larger, bringing the quasichemical results still closer to the low temperature limit. Furthermore, for increasing α, from 0.5 to 1, the difference between the two models becomes even smaller.

Although the quasichemical model is not rigorous, the present calculations justify the earlier treatment[6] of the potential of the counterions which was based on the low temperature limit. This model is simpler than the quasichemical distribution and, for our purposes, not significantly different. For this reason we adopt the low temperature approximation also in our further calculations.

Potential Fluctuations and Average Position of Counterions in the Stern Layer

We now turn to the cell model which is viewed as a refinement of the lattice model of the Stern layer. Each ion is confined to a cell formed by the boundaries of the Stern layer, and by its nearest neighbor ions at adjacent lattice sites. According to eq 22 a counterion always has six head groups on its nearest neighbor sites. This occupation and the geometrical features defined earlier with the help of Figures 1 and 2 determine the cell of a counterion.

The potential energy W_c of a counterion depends on its position (X, Y, Z) in the cell. The nearest neighbor contributions to W_c are given by eq 16 and 17, with the relative coordinates defined in eq 7 and 8. We consider only fully charged head groups, $\lambda = 1$. We add to W_c also the increase of self-potential of the counterion when it moves from the bulk of the aqueous solution into the Stern layer near the apolar micelle core. As derived previously[6] this increase $\Delta\phi$ depends on b, r, and ω as follows

$$\Delta\phi = \frac{e^2(1 - \omega)b}{2\epsilon_w(1 + \omega)(r^2 - b^2)} - \frac{e^2(1 - \omega)}{2\epsilon_w b(1 + \omega)}\left(\frac{b}{r}\right)^{2\omega/(1+\omega)} \int_0^{(b/r)^{2/(1+\omega)}} \frac{dy}{1 - y^{1+\omega}} \qquad (23)$$

With eq 17 and 23 we now have

$$W_c = -\sum_{i=1}^{6} e\psi_i + \Delta\phi \qquad (24)$$

The summation in eq 24 is over the six nearest neighbor head groups. The more distant ions add a nearly constant term to W_c and need not be considered here. Figure 4

TABLE II: Average Fluctuations in Counterion Cell for $\lambda = 1$[a]

	n	W_c^0, kT	V, Å^3	$(\langle W\rangle - W_c^0), kT$	$-\ln (V_f/V)$
$C_8H_{17}SO_3Na$	23.7	−5.28	147.7	−0.16	−0.14
	47.8	−6.51	83.7	−0.11	−0.08
$C_{12}H_{25}SO_4Na$	57.3	−6.31	105.5	−0.08	−0.11
	123	−7.60	60.4	−0.07	−0.05
$C_{12}H_{25}NH_2Cl$	100.7	−8.05	25.7	−0.26	−0.25
	163	−8.72	22.9	−0.24	−0.23

[a] Based on eq 27-29. Test of different treatments with eq 30.

shows variations of W_c inside the sodium cell for micelles of sodium dodecyl sulfate in water at 25°, with $n = 57.3$ monomers per micelle and assuming $\alpha = 0.5$. The potential is plotted vs. distance along four different lines in the surface $Y = 0$. The curves demonstrate that the fluctuations of W_c with position in the cell are quite substantial, up to $1kT$.

For the evaluation of cell averages it is useful to simplify the representation of the potential field. Calculations have shown that parallel to the micelle surface, for Z = constant, the deviations of W_c from circular symmetry are less than $0.03kT$. Therefore, a very good approximation is

$$W_c(X, Y, Z) = W_c(\rho, Z) \quad (25)$$

where $\rho = (X^2 + Y^2)^{1/2}$ is the radial coordinate shown in Figure 2. With eq 25 one reduces the number of variables by one, thus decreasing the amount of labor required in the numerical integrations for obtaining cell averages. For instance, the average position of the counterion along the central axis (0, 0, Z) in the cell may be obtained from

$$\langle Z\rangle = \int Z \exp(-W_c/kT)\, dV / \int \exp(-W_c/kT)\, dV \quad (26)$$

with integrations over the cell volume as defined in eq 6. Table I presents data on some cases that cover the range of micelles under investigation. It is found that $\langle Z\rangle$ is quite insensitive to micelle size and close to $(s - r_c)/2$, the midpoint of Z in the cell.

We proceed with the average fluctuations of W_c and their contribution to the electrochemical potential μ_c of the counterions in the Stern layer. The most straightforward approach is perhaps to introduce in μ_c the average potential

$$\langle W_c\rangle = \int W_c \exp(-W_c/kT)\, dV / \int \exp(-W_c/kT)\, dV \quad (27)$$

However, common practice in cell theory[7] is to incorporate in μ_c not the average potential, but the potential at the average position in the cell, that is, in the present case

$$W_c^0 = W_c(0, 0, \langle Z\rangle) \quad (28)$$

It is customary[7] to account for fluctuations through a change of the cell volume V to the free cell volume V_f defined with

$$V_f = \int \exp[-(W_c - W_c^0)/kT]\, dV \quad (29)$$

In this case the contribution of the potential fluctuations to μ_c is $-kT \ln (V_f/V)$, instead of $\langle W_c\rangle - W_c^0$ in the first approach. In Table II results of the two methods are compared and found to be approximately the same. Indeed, for sufficiently small fluctuations the equality of the results

$$\langle W_c\rangle - W_c^0 = -kT \ln (V_f/V) \qquad W_c - W_c^0 \ll kT \quad (30)$$

can be derived with eq 27 and 29. Although the variations of W_c in the cell are quite large, compare Figure 4, the data in Table II show that eq 30 is approximately satisfied, and that the net fluctuation contributions to μ_c are relatively small.

Fluctuations of Head Group Potential in Cell Model of the Stern Layer

The head groups are located at a fixed distance t from the micelle center and, therefore, the head group cell is a surface, bounded by f_h counterions and $6 - f_h$ other head groups on the nearest neighbor sites. The low temperature distribution is assumed with f_h from eq 21. A schematic cross section for a sulfate group cell in a micelle of sodium alkyl sulfate is given in Figure 5. We assume circular cells with radius $\rho_0 = a - \sigma + 0.3$ Å, in line with eq 5 and with Figure 2 for the sodium ion cells. We assume $\alpha = 0.5$ and, looking ahead to the imaginary charging process, we allow the charging parameter λ to vary between 0 and 1. So the potential energy of the central head group is with eq 8 and 17

$$W_h = \lambda^2 \sum_i e\psi_i(t, t, \theta_i) - \lambda \sum_j e\psi_j(t, r, \theta_j) \quad (31)$$

The first summation in eq 31 is over nearest neighbor head groups with charge $-\lambda e$, and the second term sums over nearest neighbor counterions with charge $+e$. For the counterions, in eq 7 for r, we set $Z = \langle Z\rangle$. In view of the data in Table I we take $\langle Z\rangle = 1.1$ Å for all sodium alkyl sulfates, and $\langle Z\rangle = 0.35$ Å for all dodecyl ammonium chloride micelles. We are only interested in the variations of $W_h(X, Y)$ with position in the cell. The self-potential of the head group does not vary in the cell. So we disregard this and other (nearly) constant contributions to W_h.

The potential of the head group depends on the average occupation of the nearest neighbor sites and, except at the cell center, also on the ion configuration. When λ runs from 0 to 1, and $\alpha = 0.5$, eq 21 gives 0 to 3 counterions and 6 to 3 head groups as nearest neighbors. The configuration of these ions is expressed as a circular sequence. For instance, the configuration of three head groups h alternating with three counterions c is represented by the sequence a = (hchchc) or (chchch). This is the only configuration of interest for $\lambda = 1$, because the low temperature model does not allow (cc) pairs. For $\lambda = \frac{2}{3}$ eq 21 gives $f_h = 2$ counterions and four head groups. The two allowed configurations are represented by b = (hchchh) and c = (hchhch). For $\lambda = \frac{1}{3}$ each head group has only one counterion as nearest neighbor, for example, in d = (hchhhh). Finally, for $\lambda = 0$ there are head groups only, the sequence e = (hhhhhh). These are the only configurations on the hexagonal lattice that satisfy the condition $N_{cc} = 0$ of the low temperature distribution. For intermediate values of λ and $\alpha \leq 0.5$ one expects appropriate mixtures of these configurations.

TABLE III: Average Fluctuations in Head Group Cell Based on Eq 32-34[a]

		$(\langle W_h \rangle - W_h^0), kT$				$-\ln (A_f/A)$			
	n	a $\lambda = 1$	b $\lambda = 2/3$	c $\lambda = 2/3$	d $\lambda = 1/3$	a $\lambda = 1$	b $\lambda = 2/3$	c $\lambda = 2/3$	d $\lambda = 1/3$
$C_8H_{17}SO_4Na$	23.7	−0.01	−0.09	−0.03	−0.01	0.00	−0.03	+0.01	0.00
	47.8	0.00	−0.09	−0.02	−0.02	−0.01	−0.03	+0.01	0.00
$C_{12}H_{25}SO_4Na$	57.3	−0.01	−0.10	−0.02	−0.02	−0.01	−0.04	+0.01	0.00
	123	0.00	−0.09	−0.01	−0.01	−0.01	−0.04	+0.01	0.00
$C_{12}H_{25}NH_3Cl$	100.7	−0.02	−0.21	−0.06	−0.03	−0.03	−0.07	+0.01	0.00
	163	0.00	−0.21	−0.06	−0.03	−0.04	−0.08	+0.01	0.00

[a] Test of eq 35.

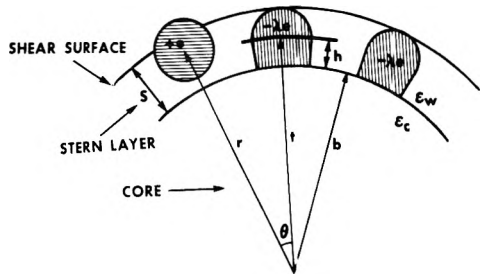

Figure 5. Partial cross section through alkyl sulfate micelle. Heavy line indicates cell of sulfate head group.

In any configuration the fluctuations of W_h are greatest along the rim of the cell, at distance ρ_0 from the cell center. For the range of micelles in Table I it is found that the variations of W_h along the cell rim are smallest for sodium dodecyl sulfate with $n = 123$, $0.59kT$ for $\lambda = 1$, and greatest for micelles of dodecyl ammonium chloride with $n = 100.7$, $1.93kT$ for $\lambda = 1$. For the latter micelles the rim potential is shown in Figure 6 for all configurations of interest. For $\lambda = \frac{2}{3}$ the maximum variations of $W_h(\rho_0)$ are $2.49kT$ for configuration b and $1.71kT$ for c; for $\lambda = \frac{1}{3}$, configuration d, the variation is $1.05kT$. Of course, $W_h = 0$ everywhere in the cell when $\lambda = 0$.

We proceed with the average fluctuations. In general cell properties are averaged over the surface area A of the cell. Analogous to eq 27–29 for the counterions, we define the average potential of the head groups

$$\langle W_h \rangle = \int W_h \exp(-W_h/kT)\, dA / \int \exp(-W_h/kT)\, dA \quad (32)$$

the potential at the center of the cell

$$W_h^0 = W_h(0, 0) \quad (33)$$

and the free surface area of the cell

$$A_f = \int \exp[-(W_h - W_h^0)/kT]\, dA \quad (34)$$

Equation 30 takes the form

$$\langle W_h \rangle - W_h^0 = -kT \ln (A_f/A) \qquad W_h - W_h^0 \ll kT \quad (35)$$

Representative results are given in Table III. It is found that the deviations from eq 35 are relatively large, in particular for configuration b. The reason must be the great variations in the potential, as demonstrated in Figure 6. It appears that there is no simple, self-consistent way to take the fluctuations into account. This is the price one must pay for an approximate model. It is very fortunate that, due to the cell symmetry, the contributions of the fluctuations to the average properties are quite small, of order $0.1kT$ or less per head group according to Table III. So the necessity to neglect these fluctuations does not introduce a large error in the eventual free energy results.

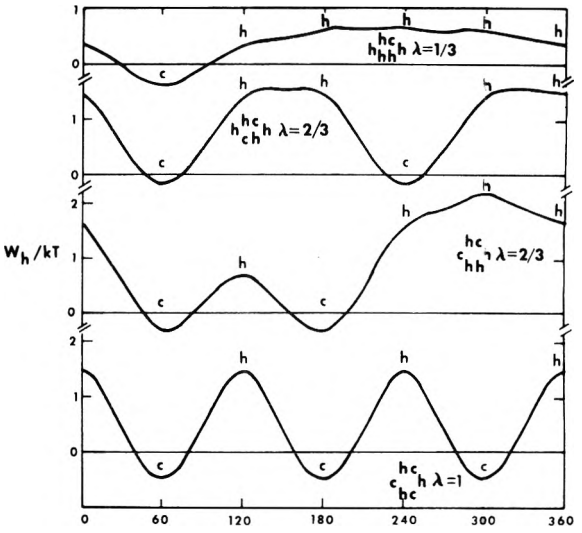

Figure 6. Head group potential W_h vs. angular distance along rim of the Stern layer cell for various configurations of nearest neighbors: head groups h with charge λe, and counterions with charge $-e$ per ion. Micelles of dodecyl ammonium chloride with $n = 100.7$, $\alpha = 0.5$, and $\lambda = 1$, $\frac{2}{3}$, and $\frac{1}{3}$.

Discussion

We have shown that a lattice model with the nonrandom, low temperature distribution of head groups and counterions is a good approximation to the ion distribution in the Stern layer. This result is in qualitative agreement with work by Kirkwood and Poirier[15] on the statistical mechanics of strong electrolyte solutions. These authors concluded that the introduction of ion size in concentrated solutions leads to stratifications of average space charge of alternating sign in the neighborhood of each ion.

The nonrandom ion distribution in the Stern layer was chosen on the basis of the statistical frequency of ion pairs of different kind on nearest neighbor lattice sites. A few remarks on the limitations of pair statistics are in order. For a one-dimensional lattice the quasichemical model counts the correct number of configurations.[7] This is no longer true for higher dimensional lattices, where configurations may be included that are physically impossible. For instance, eq 22 implies the absence of (cc) pairs, $N_{cc} = 0$, consistent with eq 13 and 10 for $\beta = 1 - 2\Theta$. However, inspec-

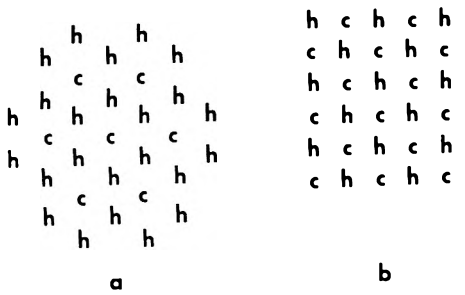

Figure 7. Regular or low temperature distribution of head groups h and counterions c in the Stern layer: (a) hexagonal lattice with $n_c = n/2$ and (b) square lattice with $n_c = n$.

tion of the two-dimensional hexagonal lattice shows that configurations with $N_{cc} = 0$ are not possible for $n_c > n/2$, compare Figure 7a. On the other hand, the low temperature condition $N_{cc} = 0$ may be satisfied for all compositions $n_c < n$ on the square lattice of Figure 7b. For $n/2 < n_c < n$ one might have a mixture of the two lattices, that is, a gradual transition from the hexagonal distribution for $n_c = n/2$ to the square distribution for $n_c = n$. In practice this transition is not important because in the calculations of the electric free energy in the next paper the range $n_c > n/2$ plays only a very minor role.

The foregoing leads into the final point of discussion, the possible errors introduced by a local decrease of the coordination number and the occurrence of vacant lattice sites. In our potential calculations such imperfections of the hexagonal lattice influence only the nearest neighbor contributions, because all more distant charges are smeared out and average charge densities are, of course, not affected by details of the lattice. Some model calculations were carried out for representative cases. It was found that, in general, lattice vacancies and lower coordination numbers have opposite effects on the central ion potential. For example, a vacancy rate of 10% reduces the counterion potential W_c in eq 24 by about $0.25kT$, while a 50% conversion from the hexagonal to a square lattice increases W_c by about $0.25kT$. In the fully charged lattice such changes do not influence the head groups at all as a first approximation, because the nearest neighbor potential vanishes in Eq 31, where $W_h = 0$ for $\lambda = 1$. In summary, imperfections of the hexagonal lattice contribute to potential fluctuations only in a minor way.

References and Notes

(1) D. Stigter, *J. Colloid Interface. Sci.*, **47**, 473 (1974).
(2) D. Stigter, *J. Phys. Chem.*, **78**, 2480 (1974).
(3) J. T. G. Overbeek in "Colloid Science", Vol. I, H. R. Kruyt, Ed., Elsevier, New York, N.Y., 1952, Chapter IV.
(4) S. Levine, J. Mingins, and G. M. Bell, *J. Electroanal. Chem.*, **13**, 280 (1967).
(5) D. Stigter, *J. Colloid Interface Sci.*, **23**, 379 (1967).
(6) D. Stigter, *J. Phys. Chem.*, **68**, 3603 (1964).
(7) T. L. Hill, "Introduction to Statistical Thermodynamics", Addison-Wesley, London, 1960, Chapter 20.
(8) "International Critical Tables", Vol. III, McGraw-Hill, New York, N.Y., 1928, p 28.
(9) A. E. Alexander and P. Johnson, "Colloid Science", Vol. 1, Oxford University Press, London, 1949, pp 86–89.
(10) E. A. Guggenheim, *Trans. Faraday Soc.*, **36**, 397 (1940).
(11) T. L. Hill, *J. Phys. Colloid Chem.*, **56**, 526 (1952).
(12) L. Benjamin, *J. Phys. Chem.*, **70**, 3790 (1966).
(13) J. M. Corkill, J. F. Goodman, and T. Walker, *Trans. Faraday Soc.*, **63**, 768 (1967).
(14) R. A. Robinson and R. H. Stokes, "Electrolyte Solutions", Butterworths, London, 1959.
(15) J. G. Kirkwood and J. C. Poirier, *J. Phys. Chem.*, **58**, 591 (1954).

Micelle Formation by Ionic Surfactants. IV. Electrostatic and Hydrophobic Free Energy from Stern–Gouy Ionic Double Layer

Dirk Stigter

Western Regional Research Center, Agricultural Research Service, U.S. Department of Agriculture, Berkeley, California 94710
(Received September 9, 1974; Revised Manuscript Received February 21, 1975)

Publication costs assisted by the U.S. Department of Agriculture

The charge effects and the hydrophobic interactions in micelle formation of ionic surfactants in aqueous salt solutions are reconsidered. The treatment is based on a Stern–Gouy model of the ionic double layer, with $(1 - \alpha)n$ counterions in a regular distribution between the ionic head groups, and the remaining αn counterions outside the hydrodynamic shear surface of the micelle in a diffuse Gouy–Chapman atmosphere. The model is developed in stages, starting from a Gouy–Chapman model used earlier. Results for the electrical free energy of the micelle, μ_n^{el}, given at each stage for representative solutions, show large effects of the discreteness-of-charge, and of the change of self-potential $\Delta\phi$ of the head groups upon micellization. In the final Stern–Gouy model results are given for the series of C_8 to C_{12} sodium alkyl sulfates and for dodecyl ammonium chloride. The uncertainty in μ_n^{el}/n is of the order of $0.5kT$, due partly to the paucity of information about α. As long as n is constant the details of micelle shape and ionic radii have little influence on μ_n^{el}. The residual free-energy change $\mu_n^0 - n\mu_1^0$, obtained from the equilibrium equation, is attributed mainly to hydrophobic interactions. This free-energy change is related to the hydrocarbon/water contact area, A_n for a micelle and A_1 for a monomer. In the bilinear form $\mu_n^0/n - \mu_1^0 = a_1A_n/n + a_2A_1 + a_3$, the coefficients are $a_1 \approx 33$ ergs/cm^2, $a_2 \approx -25$ ergs/cm^2 or -740 cal/mol per methylene group, and $a_3 \approx 1.6kT$ per monomer. A discrepancy in the Gouy–Chapman model between alkyl sulfate and dodecyl ammonium micelles is eliminated in the Stern–Gouy model, mainly due to the introduction of the self-potential term $\Delta\phi$. Corrections for salting-out effects on μ_1^0 bring the calculated results in concentrated sodium chloride solutions, up to 1 M, in line with those in more dilute solutions.

Introduction

The first three papers of this series deal with free-energy calculations for the Gouy–Chapman model of the electrical double layer around ionic micelles,[1] and with improvements of the model.[2,3] In the preceding paper[3] the ion distribution was discussed between the surface of the micelle core and the hydrodynamic shear surface of the micelle, the Stern layer which contains the head groups and about half the countercharge. It was concluded that a good approximation is the "low temperature" distribution which maximizes alternation of head groups and counterions on the sites of a two-dimensional hexagonal lattice. This distribution is used in the present paper to treat the electrical free energy of the micelle. We assume that the counterions in the Stern layer are at the average positions, with their center a short distance $\langle Z \rangle$ further than the ionic radius from the core surface. The remaining counterions are outside the shear surface, in a diffuse, Gouy–Chapman type, atmosphere. On the basis of this model we evaluate the free-energy changes that accompany micellization.

The thermodynamic framework has been developed earlier.[1] We recall that there are two different approaches to the equilibrium between monomers and micelles. The first one refers to the integral process, that is, the formation of a new micelle D_n^{n-} from n monomers D_1^-

$$nD_1^- \rightleftharpoons D_n^{n-} \tag{1}$$

subject to the equilibrium condition

$$\underset{\text{experiment}}{kT \ln x_n} - nkT \ln f_1x_1 + \underset{\text{theory}}{\mu_n^{el}} + \underset{\text{residue}}{\mu_n^0 - n\mu_1^0} = 0 \tag{2}$$

where x_n and x_1 are the mole fractions of micelles and of monomeric surfactant, μ_n^{el} is the electrical and μ_n^0 the nonelectrical part of the standard state chemical potential of the micelle, f_1 is the activity coefficient, and μ_1^0 the standard state chemical potential of the monomer. We shall deal with equilibria near the critical micelle concentration (cmc) where the activity coefficient of the micelles may be assumed equal to unity.

The second approach considers the growth process

$$D_n^{n-} + D_1^- \rightleftharpoons D_{n+1}^{(n+1)-} \tag{3}$$

which obeys, at the optimum micelle size, the differential equilibrium equation

$$\underset{\text{experiment}}{-kT \ln f_1x_1} + \underset{\text{theory}}{(\partial\mu_n^{el}/\partial n)_x} + \underset{\text{residue}}{(\partial\mu_n^0/\partial n)_x} - \mu_1^0 = 0 \tag{4}$$

The subscript x in eq 4 indicates that the pressure, the temperature, and the composition of the solution are constant in the differentiation.

For the purpose of this discussion we distinguish three different groups of terms, as indicated in eq 2 and 4. First, the concentration terms are determined from experiments, and so is the micelle number n. Secondly, the electrical terms are evaluated from the theoretical model summarized above. Finally, the nonelectrical parts of the standard free-energy changes are obtained as the remainder in the equilibrium equations. Current thinking is that the main contributions to these residual terms arise from hydrophobic interactions. It is interesting that, with the Gouy–Chapman model for the electrical terms, the residues for the C_8 to C_{12} series of alkyl sulfates were found to vary linearly

with the changes of the hydrocarbon/water contact area in micelle formation.[1] The main purpose of this paper is to investigate in how far this linearity persists when major shortcomings of the Gouy–Chapman theory are corrected. The previous work[1] was based on some fairly accurate sets of experimental data on micellar solutions of sodium alkyl sulfates and of dodecyl ammonium chloride available in the literature.[4-7] These data are used again in the present paper. The quality of the results from eq 2 and 4 depends mainly on the treatment of the electrical free energy. Unless indicated otherwise, the Stern layer is defined with the parameter values used or established in the preceding paper.[3] The discussion is given for micelles of cationic surfactants. The minor changes for anionic surfactants are obvious.

A suitable expression for μ_n^{el} is derived from an imaginary charging process of the micelle,[1] at constant micelle size and constant ionic strength, with an additional term $n\Delta\phi$ for the change of self potential[2] of the surfactant charge upon micellization.

$$\mu_n^{el} = \int_0^{ne} \psi_h(\lambda)\, d(ne\lambda) + n\Delta\phi \qquad (5)$$

The electrostatic potential of the head group ψ_h is a function of the charging parameter λ and takes into account the interionic interactions. The intraionic effects represented by $\Delta\phi$ in eq 5 depend on the change in dielectric environment when a surfactant head group moves from the bulk of the aqueous solution to the vicinity of the apolar micelle core. When the head group is regarded as a point charge $\Delta\phi$ is given[3] by eq P23.

Development of a Model for Electrical Free Energy μ_n^{el}

The preferred model for μ_n^{el} is developed in stages, starting from the Gouy–Chapman model used previously.[1] For this and for other intermediate models, values for μ_n^{el} are compared in Table I for a variety of micelles. The micellar solutions are characterized by the ionic strength and by the micelle number n. Further details are given elsewhere.[1,7] The columns in Table I refer to models a to f described below. The change of self potential is introduced in model e. So $\Delta\phi = 0$ for models a to d.

(a) We begin with the model of ref 1, spherical micelles whose radius R is calculated from the micellar weight and from the density of the micellized surfactant. The micelle has a uniform surface charge λne, and is surrounded by a diffuse, Gouy–Chapman ionic atmosphere with a thickness or Debye length $1/\kappa$ related to the ionic strength in the bulk of the aqueous solution far from the micelles. We identify the head group potential with the surface potential of the micelle

$$\psi_h = \frac{\lambda ne}{\beta\epsilon_w R(1 + \kappa R)} \qquad (6)$$

The parameter β is a function of κR and of $e\psi_h/kT$, and has been represented as a double expansion in powers of these variables.[8] Results for μ_n^{el}/nkT from eq 5 are presented in Table I under column a. The data for the alkyl sulfates do not differ significantly from those reported by Huisman[7] for the same systems.

For future reference we derive the contribution ψ_{dl} of the diffuse layer to ψ_h. The potential of the surface charge is $\lambda ne/\epsilon_w R$. So by difference one finds with eq 6

$$\psi_{dl} = \frac{Q}{\epsilon_w R}\left\{\frac{1}{\beta(1 + \kappa R)} - 1\right\} \qquad (7)$$

where $Q = \lambda ne$. The diffuse layer has spherical symmetry, and its charge inside the micelle vanishes. Therefore, the potential of the diffuse layer is constant and equal to ψ_{dl} everywhere within the surface R = constant.

(b) In the second model eq 6 is used again, but the charged micelle surface is now shifted to the surface of the head group charges in the Stern layer, compare Figure P1 in ref 3. According to Table I this choice, $R = t$, reduces μ_n^{el} somewhat compared with model a.

(c) The distance of closest approach between head groups and counterions is $\sigma = r_h + r_c$. For this reason the diffuse layer is now moved outward and its potential ψ_{dl} is obtained from eq 7 with $R = t + \sigma$, see Figure P1 in ref 3. The head group charges are smeared out in the surface t = constant as before in model (b), and contribute $\lambda ne/\epsilon_w t$ to ψ_h. The results in Table I indicate that the shift of the diffuse layer, column b to c, increases μ_n^{el}/n by amounts varying from $0.92kT$ to $2.36kT$. In a discussion of a very similar model Mukerjee[9] has pointed out that results for the surface potential of the micelle are too high and the dependence on ionic strength is unreasonable. The main reason is the assumption that $\alpha = 1$, that is, no counterions in the Stern layer. In the final model more realistic values, about $\alpha = 0.5$, will be taken. However, in order to show the various discrete ion effects, we shall assume $\alpha = 1$ in the intermediate models d, e, and f.

(d) This model introduces the largest discrete ion correction. Around a head group one assumes a charge-free circular surface with area $4\pi t^2/n$, the average area per head group. In the rest of the surface t = constant the uniform charge density $\lambda ne/4\pi t^2$ is unchanged. A schematic cross section of the micelle is given in Figure 1, with the head group charge at P for $r = t$. Looking ahead to the interaction with counterions in the Stern layer, we need also the more general case $r \neq t$, when the potential in P is given by[10]

$$\psi = \frac{ne}{2\epsilon_w t}\left\{1 + \frac{t}{r} - \left(1 - 2\frac{t}{r}\cos\theta + \frac{t^2}{r^2}\right)^{1/2}\right\} + \frac{ne(1 - \omega)}{2\epsilon_w b(1 + \omega)}\left\{1 - x - (1 - 2x\cos\theta + x^2)^{1/2} + x^{\omega/(1+\omega)} \times \int_0^{x^{1/(1+\omega)}} \frac{(1 - 2y^{1+\omega}\cos\theta + y^{2+2\omega})^{1/2} - 1 + y^{1+\omega}}{y^{1+\omega}}\, dy\right\} \qquad (8)$$

where x and ω have the same meaning as before[3] in eq P17.

Following spherical geometry the charge-free surface area associated with the angle θ in Figure 1 is equal to $2\pi t^2(1 - \cos\theta)$. So the contributions of the smeared-out neighboring head groups to ψ_h are obtained from eq 8 with $\cos\theta = 1 - 2/n$ and $r = t$. The diffuse layer contribution remains the same as before. The comparison of columns c and d in Table I shows that the discrete ion correction for the central head group lowers μ_n^{el}/n by an appreciable amount, from $1.51kT$ to $2.59kT$. The present discrete ion effect was first introduced by Overbeek and Stigter[11] whose approximate corrections for dodecyl sulfate micelles ranged from $1.76kT$ to $1.89kT$. This compares well with the results in Table I, $1.69kT$ to $1.94kT$ for essentially the same micelles. A similar correction has been applied by Grahame[12] in the "cut-off disk" model for counterions adsorbed at the mercury/water interface.

(e) The self-potential change $\Delta\phi$ of the central head

TABLE I: Electrical Free Energy for the Different Micelle Models a to f as Described in the Text

	c_{salt},[a] M	n	μ_n^{el}/nkT a	b	c	d	e	f
$C_8H_{17}SO_3Na$	0.134	23.7	2.44	2.05	2.97	1.46	1.78	1.72
	1.03	47.8	1.67	1.40	3.17	1.41	1.78	1.68
$C_{12}H_{25}SO_4Na$	0.0081	57.3	4.72	4.44	5.71	4.02	4.41	4.31
	0.3	123	2.62	2.40	4.69	2.75	3.19	3.06
$C_{12}H_{25}NH_3Cl$	0.0156	100.7	4.84	4.80	6.69	4.26	6.20	6.01
	0.066	163	4.06	3.90	6.26	3.67	5.67	5.46

[a] cmc + c_{NaCl}.

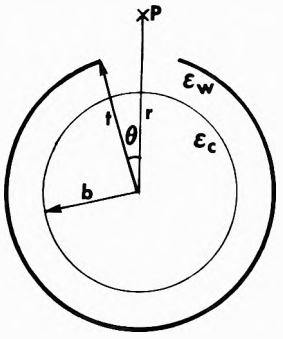

Figure 1. Cross section through the dielectric sphere. Part of concentric surface with radius t, heavy curve, has uniform charge density $ne/4\pi t^2$. Potential in P is given by eq 8.

group, calculated[3] with $r = t$ in eq P23, is now added to μ_n^{el}/n. Inspection of columns c, d, and e of Table I shows that allowing for $\Delta\phi$ partially compensates the previous correction in model d for the smeared-out central charge. Both corrections are strongly dependent on the distance between head group charge and core surface, $t - b$ in Figure 1.

(f) We now introduce the lattice model of the Stern layer, with discrete head groups on the six nearest neighbor sites of the central head group. Their contribution to $\psi_h(\lambda)$ is evaluated[3] with eq P17, with $r = t$ and with λe instead of e, and with $M = n$ in eq P3 and P4 for θ. The $n - 7$ more distant head groups remain smeared out as before. For these ions we use eq 8, again with $r = t$. In order to account for the larger charge free area corresponding to 7 out of n sites, we now have in eq 8 $\cos\theta = 1 - 14/n$. Following columns e and f in Table I the present changes do not decrease μ_n^{el}/n a great deal, only $0.06kT$ to $0.23kT$. This confirms the earlier finding[10] that the smearing out of the nearest neighbor ions does not change the results very much.

At this point we are ready for the final model of the series in which counterions are admitted in the Stern layer, and the equilibrium of the charge distribution comes into play. The n head groups and $n_c = (1 - \alpha)\lambda n$ counterions are distributed over $M = n + n_c$ lattice points. Following the low temperature approximation,[3] eq P21, each head group has as nearest neighbors $f_h = 6(1 - \alpha)\lambda$ counterions with charge $-e$ and $6 - f_h$ head groups with charge $+\lambda e$. The contributions of these ions to ψ_h are obtained[3] with eq P17, P3, and P4. Outside the area allocated to these seven discrete ions the remaining charges in the Stern layer are smeared out uniformly and their potential is calculated with eq 8 where $\cos\theta = 1 - 14/M$. It is observed in eq P17 and 8 that head groups are at distance $t = b + h$, and counterions are at distance $r = b + r_c + \langle Z \rangle$ from the micelle center, as indicated[3] in Figure P1. The potential of the diffuse layer is obtained from eq 7, with $R = t + \sigma$ as before, and with $Q = \alpha\lambda ne$. In this way the calculation of the head group potential $\psi_h(\lambda)$, and hence of μ_n^{el}, is straightforward, provided that α is known as a function of λ.

Variable Parameters in the Evaluation of μ_n^{el}

As mentioned already, experiments suggest a roughly equal distribution of counterions between the Stern layer and the diffuse layer. This means that for fully charged micelles, $\lambda = 1$, the equilibrium is around $\alpha = 0.5$. The main problem now is to choose a function $\alpha(\lambda)$ such that an equilibrium distribution of counterions, consistent with the model, is maintained during the entire charging process. Strictly speaking, one should require that the electrochemical potential of the counterions in the Stern layer be independent of λ, and always equal to that in the bulk solution. The application of this condition entails the evaluation of the adsorption isotherm of the counterions, i.e., $n_c(\lambda)$, from a model of the Stern layer. In the earlier work[10] the adsorption of counterions in the fully charged Stern layer, $\lambda = 1$, was treated with a cell model, consistent with our present assumptions of the Stern layer. Unfortunately, further, exploratory calculations have shown that the function $n_c(\lambda)$ is very sensitive to some uncertain details of the model, such as the cell size as a function of $M(\lambda) = n + n_c(\lambda)$. Such details do not otherwise enter into the evaluation of μ_n^{el}. Moreover, the cell model for counterion adsorption is by no means exact. For these reasons the attempts to derive $n_c(\lambda)$ were abandoned in favor of a comparison between results of μ_n^{el} for two different, assumed functions for $n_c(\lambda) = (1 - \alpha)\lambda n$, that is, two functions for $\alpha(\lambda)$ which are intuitively reasonable.

We choose the two functions $\alpha(\lambda)$ by considering the diffuse layer. For very low potentials, $e\psi_h(\lambda) \ll kT$, the Debye–Hückel approximation applies, and the relative distribution of countercharge in space is constant. Therefore

$$\alpha(\lambda) = \alpha(1) \tag{9}$$

should be a reasonable first approximation for any λ. In the Gouy–Chapman theory one finds that relatively more countercharge accumulates in the high potential region, near the charged interface. This suggests that α may decrease with increasing λ, for instance, linearly as the function

$$\alpha(\lambda) = 0.5(1 + \alpha(1)) - 0.5(1 - \alpha(1))\lambda \tag{10}$$

The two functions are shown in Figure 2 for $\alpha(1) = 0.55$, with the corresponding curves for n_c/n. With these functions we have carried out the integration in eq 5 to obtain

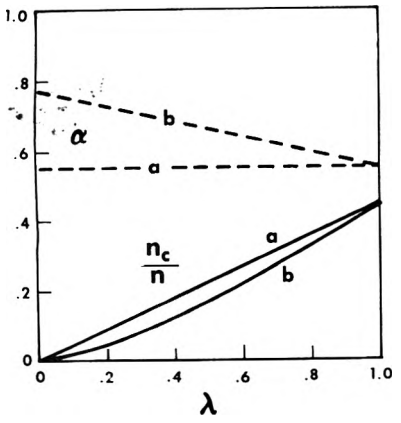

Figure 2. Distribution of countercharge around micelles vs. charging parameter λ; α is fraction of countercharge in Gouy–Chapman layer; n_c/n is ratio of counterions and head groups in Stern layer. Curves a and b correspond to eq 9 and 10, respectively. In all cases $\alpha(1) = 0.55$.

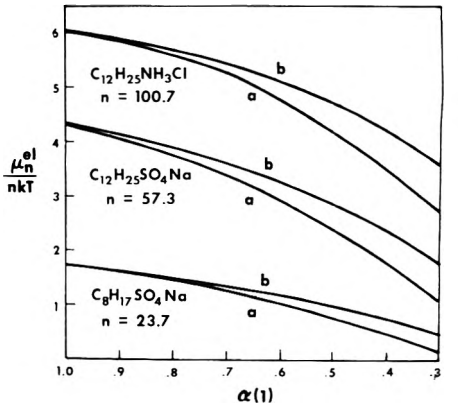

Figure 3. Electrical free energy of micelle, per monomer, in various micellar solutions defined in Table I, vs. fraction of countercharge in Gouy–Chapman layer. Curves a and b correspond to different charge distributions in the charging process, eq 9 and 10, respectively.

μ_n^{el} for a variety of micelles and a range of $\alpha(1)$ values. Representative results are plotted in Figure 3. It appears that there is considerable dependence of μ_n^{el} on $\alpha(1)$ and on the distribution function $\alpha(\lambda)$. We return to this point in the next section.

We have also tested the influence of other parameters of the model. For $\alpha(\lambda) = \alpha(1)$, and using practical values of $\alpha(1)$, Table II gives the effects of varying the ionic radii. Columns a and b show that a decrease of 0.5 Å in the distance of closest approach σ between ions, that is, in the radius R in eq 7, decreases μ_n^{el}/n by $0.04kT$ to $0.09kT$. So the uncertainty in the ionic radii does not affect the results significantly.

We now turn to the effects of micelle shape. It is assumed that micelles are spherical if the length l_i of the stretched alkyl chain of the C_i surfactant exceeds the core radius b. Taking 2.0 Å for the radius of the terminal methyl group,[13] the core surface at $d = 0.8$ Å above the α-carbon atoms,[2] and 1.257 Å between successive carbon atoms along the chain,[13] we have

$$l_i = 1.257(i - 1) + 2.8 \text{ Å} \qquad (11)$$

If the core radius $b = l_i$, let the micelle number be $n = n_1$. With eq 11 and with the core density[3] from eq P1, one finds for the C_8 to C_{12} micelles $n_1 = 26.8$ (for C_8), 32.9 (C_9), 39.4 (C_{10}), 46.7 (C_{11}), and 54.5 (C_{12}).

It is convenient to express the core radius in terms of n, n_1, and l_i. For small, spherical micelles the core radius is

$$b = l_i(n/n_1)^{1/3} \qquad n < n_1 \qquad (12)$$

Larger, wormlike[14] micelles are assumed to have a cylindrical section that may be bent, and is capped by two half spheres, with diameter $2l_i$. The length L of the central axis of the cylinder is

$$L = 4l_i(n - n_1)/(3n_1) \qquad n > n_1 \qquad (13)$$

If the central axis of the micelle is straight, it is easily found that the surface area of the core is

$$S_n = 4\pi l_i^2(2n + n_1)/(3n_1) \qquad n > n_1 \qquad (14)$$

The surface area of a bent cylinder, such as a torus, does not depend on the curvature of the cylinder axis. Consequently, eq 14 is valid for wormlike micelles with arbitrary curvature of the central axis.

Since the electrostatic calculations are made only for spheres, the wormlike micelle is replaced by an equivalent sphere. We compare the results for two different substitutions. One is based on constant volume of the core, in which case eq 12 is used for $n > n_1$. In a second method the surface area of the core is kept constant and, in view of eq 14, the core radius becomes

$$b = l_i(2n + n_1)^{1/2}(3n_1)^{-1/2} \qquad n > n_1 \qquad (15)$$

The comparison of results for μ_n^{el} based on eq 12 and 15 gives an idea of the effect of micelle shape on μ_n^{el}. In fact, Table II, columns a and c, shows no more than minor differences, at most $0.17kT$ between the two calculations. It is clear that the effect of micelle shape on μ_n^{el} is not very important. In the rest of this paper we shall use the wormlike model, eq 15 for $n > n_1$.

Finally, we consider variations of the core/water interface where the dielectric constant changes from $\epsilon_c = 2$ to $\epsilon_w = 78.5$. This interface was found[2] at $d = 0.8 \pm 0.4$ Å above the α-carbon atoms of the micellized surfactants. Table II gives results of μ_n^{el}/n and of $\Delta\phi$ for the limiting values $d = 0.4$ and 1.2 Å in columns d and e. It is observed that the changes of μ_n^{el}/n are close to those in $\Delta\phi$. Between $d = 0.4$ and 1.2 Å μ_n^{el}/n varies up to $3.68kT$, while $\mu_n^{el}/n - \Delta\phi$ changes at most $0.29kT$. This means that only the self potential $\Delta\phi$ of the head groups is sensitive to the exact change of the dielectric constant through the micelle surface. However this change is not of major influence on the interaction between the ions. This result, expected from the nearly spherical symmetry of the charge distribution, has been used already in the previous paper.[2]

The discussion of the model for μ_n^{el} is now concluded. The rest of the paper deals with the application of the theory to the experimental data used in ref 1.

Evaluation of Residual Free Energy in Equilibrium Equation

The analysis of the residual terms in eq 2 follows largely the procedure developed earlier for the Gouy–Chapman model.[1] We take advantage of the outstanding feature of ionic interactions in water, their great sensitivity to the ionic strength. As we add salt to a micellar solution, the equilibrium shifts and all thermodynamic terms, including $\mu_n^0 - n\mu_1^0$, sweep through a range of values. This magnifies the experimental output and is of considerable help in testing any kind of micelle theory. We start with a cor-

TABLE II: Influence of Model Parameters on Electrical Free Energy of Micelles, μ_n^{el}, and on Self Energy of Head Groups, $\Delta\phi$

			μ_n^{el}/nkT	$\Delta\phi/kT$	μ_n^{el}/nkT		μ_n^{el}/nkT	$\Delta\phi/kT$	μ_n^{el}/nkT	$\Delta\phi/kT$
	n	α	a		b	c	d		e	
$C_8H_{17}SO_4Na$	23.7	0.50	0.78	0.32	0.74	0.78	0.73	0.24	0.86	0.43
	47.8	0.50	0.69	0.36	0.61	0.71	0.65	0.28	0.76	0.49
$C_{12}H_{25}SO_4Na$	57.3	0.50	2.41	0.39	2.37	2.41	2.36	0.31	2.48	0.52
	123	0.50	1.45	0.44	1.36	1.54	1.42	0.35	1.52	0.58
$C_{12}H_{25}NH_3Cl$	100.7	0.41	3.59	1.94	3.53	3.64	2.88	1.12	6.56	5.05
	163	0.41	3.14	2.00	3.05	3.31	2.45	1.17	6.12	5.13

[a] Reference values. [b] Test of ionic radii, with σ 0.5 Å smaller than in a. [c] Test of micelle shape: spheres, eq 12, compared with wormlike micelles, eq 15 for $n > n_1$, in a. [d,e] Test of dielectric constant, with d = 0.4 Å in d and 1.2 Å in e compared with d = 0.8 Å in a.

rection for the salting-out effect on the alkyl group of the unassociated surfactant.

When $\mu_n^0 - n\mu_1^0$ is obtained as the residue in eq 2, μ_1^0 refers to the particular salt solution in which the micellar equilibrium has been studied. In general this value, μ_1^0(salt), differs from the value in pure water, μ_1^0(water). In the following discussion of $\mu_n^0 - n\mu_1^0$ we shall use water at 25° as a reference solvent for μ_1^0, after conversion of the data with

$$\mu_1^0(\text{water}) = \mu_1^0(\text{salt}) - (0.129 + 0.0645i)kTc_{salt} \quad (16)$$

In this expression c_{salt} is the total molarity of cmc and added sodium chloride, and i is the number of carbon atoms in the alkyl chain of the surfactant. Equation 16 is based on the solubilities of ethane, propane, and n-butane in water and in 1 M sodium chloride solutions, reported by Morrison and Billett.[15]

As explained above, a major problem is the function $\alpha(\lambda)$ for the distribution of the counterions between the Gouy–Chapman and the Stern layer, that is, outside and inside the shear surface of the micelle. For the fully charged micelle this function, $\alpha(1)$, can be evaluated from transport measurements.[16] Figure 4 shows the data available for sodium dodecyl sulfate (SDS) as open points, and for dodecyl ammonium chloride (DACl) as solid points. As stated earlier,[16] it is likely that the conductivity results (triangles) are more reliable at low ionic strength, and that the electrophoretic data (circles) are more accurate at high ionic strength.

On the basis of Figure 4 we select $\alpha(\lambda) = \alpha(1) = 0.5$ for SDS and $\alpha(\lambda) = \alpha(1) = 0.41$ for DACl to evaluate the electrostatic terms in eq 2 and 4. The residues are plotted vs. n in Figure 5a. The integral and the differential data are compared using the method of ref 1 as follows. The open points for $\mu_n^0/n - \mu_1^0$ from eq 2 are fitted with a second degree polynomial in ln n (least-squares test), the solid curves in Figure 5. The corresponding differential polynomials for $(\partial\mu_n^0/\partial n)_x - \mu_1^0$ are the broken curves which for good experiments and a good theory should match the filled points for the residues from eq 4. It is obvious from the large discrepancy between broken lines and filled points in Figure 5a that something is wrong, either in the experiments or in the theory. Now, for SDS the circles and the triangles have been derived from two different sets of light scattering experiments on different SDS preparations. The difference between the two sets of results is relatively small, so it is not the experiments but the theory that fails the test of the differential residues in Figure 5a.

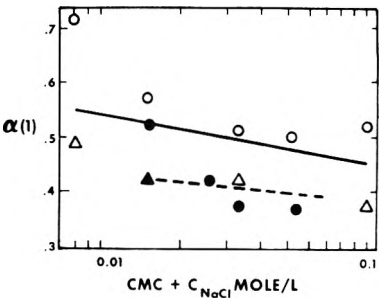

Figure 4. Fraction of countercharge outside shear layer of micelles vs. ionic strength: open points, sodium dodecyl sulfate; filled points, dodecyl ammonium chloride; circles, from electrophoresis; triangles, from electric conductance.

There is considerable latitude in the choice of $\alpha(1)$. For instance, the straight lines in Figure 4 are well within the uncertainty of the experimental points. The solid line for SDS is given by

$$\alpha(1) = 0.5 - 0.0174 \log (c_{salt}/0.031) \quad (17)$$

The broken line for DACl is

$$\alpha(1) = 0.41 - 0.0087 \log (c_{salt}/0.031) \quad (18)$$

Equations 17 and 18 for $\alpha(1)$ have been used with the two functions $\alpha(\lambda)$ of eq 9 and 10. Figure 5b is based on eq 9 for constant $\alpha(\lambda)$, and Figure 5c on the variable function $\alpha(\lambda)$ in eq 10. In both Figure 5b and 5c the broken lines are close to the filled points for the differential residues. This means that such self-consistency depends mainly on $\alpha(1)$ as a function of ionic strength, or of micelle size, but not much on the particular function $\alpha(\lambda)$. As explained above, there are theoretical grounds to prefer a variable function $\alpha(\lambda)$. Equation 10 is a simple, linear example of such a function. Unfortunately, at the present time there is no objective criterion by which to narrow the choice of $\alpha(\lambda)$ any further. The difference between the results in Figure 5b and 5c is indicative of this uncertainty in $\alpha(\lambda)$.

Changes of Free Energy and of Interfacial Area

In this section we consider the correlation between $\mu_n^0 - n\mu_1^0$ and the change of hydrocarbon/water contact area, $A_n - nA_1$, in micellization. For the monomer, a cylindrical alkyl group with a rounded end of radius r_1 = 2.615 Å and length l_i from eq 11, the contact area with water is

$$A_1 = 2\pi l_i r_1 \quad (19)$$

For micelles the surface area of the core is $4\pi b^2$, with b from eq 12 and 15 for spherical and wormlike micelles, re-

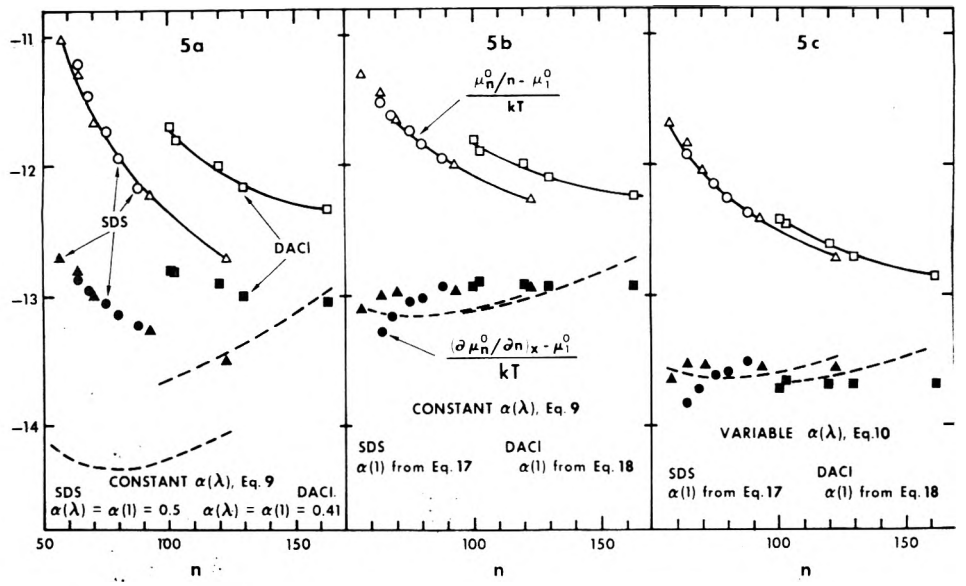

Figure 5. Comparison of average and differential free energy changes as a function of micelle number n in aqueous sodium chloride solutions: circles and triangles, sodium dodecyl sulfate (SDS); squares, dodecyl ammonium chloride (DACl); open points and solid curves, $(\mu_n^0/n - \mu_1^0)/kT$; filled points and broken curves, $((\partial\mu_n^0/\partial n)_x - \mu_1^0)/kT$. Points in 5a, 5b, and 5c are based on different distributions for counterions between the Stern layer and Gouy–Chapman layer from eq 9, 10, 17, and 18.

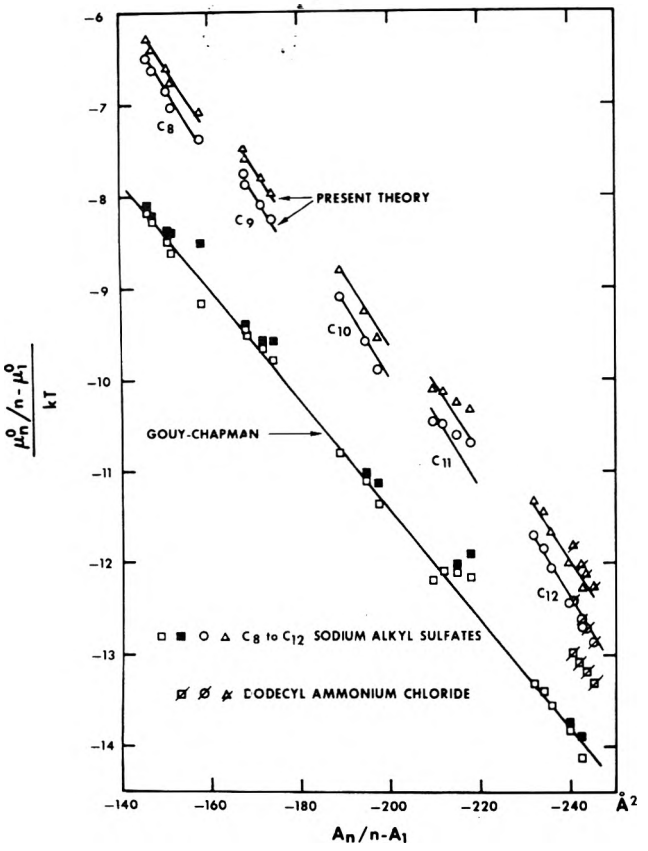

Figure 6. Residual free-energy change, $\mu_n^0/n - \mu_1^0$ from eq 2 vs. change of hydrocarbon/water contact area, $A_n/n - A_1$, for micellization of C_8 to C_{12} sodium alkyl sulfates and of dodecyl ammonium chloride (DACl) in aqueous sodium chloride solutions: open squares, Gouy–Chapman model, ref 1; filled squares, same with correction for salting-out effects; triangles and circles, present theory, with $\alpha(1)$ from eq 17 for alkyl sulfates and from eq 18 for DACl; triangles, constant $\alpha(\lambda)$, eq 9; circles, variable $\alpha(\lambda)$, eq 10.

spectively. Subtracting the area shielded by the head groups we have

$$A_n = 4\pi b^2 - n\pi r_1^2 \tag{20}$$

Figure 6 shows $\mu_n^0/n - \mu_1^0$ vs. $A_n/n - A_1$ for the series of C_8 to C_{12} sodium alkyl sulfates and for dodecyl ammonium chloride. The several sets of points have been calculated with the same experimental data in eq 2, but with different models for μ_n^{el}. The triangles correspond to the model of Figure 5b, and the circles to Figure 5c. These results are compared with the open squares which are based on the Gouy–Chapman model of ref 1. It is found that the present Stern–Gouy model, besides being more realistic, raises μ_n^0/n by $1.5kT$ to $2kT$, while the remaining uncertainty is of the order of $0.5kT$.

The filled squares in Figure 6 are obtained after correcting the Gouy–Chapman results of ref 1 for the salting-out effects on μ_1^0 with eq 16. This correction becomes important only at high ionic strength, 0.3 m or more.

As discussed in ref 1 the Gouy–Chapman theory produces a discrepancy between the results for SDS and DACl, the open squares without and with cross bars in the lower right-hand corner of Figure 6. It is observed that in the Stern layer theory this discrepancy disappears. This is largely due to the introduction of the self potential $\Delta\phi$ in μ_n^{el}/n, compare Table II.

The most important feature of Figure 6 is the functional relation between the data. In ref 1 the Gouy–Chapman results were fitted with a linear relation between $\mu_n^0/n - \mu_1^0$ and $A_n/n - A_1$. It is interesting that in the Stern layer model a linear relation is preserved to such a large extent. The main change is a parallel shift of the points. The new results have been fitted with a bilinear form in A_n/n and A_1, the line segments in Figure 6. Least-squares analysis gives

$$\mu_n^0/n - \mu_1^0 = (0.0758A_n/n - 0.0588A_1 + 1.60)kT \tag{21}$$

for constant $\alpha(\lambda)$, the triangles in Figure 6. The circles for variable $\alpha(\lambda)$ are represented by

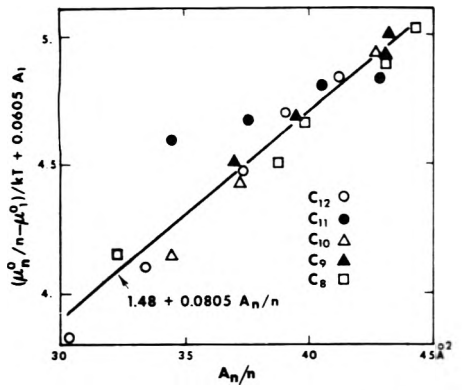

Figure 7. Correlation of residual free-energy change in eq 2 with core/water contact area for micelles of C_8 to C_{12} sodium alkyl sulfates in aqueous sodium chloride solutions. Variable $\alpha(\lambda)$, and $\alpha(1)$ from eq 17.

$$\mu_n^0/n - \mu_1^0 = (0.0805A_n/n - 0.0605A_1 + 1.48)kT \quad (22)$$

It is noted that the change of $\mu_n^0/n - \mu_1^0$ with chain length does not depend significantly on the theory for μ_n^{el}. In all three cases in Figure 6 the correlation between the various clusters gives a linear relation with A_1, with a coefficient of about $0.060kT/Å^2$. This gives around $-1.25kT$ per methylene group, or −740 cal/mol, for transfer from bulk water to the interior of the micelle core.

We now consider the correlation between free energy and micelle core/water interface. For the results of variable $\alpha(\lambda)$, eq 22, Figure 7 presents $\mu_n^0/n - \mu_1^0 + 0.0605A_1$ as a function of A_n/n. In this plot the dependence of the free energy on A_1 has been eliminated. It appears that the remainder of the free energy depends linearly on A_n/n within the scatter of the data, and yields a core/water interfacial free energy of $0.080kT/Å^2$ = 33 ergs/cm². This result is between that of the alkyl/water interface above, $0.060kT/Å^2$ = 25 ergs/cm², and of a macroscopic hydrocarbon/water interface, about 50 ergs/cm².

It is observed that the results in Figure 7 are not only for different micelle sizes, but also for different chain lengths, that is, in solutions of different ionic strength. The present Stern–Gouy theory includes a correction for the salting-out effect on μ_1^0 which is particularly important at high ionic strength, compare Figure 6. The good agreement of the data with a single curve in Figure 7 suggests that the Stern–Gouy model applies equally well in solutions of high and low ionic strength, at least at the present level of accuracy.

Discussion

As pointed out above, the difference between the coefficients of A_n/n and of A_1 is not surprising. The absolute values obtained here should not be taken too serious in view of the approximate nature of the treatment. Corrections for van der Waals interaction might give significant changes in all terms of eq 21 and 22. Furthermore, for a molecular interpretation the present models for A_1 and for A_n/n are crude. A more precise model for the alkyl chain, perhaps along the lines suggested by Hermann,[17] would increase the effective contact area with water and, therefore, reduce the coefficient of A_1 in eq 21 and 22. Any deviation from a smooth core surface enlarges A_n and, hence, decreases the coefficient of A_n/n below the present values.

The present model for μ_n^{el} is more detailed than the earlier Gouy–Chapman model.[1] Consequently, one needs more experimental information to fix the model parameters. Unfortunately, this information is incomplete, in particular as far as α is concerned, and this has restrictive consequences. In the first place, in Figure 5 we have used the differential relation eq 4 to choose α as a function of ionic strength. This procedure compromises further results of eq 4. For this reason a comparison of integral and differential results, as in Figure 3 of ref 1 for the Gouy–Chapman model, would be less meaningful in the present treatment. Secondly, in the Stern model α has not been defined as a function of n. Hence, one cannot obtain unique micelle distributions such as calculated[18] for the Gouy–Chapman model.

For further progress it would be very helpful to have new sets of experimental data on light scattering, electrophoresis, electric conductance, and viscosity for a variety of selected micellar systems. The concerted analysis of such data[16] would not only specify the Stern layer for various micelles and set up trail markers for an improved treatment of α, but might serve also to further elucidate the specificity of surfactant head groups. Effects of head groups on the cmc have been discussed in ref 2. The specific effects on micelle size are at least as interesting, but not well documented. Differences between SDS and DACl, compare Table I in ref 1, suggest that surfactants with head groups of smaller cross sectional area form larger micelles. This qualitative rule is consistent with considerations of the packing of ions in the Stern layer, as balanced by the extent of the micelle core/water contact area in the differential relation, eq 4, for the optimal micelle size. A somewhat similar approach, using a variant of eq 4, has been explored in recent work by Tanford[19,20] who has made very interesting connections with the properties of monolayers and with the architecture of biological membranes. This area of research would greatly benefit from further experimental work on micellar solutions as indicated above, including solutions of partially ionized surfactants[21–23] where almost all information on micelle size is lacking.

It remains to point out some limitations inherent in the model. The discontinuity in the ion distribution between the Stern layer and the Gouy layer is an unsatisfactory feature which cannot be easily remedied by refining the present ad hoc model. An improved statistical treatment of the entire micellar double layer is difficult, although several important elements of a more rigorous theory have been worked out in the case of flat double layers.[24–26] The present theory also neglects the effects of ion fluctuations, a well-known hurdle in the path of extending the Debye–Hückel theory of strong electrolytes to higher concentrations.[27] It is likely that the total fluctuation corrections to μ_n^{el}/n are of the same order of magnitude as activity effects in salt solutions,[28] that is, of the order of $0.2kT$ for monovalent ions. This surmise is consistent with the finding in the preceding paper[3] that potential fluctuations in the Stern layer are of the order of $0.2kT$.

References and Notes

(1) D. Stigter, *J. Colloid Interface Sci.*, **47**, 473 (1974).
(2) D. Stigter, *J. Phys. Chem.*, **78**, 2480 (1974).
(3) D. Stigter, *J. Phys. Chem.*, preceding paper. References to equations, tables, and figures in paper III of this series are preceded by a P.
(4) R. J. Williams, J. N. Phillips, and K. J. Mysels, *Trans. Faraday Soc.*, **51**, 728 (1955).
(5) K. J. Mysels and L. H. Princen, *J. Phys. Chem.*, **63**, 1696 (1959).
(6) L. M. Kushner, W. D. Hubbard, and R. A. Parker, *J. Res. Natl. Bur. Stand.*, **59**, 113 (1959).

(7) H. F. Huisman, *Proc. K. Ned. Akad. Wet., Ser. B*, **67**, 407 (1964).
(8) D. Stigter, *J. Electroanal. Chem.*, **37**, 61 (1972). A computer program, coded in Fortran, for the evaluation of the potential and of other double layer functions may be requested from the author.
(9) P. Mukerjee, *J. Phys. Chem.*, **73**, 2054 (1969).
(10) D. Stigter, *J. Phys. Chem.*, **68**, 3603 (1964).
(11) J. T. G. Overbeek and D. Stigter, *Recl. Trav. Chim. Pays-Bas*, **75**, 1263 (1956).
(12) D. C. Grahame, *Z. Elektrochem.*, **62**, 264 (1958).
(13) L. Pauling, "The Nature of the Chemical Bond", Cornell University Press, New York, N.Y., 1960.
(14) D. Stigter, *J. Phys. Chem.*, 70, 1323 (1966).
(15) T. J. Morrison and F. Billett, *J. Chem. Soc.*, 3819 (1952).
(16) D. Stigter, *J. Colloid Interface Sci.*, **23**, 379 (1967).
(17) R. B. Hermann, *J. Phys. Chem.*, **76**, 2754 (1972).
(18) D. Stigter and J. T. G. Overbeek, *Proc. Int. Congr. Sur. Act., 2nd, 1957*, **1**, 311 (1957).
(19) C. Tanford, *Proc. Natl. Acad. Sci. USA*, **71**, 1811 (1974).
(20) C. Tanford, "The Hydrophobic Effect: Formation of Micelles and Biological Membranes", Wiley, New York, N.Y., 1973.
(21) A. Veis and C. W. Hoerr, *J. Colloid Sci.*, **15**, 427 (1960).
(22) F. Tokiwa and K. Ohki, *J. Phys. Chem.*, **71**, 1824 (1967); *Bull. Chem. Soc. Jpn.*, **41**, 2828 (1968).
(23) H. Maeda, M. Tsunoda, and S. Ikeda, *J. Phys. Chem.*, **78**, 1086 (1974).
(24) F. H. Stillinger, Jr., and J. G. Kirkwood, *J. Chem. Phys.*, **33**, 1282 (1960).
(25) F. H. Stillinger, Jr., *J. Chem. Phys.*, **35**, 1584 (1961).
(26) F. P. Buff and F. H. Stillinger, Jr., *J. Chem. Phys.*, **39**, 1911 (1963).
(27) H. S. Harned and B. B. Owen, "The Physical Chemistry of Electrolytic Solutions", 3rd ed, Reinhold, New York, N.Y., 1958, p 57.
(28) D. Stigter, *J. Phys. Chem.*, **64**, 838 (1960).

A Molecular Theory of Fluid–Fluid Equilibria[1]

R. O. Neff* and D. A. McQuarrie

Department of Chemistry, Indiana University, Bloomington, Indiana 47401 *(Received July 19, 1974; Revised Manuscript Received December 5, 1974)*

The pure-fluid statistical mechanical perturbation theory of Weeks, Chandler, and Andersen and the various n-fluid corresponding states theories of fluid mixtures have been used to predict fluid–fluid equilibrium over wide ranges of pressure. It appears that the van der Waals one-fluid theory is the most reliable of the n-fluid mixture theories. The approach used to test the various mixture emphasizes the mole fraction-, pressure-, and temperature-dependence of the free energy more than a quantitative prediction of the free energy of mixing. Our work indicates that there are actually two factors that determine the fluid–fluid critical locus of a simple mixture: the ratio of the well depth of the mixed interaction to the largest well depth of the pure interaction ($\epsilon_{12}/\epsilon_{11}$) and the ratio of the molecular diameters (σ_{22}/σ_{11}). As $\epsilon_{12}/\epsilon_{11}$ becomes larger the region of fluid–fluid equilibrium decreases. $\epsilon_{12}/\epsilon_{11}$ is a measure of the gain in stability on mixing due to 1–2 interactions vs. separating to increase 1–1 interactions. As σ_{22}/σ_{11} increases the region of the fluid–fluid equilibrium increases. As the component 2 molecules become larger they disrupt the 1–1 interactions more effectively. A series of figures is given in reduced units that allows one to predict the critical locus of any binary mixture given the appropriate intermolecular potential parameters.

Introduction

The purpose of this paper is to investigate the effect of intermolecular parameters on the critical loci of binary mixtures that are known to exhibit fluid–fluid equilibrium.[2a] This is done by using the van der Waals one-fluid theory of mixtures, which has been shown elsewhere[2b,3] to be not only the best of the so-called n-fluid mixture theories but also in fairly good agreement with more rigorous (and costly) statistical mechanical calculations. Hopefully this will help us to understand the phenomenon from a molecular point of view.

Five types of two-phase equilibria in binary mixtures are known, these being solid–solid, solid–liquid, solid–gas, liquid–liquid, and liquid–gas. It has been suggested that there exists a sixth additional type of heterogeneous equilibrium in binary mixtures, gas–gas equilibrium.[2] One of the simplest systems where gas–gas equilibrium occurs is in mixtures of helium and xenon. In 1966, de Swaan Arons and Diepen[4] published results of an experimental study of the high-pressure phase equilibrium in He and Xe. they successfully predicted and then observed gas–gas immiscibility. A sample of their results is shown in Figure 1. This is a plot of total pressure of the mixture vs. mole fraction of xenon. The temperature is constant and above the critical temperatures of both helium and xenon. The two regions that exist, one and two phases, are clearly labeled. The line separating the two regions is called the coexistence curve. Below these pressures the solution is miscible in all proportions. For example, if we start with an equimolar mixture of helium and xenon at 25° and some low pressure (e.g., 1 atm), we will have what is clearly a homogeneous mixture of two gases. If we then increase the pressure at constant temperature, at about 450 atm two separate phases will form, one about 40% xenon, the other about 65% xenon. As we then continue to increase the pressure, the helium rich phase, which is originally present in a larger molar amount, becomes richer in helium and smaller in extent. From the above hypothetical experiment, one can see why the term "immiscibility of gases" was used to describe this phase separation. The idea that two gases could be immiscible is surprising to one's normal physical point of view of the gas

* Address correspondence to this author at the Science Research Laboratory, United States Military Academy, West Point, N.Y. 10996.

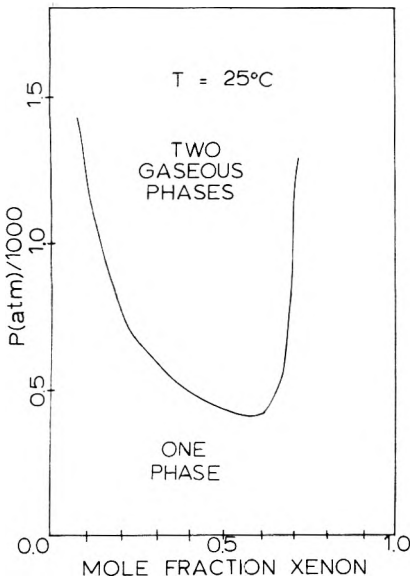

Figure 1. Gas–gas equilibrium in helium–xenon mixtures (from de Swaan Arons et al.).

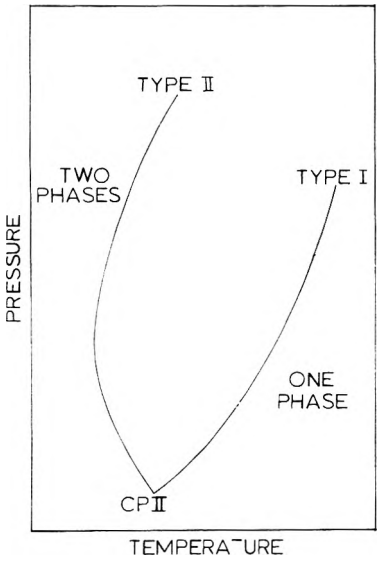

Figure 2. The two types of fluid–fluid equilibria.

phase. The use of the term gas–gas equilibrium to describe the above phenomenon has been challenged.[5]

There are two types of fluid–fluid equilibrium, which are best illustrated in terms of the temperature–pressure projections of the critical loci as shown in Figure 2. In this figure CPII denotes the critical point of the less volatile component. In the region labeled two phases the fluid mixture separates into two immiscible fluid phases. In the one-phase region the components are miscible in all proportions. For a system that exhibits fluid–fluid equilibrium of the first type the critical locus has a positive slope on leaving the critical point of the less volatile component and proceeds to higher temperature as the pressure is increased. A system exhibiting type II equilibrium will have a critical locus with a negative slope near the critical point of the less volatile component. At higher pressures the slope becomes positive and proceeds to higher temperatures at higher pressures.

The variety of critical loci that have been obtained for

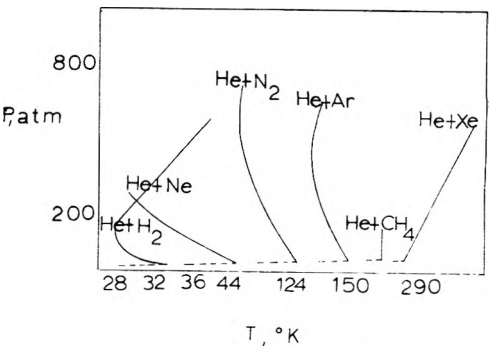

Figure 3. Critical loci for a series of binary mixtures with helium as a component (from Streett).

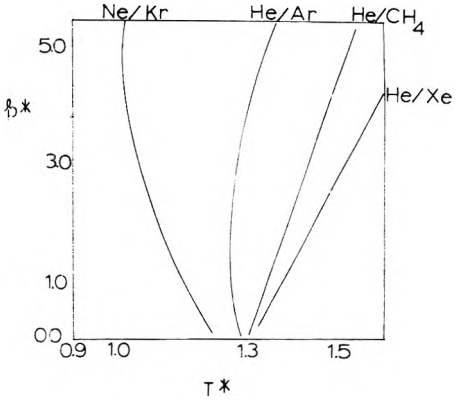

Figure 4. Critical loci for a series of binary mixtures as a function of reduced pressure and temperature.

various binary mixtures exhibiting fluid–fluid equilibria is best shown in Figure 3. This is taken from the work by Streett.[6] The critical loci for a series of binary mixtures with helium as one component are plotted on a common graph. As the difference of the size of the attractive forces between the two components becomes greater, the critical locus changes from type II to type I. Helium with hydrogen is obviously of the second type while helium with xenon is the first type. Helium with methane seems to be an intermediate case but this line was drawn from the critical point of methane and one experimental critical solution point. Similarly, the helium–argon critical locus has been extended past the experimental points. Since this graph appeared, Streett and coworkers have made more extensive experimental studies of the systems helium with argon,[7] nitrogen,[7] methane,[8] and hydrogen.[9] The results show that helium–methane mixtures clearly exhibit fluid–fluid equilibrium of the first type and helium–argon mixtures, fluid–fluid equilibrium of the second type. We have plotted the most recent experimental critical loci on a graph of reduced pressure vs. reduced temperature for the less volatile component (Figure 4). The pressure and temperature are reduced with the Lennard-Jones 6–12 intermolecular potential parameters of the less volatile component as obtained from molecular beam experiments and second virial coefficient measurements. The parameters are included in Table I.

With modern improvements in experimental high-pressure techniques, fluid–fluid equilibria have been observed in a number of systems. In a recent review article, Schneider[10] summarizes the current experimental results. All the first-type systems have helium as one component except

TABLE I: Lennard-Jones 6–12 Potential Parameters

Species	ϵ/k, °K	σ, Å
He–He[a]	10.2	2.556
H_2–H_2[b]	37.0	2.928
Ne–Ne[c]	35.8	2.75
N_2–N_2[d]	95.2	3.745
Ar–Ar[d]	117.7	3.504
CH_4–CH_4[d]	148.9	3.783
Kr–Kr[d]	164.0	3.827
Xe–Xe[d]	222.3	4.099

[a] P. E. Siska, J. M. Parson, T. P. Schafer, and Y. T. Lee, *J. Chem. Phys.*, **55**, 5762 (1971). [b] A. Michels and M. Goudeket, *Physica*, 8, 347 (1941). [c] J. S. Rowlinson, *Annu. Rep. Prog. Chem.*, **56**, 22 (1959). [d] A. E. Sherwood and J. M. Prausnitz, *J. Chem. Phys.*, 41, 429 (1964).

for argon and water. The majority of second type systems contain a highly polar, hydrogen bonding component, either ammonia or water.

Since systems with very simple intermolecular forces, e.g., noble gases, display a wide variety of high-pressure phase equilibria, we feel that modern statistical mechanical theories of mixtures should be able to describe, explain, and predict this behavior.

Previous Theoretical Studies

In 1894 van der Walls[11] predicted that regions of heterogeneous phase equilibria would exist past both critical temperatures at high pressure for binary mixtures that differed greatly in volatility. He predicted the two different types with their characteristic critical loci. He also predicted that at high pressures the critical locus would go through first a temperature and then a pressure maximum as it turned back on itself. The locus would then end at the critical point of the more volatile component. This reversal of the critical locus has never been observed experimentally. It was Kamerlingh Onnes and Keesom[12] who, several years later, suggested that the equilibrium was an immiscibility of gases.

Starting with the van der Waals equation of state modified for a mixture, Tempkin[13] derived criteria for the existence of fluid–fluid equilibrium in terms of the various van der Waals' constants. The van der Waals equation

$$\left(p + \frac{a}{\bar{V}^2}\right)(\bar{V} - b) = RT \tag{1}$$

can be used to describe a solution if the constants a and b are expressed in terms of constants describing solvent–solvent, solvent–solute, and solute–solute interactions. Tempkin expressed the van der Waals a for a mixture as

$$a = x_1^2 a_{11} + 2x_1x_2a_{12} + x_2^2a_{22} \tag{2}$$

where x_2 is the mole fraction of component 2, and a_{11} and a_{22} are the constants for the pure components and a_{12} can be determined by some experimental study of the same mixture or from a_{11} and a_{22} by some combination rule. Similarly

$$b = x_1^2 b_{11} + 2x_1x_2b_{12} + x_2^2 b_{22} \tag{3}$$

where b_{11} and b_{22} are the constants for the pure components and b_{12} was assumed to be equal to the arithmetic mean of b_{11} and b_{22}. This equation of state was then integrated to obtain an expression for the Helmholtz free energy. Following the work of van der Waals, Tempkin recognized regions of fluid immiscibility as regions above the two critical points where

$$(\partial^2 A/\partial x^2)_{V,T} < 0 \tag{4}$$

in other words, regions where a plot of the Helmholtz free energy vs. mole fraction is concave downward. He then determined the values of the a_{ij}'s and b_{ij}'s within these regions. His results are the following:

$$b_{11}/b_{22} > 0.42 \tag{5}$$

$$a_{12} < 0.5(a_{11} + a_{22}) - 8a_{22}/27 \tag{6}$$

where component 2 is the less volatile component. If one assumes that a_{12} is the geometric mean of a_{11} and a_{22}, then the second criterion above reduces to

$$a_{11}/a_{22} < 0.053 \tag{7}$$

Tempkin's results have been fairly successful in predicting the occurrence of fluid–fluid equilibria. de Swaan Arons and Diepen[4] used his approach in predicting fluid–fluid equilibrium in mixtures of helium and xenon. Problems have occurred with such systems as helium with propane, benzene, and ethylene. Tempkin's criterion incorrectly predicted that no fluid phase immiscibility would exist. A similar approach using the van der Waals' equation of state was used by van Konynenburg and Scott in studying various phase equilibria in hydrocarbon mixtures.[14]

The theoretical approaches that we have discussed up to now have been semiempirical or at least not molecular. One of the more fundamental and molecular approaches to mixtures is that based on the radial distribution function. Just as in the theories of pure fluids, the experimental properties of the mixture can be expressed in terms of the radial distribution function. The energy equation, which is well known from the theory of pure fluids, is the following for a mixture:

$$E = \frac{3}{2}NkT + 2\pi N\rho\sum_{i,j}x_ix_j\int_0^\infty dr\, r^2u_{ij}(r)\, g_{ij}(r) \tag{8}$$

where E is the internal energy of a mixture of N total molecules at temperature T, total density ρ, and mole fractions x_i and $u_{ij}(r)$ is the two-body intermolecular potential. $g_{ij}(r)$ is the two body mixture radial distribution function which describes the distribution of j molecules about a central i molecule (or vice versa) as a function of intermolecular separation. It is important to realize that $g_{11}(r)$ is *not* the same as the radial distribution function in pure component 1 but that the distribution of 1 molecules about each other is dependent on the presence of other components. Each mixture radial distribution function is a function of sizes of and interactions between all the different species, e.g., for a binary mixture

$$g_{11}(r) = g_{11}(r/\sigma_{11},\ kT/\epsilon_{11},\ \sigma_{12}/\sigma_{11},\ \sigma_{22}/\sigma_{11},\ \epsilon_{12}/\epsilon_{11},\ \epsilon_{22}/\epsilon_{11},\ x_i\text{'s}) \tag{9}$$

If these complicated mixture radial distribution functions were known, one could easily calculate the properties of the mixture. Since they are not known, we must consider approximations which allow us to predict experimental properties.

Equation 8 can be used as the starting point of the derivation of all the n-fluid theories. Perhaps the simplest approximation that can be proposed is that all of the radial distribution functions in a mixture are equal. Using this in eq 8, the sum of three integrals (for a binary mixture) reduces to one integral over an average potential function, i.e.

$$E = \frac{3}{2}NkT + 2\pi N\rho\int_0^\infty dr\, r^2\bar{u}(r)\, g(r) \qquad (10)$$

where

$$\bar{u} = \sum_{i,j} x_i x_j u_{ij}(r)$$

For the radial distribution function we select that of the pure fluid that interacts by the potential $\bar{u}(r)$. If we assume a Lennard-Jones 12–6 potential function, the above relation for $\bar{u}(r)$ gives the following expressions for the parameters of the average potential:

$$\bar{\epsilon} = \left(\sum_{i,j} x_i x_j \epsilon_{ij}\sigma_{ij}^{\,6}\right)^2 \Big/ \sum_{i,j} x_i x_j \epsilon_{ij}\sigma_{ij}^{\,12} \qquad (11)$$

$$\bar{\sigma} = \left\{\sum_{i,j} x_i x_j \epsilon_{ij}\sigma_{ij}^{\,12} \Big/ \sum_{i,j} x_i x_j \epsilon_{ij}\sigma_{ij}^{\,6}\right\}^{1/6} \qquad (12)$$

where ϵ_{ij} and σ_{ij} are the parameters of the potential $u_{ij}(r)$. Effectively, we have said that the configurational properties of our mixture (contributions arising from the configurational integral) are the same as those of one *pure* fluid with potential parameters $\bar{\epsilon}$ and $\bar{\sigma}$. As a result this theory is known as a one-fluid theory of mixtures. The approach was first introduced by Prigogine and coworkers[15] in work on cell theories of liquid mixtures and has come to be known as the *random mixture model.*

Zandbergen, Knaap, and Beenakker[16] used the random mixture model with the law of corresponding states to predict fluid–fluid equilibrium in mixtures of helium and xenon. The excess Gibbs' free energy of some solution at the pressure p, temperature T, and mole fraction x is given by

$$\frac{G^{xs}(p,\ T,\ x)}{RT} = \frac{G_{ref}{}^{xs}(p',\ T')}{RT} \qquad (13)$$

where

$$p' = p(\bar{\sigma}^3/\sigma_{ref}{}^3)(\epsilon_{ref}/\bar{\epsilon})$$

and

$$T' = T(\epsilon_{ref}/\bar{\epsilon})$$

$G_{ref}{}^{xs}$ is the excess Gibbs' free energy of some pure substance used as a reference system and ϵ_{ref} and σ_{ref} are the potential parameters of the reference system. Zandbergen et al. looked for regions in the pressure, temperature, and mole fraction diagram that were materially unstable by plotting the Gibbs' free energy vs. mole fraction for some pressure and temperature. For a solution that is materially unstable

$$(\partial^2 G/\partial x^2)_{p,T} < 0 \qquad (14)$$

Geometrically, this corresponds to a region in plots of Gibbs' free energy vs. mole fraction that are concave downward. For a completely miscible solution

$$(\partial^2 G/\partial x^2)_{p,T} > 0 \qquad (15)$$

i.e., the free-energy curve is concave upward for all mole fractions. The pressure and temperature where the concave downward construction has just disappeared is a point on the critical locus. Zandbergen et al. used nitrogen, for which extensive tables of experimental properties exist, as a reference system for mixtures with mole fraction of xenon greater than 0.45. For mole fractions of xenon less than 0.1 they used the virial expression for the Gibbs' free energy and the second virial coefficient for helium. For intermediate mole fractions they extrapolated between the calculated values. From free-energy plots at p = 200 atm and several temperatures, they predicted the critical point shown in their Figure 7 as a triangle. The solid line is the experimental curve of deSwaan Arons and Diepen.

The average potential model is a refinement of the random mixture model that was also introduced by Prigogine.[15] In this model we assume that

$$g_{12}(r) = [g_{11}(r) + g_{22}(r)]/2 \qquad (16)$$

With this approximation, eq 8 reduces to the sum of two integrals

$$E = \frac{3}{2}NkT + 2\pi N\rho\sum_{i=1}^{2} x_i\int_0^\infty dr\, r^2\bar{u}_i(r)\, g_{ii}(r) \qquad (17)$$

where

$$\bar{u}_i(r) = x_i u_{ii}(r) + x_j u_{ij}(r)$$

We further assume that the two radial distribution functions are those for the pure fluids that interact by the potentials $\bar{u}_1(r)$, $\bar{u}_2(r)$. For the Lennard-Jones 12–6 potential, the parameters of the ith hypothetical pure fluid are

$$\epsilon_i = \left(\sum_j x_j \epsilon_{ij}\sigma_{ij}^{\,6}\right)^2 \Big/ \sum_j x_j \epsilon_{ij}\sigma_{ij}^{\,12} \qquad (18)$$

$$\sigma_i = \left\{\sum_j x_j \epsilon_{ij}\sigma_{ij}^{\,12} \Big/ \sum_j x_j \epsilon_{ij}\sigma_{ij}^{\,6}\right\}^{1/6} \qquad (19)$$

The average potential model, which is a two-fluid theory, has not yet been applied to fluid–fluid equilibria, although Zandbergern, Knaap, and Beenakker predicted that it would probably give good agreement with experiment.[16]

Scott[17] proposed a three-fluid theory of binary mixtures. In this approach the radial distribution functions in eq 8 are replaced by those of the pure components, e.g.

$$g_{11}(r,\ \epsilon_{11},\ \epsilon_{12},\ \epsilon_{22},\ \sigma_{11},\ \sigma_{12},\ \sigma_{22},\ x_i,\ T) = g_{11}{}^{pure}(r,\ \epsilon_{11},\ \sigma_{11},\ T)$$

For $g_{12}(r)$, the distribution function of some hypothetical pure fluid with parameters ϵ_{12} and σ_{12} is substituted. The energy equation remains a sum of three integrals but each one is now for a pure fluid. The three potential functions are just those of the three types of binary interactions in the mixture.

Zandbergen, Knaap, and Beenakker[16] also applied the three-fluid theory to mixtures of helium and xenon. Since this theory gives a much simpler mole fraction dependence of the free energy, the criteria for the critical locus, i.e.

$$(\partial^2 G/\partial x^2)_{p,T} = 0 \qquad (20)$$

$$(\partial^3 G/\partial x^3)_{p,T} = 0 \qquad (21)$$

were applied directly to give implicit expressions for p_c and T_c. The above expressions predict a critical mole fraction of 0.5 for all p_c and T_c with the three-fluid model, which makes it less satisfactory than the random mixture *model*. The results from this work will be discussed later with the discussion of our results for the same theories.

Very recently, Breedveld and Prausnitz[18] extended the application of the three-fluid theory to helium–xenon mixtures to higher pressures. This was possible by extending the known experimental properties of a series of simple fluids to higher pressures and using these data as a reference system for the three-fluid theory. The authors also applied a two-fluid theory to the same system.

Tan, Luks, and Kozak[19] have applied conformal solution theory to mixtures of helium and xenon. They used the second-order theory, i.e., they included terms in the series up

to quadratic differences in the potential parameters. Since the mole fraction dependence of the Gibb's free energy is simple, one can apply the criteria for the critical locus directly as for the three-fluid model discussed earlier. They show that conformal solution theory is very dependent on the choice of the reference system.

Rigby, Alder, Sapse, and Hecht[20] applied the augmented van der Waals theory to predict fluid–fluid critical loci for mixtures. They treated special systems that allowed them to utilize many pure fluid results, e.g., a mixture of square well molecules and point spheres or a mixture of hard spheres and square well molecules of the same size. They were able to see some trends but could not make predictions of experimental results.

Trappeniers, Schouten, and Ten Seldam[21] have applied a two-component lattice–gas model to gas–gas equilibrium. By varying the interaction parameters they were able to predict a variety of critical loci but, due to the simplicity of the model, it is not possible to compare these results to realistic, experimental systems. On the other hand, the very simplicity of the lattice gas model can be used as a basis for general theoretical studies, and this area has seen a great deal of activity recently. Although lattice gas models lie somewhat outside of the scope of the present work, ref 22–24 give an introduction to recent lattice gas studies.

Equation 8 can be used to derive another set of n-fluid theories, called the van der Waals theories, which are known to be much more satisfactory than the simple n-fluid theories introduced and discussed above.

van der Waals n-Fluid Theories

The radial distribution function depends, not on just the distance between the two molecules concerned but on a reduced distance r/σ_{ij} where σ_{ij} is the characteristic distance parameter for the interaction of i and j molecules. Since σ_{ij} is also the distance parameter of the intermolecular potential $u_{ij}(r/\sigma_{ij})$ we can rewrite the energy equation in terms of reduced integrals

$$E = \frac{3}{2}NkT + \sum_{i,j} x_i x_j \epsilon_{ij} \sigma_{ij}^3 \int \mathrm{d}x\, x^2 \mathrm{f}(x)\ \mathrm{g}(x) \quad (22)$$

where we have assumed conformal potentials with functional form $\mathrm{f}(r/\sigma)$

$$u_{ij}(r/\sigma_{ij}) = \epsilon_{ij} \mathrm{f}(r/\sigma_{ij}) \quad (23)$$

These reduced integrals differ from that of some pure hypothetical fluid by their density dependence. We now assume that the three integrals in the mixture are all equal to that of some pure fluid with a reduced density that is just the average of the three reduced densities in the mixture and obtain

$$\bar{\sigma}^3 = \sum_{i,j} x_i x_j \sigma_{ij}^3 \quad (24)$$

$$\overline{\epsilon\sigma}^3 = \sum_{i,j} x_i x_j \epsilon_{ij} \sigma_{ij}^3 \quad (25)$$

These two rules are known as the vdWI theory. Essentially, we have assumed that in some binary mixture at some density ρ and mole fraction x

$$\mathrm{g}^{11}(r^*, \rho, x) = \mathrm{g}^{12}(r^*, \rho, x) = \mathrm{g}^{22}(r^*, \rho, x) \quad (26)$$

This is clearly a more reasonable assumption than that of the random mixture theory which is equivalent to the assumption

$$\mathrm{g}^{11}(r, \rho, x) = \mathrm{g}^{12}(r, \rho, x) = \mathrm{g}^{22}(r, \rho, x) \quad (27)$$

Similar to the extension of the random mixture model to the average potential model, the vdWI model can be extended to a two-fluid model where the parameters of each fluid are given by

$$\overline{\epsilon_j \sigma_j^3} = \sum_i x_i x_j \epsilon_{ij} \sigma_{ij}^3 \quad (28)$$

$$\bar{\sigma}_j^3 = \sum_i x_i x_j \sigma_{ij}^3$$

In summary, then, a one-fluid theory predicts the excess free energy of the mixture from that of one pure fluid,[25] e.g.

$$G_{\mathrm{mix}}^{\mathrm{xs}}(p, t) = G_{\mathrm{pure}}^{\mathrm{xs}}\left(\frac{p(\bar{\sigma}^3)}{\bar{\epsilon}}, \frac{T}{(\bar{\epsilon})}\right) \quad (29)$$

where $\bar{\sigma}$ and $\bar{\epsilon}$ are the potential parameters of the pure fluid. In this work we have discussed and examined two one-fluid theories which differ in their expressions for $\bar{\epsilon}$ and $\bar{\sigma}$. The expressions for the various theories are summarized as follows: random mixture

$$\bar{\epsilon} = \left[\sum_i \sum_j x_i x_j \epsilon_{ij} \sigma_{ij}^6\right]^2 \Big/ \left[\sum_i \sum_j x_i x_j \epsilon_{ij} \sigma_{ij}^{12}\right]$$

$$\bar{\sigma} = \left\{\left[\sum_i \sum_j x_i x_j \epsilon_{ij} \sigma_{ij}^{12}\right] \Big/ \left[\sum_i \sum_j x_i x_j \epsilon_{ij} \sigma_{ij}^6\right]\right\}^{1/6} \quad (30)$$

van der Waals one-fluid

$$\bar{\epsilon} = \left[\sum_i \sum_j x_i x_j \epsilon_{ij} \sigma_{ij}^3\right] \Big/ \left[\sum_i \sum_j x_i x_j \sigma_{ij}^3\right]$$

$$\bar{\sigma} = \left[\sum_i \sum_j x_i x_j \sigma_{ij}^3\right]^{1/3} \quad (31)$$

A two-fluid theory predicts the excess free energy of the mixture from that of two pure fluids, e.g.

$$\frac{G_{\mathrm{mix}}^{\mathrm{xs}}}{RT}(p, T) = x_1 \frac{G_{\mathrm{AA}}^{\mathrm{xs}}}{RT}\left(\frac{p\sigma_{\mathrm{A}}^3}{\epsilon_{\mathrm{A}}}, \frac{T}{\epsilon_{\mathrm{A}}}\right) + x_2 \frac{G_{\mathrm{BB}}^{\mathrm{xs}}}{RT}\left(\frac{p\sigma_{\mathrm{B}}^3}{\epsilon_{\mathrm{B}}}, \frac{T}{\epsilon_{\mathrm{B}}}\right) \quad (32)$$

where $G_{\mathrm{AA}}^{\mathrm{xs}}$ and $G_{\mathrm{BB}}^{\mathrm{xs}}$ are the excess free energies of the two pure fluids with the Lennard-Jones 6–12 potential parameters ϵ_{A}, σ_{A} and ϵ_{B}, σ_{B}, respectively. Expressions for the potential parameters from the theories we have discussed are the following: average potential model

$$\epsilon_{\mathrm{A}} = [x_1\epsilon_{11}\sigma_{11}^6 + x_2\epsilon_{12}\sigma_{12}^6]^2/[x_1\epsilon_{11}\sigma_{11}^{12} + x_2\epsilon_{12}\sigma_{12}^{12}]$$

$$\sigma_{\mathrm{A}} = \{[x_1\epsilon_{11}\sigma_{11}^{12} + x_2\epsilon_{12}\sigma_{12}^{12}]/[x_1\epsilon_{11}\sigma_{11}^6 + x_2\epsilon_{12}\sigma_{12}^6]\}^{1/6}$$

$$\epsilon_{\mathrm{B}} = [x_1\epsilon_{12}\sigma_{12}^6 + x_2\epsilon_{22}\sigma_{22}^6]^2/[x_1\epsilon_{12}\sigma_{12}^{12} + x_2\epsilon_{22}\sigma_{22}^{12}]$$

$$\sigma_{\mathrm{B}} = \{[x_1\epsilon_{12}\sigma_{12}^{12} + x_2\epsilon_{22}\sigma_{22}^{12}]/[x_1\epsilon_{12}\sigma_{12}^6 + x_2\epsilon_{22}\sigma_{22}^6]\}^{1/6} \quad (33)$$

van der Waals two-fluid

$$\epsilon_{\mathrm{A}} = (x_1\epsilon_{11}\sigma_{11}^3 + x_2\epsilon_{12}\sigma_{12}^3)/(x_1\sigma_{11}^3 + x_2\sigma_{12}^3)$$

$$\sigma_{\mathrm{A}} = (x_1\sigma_{11}^3 + x_2\sigma_{12}^3)^{1/3}$$

$$\epsilon_{\mathrm{B}} = (x_1\epsilon_{12}\sigma_{12}^3 + x_2\epsilon_{22}\sigma_{22}^3)/(x_1\sigma_{12}^3 + x_2\sigma_{22}^3)$$

$$\sigma_{\mathrm{B}} = (x_1\sigma_{12}^3 + x_2\sigma_{22}^3)^{1/3} \quad (34)$$

The three-fluid theory predicts the excess free energy of the mixture from those of three pure fluids

$$\frac{G_{mix}^{xs}}{RT}(p, T) = x_1^2 \frac{G_{11}^{xs}}{RT}\left(\frac{\rho\sigma_{11}^3}{\epsilon_{11}}, \frac{T}{\epsilon_{11}}\right) + 2x_1x_2\frac{G_{12}^{xs}}{RT}\left(\frac{\rho\sigma_{12}^3}{\epsilon_{12}}, \frac{T}{\epsilon_{12}}\right) + x_2^2\frac{G_{22}^{xs}}{RT}\left(\frac{\rho\sigma_{22}^3}{\epsilon_{22}}, \frac{T}{\epsilon_{22}}\right) \quad (35)$$

where G_{ij}^{xs} is the free energy of the pure fluid with potential parameters σ_{ij} and ϵ_{ij}.

Computational Considerations

The n-fluid theories permit two alternative methods to calculate thermodynamic properties of some mixture at a given pressure, density, and temperature. One can calculate the free energy of the mixture from that of the pure fluid at the proper corresponding pressure and temperature, e.g.

$$\frac{G_{mix}^{xs}}{RT}(p, T) = \frac{G_{pure}^{xs}}{RT}\left(\frac{p\sigma^3}{\epsilon}, \frac{T}{\epsilon}\right) \quad (36)$$

or from that of the pure fluid at the corresponding density and temperature, e.g.

$$\frac{G_{mix}^{xs}}{RT}(\rho, T) = \frac{G_{pure}^{xs}}{RT}\left(\rho\sigma^3, \frac{T}{\epsilon}\right) \quad (37)$$

Of course, if the theory were exact and gave the exact compressibility factor, the two approaches would be the same. Because of the approximate nature of the theory the two approaches will differ. Because most of the experimental data for fluid–fluid equilibrium were obtained at constant pressure and temperature and because previous work[3] has shown that the first of the two approaches (eq 36) gives slightly better agreement with experiment we have used it exclusively throughout this work.

The three-fluid theory is the simplest of the n-fluid theories to apply. Applying the criterion for material stability $(\partial^2 G/\partial x^2)_{p,T} > 0$ to the three-fluid expression for the Gibbs free energy gives the simple result that the critical mole fraction is 0.5 for all pressures and temperatures. One also obtains an implicit equation for the critical properties and temperatures in terms of the free energies of the three pure fluids.

For one- and two-fluid theories a different approach is used. The Gibbs free energy of mixing is predicted by a relation such as

$$\frac{\Delta G}{RT}(p, T) = \frac{G_{pure}^{xs}}{RT}\left(\frac{p\bar{\sigma}(x)^3}{\bar{\epsilon}(x)}, \frac{T}{\bar{\epsilon}(x)}\right) - x_1\frac{G_1^{xs}}{RT}(p, T) - x_2\frac{G_2^{xs}}{RT}(p, T) + \sum_i x_i \ln x_i \quad (38)$$

where the mole fraction dependence of the potential parameters is given by one of the appropriate relations (eq 30–34). Since this mole fraction dependence is so much more complicated than the three-fluid theory we did not apply the relation for material stability directly. To find regions where

$$(\partial^2 \Delta G/\partial x_1^2)_{p,T} < 0 \quad (39)$$

and therefore two immiscible phases exist we used the following three approaches: (1) the Gibbs free energy of mixing was plotted as a function of mole fraction at constant pressure and temperature and the graphs were examined for regions where the curve was concave downward; (2) the derivative $(\partial \Delta G/\partial x_1)_{p,T}$ was calculated numerically and examined for regions where the derivative was not monotonically increasing as x_1 changes from zero to one; (3) by numerically calculating the derivative $(\partial^2 \Delta G/\partial x_1^2)_{p,T}$ and looking for negative values. Of the three approaches the first two were equally successful while the third became unreliable for mixtures in regions where they were not very immiscible. The results reported here were obtained by the first two of the above methods.

Once again, by looking for regions where $(\partial^2 \Delta G/\partial x_1^2)_{p,T} < 0$ for pressures and temperatures covering the appropriate region of the phase diagram, we were able to locate regions of fluid–fluid equlibrium and the fluid–fluid critical locus.

One advantage to applying n-fluid theories to fluid–fluid equilibrium using pure fluid perturbation theory as the reference system is that the calculations can be extended to very high pressures, near solidification. The model or interpretation that we have used here is that an n-fluid theory predicts solidification of the mixture when the pure fluid (or one of the pure fluids) representing it solidifies. As an example, the three-fluid model predicts that the mixture will solidify when the less volatile component solidifies. This is quite inaccurate as it predicts that mixtures of all compositions solidify at the same pressure and temperature. The three-fluid model was never meant to be extended to pressures where solidification occurs and so it is not surprising that this prediction is so poor.

Because of our method of determining material stability, i.e., examining the second derivative of the Gibbs' free energy of mixing

$$\Delta G = G_{mixture} - x_1G_1 - x_2G_2 \quad (40)$$

problems developed at pressures above the solidification of the less volatile component. For each mole fraction ΔG mixing depends on the Gibbs free energy of the less volatile component and therefore, at high pressures, the less volatile component is in the solid state and the fluid theories do not apply. It would have been equivalent to determine material stability by examining the second derivative of the mixture free energy. The reason we looked at free energies of mixing instead of mixture free energies is that the changes in the concavity of the curve in regions of instability were more pronounced in the former and therefore easier to detect graphically and computationally.

We extended our calculations just to pressures in the region the less volatile component would solidify. Although this does not include behavior at the extremely high pressures recently investigated by Streett and coworkers, it includes most of the fluid–fluid critical locus and far exceeds most other experimental work and all previous theoretical work.

By selecting the pressure–temperature approach discussed above, it is necessary to calculate the Gibbs free energy of the pure reference fluid at some given pressure and temperature. The last few years has seen the development and successful application of statistical mechanical perturbation theory to the calculation of the thermodynamic properties of pure fluids. The two most successful perturbation theories are due to Barker and Henderson[26] and Weeks, Chandler, and Andersen.[27] These two theories differ in the way the actual intermolecular potential is divided into a reference and a perturbation part. Each theory has its advantages and disadvantages but both are quite successful and yield essentially equivalent results. In this work

we chose to use the Weeks, Chandler, and Andersen theory to calculate the properties of the pure fluid. Both perturbation theories express the thermodynamic properties as explicit functions of the density and temperature. In order to calculate the Gibbs free energy at some pressure and temperature, we calculated the pressures and corresponding Gibbs free energies at the desired temperature and a series of densities scanning the fluid region and then interpolated this set of values to obtain the value of the free energy at the desired pressure. For temperatures above the critical point of our reference fluid (e.g., $kT_c/\epsilon \simeq 1.458$ for the Weeks–Chandler–Andersen fluid) the procedure was straightforward and one only had to worry about stopping at a density just below solidification. The gas–liquid region should not cause problems in this application to mixtures since we are looking for regions that are materially unstable ($(\partial^2 G/\partial x_1^2)_{p,T} < 0$). The gas–liquid region is mechanically unstable ($(\partial^2 A/\partial V^2)_T < 0$) and, regions of mechanical instability are contained within those of material instability.[28] For computational ease, we restricted our calculations to reduced pressures greater than or equal to 0.5 ($\geq$0.7 for $1.30 \leq kT/\epsilon < 1.40$). Thus we stopped our evaluation of the critical locus about 0.3 reduced pressure above the critical point of the less volatile component. This is no limitation in determining the form of the critical locus and characterizing the type of fluid–fluid equilibrium, as we shall see in the following sections.

Choice of Mixture Theories

One of the original goals of this work was to determine which of the n-fluid theories could best predict fluid–fluid critical loci. After extensive computation and comparison to experimental data we find, in agreement with other workers, that the van der Waals one-fluid theory yields the most satisfactory results. Much of this work can be summarized in Figure 5.

Once again this is the pressure–temperature projection of the critical locus. The solid dots are from the experimental work of de Swaan Arons and Diepen and the critical locus terminates at the critical point of the less volatile component. The critical locus predicted by the van der Waals one-fluid theory has the proper slope but is shifted to higher temperatures. If one recalls that this approach uses the Weeks–Chandler–Andersen fluid as the reference system (its critical point is at $kT/\epsilon = 1.46$, $p\sigma^3/\epsilon = 0.18$) we see that the van der Waals one-fluid theory properly predicts that the critical locus terminates at the critical point of the less volatile component. This apparent disagreement is due to an inadequacy of the Weeks–Chandler–Andersen pure fluid perturbation theory rather than an inadequacy of the van der Waals one-fluid mixture theory. Presumably this disagreement would disappear if actual experimental data of the pure fluids were used. Both the three-fluid and van der Waals two-fluid theories predict the wrong slope for the critical locus and that the critical locus continues to lower temperatures at lower pressures without intersecting the pure critical point. Recently, Breedveld and Prausnitz[18] applied the van der Waals two-fluid theory and the three-fluid theory to the same system and also found that the predicted critical locus did not begin at the critical point of the less volatile component. The best theory is the van der Waals one-fluid theory which predicts a critical locus shifted to higher temperature just as the critical point of the pure reference fluid is shifted to higher temperatures.

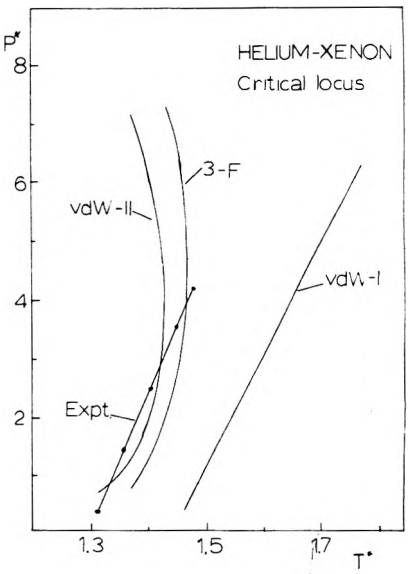

Figure 5. The helium–xenon critical locus for the van der Waals n-fluid theories.

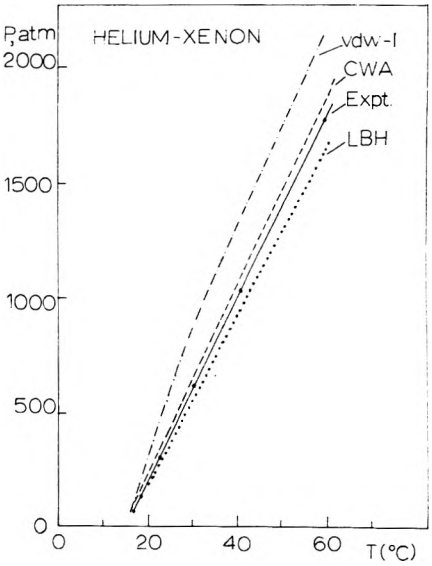

Figure 6. A comparison of the rigorous extensions of the Weeks–Chandler–Andersen theory (WCA), the Barker–Henderson theory (LHB), and the approximate van der Waals one-fluid theory to the equation of state of helium–xenon along the critical locus.

Recent work by Pailthorpe and McQuarrie[2b] has led to similar results. They have calculated the equation of state of helium–xenon mixtures along the critical locus by using rigorous extensions of the Barker–Henderson and Weeks–Chandler–Andersen theories. The comparison of these results to experiments, and to the van der Waals one-fluid theory as well, is shown in Figure 6, taken from their paper. Although the agreement of these perturbation theory extensions with experiment is quite good, it should be pointed out that the difference in computer time between these calculations and those for the vdWI is close to a factor of 100. Thus their work shows that the vdWI theory appears to not only compare satisfactorily with experiment or exact calculations but is computationally very convenient as well. Comparisons of the van der Waals two-fluid and three-fluid theory were found to be much less satisfactory.

The Critical Locus as a Function of Potential Parameters

After having examined all of the various n-fluid mixture theories and determining how well they predict experimental results, we now use the most successful theory, the van der Waals one-fluid theory, to make predictions and investigate the phenomenon more thoroughly. The four parameters that are necessary to fully determine the three types of intermolecular interactions found in binary mixtures are the following: $\epsilon_{22}/\epsilon_{11}$, $\epsilon_{12}/\epsilon_{11}$, σ_{22}/σ_{11}, and σ_{12}/σ_{11}, where we have used the convention that component 1 has the higher critical temperature. We have used the quantity k_{12} defined by the relation $\epsilon_{12} = (1 - k_{12})(\epsilon_{11}\epsilon_{22})^{1/2}$ to fix the ratio $\epsilon_{12}/\epsilon_{11} = (1 - k_{12})(\epsilon_{22}/\epsilon_{11})^{1/2}$ for fixed values of ϵ_{11} and ϵ_{22}. This parameter is well-discussed by Hiza and Duncan.[29]

With four parameters characterizing the critical locus, there is a large number of combinations of parameters that are possible and it would be difficult for us to predict a critical locus for each. Fortunately, it is possible to restrict our work and still consider most experimentally important systems. The values of the potential parameters listed in Table II cover most of the experimentally realizable systems.

Figures 7–12 show the critical loci that we predict for all the various combinations of values of $\epsilon_{22}/\epsilon_{11}$, k_{12}, and σ_{22}/σ_{11} mentioned above. Our approach has been to specify a ratio of molecular diameters, and a value of k_{12} and determine the critical locus at $\epsilon_{22}/\epsilon_{11} = 0.02$. We then determine the critical locus at increasing values of $\epsilon_{22}/\epsilon_{11}$ until we reach a ratio where no fluid–fluid equilibrium is predicted (the region of fluid–fluid equilibrium decreases with increasing $\epsilon_{22}/\epsilon_{11}$). Fluid–fluid equilibrium is not observed at high values of $\epsilon_{22}/\epsilon_{11}$ (greater than 0.5) except for values of $k_{12} = 0.4$. However, the equilibrium seen at $k_{12} = 0.4$ and $\epsilon_{22}/\epsilon_{11}$ near 1.0 has no physical meaning. This corresponds to a mixture with a similar potential well depths and a large value of k_{12}. However large values of k_{12} are only found in systems with very different well depths. As a result we have not included the critical loci that are predicted for $k_{12} = 0.4$ and $\epsilon_{22}/\epsilon_{11}$ near 1.0.

The most obvious effect of the potential parameters is that increasing k_{12} increases the region of fluid–fluid equilibrium and changes the equilibrium from type II to type I. This directly decreases the well depth of the 1–2 interactions relative to the 1–1 and 2–2 interactions.

The effect of the ratio of the pure potential well depths is not as straightforward. We originally felt that large differences in the ϵ_{11} and ϵ_{22} were one of the reasons for the occurrence of the phenomenon. It is now more apparent that the reason the critical loci of Figures 7–12 shift to the higher temperatures as $\epsilon_{22}/\epsilon_{11}$ decreases is that $\epsilon_{12}/\epsilon_{11}$ is decreasing.

The effect of increasing σ_{22}/σ_{11} is to increase the region of fluid–fluid equilibrium. For a given k_{12} and $\epsilon_{22}/\epsilon_{11}$, fluid–fluid equilibrium is most favored for equal size molecules. If the component 2 molecules are of the same size as the component 1 molecules, they are more effective in disrupting the energetically more stable 1–1 interactions. If the component 2 molecules are small, they can "fit" better between the component 1 molecules and cause less disruption of the more stable interactions. Using helium–xenon mixtures as an example, the region of immiscibility shifts to mixtures with less xenon as the pressure increases. When there is mostly xenon, the smaller helium atoms can occupy

TABLE II: Potential Parameters Used in Calculations

Potential parameter	Range of values
σ_{22}/σ_{11}	0.6, 0.8
k_{12}	0.0, 0.2, 0.4
$\epsilon_{22}/\epsilon_{11}$	0.02 to 1.0

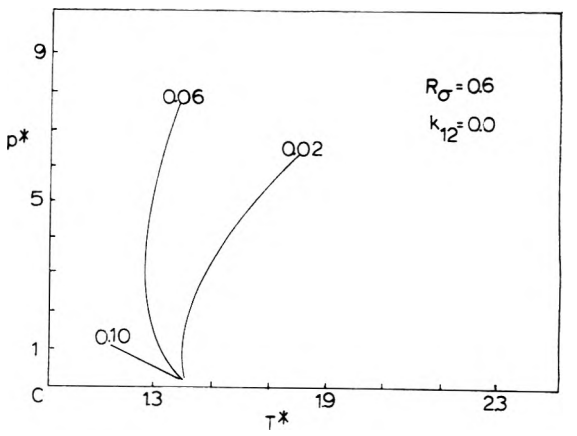

Figure 7. Critical loci predicted by the van der Waals one-fluid theory for $R_\sigma = \sigma_{22}/\sigma_{11} = 0.6$ and $k_{12} = 0.0$. The curves are labeled with the value of $\epsilon_{22}/\epsilon_{11}$.

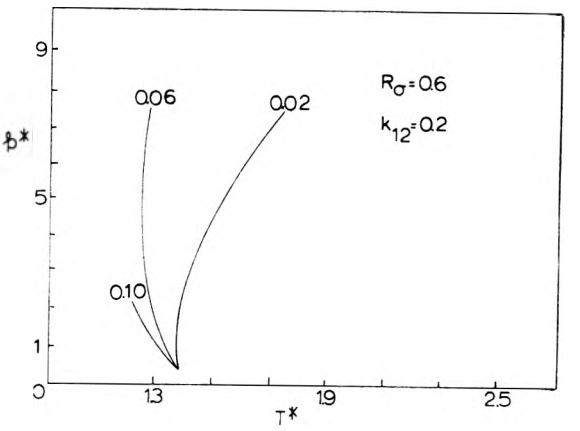

Figure 8. Same as Figure 7 with $R_\sigma = 0.6$ and $k_{12} = 0.2$.

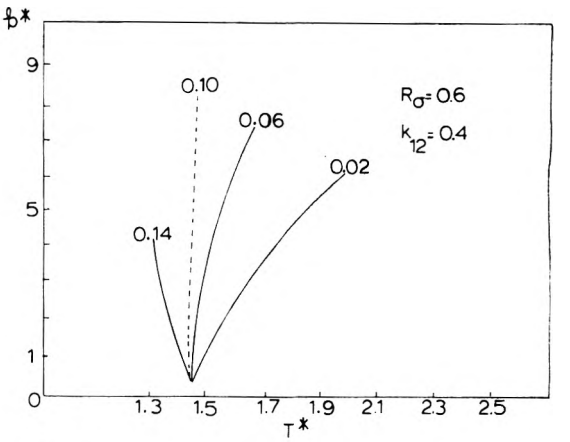

Figure 9. Same as Figure 7 with $R_\sigma = 0.6$ and $k_{12} = 0.4$.

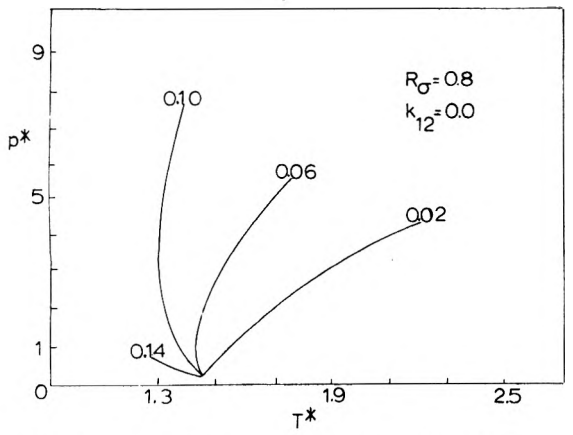

Figure 10. Same as Figure 7 with $R_\sigma = 0.8$ and $k_{12} = 0.0$.

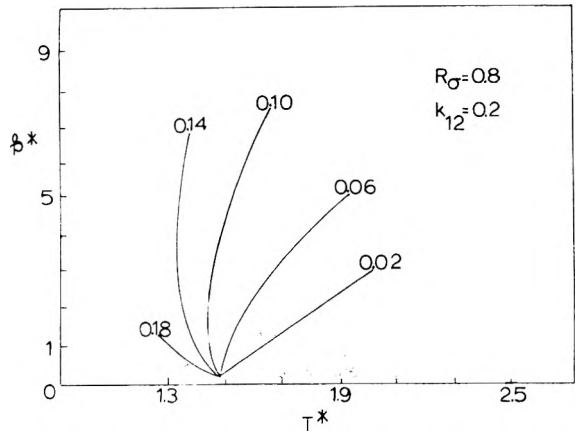

Figure 11. Same as Figure 7 with $R_\sigma = 0.8$ and $k_{12} = 0.2$.

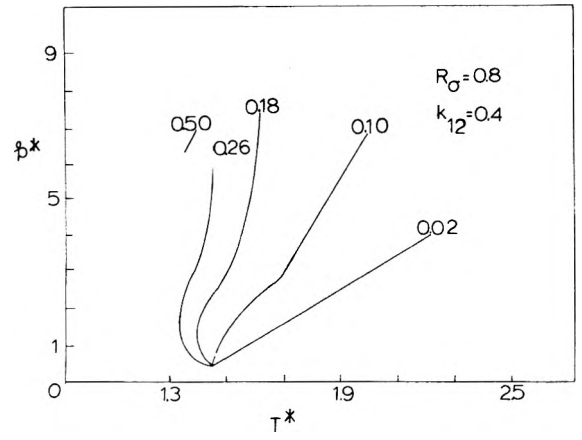

Figure 12. Same as Figure 7 with $R_\sigma = 0.8$ and $k_{12} = 0.4$.

vacancies between the xenon atoms without causing so much disruption of attractions as to cause separation. It is important to note that the size effects are of secondary importance. The 1–2 interactions must be weak.

We also examine the effects of the potential parameters on the pressure–mole fraction dependence. Although the shift of the mole fraction is surprisingly independent of k_{12} and $\epsilon_{22}/\epsilon_{11}$, it does vary with the ratio of the molecular diameters. One measure of the shift of the critical locus is the critical mole fraction at the highest pressure, just before solidification. For molecules of equal size the critical locus shifts to a final mole fraction of 0.5. With the ratios σ_{22}/σ_{11} = 0.8 and 0.6 the final mole fractions are 0.24–0.28 and 0.08–0.12, respectively. As the difference in sizes becomes greater, the critical mole fraction changes to higher concentrations of the smaller component. As we mentioned earlier, it is more difficult for the small molecules to disrupt the interactions.

TABLE III: Potential Parameters of Systems Exhibiting Fluid-Fluid Equilibrium

System	$\epsilon_{22}/\epsilon_{11}$	σ_{22}/σ_{11}	k_{12}
Ne–Kr	0.218	0.718	0.2
He–Ar	0.086	0.729	0.22
He–CH_4	0.068	0.68	0.4
He–Xe	0.046	0.62	0.4
He–N_2	0.11	0.69	0.25

As a test of our series of critical loci in Figures 7–12, we can compare its predictions to a series of experimental results. Table III contains five simple nonassociating binary mixtures along with the appropriate potential data. We shall see how these are accomodated by Figures 7–12. For example, from the parameters of helium–methane we can see that it is intermediate between Figures 9 and 12. For σ_{22}/σ_{11} = 0.6 and k_{12} = 0.4, Figure 9 shows that for 0.06 < $\epsilon_{22}/\epsilon_{11}$ < 0.1 the equilibrium is barely type I. Similarly Figure 12 shows that for σ_{22}/σ_{11} = 0.8, k_{12} = 0.4 and 0.02 < $\epsilon_{22}/\epsilon_{11}$ < 0.10 the equilibrium is an extreme type I. Our theoretical prediction would be intermediate between the two curves which agrees with the experimental locus. In a similar manner, Figure 11 predicts type II for helium–argon and Figures 8 and 11 predict an extreme type II locus for neon–krypton. The agreement with experiment is quite good. The only problem is differentiating between no fluid–fluid equilibrium and an extreme type II equilibrium. One would have to evaluate the critical locus at kT/ϵ less than 1.30 to determine this.

Conclusions

Combining the pure-fluid perturbation theory of Weeks–Chandler–Andersen with the various n-fluid corresponding states theories has permitted an extensive test of the ability of these theories to predict fluid–fluid equilibrium over wide ranges of pressure. The van der Waals one-fluid theory has proven to be the best of the n-fluid theories. Breedveld and Prausnitz[18] found that the van der Waals one-fluid theory was not as successful at predicting Gibbs free energies of mixing as the van der Waals two-fluid theory. Our approach to testing the theories has emphasized the mole fraction, pressure-, and temperature-dependence of the free energies more than quantitative prediction of free energies of mixing. Our results for the van der Waals two-fluid theory are surprising. We really expected its results to be much more similar to the van der Waals one-fluid theory. It would be most interesting to conduct a more extensive study of the van der Waals two-fluid theory with a reference system such as that of Breedveld and Prausnitz[18] to see if the results are similar to ours. We predict that the results will be essentially the same.

Our work indicates that there are actually two factors that determine the fluid–fluid critical locus of a simple mixture: the ratio of the well depth of the mixed interaction to the largest well depth of the pure interaction (ϵ_{12}/

ϵ_{11}) and the ratio of the molecular diameters (σ_{22}/σ_{11}). As $\epsilon_{12}/\epsilon_{11}$ becomes larger the region of fluid–fluid equilibrium decreases. $\epsilon_{12}/\epsilon_{11}$ is a measure of the gain in stability on mixing due to 1–2 interactions vs. separating to increase 1–1 interactions. As σ_{22}/σ_{11} increases the region of the fluid–fluid equilibrium increases. As the component 2 molecules become larger they disrupt the 1–1 interactions more effectively.

In summary, Figures 7–12 allow one to predict the critical locus of any binary mixture given the appropriate intermolecular potential parameters.

Acknowledgment. The authors wish to thank B. Pailthorpe, J. Ely, and M. Hiza for helpful discussions.

References and Notes

(1) Contribution No. 2556 from the Chemistry Department of Indiana University.
(2) (a) R. O. Neff, doctoral thesis, Chemistry Department, Indiana University, 1974. (b) B. A. Pailthorpe and D. A. McQuarrie, *Mol. Phys.*, in press.
(3) D. Henderson and P. J. Leonard in "Physical Chemistry, An Advanced Treatise", Vol. VIII B, H. Eyring, D. Henderson, and W. Jost, Ed., Academic Press, New York, N.Y., 1971, pp 413–510.
(4) J. de Swaan Arons and G. A. M. Diepen, *J. Chem. Phys.*, **44**, 2322 (1966).
(5) J. S. Rowlinson, "Liquids and Liquid Mixtures", Plenum Press, New York, N.Y., 1969, Chapter 1.
(6) W. B. Streett, *Trans. Faraday Soc.*, **65**, 696 (1969).
(7) W. B. Streett and A. L. Erickson, *Phys. Earth Planet. Inter.*, **5**, 357 (1972).
(8) W. B. Streett, A. L. Erickson, and J. L. E. Hill, *Phys. Earth Planet. Inter.*, **6**, 69 (1972).
(9) W. B. Streett, *Astrophys. J.*, **186**, 1107 (1973).
(10) See G. M. Schneider, *Adv. Chem. Phys.*, **17**, 1 (1970), for a recent review of the phenomenon of fluid–fluid equilibrium.
(11) J. D. van der Waals, *Zittinsversl. Kon. Acad. Wetensch. (Amsterdam)*, 133 (1894).
(12) H. Kamerlingh Onnes and W. H. Keesom, *Commun. Phys. Lab. Univ. Leiden*, **98a, 98b, 98c** (1906); Suppl. No. 15, 16 (1907).
(13) M. I. Tempkin, *Russ. J. Phys. Chem.*, **33**, 275 (1959).
(14) P. van Konynenburg, Ph.D. Thesis, University of California, Los Angeles, 1968; see also R. L. Scott and P. H. van Konynenburg, *Discuss. Faraday Soc.*, **49**, 87 (1970); R. L. Scott, *Ber. Bunsenges. Phys. Chem.*, **76**, 296 (1972).
(15) I. Prigogine, A. Bellemans, and A. Englert-Chwoles, *J. Chem. Phys.*, **24**, 518 (1956); I. Prigogine, "The Molecular Theory of Solutions", North-Holland, Amsterdam, and Interscience, New York, N.Y., 1957.
(16) P. Zandbergen, H. F. P. Knaap, and J. J. M. Beenakker, *Physica*, **33**, 379 (1967).
(17) R. L. Scott, *J. Chem. Phys.*, **25**, 193 (1956).
(18) G. J. F. Breedveld and J. M. Prausnitz, *AIChE J.*, **19**, 783 (1973).
(19) P. Y. Tan, K. D. Luks, and J. J. Kozak, *J. Chem. Phys.*, **55**, 1012 (1971).
(20) M. Rigby, B. J. Alder, A. M. Sapse, and C. E. Hecht, *J. Chem. Phys.*, **52**, 3665 (1970).
(21) N. J. Trappeniers, J. A. Schouten, and C. A. Ten Seldam, *Chem. Phys. Lett.*, **5**, 541 (1970).
(22) J. A. Schouneu, C. A. Ten Seldam, and N. J. Trappeniers, *Physica*, **73**, 556 (1974).
(23) G. W. Mullholland and J. J. Rehr, *J. Chem. Phys.*, **60**, 1297 (1974).
(24) J. T. Bartis and C. W. Hall, to be submitted for publication.
(25) Our convention for excess properties is

$$G_{pure}^{xs}(p, T) = G_{pure}(p, T) - G^{i}(p, T)$$

$$G_{mix}^{xs}(p, T) = G_{mix}(p, T) - x_1 G_1^{i}(p, T) - x_2 G_2^{i}(p, T) - RT \sum_j x_j \ln x_j$$

where G is the free energy of the ideal gas and G_{mix} is the free energy of the mixture. One should also remember that the free energy of mixing (ΔG)

$$\Delta G = G_{mix} - x_1 G_1 - x_2 G_2$$

is the following in terms of excess properties:

$$\Delta G = G_{mix}^{xs} - x_1 G_1^{xs} - x_2 G_2^{xs} + RT \sum_j x_j \ln x_j$$

(26) J. A. Barker and D. Henderson, *Acc. Chem. Res.*, **4**, 303 (1971).
(27) J. D. Weeks, D. Chandler, and H. C. Andersen, *J. Chem. Phys.*, **54**, 5237 (1971).
(28) I. Prigogine and R. Defay, "Chemical Thermodynamics", Section 16-8, Longmans Green and Co., London, 1954.
(29) M. J. Hiza and A. G. Duncan, *AIChE J.*, **16**, 733 (1970).

Hydroxyl Radical Induced Oxidation of Nitrobenzene[1]

Kishan Bhatia*

Radiation Research Laboratories and Department of Chemistry, Mellon Institute of Science, Carnegie-Mellon University, Pittsburgh, Pennsylvania 15213 *(Received August 29, 1974; Revised Manuscript Received January 8, 1975)*

Publication costs assisted by Carnegie-Mellon University

The hydroxylation of nitrobenzene by radiolytic techniques was examined by high-performance liquid chromatographic techniques. Owing to improvements in the method of analysis it was possible to measure phenol in air-saturated nitrobenzene solutions irradiated to low doses. The initial yields for the consumption of nitrobenzene and the formation of phenol and isomeric nitrophenols in N_2O- and air-saturated systems were measured in order to establish the primary reactions of hydroxyl radicals with nitrobenzene. The initial yields for the consumption of nitrobenzene were 3.7 and 2.6 and that for total phenol were 2.3 and 2.4 in N_2O- and air-saturated systems, respectively, in samples irradiated at low dose rates (0.8 krad g^{-1} min^{-1}). Nearly 80% of the hydroxynitrocyclohexadienyl radicals disproportionate to produce isomeric nitrophenols and nitrobenzene in N_2O-saturated systems without added oxidants upon irradiation at low dose rates. For a given dose the distribution of nitrophenols was dependent upon the dose rate. Observed dose rate dependence of nitrophenol production and dose rate independence of nitrobenzene consumption indicate that reactions other than disproportionation and dimerization play a significant role at high dose rates. The examination of the effect of added ferricyanide ion in N_2O-saturated systems showed that reliable production measurements of *o*- and *p*-nitrophenol cannot be made because of complicating secondary reactions. The initial yield for the production of *m*-nitrophenol was higher by a factor of >3 in the presence than in the absence of ferricyanide ion. This result indicates that in the cross disproportionation reaction of *m*- and *o*- or *p*-hydroxynitrocyclohexadienyl radicals the meta isomer acts as an oxidizing agent and ortho and para isomers act as reducing agents.

Introduction

The mechanistic studies of the reactions of the hydroxyl radical with benzene and its derivatives by radiolytic techniques have been hampered until recently in spite of the fact that radiation-induced hydroxylation offers a system simpler than chemical systems. An accurately known number of hydroxyl radicals are generated in situ in radiolytic experiments. As a result, complications associated with the necessity of adding reagents to the system are avoided. A prime difficulty has been the lack of rapid and sensitive analytical techniques necessary for the quantitative determinations of the reactant and reaction products. The recently developed high-performance liquid chromatographic techniques (ALC) have made it practical to perform these determinations rapidly at product concentrations down to micromolar or less providing that the material being examined absorbs sufficiently strongly (extinction coefficient, $\epsilon > 500\ M^{-1}\ cm^{-1}$).[2-7] We report here our studies on the radiolytic hydroxylation of nitrobenzene using an ALC equipped with a commercially available continuously variable wavelength (~210 to 350 nm) uv spectrophotometric detector which allowed detection of the various individual products to be optimized. The hydroxylation of nitrobenzene has previously been the subject of several steady-state investigations in which measurements of isomeric nitrophenols on a concentrate of the irradiated solutions were reported.[8-10] Preliminary concentration steps are undesirable, as they are time consuming and they may alter molecular structure and/or relative distribution of the components. Even though phenol was detected in aerated nitrobenzene solutions irradiated to high doses,[8] phenol measurements were not reported apparently because of the limitations of analytical techniques.

It is frequently of interest to make independent measurements of the radiolytically generated secondary organic radicals for the purpose of comparing it to those of primary radicals. Such comparisons are essential to establish the number of secondary organic radicals produced by the reactions of a primary radical with an organic solute. Radiolytically generated hydroxyl radicals, for example, have been postulated to react with benzene to produce two radicals, viz. the hydroxycyclohexadienyl radical by an addition mechanism and the phenyl radical by an abstraction mechanism.[11] It was recently shown that the radiolytically generated hydroxyl radical quantitatively adds to benzene to produce a hydroxycyclohexadienyl radical thereby eliminating the postulated formation of phenyl radicals in the system.[7] An estimate of the initial yields of secondary organic radicals can be made in well-defined systems from the consumption of organic solute and the production of products.[3,4,7] Unlike some previous studies,[9,10] we have made detailed yield–dose studies for the consumption of nitrobenzene and the production of phenol and isomeric nitrophenols in air- and N_2O-saturated systems. We have also examined the effect of added ferricyanide ion in N_2O-saturated systems in an effort to obtain a product balance because ferricyanide ion was shown to oxidize the hydroxycyclohexadienyl radical with unit efficiency.[7] These studies clearly demonstrate that the yield measurements made in the region of >10% consumption of nitrobenzene represent only rough lower limits to initial yields.

The results reported by Fendler and Gasowski[8] on the production of *o*-nitrophenol contradicted the observation of Matthews and Sangster[10] that in aerated systems the production of *o*-nitrophenol was dose rate dependent. We

* Address correspondence to the Allied Chemical Corp., P.O. Box 1021-R, Morristown, N.J. 07960.

find that for a given dose the distribution and the yields of all three isomers of nitrophenol are dose rate dependent in N_2O- and air-saturated systems but not in N_2O-saturated systems containing ferricyanide ion. These observations suggest that the observed differences in the product mixture and concentration ratios in the pulse[12] and γ-radiolysis conditions may be a result of different initial concentration of radicals produced in nitrobenzene solution by these two radiolytic techniques.

Experimental Section

A prototype liquid chromatograph and the modifications made to it to improve its performance have been described elsewhere.[2,6] The ALC unit for the present studies was rebuilt to incorporate a Varian 635 spectrophotometer and a high-pressure stop–flow valve (15,000 psi, taper seal two-way valve, High Pressure Equipment Co., Inc., Erie, Pa. 16505) between the pump outlet and column inlets. The spectrophotometric cells have a volume of 8 μl and a path length of 1 cm. An added feature of the new ALC unit is the stop–flow capability to trap chromatographic peaks in the detector cells for the recording of the spectra of the trapped peaks. Samples were introduced on the column through a loop-sampling valve with 190 μl volume.

The output of the uv detector corresponds to a signal of 100 mV for an optical absorbance of 0.1. The uv detector has a built-in fixed dampening capability (time constant 1 sec) for low signal-to-noise conditions. Using the damper we found it possible to spread an absorption of 0.005 full scale (i.e., 5 mV output) on a 10-in. recorder with, under optimum conditions, a short-term noise level of ~0.5 in. (0.25 mV). The long-term drift on a well-conditioned column was found to be comparable to the short-term noise. Most of the measurements reported here were performed at a signal-to-noise ratio of >3 (i.e., minimum absorbance of 0.001).

The nitrobenzene used was reagent grade. Chromatographic analyses of nitrobenzene saturated water (~0.01 *M*) indicated that the nitrobenzene was free from detectable impurities. Water was triply distilled. To prepare the N_2O-saturated system oxygen was purged from nitrobenzene solutions (~2.5×10^{-4} *M*, 5 ml without added buffer, pH ~6) at atmospheric pressure by bubbling with N_2O.[3,6] Nitrobenzene concentrations were chromatographically determined for each sample by withdrawing a sample (~0.4 ml) prior to irradiation. A 8.6×10^{-5} *M* nitrobenzene solution was used for studies of air-saturated systems.

Steady-state irradiations were carried out in cobalt sources at a dose rate of 4.77 or 65.5×10^{16} eV g^{-1} min^{-1}. The absorbed doses were generally in the range of 9.5–164 $\times 10^{16}$ eV g^{-1} (i.e., 1.52 to 26.4 krads).

The irradiated samples were analyzed immediately (usually within 1 min) after completion of the irradiation to avoid possible complications due to post-irradiation reactions such as those observed for the benzene system.[6] Measurements of nitrobenzene and phenolic products were made at the wavelength (~230, ~270, or ~314 nm) of maximum absorption as each component eluted from the chromatographic column.

Chromatographic analyses were performed either on a column (2.1 mm × 1 m) packed with the acetate form of a quanternary ammonium-substituted methylmethacrylate polymer, coated ~1% by weight on spherical silicious particles (Zipax, SAX, 25–37 μm), or a column (2.1 mm × 2 m) packed with octadecylsilyl bonded silicious material (Waters, nominal 40-μm particles).[2] The latter nonpolar column was used only for qualitative analyses.

A good separation of phenol and isomeric nitrophenols in irradiated ~10^{-4} *M* nitrobenzene solutions was necessary to make reliable measurements down to micromolar level. The anion exchange column upon elution with water containing 100 m*M* sodium acetate and 0.25 m*M* sodium perchlorate, pH 7.3, produced a baseline separation of these compounds from each other, Figure 1a. Perchlorate ion concentration was adjusted at 0.3 and 0.5 m*M* to obtain desired separations and to measure phenols in the irradiated solutions at either 270 or 314 nm (i.e., optimum detection conditions), Figure 1b and 1c. The retention time of nitrobenzene was independent of perchlorate ion concentrations. A summary of chromatographic data pertinent to present studies is reported in Table I. The data indicate that measurement of all but *p*-nitrophenol could be readily made down to ~2 μM level and that for *p*-nitrophenol down to ~3 μM. In a given series of experiments chromatographic peak heights were reproducible to within 1% and the estimated accuracy for most determinations was ~2%. Error in the measurements may be somewhat higher for samples irradiated to low doses. The nonpolar column was used only for qualitative analysis because separation of *m*- from *p*-nitrophenol and of *o*-nitrophenol from nitrobenzene was incomplete. The nonpolar column was eluted with 20 m*M* phosphate buffer, pH 5.3.[2,6]

Results and Discussions

The hydroxyl radicals together with the solvated electrons, hydrogen atoms, hydrogen molecules, hydrogen peroxide, and protons are the chemical species formed by γ irradiation of water.[13] The hydroxyl radical reactions are studied in the presence of N_2O since the reaction

$$H_2O + e_{aq}^- + N_2O \longrightarrow {}^{\bullet}OH + N_2 + OH^- \quad (k = 5.6 \times 10^9\ M^{-1}\ \text{sec}^{-1})^{14} \quad (1)$$

leads to an increase in the amount of ·OH radicals in the system. The rate constant[12] for the reaction of nitrobenzene with e_{aq}^- is $3 \times 10^{10}\ M^{-1}$ sec^{-1}, so that in ~200 μM nitrobenzene solutions used in the present study all but 5% of e_{aq}^- was converted to ·OH radicals by reaction 1. Therefore, in N_2O-saturated systems ·OH radicals are produced with a yield of 5.7, taking $G_{OH} = 2.7$ and the yield of electron scavenged by the N_2O as 3.0.[15] The yield–dose plots for the consumption of nitrobenzene in N_2O- and air-saturated systems in the presence and absence of ferricyanide ion are shown in Figure 2. These results were obtained on samples irradiated to a dose of 1.5 to 26 krads. Previous product analyses studies[8-10] on the radiation-induced hydroxylation of nitrobenzene were performed on samples irradiated to a dose of at least ~20 krads. There is considerable curvature to the plots and it is obvious that the yields determined in the region of >10% consumption represents only very rough lower limits to initial yields. The nitrobenzene consumption in N_2O-saturated systems is not influenced by the presence of an oxidizing agent, ferricyanide ion, or by dose rate. At higher doses nitrobenzene consumption drops because of the competition from products to scavenge primary radicals. It has been pointed out that the problem of determining the initial yields (the true $G_{(zero)}$ values) from such observed data becomes one of properly taking into account the effect of buildup of products as the reaction progresses.[3] If one assumes that the rate constant for reaction of the intermediate with the

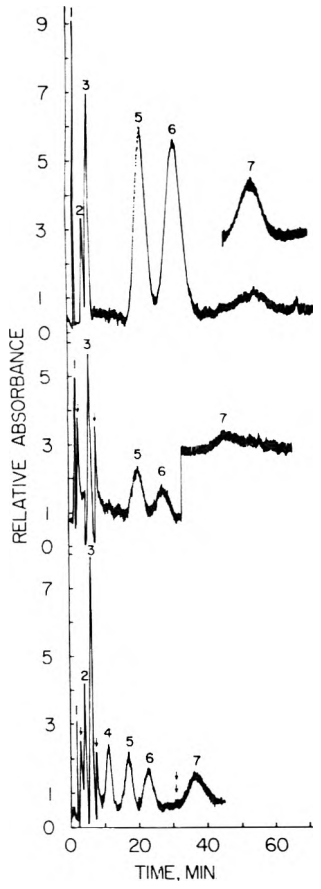

Figure 1. Liquid chromatograms of (top to bottom) a synthetic mixture, an irradiated (dose = 5.25 krads) N_2O-saturated nitrobenzene (~200 μM) system containing $Fe(CN)_6^{3-}$ (100 μM), and an irradiated (dose = 15.75 krads) air-saturated nitrobenzene (86 μM) system, respectively. Peaks are (1) solvent, (2) phenol, (3) nitrobenzene, (4) unknown, (5) *o*-nitrophenol, (6) *m*-nitrophenol, and (7) *p*-nitrophenol. The column was eluted at a flow of 1 ml/min which produced a pressure drop of 1500 psi. The ionic strength of the eluent (100 μM sodium acetate, pH 7.3) was adjusted to 0.25, 0.3, and 0.5 mM to obtain top, middle, and bottom chromatograms, respectively. Increasing the ionic strength decreases retention times and enhances the sensitivity. The top chromatogram was recorded at 270 nm. The insert for *p*-nitrophenol (peak 7, top chromatogram) recorded at 314 nm is included to indicate improvement in sensitivity for this peak in switching from 270 to 314 nm. In irradiated solutions the *p*-nitrophenol peak is recorded at 314 nm and other peaks at 270 nm. Peaks 1–3 in the top chromatogram and peaks 1 and 3 in the other two chromatograms were recorded at ×50 and all other peaks were recorded at ×10. Single arrows indicate attentuation. In the middle chromatogram peak 7 is shifted because the base line was not adjusted after a change from 270 to 314 nm. In the bottom chromatogram double arrows indicate change from 270 to 314 nm along with base line adjustment.

product is equal to that for reaction with the initial reactant then the initial slope is given by $[S]_0 \ln 2/D_{1/2}$ where $D_{1/2}$ is the dose for 50% reaction as determined from a semilogarithmic plot of the data and $[S]_0$ is the original concentration of the solute of interest. A semilogarithmic plot of the data of Figure 2 upon extrapolation to 50% reaction gives $D_{1/2}$ of 2.38×10^{18} and 1.48×10^{18} eV/g for N_2O- and air-saturated systems, respectively. These values correspond to an initial radiation chemical yield of 3.7 and 2.6 for the consumption of nitrobenzene in N_2O- and air-saturated systems, respectively. The slopes representing G values of 3.7 and 2.6 are shown in Figure 2.

Nitrobenzene Consumption in N_2O Systems. Allowing a yield of ~0.3 for the reaction of nitrobenzene with hydrogen atoms ($G_H = 0.6$, $k = 5.6 \times 10^9\ M^{-1}\ sec^{-1}$),[12] the yield for reaction with OH radicals is only ~3.4. Because the rate constant for the reaction of ·OH radicals with nitrobenzene is high ($k = 4.7 \times 10^9\ M^{-1}\ sec^{-1}$),[12] it is reasonable to assume that additions will be quantitative and the yield of $\cdot OHC_6H_5NO_2$ radicals will also be 5.7. The observed yield of 3.4 is only ~60% of the expected yield, indicating that ~40% of the $\cdot OHC_6H_5\ NO_2$ radicals regenerate nitrobenzene.

Nitrobenzene Consumption in Aerated Systems. The rate constant for the reactions of O_2 with e_{aq}^- and with ·H atom is $2 \times 10^{10}\ M^{-1}\ sec^{-1}$.[14] The concentrations of oxygen in air-saturated systems is $2.3 \times 10^{-4}\ M$. In air-saturated systems the yield for e_{aq}^- was taken to be 2.6[15] and that for ·H atom to be 0.6. The rate constants for the reaction of nitrobenzene with e_{aq}^- ($3 \times 10^{10}\ M^{-1}\ sec^{-1}$) and ·H atoms ($5.6 \times 10^9\ M^{-1}\ sec^{-1}$)[12] are also high. From these data it was estimated that only 36%, i.e., $G = 0.9$, of e_{aq}^- and 50%, or $G = 0.3$, of ·H atoms are available for the reaction with nitrobenzene ($8.6 \times 10^{-5}\ M$) in air-saturated systems. Taking $G_{OH} = 2.7$ it was estimated that initial yield for the consumption of nitrobenzene in air-saturated systems would be ~3.8. The initial yield for the consumption of nitrobenzene in air-saturated systems is 2.6 or ~65% of estimated yield. Clearly, ~35% of the radicals formed by reaction between nitrobenzene and the primary radicals (i.e., OH, ·H, and e_{aq}^-) regenerate nitrobenzene.

The product of the reduction of nitrobenzene by e_{aq}^- is the nitrobenzene radical anion which was detected by ESR[16] or nitrosobenzene if the reaction goes to completion.[17] Nitrosobenzene will be oxidized back to nitrobenzene by oxidants such as hydrogen peroxide which is produced with a yield of ~1.9 in this system.[8] The oxidation of nitrosobenzene to nitrobenzene by a variety of oxidants is known.[18] The mechanism for the formation of nitrosobenzene involves protonation of the nitrobenzene radical anion ($pK_a = 3.2$)[17] followed by the disproportionation of the protonated radical to nitrobenzene and nitrosobenzene hydrate, $C_6H_5N(OH)_2$. In our experiments (pH ~6.0) most of the nitrobenzene radical anion will not be converted to the protonated form. It is reasonable to assume that the nitrobenzene radical anion also is oxidized back to nitrobenzene just as readily as the nitrosobenzene. It is therefore reasonable to assign most of the observed initial yield for the consumption of nitrobenzene in air-saturated systems to the reaction with ·OH radicals. Allowing ~0.2 of the yield for reaction with ·H atoms, a yield of ~2.4 is ascribable to the reactions of the ·OH radical with nitrobenzene in air-saturated systems.

Production of Nitrophenols and Phenol. The addition product of the hydroxyl radical to nitrobenzene is the hydroxynitrocyclohexadienyl radical which has been observed by pulse radiolysis studies.[12] The disproportionation of hydroxynitrocyclohexadienyl radicals (II) will result in the

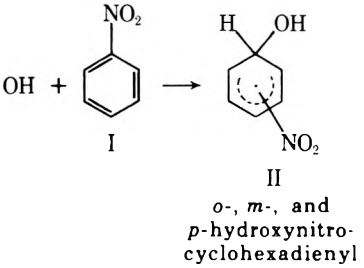

o-, *m*-, and *p*-hydroxynitrocyclohexadienyl radicals

TABLE I: Aqueous Liquid Chromatographic Retention Data and Detection Limit of a Spectrophotometric Detector[a,b]

	Anion exchange column						
	t_R, min		Peak width at half height, min		Rel sensitivities,[c] $\mu M/10^{-3}$ OD		Nonpolar column
Compound	a	b	a	b	a	b	t_R, min
Dead volume	0.18	0.20					5.5
Phenol	0.40	0.44	0.055	0.06	2.5	2.95	13.5
Nitrobenzene	0.58	0.59	0.08	0.09	0.575	0.68	73.0
m-Nitrophenol	1.65	1.90	0.26	0.33	2.45	2.90	29.5
o-Nitrophenol	2.22	2.72	0.37	0.45	4.30	5.07	68.0
p-Nitrophenol	3.60	4.70	0.52	0.74	6.65	7.85	22.0
Unknown[d]	1.15		0.17				

[a,b] t_R = retention times. Columns and eluents are described in the text. Anion exchange column at 30° and nonpolar column at 40° were eluted at a flow rate of 1 and 0.6 ml/min respectively. Ionic strength of the eluent was adjusted with (a) 0.5 and (b) 0.3 m*M* sodium perchlorate. Detection limit range for phenols by anion exchange chromatography was ~1 to ~2 μM at a signal-to-noise ratio of >2. [c] Sensitivities for all but *p*-nitrophenol at 270 nm. Sensitivity for *p*-nitrophenol at 314 nm. OD = optical density. [d] Detected in irradiated air-saturated systems, Figure 1c.

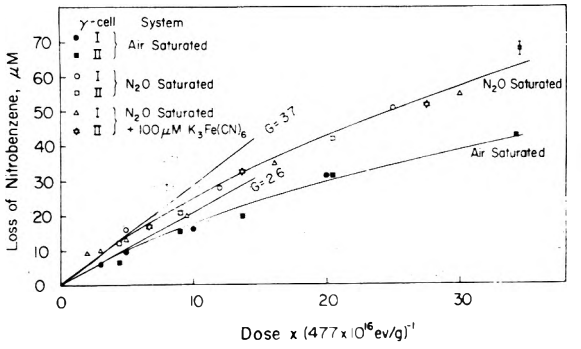

Figure 2. The consumption of nitrobenzene in N_2O-saturated systems with and without added $Fe(CN)_6^{3-}$ and air-saturated systems. The nitrobenzene concentration prior to irradiation was ~200 and 86 μM in N_2O- and air-saturated systems, respectively. The dose rates for the cobalt source I and II were 4.77 and 65.5 × 10^{16} eV g^{-1} min^{-1}, respectively.

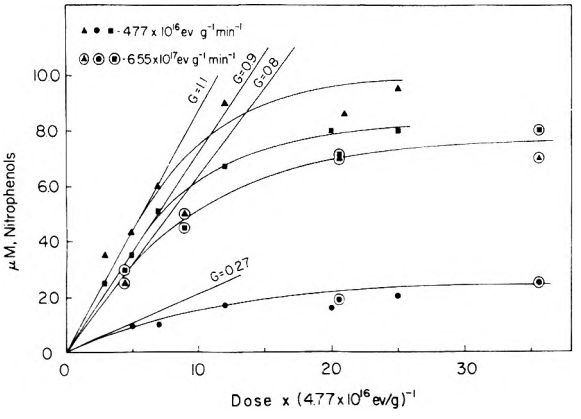

Figure 3. The production of nitrophenols in N_2O-saturated nitrobenzene (~200 μM) systems upon irradiations at different dose rates: (▲, ⊜) *o*-, (●, ⊙) *m*-, and (■, ⊛) *p*-nitrophenols.

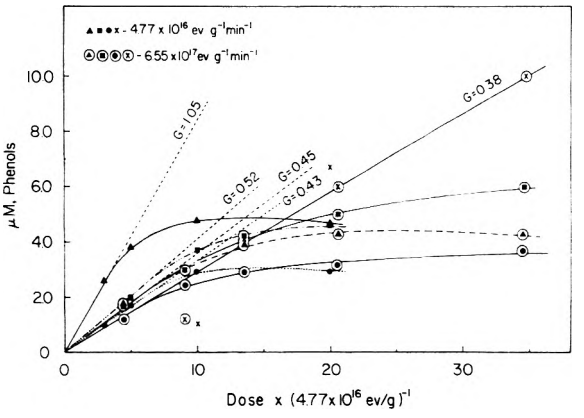

Figure 4. The production of phenols in air-saturated nitrobenzene (86 μM) systems upon irradiation at different dose rates: (X, ⊗) phenol and (▲, ⊜) *o*-, (●, ⊙) *m*-, and (■, ⊛) *p*-nitrophenol.

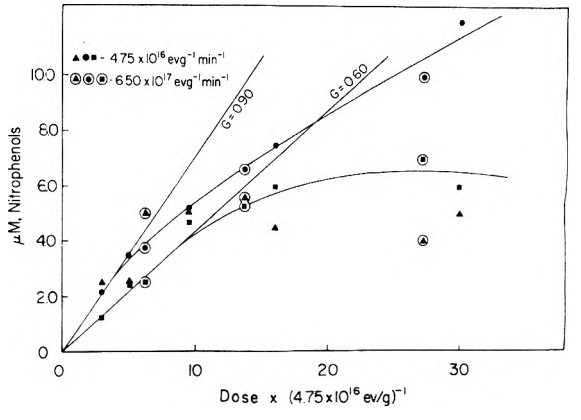

Figure 5. The production of nitrophenols in N_2O-saturated nitrobenzene (~200 μM) systems containing $K_3Fe(CN)_6$ (100 μM) at different dose rates: (▲, ⊜) *o*-, (●, ⊙) *m*-, and (■, ⊛) *p*-nitrophenol.

formation of nitrophenols. Three isomeric hydroxynitrocyclohexadienyl radicals must be formed to account for the observation of three isomeric nitrophenols.

The production of nitrophenols in N_2O- and air-saturated systems is presented in Figures 3–5. We find that for a given dose the distribution of nitrophenols is dependent upon the dose rate. Matthews and Sangster observed a pronounced dependence of *o*-nitrophenol yield on dose rate in the air-saturated system.[10] The yields of all three isomers of nitrophenol are dose rate dependent in N_2O- and air-saturated systems but not in N_2O-saturated systems containing ferricyanide ion.

TABLE II: Initial Yield of Irradiation Product in Aqueous Nitrobenzene Solutions[a]

System	Co source[b]	G value: Nitrobenzene consumption	G value: o-Nitrophenol	G value: m-Nitrophenol	G value: p-Nitrophenol	G value: Phenol	G value: Σ phenol	% o-Nitrophenol	% m-Nitrophenol	% p-Nitrophenol	% Phenol
N_2O saturated[c]	I	3.7	1.1	0.27	0.9	ND[g]	2.3	48	12	39	
	II	3.7	0.8	0.27	0.8	ND	1.9	42	15	42	
N_2O saturated[c,d]	I	3.7	0.6	0.9	0.6	ND	2.1	29	42	29	
+ $Fe(CN)_6^{3-}$	II	3.7	(0.6)[f]	0.9	0.6	ND	2.1	29	42	29	
Air saturated[e]	I	2.6	1.05	0.43	0.52	0.38	2.4	43	17	22	17
	II	2.6	0.45	0.40	0.45	(0.40)[f]	1.7	26.5	23.5	26.5	23.5

[a] pH ~6.0, without added buffer. [Nitrobenzene] = 8.6 and ~20 × 10^{-5} M in air- and N_2O-saturated systems, respectively. [b] Dose rates in cobalt source I and II were 4.77 and 65.5 × 10^{16} eV g^{-1} min^{-1}, respectively. [c] $[N_2O]$ = 2 × 10^{-2} M. [d] $[Fe(CN)_6^{3-}]$ = 10^{-4} M. [e] $[O_2]$ = 2.3 × 10^{-4} M. [f] Estimates. [g] Not detected.

From an analysis of the yield–dose plots, initial yields for the production of each phenol were calculated. These data are summarized in Table II. Total initial nitrophenol yield in N_2O-saturated systems in the absence of oxidizing agent is higher (~15%) in solutions irradiated at a lower dose rate than the solutions irradiated at a higher dose rate. The highest observed total nitrophenol yield in N_2O-saturated systems without added oxidant is 2.3 or ~70% of the observed initial yield for the consumption of nitrobenzene. The hydroxynitrocyclohexadienyl radical apparently disproportionates to produce nitrophenols and nitrobenzene. If the disproportionation involves electron transfer, the products will be nitrophenols and nitrobenzene (eq 2).

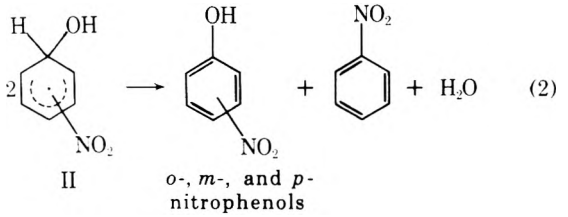

(2)

If the disproportionation involves hydrogen transfer, the products will be nitrophenols and nitrocyclohexadienols (eq 3). The dehydration of nitrocyclohexadienols will re-

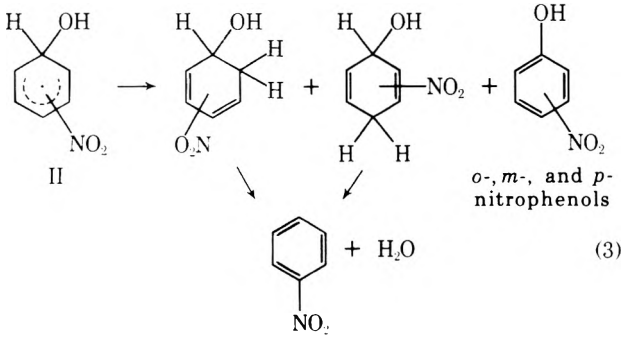

(3)

generate the starting material required to explain results on the consumption of nitrobenzene. The dehydration of substituted cyclohexadienols was postulated to explain the observed formation and build up of biphenyl and phenol in irradiated N_2O-saturated benzene systems.[6,19] Thus, for every molecule of nitrophenols produced one molecule of nitrobenzene is regenerated in the disproportionation reaction. Consequently, the initial yield for the consumption of nitrobenzene is 3.4 + 2.3 = 5.7, which is comparable to the estimated yield of ·OH radicals. This mechanism accounts for nearly 80% of hydroxynitrocyclohexadienyl radicals. The remaining 20% or equivalent to a yield of ~1.1 of hydroxynitrocyclohexadienyl radicals must be accounted for by dimerization processes. We did not look for dimeric products in our irradiated systems.

Evidence for the dimerization of the hydroxynitrocyclohexadienyl radical under pulse radiolysis conditions has been presented and a rate constant of 6 × 10^8 M^{-1} sec^{-1} has been measured.[12] It was estimated that ~25% of initially formed hydroxynitrocyclohexadienyl radicals disproportionated and ~75% of the radicals dimerized under pulse radiolysis conditions. For a given dose, radical concentration under the reported pulse radiolysis compared to the present γ-radiolysis condition was higher by ~4 to 5 orders of magnitude. As a result, differences in the product mixture and concentration ratios are anticipated under the pulse and γ-radiolysis conditions. Indeed, in a product analysis study of radiation-induced hydroxylations of benzene this was observed to be the case.[6]

The ratio of the dose rates for the cobalt source II to cobalt source I used in the present study is 13.7. Nitrophenol production is and nitrobenzene consumption is not dependent on the dose rate. Clearly, nitrobenzene is re-formed at high dose rates by some mechanism in addition to disproportionation. Observed dose rate dependence of phenol production and dose rate independence of nitrobenzene consumption indicates that reactions in addition to disproportionation and dimerization play a significant role at higher dose rates.

The hydroxycyclohexadienyl radicals formed in air-saturated systems will be oxidized by oxygen to phenols.[20] The oxidation of the *p*-hydroxynitrocyclohexadienyl radical is shown in eq 4 and the ortho and meta isomers of this radi-

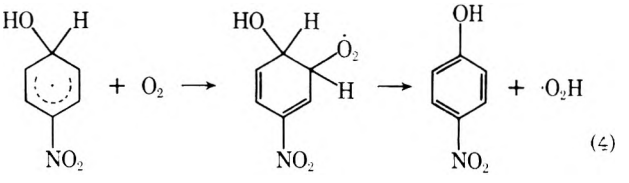

(4)

cal will also undergo the same reactions. The total phenol yield in air-saturated nitrobenzene systems was 2.4 and 1.7 when irradiated respectively at the low and the high dose

rates. Whereas, nearly all of the hydroxynitrocyclohexadienyl radicals appear to be converted to phenols when irradiated with a low dose rate only ⅔ of the radicals (II) are converted to phenols upon irradiation with high dose rate. The rate constant[12] for the addition of oxygen to hydroxynitrocyclohexadienyl radical is $2.5 \times 10^6\ M^{-1}\ \text{sec}^{-1}$. This rate constant is nearly a factor of 240 lower than that for the dimerization of the hydroxynitrocyclohexadienyl radical. Nearly a third of the hydroxynitrocyclohexadienyl radicals produced at the high dose rate are converted to dimers.

In irradiated air-saturated systems in addition to isomeric nitrophenols phenol with a yield of 0.4 was also present. Fendler and Gasowski have measured a yield of 0.5 for the nitrate ion in this system.[8] Presumably the oxidation of a portion of the hydroxynitrocyclohexadienyl radical by oxygen results in the formation of phenoxide and nitrate ions.

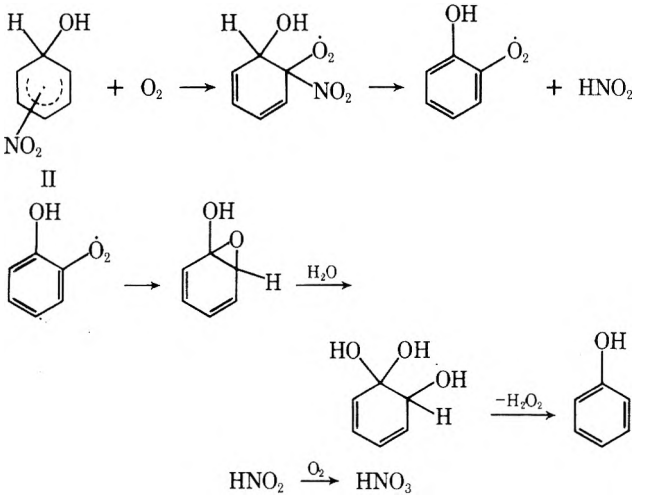

In irradiated air-saturated systems only, an unknown product was also identified, Figure 1c. As a result of the lack of its identity, it was neither possible to determine the reaction responsible for its formation nor its yield.

Effect of Ferricyanide in N_2O Systems. Ferricyanide ion was shown to quantitatively oxidize hydroxycyclohexadienyl radicals to phenol.[7] When metal ions are used to oxidize radical intermediates it is necessary to ensure that the products are stable in the presence of reduced and oxidized forms of the metal ion. Selected metal ion must be thermodynamically capable of undergoing only one electron transfer reaction at a sufficiently fast rate to produce stable products. These conditions were met by ferricyanide ion in the study of radiation-induced hydroxylation of benzene. In order to test the usefulness of ferricyanide ion to oxidize isomeric hydroxynitrocyclohexadienyl radicals the consumption of nitrobenzene and the production of nitrophenols in N_2O-saturated systems containing ferricyanide ion were examined and the results are given in Figures 2 and 5.

The initial yields for the consumption of nitrobenzene in the presence and absence of ferricyanide ion are the same indicating that only 60% of the $\cdot OHC_6H_5NO_2$ radicals produced by the addition reactions of ·OH radical to nitrobenzene are oxidized to nitrophenols. It is possible that nitrobenzene is regenerated by the reduction of $\cdot OHC_6H_5NO_2$ radicals with ferroyanide ion which is produced in the system by the reduction of ferricyanide ion.

$$\cdot OH + C_6H_5NO_2 \longrightarrow \cdot OHC_6H_5NO_2$$

$$\cdot OHC_6H_5NO_2 + Fe(CN)_6^{3-} \longrightarrow OHC_6H_5NO_2 + Fe(CN)_6^{4-}$$

$$\cdot OHC_6H_5NO_2 + Fe(CN)_6^{4-} \longrightarrow C_6H_5NO_2 + Fe(CN)_6^{3-} + OH^-$$

Comparison of the nitrophenol production in the presence and absence of ferricyanide ion revealed that the initial yields for the *m*-nitrophenol improved by a factor of >3 and that the yields for *o*- and *p*-nitrophenols were decreased by ~25–45%. Clearly *o*- and *p*-nitrophenols are undergoing secondary reactions in the presence of added metal ion. It is seen in Figure 5 that most of the data for *m*-nitrophenol does but that for *o*- and *p*-nitrophenol does not fall on linear curves. Indeed the highest measured *o*- and *p*-nitrophenol concentrations is <6 μM for each compound. It is therefore concluded that even if ferricyanide ion is a suitable oxidant to oxidize all isomeric hydroxynitrocyclohexadienyl radicals, reliable production measurements of *o*- and *p*-nitrophenols cannot be made because of the complicating secondary reactions.

Conclusions regarding the initial yields of the radical intermediates have been drawn based upon product measurements.[7] Product studies sometimes do give useful indications of the mechanism of radiation-induced reactions.[3-7] The distribution of isomeric nitrophenols along with a knowledge of the mechanism of its formation is necessary to estimate initial yields of the corresponding radical intermediates. The initial yield for the production of *m*-nitrophenol was higher by a factor >3 in the presence than in the absence of added ferricyanide ion. The initial yield for the production of *m*-nitrophenol was also higher in air-saturated systems compared to that in N_2O-saturated systems without added ferricyanide. Clearly only a small portion of *m*-hydroxynitrocyclohexadienyl radical is converted to *m*-nitrophenol in the absence of added oxidants. Contrary to predictions made by Eberhardt and Yoshida,[9] our results indicate that in the cross disproportionation reaction between *m*- and *o*- or *p*-hydroxynitrocyclohexadienyl radicals the meta isomer acts as an oxidizing agent and ortho or para isomers act as reducing agents.

Distribution of Nitrophenols. The yields of isomeric nitrophenols in aerated nitrobenzene solution irradiated at different dose rates (2 and 3.5 krads/min,[8] 0.875 krad/min,[9] and 0.2 and 14.0 krads/min[10]) have been reported. Our measurement of the initial yields of isomeric nitrophenols in solutions irradiated at a dose rate of 0.77 or 10.5 krads/min are reported in Table II. A rigorous comparison of the present results with those reported previously cannot be made because the yields of isomeric nitrophenols are dose rate dependent and also because unlike some previous studies[9,10] we obtained initial yields from detailed yield–dose studies. We observed higher yields (~10 to 15%) compared to those reported by Matthews and Sangster for isomeric nitrophenols in aerated samples irradiated at low dose rates. These differences are as expected because the yields reported by Matthews and Sangster are at a fixed dose (~20 krads) and in the region of ~10% nitrobenzene consumption. Our result for total phenol yield in aerated system is also higher by ~18 and ~33% than that reported by Eberhardt and Yoshida. The total phenol yields in aerated system reported by Eberhardt and Yoshida are 1.69 and 1.52 for samples (~5 and 1 mM initial nitrobenzene concentrations, respectively) irradiated to a dose of 52.5 and 26.25 krads, respectively. The agreement between our yields for *o*-nitrophenol in samples irradiated at low dose rates and those reported by other two groups[8,9] is poor. Our results for *o*-nitrophenol yields are higher by ~33%[9] and a

factor of 2^8 compared to those reported previously for low dose experiments. It is believed that some of the observed differences may be, at least in part, due to different methods of analyses.

The percentages for the distribution of phenols in air- and N_2O-saturated systems are also reported in Table II. Because it is not readily possible to estimate the degree of cross disproportionation relative to disproportionation between the same radicals, the ratios of the observed distribution of nitrophenols in N_2O-saturated systems without added oxidants cannot be related to the initial yields of corresponding radicals. It is clear from our results that extreme caution must be exercised to interpret observed product distribution in terms of the yield of radical intermediates.

Acknowledgment. We thank our colleagues at the Radiation Research Laboratories for their suggestions during the preparation of this manuscript. Discussions with R.H. Schuler were particularly helpful.

References and Notes

(1) Supported in part by the U.S. Atomic Energy Commission.
(2) K. Bhatia, *Anal. Chem.*, **45**, 1344 (1973).
(3) K. Bhatia and R. H. Schuler, *J. Phys. Chem.*, **77**, 1356 (1973).
(4) K. Bhatia and R. H. Schuler, *J. Phys. Chem.*, **77**, 1888 (1973).
(5) M. A. Schuler, K. Bhatia, and R. H. Schuler, *J. Phys. Chem.*, **78**, 1063 (1974).
(6) K. Bhatia, *Radiat. Res.*, **59**, 537 (1974).
(7) K. Bhatia and R. H. Schuler, *J. Phys. Chem.*, **78**, 2335 (1974).
(8) For a summary of previous work on this subject see J. H. Fendler and G. L. Gasowski, *J. Org. Chem.*, **33**, 1865 (1968).
(9) M. K. Eberhardt and M. Yoshida, *J. Phys. Chem.*, **77**, 589 (1973).
(10) R. W. Matthews and D. F. Sangster, *J. Phys. Chem.*, **71**, 4056 (1967).
(11) M. K. Eberhardt, *J. Phys. Chem.*, **78**, 1795 (1974).
(12) K.-D. Asmus, B. Cercek, M. Ebert, A. Henglein, and A. Wigger, *Trans. Faraday Soc.*, **63**, 2435 (1967).
(13) M. Anbar, "Fundamental Processes in Radiation Chemistry", P. Ausloos, Ed., Interscience, New York, N.Y., 1968, p 651.
(14) M. Anbar and P. Neta, *Int. J. Appl. Radiat. Isotopes*, **18**, 493 (1967).
(15) T. I. Balkas, J. H. Fendler, and R. H. Schuler, *J. Phys. Chem.*, **74**, 4497 (1970).
(16) K. Eiben and R. W. Fessenden, *J. Phys. Chem.*, **75**, 1186 (1971).
(17) K.-D. Asmus, A. Wigger, and A. Henglein, *Ber. Bunsenges. Phys. Chem.*, **70**, 862 (1966).
(18) J. H. Boyer, "The Chemistry of the Nitro and Nitroso Groups", H. Feuer, Ed., Interscience, New York, N.Y., 1969, p 264.
(19) A. Mantaka, D. G. Marketos, and G. Stein, *J. Phys. Chem.*, **75**, 3885 (1971).
(20) L. M. Dorfman, I. A. Taub, and R. E. Bühler, *J. Chem. Phys.*, **36**, 3051 (1962).

COMMUNICATIONS TO THE EDITOR

Comment on "The Debye–Bjerrum Treatment of Dilute Ionic Solutions", by J. C. Justice[1]

Publication costs assisted by the Office of Saline Water

Sir: In 1957, Fuoss and Onsager presented a conductance equation[2] which was derived using as their model rigid charged spheres of diameter a in a continuum to represent the solution (the primitive model). Later,[3] the integrations were repeated in order to obtain terms of order $c^{3/2}$ which had been neglected in the earlier derivation; the Fuoss–Hsia equation[3] $\Lambda = \Lambda(c; \Lambda_0, K_A, a)$ was the result. In 1968, Justice[4] replaced a by the Bjerrum distance $q = e^2/2DkT$ and used the equation $\Lambda = \Lambda(c; \Lambda_0, K_A, q)$ in the analysis of conductance data.[5] Fuoss[6] protested that the Justice equation could be derived only if the original Fuoss–Onsager model were replaced by a model in which the ions were surrounded by rigid spheres of radius $q/2$. Justice[1] then attempted to show that his equation was consistent with the primitive model.

His arguments stem from his failure to understand the physical significance of one of the Fuoss–Onsager boundary conditions; he confused relative and absolute velocities. The boundary condition[7] is

$$[(f_{ij}\mathbf{v}_{ij} - f_{ji}\mathbf{v}_{ji})\cdot\mathbf{r}]_{r=a} = 0 \qquad (1)$$

Since $f_{ji} = f_{ij}$, this is derived from

$$[f_{ji}(\mathbf{v}_{ij} - \mathbf{v}_{ji})\cdot\mathbf{r}]_{r=a} = 0 \qquad (2)$$

which is the mathematical statement of the physical fact that the *radial component of RELATIVE velocity* (RCRV) vanishes when the center-to-center distance r_{ij} between two ions equals a. If a in (2) is replaced by another distance R, for example, $R = q$, then (2) clearly requires that the RCRV vanish at $r_{ij} = q$, because a component of velocity vanishes only at a rigid barrier normal to the direction of that component. However if the meaning of r is changed in the *equation*, a concommitant change must be made in the *model;* therefore Justice's replacement of a in (2) by q requires a model in which charges are centered in spheres whose contact distance is q. In short, the Justice equation does not derive from the primitive model for which the contact distance is a, but rather for one with q as the contact distance.

Justice repudiates this ridiculous model and asserts that the primitive model satisfies a boundary condition which he writes

$$[(g_{ij}\mathbf{v}_{ij} - g_{ji}\mathbf{v}_{ji})\cdot\mathbf{r}]_{r=R} = 0 \qquad (3)$$

thereby seemingly justifying his "modification" of the Fuoss–Hsia equation. Since $f_{ji} = g_{ji}$, (3) looks deceptively like (2), with a replaced by R. *However the symbols for vec-*

tor velocities in (3) have a different meaning from those in (2)! Justice defines $\mathbf{v}_{ij}$ as the *mean velocity vector* of a j ion, located with respect to an i ion by the vector $\mathbf{r}_{ij}$, so eq 3 states that the difference of the scalar products of the mean velocities $\mathbf{v}_{ij}$ and $\mathbf{v}_{ji}$ with $\mathbf{r}$ vanish at $r = R$. In the Fuoss–Onsager boundary condition (2), $(\mathbf{v}_{ij} - \mathbf{v}_{ji})$ is the *relative* velocity of ions i and j, and $(\mathbf{v}_{ij} - \mathbf{v}_{ji})\cdot\mathbf{r}$ is therefore the *radial* component of their relative velocity; note that $(\mathbf{v}_{ij} - \mathbf{v}_{ji})$ is a vector difference. Equation 3 therefore states that the *difference of averages* dotted into $\mathbf{r}$ vanishes at $r = R$, while (2) states that the *difference* dotted into $\mathbf{r}$ vanishes at a specified value of r. Obviously (2) and (3) are completely different statements regarding the behavior of the model. Furthermore, we shall show that (3), although mathematically correct, is a trivial statement, and worse than useless as a boundary condition.

First, regarding triviality: consider the scalar product $(\mathbf{V}\cdot\mathbf{r}_{ij})$ of *any* given vector with $\mathbf{r}_{ij}$

$$(\mathbf{V}\cdot\mathbf{r}_{ij}) = |\mathbf{V}||\mathbf{r}_{ij}| \cos\varphi \tag{4}$$

where φ is the angle between $\mathbf{V}$ and $\mathbf{r}_{ij}$. Recall that $\mathbf{r}_{ij}$ is the vector which locates the j ion with respect to the i ion; since there is no directional correlation between the position of the two ions, the average of $\cos\varphi$ is zero and therefore

$$\langle\mathbf{V}\cdot\mathbf{r}_{ij}\rangle = 0 \tag{5}$$

for *all* values of $|\mathbf{r}_{ij}| \geq a$. If we set $\mathbf{V} = \mathbf{v}_{ij}$ and $|\mathbf{r}_{ij}| = R$, we have Justice's equation

$$[\mathbf{v}_{ij}(\mathbf{r}_{ij})\cdot\mathbf{r}_{ij}]_R = 0 \tag{6a}$$

and congruently

$$[\mathbf{v}_{ji}(\mathbf{r}_{ji})\cdot\mathbf{r}_{ji}]_R = 0 \tag{6b}$$

Justice's eq 3 is obtained by adding (6b) to (6a), after multiplication by $g_{ij} = g_{ji}$ and using the fact that $\mathbf{r}_{ij} = -\mathbf{r}_{ji}$. Clearly, (3) says nothing about *relative* velocities, with which the Fuoss–Onsager boundary condition is concerned; it merely states that zero minus zero is zero.

Second, regarding the possible role of (3) as a boundary condition: construct from (6) the linear combination

$$g_{ij}(\mathbf{v}_{ij}\cdot\mathbf{r}_{ij})_r + Ag_{ji}(\mathbf{v}_{ji}\cdot\mathbf{r}_{ji})_{r'} = 0 \tag{7}$$

where A is an arbitrary constant and r and r' are any values of $|\mathbf{r}_{ij}| = |\mathbf{r}_{ji}|$. Equation 3 follows from (7) by setting $A = -1$ and $r = r' = R$; there is, however, no physical justification for this choice. It is merely an efficient (albeit illegal) means of obtaining an equation which superficially resembles (2). Or, looking at the situation from the mathematical point of view, (6a) and (6b), which are independent equations by Kohlrausch's law of independent mobilities, together with the three electrostatic boundary conditions,[8] give *five* equations to determine the *four* constants of integration which appear in the Fuoss–Hsia development, an awkward dilemma indeed. Consequently Justice's equations cannot rigorously lead to eq 3.5 of ref 2 with a replaced by q, and lacking this equation, the equation in which Justice would replace a by $R = q$ cannot be derived. It has already been shown that condition (2) with a replaced by q demands a model in which ions are surrounded by rigid spheres of radius $q/2$.

In this sequence of comments on conductance equations, emphasis has been on mathematical detail, perhaps to such an extent that one fundamental feature has been obscured: namely, that theory describes the behavior of a *model* and not that of a real physical system. The concept of relative velocity has, of course, no meaning for a pair of real ions rattling around in a swarm of moving solvent molecules. For two oppositely charged spheres moving in a continuum, however, velocities can be precisely described by the classical equations of motion (in which Brownian motion is replaced by the virtual force of the Einstein kT grad c term). When a model anion and cation drift together, they may stick for a while due to electrostatic attraction; during the dwell time of the pair, their relative *radial* motion must be zero, while the motion of the center of gravity of the *pair* is determined by the laws of conservation of energy and momentum. Formation of a pair of real ions is the consequence of the diffusion of the two ions into adjacent sites in the particulate solvent; details of this process are irrelevant for the calculation of the long-range relaxation and electrophoretic effects.[9,10]

We therefore iterate previous conclusions.[6] The Justice equation is not derivable from the primitive model, and the model for which the equation can be derived using (2) with a replaced by q is physically unrealistic.

References and Notes

(1) J. C. Justice, *J. Phys. Chem.*, **79**, 454 (1975).
(2) R. M. Fuoss and L. Onsager, *J. Phys. Chem.*, **61**, 668 (1957).
(3) R. M. Fuoss and K. L. Hsia, *Proc. Natl. Acad. Sci. U.S.*, **57**, 1550; **58**, 1818 (1967).
(4) J. C. Justice, *J. Chim. Phys.*, **65**, 353 (1968).
(5) J. C. Justice, *Electrochim. Acta*, **16**, 701 (1971).
(6) R. M. Fuoss, *J. Phys. Chem.*, **78**, 1383 (1974).
(7) Reference 2, eq 3.4; ref 6, eq 7.
(8) Reference 2, eq 3.1, 3.2, 3.3; ref 6, eq 4–6.
(9) R. M. Fuoss, *Proc. Natl. Acad. Sci. U.S.*, **71**, 4491 (1974).
(10) R. M. Fuoss, *J. Phys. Chem.*, **79**, 525 (1975).

Sterling Chemistry Laboratory **Raymond M. Fuoss**
Yale University
New Haven, Connecticut 06520

Received September 7, 1974

Reply to the Comment by Raymond M. Fuoss on "The Debye–Bjerrum Treatment of Dilute Ionic Solutions"

Sir: The correct interpretation of the physical meaning of the velocity vectors $\mathbf{v}_{iP}{}^{jQ}$ and $\mathbf{v}_{jQ}{}^{iP}$, used by various authors[2-6] in the theory of electrolytes conductance,[7] can be achieved only by coming back to the definition of these quantities which is given by

$$\mathbf{v}_{iP}{}^{jQ} = \mathbf{u}_{iP}{}^{Q} + \omega_j(e_j\mathbf{X} - e_j\nabla_Q\psi_{iP}{}^{Q} - e_j\nabla_Q\psi_{jQ'}{}^{Q} - kT\nabla_Q \ln f_{iP}{}^{jQ}) \tag{1}$$

This obviously is not the *actual* velocity vector of *an ion* j at Q but a *time-average*[8] *velocity vector of ions of type* j at Q when an ion of type i is present at P. This fact is plainly recognized by Pitts,[2] Onsager,[4] and Falkenhagen.[5] Consequently the boundary condition used by Fuoss and Onsager

$$(f_{iP}{}^{jQ}\cdot\mathbf{v}_{iP}{}^{jQ} - f_{jQ}{}^{iP}\cdot\mathbf{v}_{jQ}{}^{iP})\cdot\mathbf{r} = 0 \text{ at } r = a \tag{2}$$

which is strictly equivalent to

$$v_{iP,r}{}^{jQ} = v_{jQ,r}{}^{iP} \text{ at } r = a \tag{3}$$

where the subscript r means we are dealing only with the radial components of the vectors, cannot have the meaning claimed by Fuoss. It cannot be applied to the actual[10] collision of two specified ions given the time-average nature of the quantity involved.

It is easy to show[11] from eq 1 that

$$v_{iP_r}{}^{jQ} \cdot v_{jQ_r}{}^{iP} \leq 0 \tag{4}$$

for any value of r, so that the only possibility for (3) is now

$$\left.\begin{aligned} v_{iP_r}{}^{jQ} &= 0 \\ \text{or} \\ v_{jQ_r}{}^{iP} &= 0 \end{aligned}\right\} \text{at } r = a \qquad \begin{matrix} (5) \\ \\ (5') \end{matrix}$$

Thus, all our conclusions, formerly published,[12] are exact and the present controversy solved.[13] Moreover, condition (2), *when applied to definition* (1), can be replaced by condition (5) *or* (5'). Since condition (5') is derivable alone from the combination of condition (5) with eq 1, one of the two last conditions is sufficient. This gives the solution of the "awkward dilemna" raised by Fuoss.

In conclusion, one must keep in mind that the $\mathbf{v}_{ij}$ vectors are not only average velocity vectors but also perturbation terms. As average velocity vectors their radial component may vanish when the particles encounter an infinite repulsion potential surface. As perturbation terms they can become negligible when the particles enter an area where predominates an attraction energy strong compared with the external perturbation cause. The initial condition proposed by Fuoss belongs to the first category. When used to fit into the Bjerrum model it belongs to the second category.

References and Notes

(1) R. M. Fuoss, *J. Phys. Chem.*, preceding paper in this issue.
(2) E. Pitts, *Proc. R. Soc.*, **217**, 43 (1953).
(3) R. M. Fuoss and L. Onsager, *J. Phys. Chem.*, **61**, 668 (1957).
(4) L. Onsager and S. K. Kim, *J. Phys. Chem.*, **61**, 215 (1957).
(5) H. Falkenhagen, W. Ebeling, and W. D. Kraeft, "Mass Transport Properties of Ionized Dilute Solutions", in "Ionic interactions", Vol. I, S. Petrucci, Ed., Academic Press, New York, N.Y.
(6) T. J. Murphy and E. G. D. Cohen, *J. Chem. Phys.*, **53**, 2173 (1970).
(7) These vectors are of paramount importance since, together with the distribution functions $f_{iP}{}^{jQ} = f_{jQ}{}^{iP}$, they define the continuity equation which, is at the heart of the conductance theory

$$-\partial f_{iP}{}^{jQ}/\partial t = \nabla_Q f_{iP}{}^{jQ} \mathbf{v}_{iP}{}^{jQ} + \nabla_P f_{jQ}{}^{iP} \mathbf{v}_{jQ}{}^{iP} = -\partial f_{jQ}{}^{iP}/\partial t$$

(8) In eq 1, all terms are already time average quantities: for $\psi_{iP}{}^{Q}$, $\psi_{jQ}{}^{Q}$, and $f_{iP}{}^{jQ}$, (cf. an excellent demonstration of this in Fuoss monography[9]); $\mathbf{u}_{iP}{}^{Q}$ which is the hydrodamic velocity vector of the medium at Q is also an average since it is derived later by use of the Navier–Stokes equation. As for the term containing the external field strength $\mathbf{X}$ it may be considered as constant during the time τ of averaging. (If the field is constant then there is no limit to τ, if not τ must be small compared to the period of the alternative field but great compared to collision time in the solution for the continuity equation of conductance to hold.)
(9) R. M. Fuoss and F. Accascina, "Electrolytic Conductance", Interscience, New York, N.Y., pp 117 and 118.
(10) It must be noted that if the *actual* collision of two ions in a fluid had to be described, not only the boundary condition of Fuoss should be used with another definition of the velocity vectors and with an other continuity equation but, more important, this boundary condition would be totally irrealistic for hard-spheres collisions because in that case the radial relative velocities never vanish. They undergo a discontinuity and the nature of the collision should be specified differently. As it is formulated, it could only be applied to nonbouncing collisions (*as the smooth landing of a plane, for instance* (everlasting contact)).
(11) This can be done in two ways. (1) The time-average velocity vectors vanish at equilibrium ($X = 0$) as is recognized by Fuoss[3] so that they represent a perturbation due to the external field. These perturbations on ions of opposite charges ($i \neq j$) must be opposite in direction. This was the line of demonstration adopted in the paper[12] commented on by Fuoss.[1] (2) The same conclusion can of course be reached by discussing the consequences, on each term of eq 1, of inverting the elements of each couple (i, j) and (P, Q). All the necessary material will be found in ref 3 or 9.
(12) J. C. Justice, *J. Phys. Chem.*, **79**, 454 (1975).
(13) Fuoss admits in his comment that if the involved velocities were time-average quantities, then (5) or (5') would be true.

Laboratoire d'Electrochimie **Jean-Claude Justice**
Bât. F
University of Paris VI
75230 Paris Cedex 05, France

Received December 27, 1974

Carbanion Solvation in n-Electron Donor, Aprotic, Low Dielectric Constant Solvents

Publication costs assisted by the Universidad de Bilbao

Sir: Aprotic, n-electron donor solvents (n-DS) display excellent cation solvating properties, an effect obviously due to the lone electron pairs of their oxygen or nitrogen atoms.[1] On the other hand, any anion–n-DS molecule interaction seems on the same grounds highly improbable. Many experimental results give support to this assumption. For example, recent studies of the conductivity of inorganic salts in hexamethylphosphoramide show that this strong n-donor solvent is unable to solvate the weakly basic anions ClO_4^-, NO_3^-, Br^-, and pycrate$^-$.[2] Experiments by Slates and Szwarc[3] also point in this direction. These researchers found that the diffusion coefficients of the radical anions of aromatic hydrocarbons in tetrahydrofuran (THF) as derived from ionic mobilities are very similar to those of the parent hydrocarbons.

The conclusions reached from the cited studies are in accordance with kinetic results on the anionic polymerization of styrene in n-electron donor, aprotic, low dielectric constant solvents. For example, Parry et al. found that $k_{(-)}$, the propagation rate constant of the "free" polystyryl anion in tetrahydropyran (THP) (i.e., the rate constant of the elemental reaction: "free" polystyryl anion + styrene monomer in THP) was, within experimental error, independent of the counterion.[4] Table I collects these results together with data from Hirohara et al.[5] and from Böhm and Schulz.[6]

On the other hand, kinetic experiments on sodium polystyryl in a series of ethereal solvents (i.e., same counterion, different medium) have shown that the "free" carbanion propagation rate constant is solvent independent (see Figure 1). All these results are from the same laboratory (Institut für physikalische Chemie, Universität Mainz, W. Germany) in order to be sure of the self-consistency of the data.

The reported conductometric and kinetic results seem to confirm the a priori assumption that no detectable carbanion–n-DS molecule interaction exists.

However, recent experiments by Ise et al. on the electric field effect upon the anionic polymerization of styrene in THP[5] and 2-methyltetrahydrofuran (2-MTHF)[11] have raised the question of the carbanion solvation by n-electron donor solvents, particularly ethereal solvents.

These researchers found an acceleration of the propagation reaction, i.e., an increase in k_p, the overall propagation rate constant, on increasing the electric field strength up to

TABLE I: Propagation Rate Constant $10^{-4}k_{(-)}/M^{-1}$ sec^{-1} of the "Free" Polystyryl Carbanion in THP at 25° with Different Counterions

Li^+	Na^+	K^+	Rb^+	Ref
16	13.5	14	10	4[a]
3.1	6.8	7.3		5
	12.4			6

[a] Data at 30°.

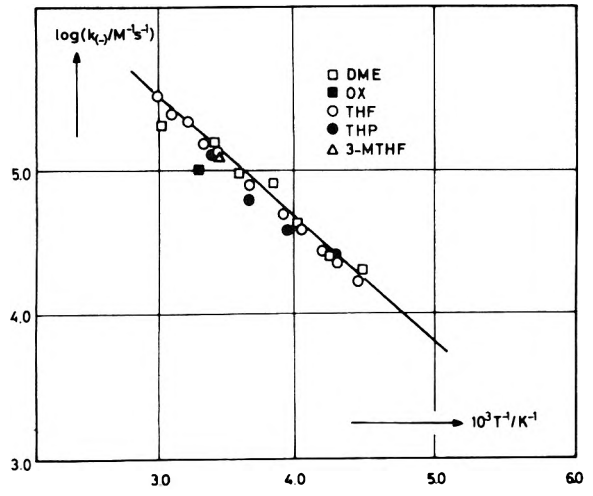

Figure 1. Arrhenius plot of the "free" carbanion propagation rate constant $k_{(-)}$ in 1,2-dimethoxyethane (DME),[7] THF,[8] THP,[6] oxepane (OX),[9] and 3-methyltetrahydrofuran (3-MTHF).[10]

about 5 kV cm^{-1}. To be precise, an analysis of their kinetic data showed the k_p increase to be due to an increase of the product $k_{(-)}K_D^{1/2}$, where K_D is the overall dissociation constant of the ion pairs into "free" ions. Ise and his associates did not find, however, an increase in the electrical conductivity of the solution with the electric field, so K_D must not change. In other words, the charge carrier concentration does not change, i.e., the second Wien effect does not occur. The obvious conclusion is that $k_{(-)}$ must increase with the electric field.

To explain the electric field effect upon $k_{(-)}$ Ise et al. supposed that a stepwise desolvation of the "free" carbanion on going to stronger fields occurred. The partially desolvated carbanions should be more reactive than the solvated ones because they can generate a more powerful electric field, and it appears proven that the polarization of the approaching monomer is the main factor affecting the rate of propagation in anionic polymerization.[12]

In this manner, the kind of charge carriers rather than their concentration would change. The mobility of the carbanionic polymer chain ends is, however, only a small fraction of the molar conductance of the solution. That means that the change from solvated to unsolvated carbanions would not appreciably affect the total electrical conductivity of the solution.

If this interpretation is correct, experiments performed in the absence of an electric field would not imply naked carbanions, as it was assumed until now, but solvated ones. On the other hand, although Ise's zero-field $k_{(-)}$ constants in THP are systematically lower than Schulz's[6] or Bywater's[4] (see Table I), one must be confident of the self-consistency of his results and admit the evidence of the reported electric field effect. So, the problem is how to reconcile the apparent absence of solvent effect on $k_{(-)}$ (see Figure 1) with a weak carbanion solvation by ether molecules.

At first consideration, one could wonder about the fact that carbanions solvated by different kinds of ether molecules behave similarly with respect to the styrene addition. At this moment one should remember the conclusion of the Mainz group about the reactivities of other ionic species, contact ion pairs and solvent separated ion pairs of sodium polystyryl, in different solvents.[6,7,13] These researchers found very similar propagation rate constants for every kind of ion pair irrespective of solvent. In the light of these results, I suggest that a plausible explanation for the discussed discrepancy could well consist in stating that also carbanions solvated by different ethers display similar reactivities. It would then not be true that carbanions are not solvated by ethers, but rather that the weak zero-field solvation does not affect their reactivities.

It should be finally noted that the stepwise increase of the carbanion reactivity upon desolvation allows us to interpret the linear relation between $k_{(-)}$ and $1/T$ (see Figure 1) as implying no temperature effect on the solvation degree of the carbanion. Apparently the increase in dielectric constant and the decrease in thermal energy of the solvent on going to lower temperatures would have no effect on the carbanion–solvent molecule interaction. Note, however, that the reported linearity refers to DME, THF, and THP (only one point, in the high-temperature region, is reported for OX and 3-MTHF). When the zero-field $k_{(-)}$ data of Takaya and Ise in 2-MTHF[11] are plotted vs. $1/T$ a deviation of the high-temperature straight line is seen at low temperatures. This deviation distinctly lies out of the experimental error. If this point could be confirmed, one would be tempted to attribute the observed deviation to a change in the carbanion–2-MTHF molecule interaction. The superposition of this physical effect to the elemental kinetic Arrhenius-type temperature effect would then explain the observed nonlinearity.

References and Notes

(1) H. E. Zaugg, *J. Am. Chem. Soc.*, **82**, 8903 (1960); H. D. Zook and W. L. Gumby, *ibid.*, **82**, 1386 (1960).
(2) P. Bruno, M. Della Monica, and E. Righetti, *J. Phys. Chem.*, **77**, 1258 (1973).
(3) R. V. Slates and M. Szwarc, *J. Phys. Chem.*, **69**, 4124 (1965).
(4) A. Parry, J. E. L. Roovers, and S. Bywater, *Macromolecules*, **3**, 355 (1970).
(5) H. Hirohara, M. Nakayama, K. Takaya, and N. Ise, *Trans. Faraday Soc.*, **66**, 1165 (1970).
(6) L. L. Böhm and G. V. Schulz, *Makromol. Chem.*, **153**, 5 (1972).
(7) J. M. Alvarino, M. Chmelir, B. J. Schmitt, and G. V. Schulz, *J. Polym. Sci., Part C*, **41**, 275 (1973).
(8) B. J. Schmitt and G. V. Schulz, *Makromol. Chem.*, **142**, 325 (1971).
(9) G. Lohr and S. Bywater, *Can. J. Chem.*, **48**, 2031 (1970).
(10) B. J. Schmitt and G. V. Schulz, *Makromol. Chem.*, **175**, 3261 (1974).
(11) K. Takaya and N. Ise, *Polymer*, **15**, 635 (1974).
(12) R. V. Slates and M. Szwarc, *J. Am. Chem. Soc.*, **89**, 6043 (1967).
(13) L. L. Böhm, M. Chmelir, G. Löhr, B. J. Schmitt, and G. V. Schulz, *Adv. Polym. Sci.*, **9**, 1 (1972).

Departamento de Química Física
Facultad de Ciencias
Universidad de Bilbao, Bilbao, Spain
J. M. Alvariño

Received November 5, 1974

Equilibrium Studies by Electron Spin Resonance. XI. The Use of g Values for the Determination of Ion Pair Dissociation Constants

Publication costs assisted by the University of Puerto Rico

Sir: To date equilibrium constants controlling the dissociation of ion pairs have been determined by the use of three different ESR techniques. These techniques include the use of (1) coupling constants,[1,2] (2) line widths (relaxation times),[3] and (3) line intensities (spin concentrations).[4,5] Here we wish to report the use of the remaining ESR parameter (g values) for the determination of equilibrium constants for the dissociation of an ion pair (β) into a free anion radical (α) and a solvated cation

$$\beta \rightleftharpoons \alpha + M^+ \quad (1)$$

Since the first accurate measurements of g values for organic anion radicals in solution, several workers have noticed changes in g values with temperature.[6-8] Recently it has been reported that the g value dependence upon temperature is at least partially due to ion pairing.[9] The ion pair and free ion of durosemiquinone in dimethoxyethane have been accurately determined for a series of counterions, and for all cases the g value is larger for the free ion than it is for the ion pair.[4]

The reduction of 2,6-di-*tert*-butylbenzoquinone in hexamethylphosphoramide (HMPA) by potassium metal results in the formation of the free anion radical,[2] which is characterized by the coupling constants given in Table I and a g value[10] of 2.004814 ± 0.000008. Successive additions of potassium iodide[11] to this solution result in a gradual decrease in the observed g value, Figure 1. This decrease is due to the formation of the ion pair, which exists in rapid equilibrium with the free ion, eq 1. The observation of a time-averaged g value is due to the fact that the time between ion association and dissociation events is small on the ESR time scale.[3] If the opposite were true the two radicals (ion pair and free ion) would be observed simultaneously.[2,5a]

The difference in the observed g value with a given quantity of KI added to the solution and that for the free ion ($\Delta\bar{g}$) is a weighted average, and it varies from zero (for a solution that contains only free ion) to the difference in g value for the free ion and ion pair ($\Delta g'$)

$$\Delta\bar{g} = \Delta g'(\beta)/[(\alpha) + (\beta)] \quad (2)$$

Combining this expression with that for the thermodynamic equilibrium constant, $K_{eq} = (\alpha)(K^+)/(\beta)$, where (K^+) represents the concentration of added KI, leads to the following expression.

$$1/\Delta\bar{g} = K_{eq}/\Delta g'(K^+) + 1/\Delta g' \quad (3)$$

Since the two jump model expressed in eq 1 (ion pair to free ion) has been shown to be correct for this system,[2] a plot of $1/\Delta\bar{g}$ vs. $1/(K^+)$ should be linear and have a slope of $K_{eq}/\Delta g'$ and an intercept of $1/\Delta g'$. Treated in this manner our data did yield a straight line, Figure 1. Table I shows a representative set of ESR parameters for various concentration of potassium ion.

At 28° the equilibrium constant determined from Figure 1 is 0.076 ± 0.009. The equilibrium constant for this reaction has been recently determined by the use of time-averaged ESR coupling constants,[2,12] and it was found to be 0.094 ± 0.01 at 28°. The equilibrium constant measured here for eq 1 by the use of g values is within experimental error with that previously reported.

TABLE I: ESR Parameters for the System 2,6-Di-*tert*-butylbenzoquinone-HMPA-K with Added KI

K^+ concn, M	A_H, G	$10^5\Delta\bar{g}$
0	2.346	0
0.051	2.260	3.18
0.061	2.245	3.52
0.080	2.223	3.95
0.150	2.182	5.29
0.328	2.122	6.94

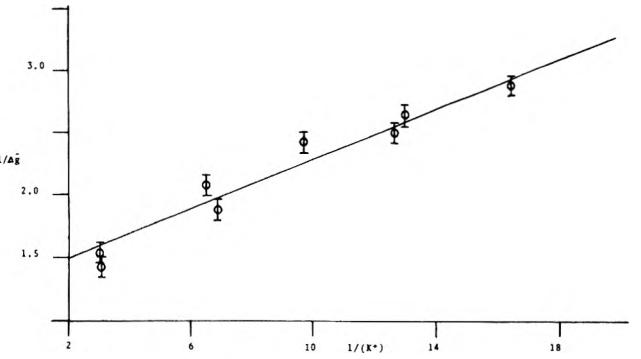

Figure 1. Plot of $10^{-4}/\Delta\bar{g}$ vs. the reciprocal of the added KI for the system 2,6-di-*tert*-butylbenzoquinone-HMPA-K. The g values used to make this graph were determined using the g value for the free ion as a standard.

Since the first attempt to study ion pair-free ion equilibria in 1960 by Atherton and Weissman,[13] this work represents the first report of the use of g values for the determination of equilibrium constants for ion pair free ion equilibria. The use of g values for the determination of equilibrium constants, however, is not unprecedented. Solvent exchange equilibria have been previously studied by means of ESR g values.[14]

Since there are many systems in which the ESR coupling constants are insensitive to ion pairing phenomena and g values are a sensitive function of ion pairing, the use of time-averaged g values should be very useful in the investigation of ion pair equilibria in these systems. Further, since g values can now be measured to high precision, accurate equilibrium constants can now be obtained.

Acknowledgments. We are grateful to Research Corporation and the National Institutes of Health for support of this work. The NIH support was from Grant No. RR-8102 of the Division of Research Resources.

References and Notes

(1) (a) N. Hirota, *J. Phys. Chem.*, **71**, 127 (1967); (b) A. M. Hermann, A. Rembaum, and W. R. Carper, *ibid.*, **71**, 2661 (1967).
(2) G. R. Stevenson and A. E. Alegria, *J. Phys. Chem.*, **78**, 1771 (1974).
(3) G. R. Stevenson and R. Concepción, *J. Am. Chem. Soc.*, **96**, 4696 (1974).
(4) R. D. Allendoerfer and R. J. Papez, *J. Phys. Chem.*, **76**, 1012 (1972).
(5) (a) G. R. Stevenson and L. Echegoyen, *J. Phys. Chem.*, **76**, 2339 (1973); (b) G. R. Stevenson and A. E. Alegria, *ibid.*, **76**, 3100 (1973).
(6) B. G. Segal, M. Kaplan, and G. K. Fraenkel, *J. Chem. Phys.*, **43**, 4191 (1965).
(7) R. D. Allendoerfer, *J. Chem. Phys.*, **55**, 3615 (1971).
(8) (a) J. Kelm and K. Mobius, *Angew. Chem., Intl. Edit. Engl.*, **9**, 73 (1970); (b) M. T. Jones, "Advances in Magnetic Resonance", Vol. VII, J. S.

Waugh, Ed., Academic Press, New York, N.Y., 1973.
(9) M. T. Jones, T. C. Kuechler, and S. Mertz, *J. Magn. Resonance*, **10**, 149 (1973).
(10) (a) The *g* values were measured on a Varian E-9 ESR spectrometer using the dual cavity technique.[10b] (b) J. E. Wertz and J. R. Bolton, "Electron Spin Resonance: Elementary Theory and Practical Applications", Mcgraw-Hill, New York, N.Y., 1972, p 464. (c) The *p*-benzosemiquinone–*tert*-butyl alcohol system was used as a *g* value standard.[6,7]
(11) (a) It has been previously observed that salts of this type are dissociated in HMPA; see P. Bruno, M. D. Monica, and E. Righetti, *J. Phys Chem.*, **77**, 1258 (1973). (b) The ion association constant for KI was found to be about 4 in HMPA.[12]
(12) G. R. Stevenson and A. E. Alegria, unpublished results.
(13) N. M. Atherton and S. I. Weissman, *J. Am. Chem. Soc.*, **83**, 1330 (1961).
(14) T. Yonezawa, T. Kawamura, M. Ushio, and Y. Nakao, *Bull. Chem. Soc. Jpn.*, **43**, 1022 (1970).

Department of Chemistry
University of Puerto Rico
Rio Piedras, Puerto Rico 00931

Gerald R. Stevenson*
Antonio E. Alegria

Received November 11, 1974

Absence of an Energy Dependence for $CH_2(^1A_1)$ Reaction with the C–H and Si–H Bonds of Dimethylsilane

Publication costs assisted by the Petroleum Research Fund

Sir: The insertion of singlet methylene radicals into Si–H bonds is one of the fastest $CH_2(^1A_1)$ reactions.[1] For various substituted alkylsilanes $CH_2(^1A_1)$ radicals formed by diazomethane photolyses at 3660 and 4358 Å insert 7–9 times faster into Si–H bonds than C–H bonds.[1,2] Though various hypotheses have been suggested, the origin of this reactivity difference has not been identified.[2]

In this work we have investigated the effect of excess methylene vibrational energy and temperature on the relative reactivity of $CH_2(^1A_1)$ radicals with dimethylsilane

$$^1CH_2 + CH_3SiH_2CH_3 \rightarrow (CH_3)_3SiH\ [TMS] \quad (1)$$

$$\rightarrow C_2H_5SiH_2CH_3\ [MES] \quad (2)$$

For many bimolecular reactions, excess vibrational energy has a significant effect on reaction cross sections and the resulting product distributions.[3] In addition, if there is an Arrhenius activation energy difference for singlet methylene insertion into Si–H and C–H bonds, it should be detectable by relative rate measurements at different temperatures.

There is a continuing controversy concerning the electronic energy difference between $CH_2(^1A_1)$ and $CH_2(^3B_1)$, which is the ground state.[4–8] The major point of dispute involves the interpretation of different chemical activation rate measurements.[7,8] It has been suggested that these differences could be reconciled if there was a threshold for singlet methylene insertion reactions.[9] Some discrepancies may also arise if there are different excitation functions for $CH_2(^1A_1)$ reactions with various types of bonds, so that some molecules select the more energetic methylenes while others react with thermalized methylene radicals. Since Si–H bonds are more highly reactive than C–H bonds, these suggestions can be partially tested by studying the effect of excess $CH_2(^1A_1)$ vibrational energy and temperature on Si–H and C–H relative insertion reactivities.

TABLE I: Experimental Trimethylsilane: Methylethylsilane Ratios for the Singlet Methylene ($^1A_1$)-Dimethylsilane Reaction

Singlet methylene precursor	Temp, °C	CF_4:DMS	TMS:MES[a]
CH_2N_2—3660 Å	24		2.30 ± 0.13
CH_2N_2—4358 Å	0		2.24 ± 0.03
CH_2N_2—4358 Å	24		2.34 ± 0.01
CH_2N_2—4358 Å	90		2.40 ± 0.08
CH_2N_2—4358 Å	24	5.4	2.30
CH_2N_2—4358 Å	24	17.0	2.28
CH_2CO—3340 Å	0		2.17 ± 0.08
CH_2CO—3340 Å	24		2.25 ± 0.02
CH_2CO—3340 Å	100		2.16 ± 0.12

[a] For experiments where no error is given only one measurement was made.

Singlet methylene insertion was studied by photolyzing ketene or diazomethane with added oxygen. Oxygen is an effective scavenger for the $CH_2(^3B_1)$ radicals.[1,2] Ketene, diazomethane, and dimethylsilane were prepared by conventional techniques.[1,2,7] The diazomethane 4358-Å photolyses were performed using a Hanovia 673 A medium-pressure mercury arc lamp with Corning colored glass filters, No. 5850 and 3389. For the rest of the photolyses a 200-W Osram high-pressure mercury arc lamp was used. Corning colored glass filter No. 5840 was used to isolate the 3130-, 3340-, and 3660-Å lines for the ketene photolyses and Corning colored glass filters No. 5860 and 7380 were used for 3660-Å photolyses of diazomethane. The reaction mixtures were photolyzed in Pyrex vessels. A normal mixture consisted of dimethylsilane–ketene or diazomethane–oxygen in a ratio of 10:1:1. Total pressures were always greater than 50 Torr so the trimethylsilane and dimethylsilane, eq 1 and 2, were collisionally stabilized.[10] Tetrafluoromethane was added to some mixtures as a moderator. Trimethylsilane (TMS) and methylethylsilane (MES) were measured by glpc.

The experimental results are listed in Table I. Though the filter used in the ketene photolyses transmitted the 3130-, 3340-, and 3660-Å mercury lines, most of the photolysis occurred at 3340 Å. The combination of the filter and Pyrex vessel removed most of the 3130-Å line and as a result of the small extinction coefficient[11] and photodissociation quantum yields[12] for CH_2CO at 3660 Å only a small fraction of the singlet methylenes were formed by 3660-Å photolyses. However, even if the 3660- and 3130-Å lines were not completely removed, it would have only a minor effect on our experiments since the average energies of singlet methylenes formed at 3660 and 3130 Å are only ~1 kcal/mol lower and higher, respectively, than those formed by 3340-Å photolyses.[8,13]

The key in comparing the results using diazomethane and ketene is the difference in the vibrational energy content of the singlet methylenes. The average vibrational energy of the singlet methylenes formed by diazomethane photolysis at 3660 Å is ~13 kcal/mol higher than that of those formed by CH_2CO photolysis at 3340 Å.[7,14] By photolyzing CH_2N_2 at 4358 Å and using CF_4 as a moderator to deactivate vibrationally the singlet methylene radicals,

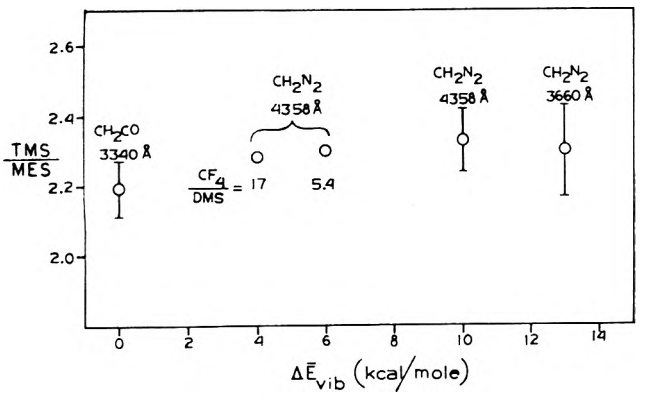

Figure 1. Plot of TMS:MES ratios vs. relative average singlet methylene vibrational energy ($\Delta\bar{E}_{vib}$). Only one measurement was made for points without error bars.

their average energy may be varied between the above extremes.[7] The TMS:MES ratios, as a function of relative singlet methylene average vibrational energy, are shown in Figure 1.

The results displayed in Figure 1 show the relative reactivities of the Si–H and C–H bonds of dimethylsilane do not change within experimental error as the average vibrational energy of $CH_2(^1A_1)$ is varied by 13 kcal/mol. This means the ratio in the excitation functions for Si–H and C–H insertion does not change with this alteration in the singlet methylene vibrational energy. Therefore, there is no discrimination on the part of C–H and Si–H bonds toward singlet methylenes with different vibrational energies. However, these results do not rule out the possibility that there are identical changes in the excitation functions as the $CH_2(^1A_1)$ vibrational energy is varied. It should be pointed out that these results do not pertain to the role dimethylsilane vibrational energy may play in the insertion dynamics.

The presence of a threshold difference for $CH_2(^1A_1)$ insertion into the Si–H and C–H of dimethylsilane can be investigated by varying the temperature. If the difference in reactivities of the Si–H and C–H bonds at 24° is solely an activation energy difference, the TMS:MES ratio for CH_2CO 3340-Å photolysis should be 2.7 and 1.5 at 0 and 100°, respectively. However, within experimental error, we find for both CH_2CO 3340-Å and CH_2N_2 4358-Å photolyses the TMS:MES ratio is independent of temperature, and if there is an activation energy difference, it is very small. Lack of an activation energy difference for singlet methylene insertion into these two different types of bonds suggests that the threshold for insertion may be small. Support for this hypothesis is found by using the rate constant of 1.9×10^{-12} cm^3 molecule^{-1} sec^{-1} for the $CH_2(^1A_1) + CH_4 \rightarrow C_2H_6$ reaction[15] and the measurement of 7.1 for the ratio of the $CH_2(^1A_1)$ reaction with dimethylsilane relative to that with methane[16] to determine the rate constant for total $CH_2(^1A_1)$ reaction with dimethylsilane equal to 1.3×10^{-11} cm^3 molecule^{-1} sec^{-1}. This rate constant is only ~50 times smaller than the collision frequency,[17] which is consistent with a maximum activation energy at 25° of 2.3 kcal/mol for singlet methylene reaction with dimethylsilane. In addition, extended Hückel[18] and MINDO/2[19] calculations have predicted that the activation energy for $CH_2(^1A_1)$ insertion into the C–H bonds of CH_4 is small.

Recent quantum mechanical calculations[18,19] suggest that $CH_2(^1A_1)$ reaction with CH_4 is a concerted reaction, with the methylene attacking along a C–H axis. It would be interesting to see if such a model without an activation energy difference for Si–H and C–H insertion can predict the experimental ratios of relative Si–H and C–H insertion in alkylsilanes and the independence of the reactivity ratios with varying amounts of $CH_2(^1A_1)$ vibrational energy.

Acknowledgments. This work was supported by the donors of the Petroleum Research Fund, administered by the American Chemical Society, and the Research Corp. W.L.H. wishes to thank Wayne State University for a Summer Research Fellowship.

References and Notes

(1) C. J. Mazac and J. W. Simons, *J. Am. Chem. Soc.*, **90**, 2484 (1968).
(2) W. L. Hase, W. G. Brieland, and J. W. Simons, *J. Phys. Chem.*, **73**, 4401 (1969).
(3) J. C. Polanyi and W. H. Wong, *J. Chem. Phys.*, **51**, 1439 (1969).
(4) P. J. Hay, W. J. Hunt, and W. A. Goddard III, *Chem. Phys. Lett.*, **13**, 30 (1972).
(5) C. F. Bender, H. F. Schaefer, D. R. Franceschetti, and L. C. Allen, *J. Am. Chem. Soc.*, **94**, 6888 (1972).
(6) M. J. S. Dewar, R. C. Haddon, and P. K. Weiner, *J. Am. Chem. Soc.*, **96**, 253 (1974).
(7) W. L. Hase, R. J. Phillips, and J. W. Simons, *Chem. Phys. Lett.*, **12**, 161 (1971); R. J. Phillips, M.S. Thesis, New Mexico State University, Las Cruces, N.M.
(8) M. G. Topor and R. W. Carr, Jr., *J. Chem. Phys.*, **58**, 757 (1973).
(9) K. C. Kim and D. W. Setser, *J. Phys. Chem.*, **77**, 2021 (1973).
(10) W. L. Hase, W. G. Breiland, P. W. McGrath, and J. W. Simons, *J. Phys. Chem.*, **76**, 459 (1972).
(11) J. W. Rabalais, J. M. McDonald, V. Scherr, and S. P. McGlynn, *Chem. Rev.*, **71**, 73 (1971).
(12) P. G. Bowers, *J. Chem. Soc. A*, 466 (1967).
(13) G. B. Kistiakowsky and B. B. Saunders, *J. Phys. Chem.*, **77**, 427 (1973).
(14) J. W. Simons and G. W. Taylor, *J. Phys. Chem.*, **73**, 1274 (1969); G. W. Taylor and J. W. Simons, *ibid.*, **74**, 464 (1970).
(15) W. Braun, A. M. Bass, and M. Pilling, *J. Chem. Phys.*, **52**, 5131 (1970).
(16) W. L. Hase and J. W. Simons, *J. Chem. Phys.*, **54**, 1277 (1971).
(17) The collision frequency was calculated using the following diameters: CH_2, 3.8 Å, $(CH_3)_2SiH_2$, 6.6 Å.
(18) R. C. Dobson, D. M. Hayes, and R. Hoffman, *J. Am. Chem. Soc.*, **93**, 6188 (1971).
(19) N. Bodor, M. J. S. Dewar, and J. S. Wasson, *J. Am. Chem. Soc.*, **94**, 9095 (1972).

Department of Chemistry
Wayne State University
Detroit, Michigan 48202
Patrick M. Kelley
William L. Hase*

Department of Chemistry
New Mexico State University
Las Cruces, New Mexico 88001
John W. Simons

Received November 22, 1974

SILICATE SCIENCE, Volumes 6 and 7

by WILHELM EITEL

Volumes 6 and 7 of this impressive treatise are thorough revisions of Volumes 1 and 2 of SILICATE SCIENCE—a work that provides investigators with information on the basic chemistry of silicates and their applications in glass, ceramic, and construction technology.

Volume 6—Silicate Structures—outlines and updates the crystallochemistry of the silicates, bringing it into harmony with the present state of research. It comprises three sections: (A) The Silicate Crystal Structures; (B) The Structures of Clay Minerals; and (C) Silicate Dispersoids. Volume 7—Constitution and Technology of Glasses—is organized on the same bibliographical principles as Volume 2 but emphasizes a quasi-encyclopedic use of information by references and text descriptions. It includes Section (A) Constitution and Physical Chemistry of Silicate Glasses, and Section (B) Silicate Glasses, Their Industrial Production Properties and Applications.

Vol. 6, 1975, 840 pp., $59.50/£28.55
Vol. 7, 1975, in preparation

EXCITED STATES, Volume 2

edited by EDWARD C. LIM

This new serial publication provides an authoritative guide to advances in fundamental research on the formation, properties, and relaxation of electronically excited states of polyatomic molecules. The study of molecular excited states has made rapid growth in recent years due to the development of various experimental and theoretical techniques, growing interest in and understanding of radiationless transitions, and increasing use of knowledge in photochemistry, radiation chemistry, photobiology, and molecular photophysics. The series will cover such topics as molecular luminescence, radiationless transitions, elementary photochemical processes, geometries and dipole moments of excited states, excitons and phonons in molecular crystals, energy transfer, and many others. It will prove invaluable to spectroscopists, photochemists, radiation chemists, photobiologists, and quantum chemists.

Contents: Geometries of Molecules in Excited Electronic States, *K. Keith Innes;* Excitons in Pure and Mixed Molecular Crystals, *Raoul Kopelman;* Some Comments on the Dynamics of Primary Photochemical Processes, *Stuart A. Rice;* Electron Donor-Acceptor Complexes in Their Excited States, *Saburo Nagakura.*

1975, 416 pp., $29.50/£14.15

FOUNDATIONS OF QUANTUM DYNAMICS

by S. M. BLINDER

In this monograph, Professor Blinder examines the mathematical formalism of nonrelativistic quantum dynamics. He describes the structure and foundations of this formalism in detail, emphasizing fundamental principles rather than concrete applications, but still slanting his approach towards application in the areas of molecular physics and quantum chemistry.

Contents: Classical Dynamics; Electrodynamics; Survey of Quantum-Mechanical Formalism; Principles of Quantum Dynamics; The Free Particle; Green's Functions; Theory of Transitions; Matter and Radiation; Appendix A: The Dirac Deltafunction; Appendix B: Fourier Analysis.

1974, 236 pp., $17.25/£6.50

ZEROVALENT COMPOUNDS OF METALS

By L. MALATESTA and S. GENINI
ORGANOMETALLIC CHEMISTRY: A Series of Monographs

Despite a recently growing number of books in the fields of coordination and organometallic compounds, this is the first work to deal with the chemistry of zerovalent compounds of metals—an area attracting an increasing number of research workers from the fields of fundamental and applied chemistry.

The first part of the volume comprises a survey of the present understanding of factors determining the existence and stability of compounds having metals in a zerovalent state and shows the results of applying discoveries achieved by the introduction of refined physico-chemical techniques such as i.r., n.m.r. and photoelectron spectroscopy and X-ray diffractometry to several problems. In the second part of the book the chemistry of complexes having tricovalent P, As and Sb derivatives as ligands is accurately reviewed, and the methods of synthesis, chemical reactivity and physico-chemical properties of these compounds are reported and discussed with reference to conclusions reached in the first section. There is also a discussion of the chemistry of isocyanide complexes, strictly related to the derivatives considered above.

1974, 242 pp., $19.75/£7.50

PROBLEMS IN THERMODYNAMICS AND STATISTICAL PHYSICS

edited by P. T. LANDSBERG
A Volume in the PION PROBLEMS FOR ADVANCED STUDENTS Series

This book is intended for teachers, undergraduates, and postgraduates in mathematics, physics, chemistry and engineering. It covers a full range of topics in thermodynamics, statistical physics, and statistical mechanics and is divided into 28 chapters. Each chapter has been designed by an expert in the field with the result that the book presents a penetrating view of statistical physics and its uses. There are new and original presentations in various areas, and in several sections recent research work has been incorporated in book form for the first time.

1971, 581 pp., $16.75/£6.50
Published by Pion Ltd. Distributed by Academic Press.

Prices subject to change without notice.

ACADEMIC PRESS, INC.

A Subsidiary of Harcourt Brace Jovanovich, Publishers
111 Fifth Avenue, New York, N.Y. 10003
24–28 Oval Road, London NW1 7DX